Università degli Studi di Torino
Doctoral School of the University of Torino
PhD Programme in Chemical and Materials Sciences XXXVI Cycle

Optimization of Ti insertion in zeolite catalysts: from TS-1 to Ti-MWW

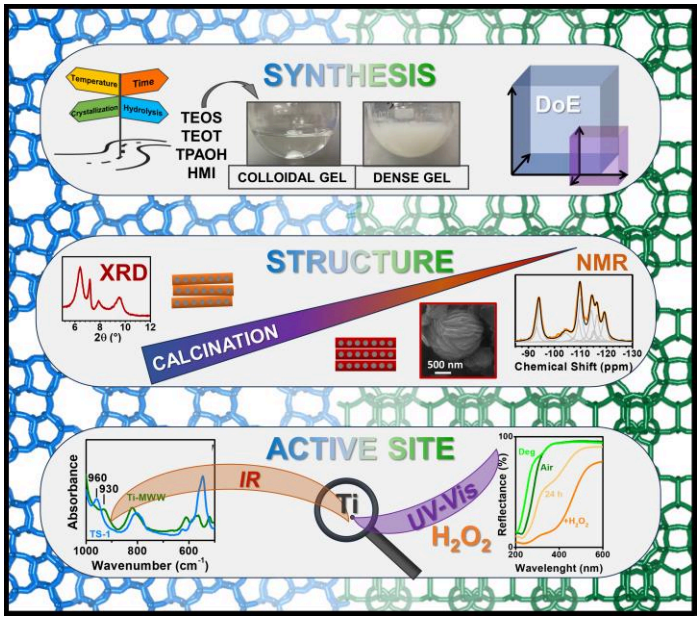

Francesca Rosso

Supervisor:
Prof. Francesca Carla Bonino

Università degli Studi di Torino

Doctoral School of the University of Torino

PhD Programme in Chemical and Materials Sciences XXXVI cycle

Optimization of Ti insertion in zeolite catalysts: from TS-1 to Ti-MWW

Candidate: **Francesca Rosso**

Supervisor: Prof. **Francesca Carla Bonino**

Jury Members: Prof. **Gabriele Ricchiardi**
Università degli Studi di Torino
Dipartimento di Chimica

Prof. **Massimo Migliori**
Università della Calabria
Dipartimento di Ingegneria dell'Ambiente (DIAm)

Prof. **Nataša Zabukovec Logar**
National Institute of Chemistry, Ljubljana
Department of Inorganic Chemistry and Technology

Head of the Doctoral School: Prof. Alberto Rizzuti
PhD Programme Coordinator: Prof. Bartolomeo Civalleri

Torino, 2024

Table of contents

Preface

This PhD project is devoted to the optimization of the Ti insertion in siliceous zeolites. The interest in the Ti-zeolites comes from the long-lasting experience in the characterization of Titanium Silicalite-1 (TS-1) catalyst in the research group where the PhD project was developed.

The synthesis of TS-1 was an unavoidable step to climb when approaching the topic. The study of TS-1 synthesis started as a "gym" for other zeolite frameworks and it ended as an interesting and challenging topic to explore. This study is exposed in Chapter 3.

The synthesis of Ti-MWW zeolite was first approached without any background knowledge about the framework, but it soon became clear that the synthesis mechanism of the siliceous zeolite with MWW framework (ITQ-1) needed to be understood first. In order to fully investigate this system, I also spent three months in the laboratory headed by Prof. Svetlana Mintova "Laboratory of Catalysis and Spectrochemistry", LCS, ENICAEN, Normandy University, Caen, France. Chapter 4 reports the study related to the synthesis and characterization of ITQ-1 zeolite and Chapter 5 the work performed on Ti-MWW catalyst.

1. INTRODUCTION

1.1. Zeolites and their applications

Zeolites are crystalline materials composed of TO_4 tetrahedra (where T may be Si^{4+}, Al^{3+}, B^{3+}, Ge^{4+}, Ti^{4+}, Ga^{4+},…) arranged in a three-dimensional (3D) framework, to form a system of ordered channels and cavities of molecular dimensions.[1–4] The Primary Building Units (PBUs) are tetrahedra in which four oxygen atoms (O) surround a central T atom; the O^{2-} moieties are shared between the tetrahedra, to form a broad set of Composite Building Units (CBU). The assembly of the CBUs forms the various infinitely extended zeolitic frameworks.[1–4]

The zeolites are applied in three fields of notable economic importance:[5–11] the catalysis (acid and redox), the gas separation (as molecular sieves and adsorbents) and the ion exchange. Depending on the valence of the T atom, the framework can be neutral (*e.g.* in silicates or germanosilicates) or charged (*e.g.* in aluminosilicates or borosilicates), requiring the presence of a counterion (*e.g.* extra-framework metal cations or protons).[4] Acid catalysis is conducted on charged zeolites (typically aluminosilicates) where the counterion is embodied by a proton that behave as a Brønsted acid center.[9–11] Redox catalysis is performed when a metal center with redox properties (Ti^{4+}, Fe^{4+}, Sn^{4+},…) is inserted in the framework.[12–14] The presence of the crystallographically defined pores is fundamental when the zeolites are applied in catalysis, since they dictate size and shape selectivity, directing the reactions to desired products.[1–3,5,6] The ion exchange processes exploits the presence of loosely bound extra-framework metal cations that can be easily exchanged.[5,11] The gas separation by adsorption exploits the different affinity of the extra-framework metal cations toward different molecules, while the

size and shape of the pores govern the separation, when zeolites are used as molecular sieves.[5–8]

In this work, neutral zeolitic frameworks composed of Si^{4+} and Ti^{4+} cations will be under investigation, with the target of study their synthesis as redox catalysts.

1.2. Brief historical background

The term zeolite (from the Greek zéō = to boil, and líthos = stone) was coined in 1756 by the chemist Axel Cronstedt, who observed that the mineral stilbite appeared to boil upon heating.[15] The first synthesized zeolite was levynite (LEV framework type) in 1862 and the first synthesized zeolites unknown as natural mineral were the P and Q later found to have KFI framework, in 1948. P and Q were obtained while exploring the hydrothermal conversion of natural minerals phases at high temperatures (170 to 270 °C), under the effect of strong salt solutions.[1,16] In 1949, the fruitful work of Robert Milton in the Linde corporation began, with the aim of producing synthetic chabazite (CHA, considered suitable for application in industrial separation processes but scarce in nature).[1] Zeolites A (LTA), B (Na-P) and C (hydroxysodalite), X (FAU) and finally CHA were synthesized within 1950 and the zeolites A[17] and X[18] were patented in 1959.

In the 1960s, the use of quaternary ammonium cations during the zeolite synthesis was first experimented,[1,19] leading to the synthesis of the first silica-rich zeolite (among others, zeolite A, Si/Al up to 1.7) and of the first high-silica zeolite, β, with $5 < Si/Al < 100$, prepared using the triethylammonium (TEA) cation, in 1967.[1,20] The significancy of the high-silica zeolites was fully appreciated in the next decade, and the field underwent a rapid development. The first patent of the ZSM-5 (MFI) was published in 1972[21] and the discovery of the silicalite-1 (S-1, MFI) occurs in 1978.[1,22] It was the first polymorphs of

silica having analogous crystalline structure to a zeolite and its discovery heavily affected the basic concepts of the zeolite synthesis, *i.e.* high-silica zeolites were now conceived as impure silica polymorphs, the modification of the zeolite properties upon increasing the Al content must be smooth for isostructural materials and any proposed synthesis mechanism must cover the whole range of compositions.[1]

The 1980s was the decade of the innovations. The possibility of performing syntheses in alkali metal-free conditions was explored: NH_4OH or NR_4OH were used to provide the necessary alkalinity, avoiding the necessity of the ion exchange step to obtain the protonic zeolite.[1] Awareness grew about the possibility of substituting limited amounts of different elements (*e.g.* transition metals) into the zeolite framework, in highly or purely siliceous frameworks, thank to their low lattice charge.[1,23–25] Among the metal-zeolites, the synthesis of the Titanium Silicalite-1 (TS-1) was patented for the first time by Taramasso, Perego and Notari, in 1983.[23,24] TS-1 is isomorphic to S-1, with few Ti^{4+} substituted to Si^{4+} in framework, tetrahedral positions. The substitution occurs similarly to what happens for Al^{3+}, but in lower amount compared to the range of Al^{3+} substitution. It was the first heterosubstituted zeolite that showed significant chemical activity, different from the acidic one. A series of post-synthesis treatments has come to be used, for the hydrothermal insertion or re-insertion of heteroatoms,[1,26] together with the proof of the reversible nature of the zeolites,[1,27] *e.g.* the ^{18}O can be exchanged in $H_2{}^{18}O$ and the hydroxyl groups can be cleaved in NH_4-ZSM-5 even at 95 °C.[27]

In the 1990s, the ordered mesoporous materials were invented, the first being the M41S family of materials.[28] They had extremely high Specific Surface Area (SSA, ≈ 900 m^2/g in MCM-41) and ordered mesopores.[1,28,29] The 2000s brought the beginning of the calculation methods applied to the zeolites: occluded templates and crystallization process were modelled.[1,2,30]

Under the experimental point of view, new structures were generated, with ring sized larger than 12-T atoms, first in the metallophosphate systems and very recently in aluminosilicate and purely siliceous systems.[1,30–33] The first approach to materials which combine different levels of porosity (hierarchical pore structures) must also be reported.[34,35]

1.3. Hydrothermal synthesis of the zeolites

The discovery of the hydrothermal preparative method was done in 1845 by Karl Emil von Schafhäutl, who prepared microscopic quartz crystals in an autoclave reactor.[36] The production of quartz is nowadays a significant use of hydrothermal chemistry.[36] It is conducted in alkaline media in a temperature gradient of 400-380 °C, at 1000 bar. The *Handbook of Hydrothermal Technology* (Second Edition, 2013)[37] define the term "hydrothermal" as "any heterogeneous reaction in the presence of aqueous solvents or mineralizers under high-pressure – high-temperature (HPHT) conditions to dissolve and recrystallize (recover) materials that are relatively insoluble under ordinary conditions" and it reports slight discrepancies among terminologies and definitions given by different authors (*e.g.* regarding the lower limits for the temperature and pressure or when novel synthetic routes are involved, *e.g.* solvothermal procedures or use of a microwave heating source).

The two main components involved in the hydrothermal synthesis in general are the water and the mineralizer.[36,37] Two other important components when zeolites are involved are the organic compounds and the T atom source.[38] In the following, each of them will be discussed briefly.

1.3.1. Water

The water is the main actor in the hydrothermal synthesis. Its PVT data and other physical and chemical properties (such as viscosity, dielectric constant, density and dissociation constants) are accurately known up to 1000 °C and 10 kbar. Its PT diagrams are particularly important when laboratory scale hydrothermal treatments are conducted.[36,37] Figure 1.3.1.1 shows the variation of the internal pressure of the autoclave depending on the temperature and the degree of filling. When 80-90% of filling were used, the pressure rises very steeply even below 200 °C, determining very serious safety issues, but the hydrothermal synthesis of the zeolites is conducted in mild conditions, generally at temperatures comprised between 80 °C and 200 °C, at autogenous pressure (yellow rectangle in Figure 1.3.1.1).[2,3,36,37]

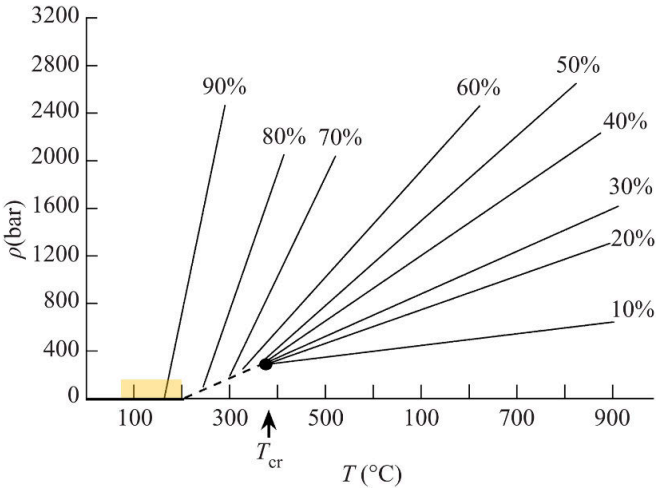

Figure 1.3.1.1. Diagram showing the dependence of pressure on the temperature and of the degree of filling (%) for pure water in an autoclave. The black point indicates the critical temperature (T_{cr} = 374.1 °C) and the critical pressure (ρ = 221.2 bar). The yellow rectangle shows the region exploited for the synthesis of zeolites. Reproduced from Ref. 36.

In the present thesis work, degrees of filling higher than 66% were never used, as indicated in the Safety Data Sheets of the vendors of the used autoclaves and Teflon liners. In these conditions, the autogenous pressure is substantially governed by the water vapor pressure, when pure water is used (Figure 1.3.1.2).[39,40] This topic will be further discussed in Chapter 4. Finally, the water proved to have extremely effective solvating abilities, allowing the dissolution and mixing of the liquid and solid components used in the synthesis of the zeolites, under hydrothermal conditions.[30,36] This is believed to be the reason of the success and versatility of the hydrothermal treatment in the synthesis of microporous materials. [36]

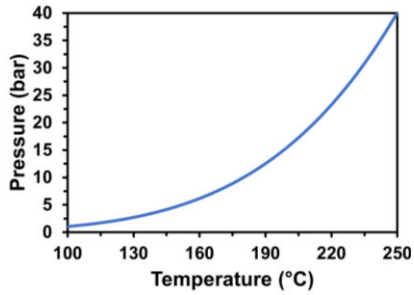

Figure 1.3.1.2. Plot of the vapor pressure of pure water in the 100-250 °C and 0-40 bar ranges of temperature and pressure, respectively.

1.3.2. Mineralizer

The mineralizer must play the following roles: (i) convert the starting materials into mobile forms (*e.g.* solubilizing the silica source), (ii) act as transport means for the mobile units, so that they can react together to form T-O-T bonds and hence the zeolite framework and (iii) ensure the reversibility of point (ii). If the T-O-T bonds formed during point (ii) were not reversible, the formation of fractal structures would be observed.[1,2,37]

The most common mineralizer is the OH^- anion. In this case, the synthesis is conducted in basic medium and the condensation equilibria are the following: [2,41]

$$T-OH \;+\; {}^-OH \;\rightleftarrows\; T-O^- \;+\; H_2O \qquad (1.1)$$

$$T-OH \;+\; T-O^- \;\rightleftarrows\; T-O-T \;+\; {}^-OH \qquad (1.2)$$

$$T-OH \;+\; T-OH \;\rightleftarrows\; T-O-T \;+\; H_2O \qquad (1.3)$$

Most of the research conducted on the nucleation and growth process during the zeolite formation was conducted on systems containing OH^-.[2]

Alternatively, the fluoride anion (F^-) can be used as mineralizer.[2,30] Its use is advantageous when a wide range of pH is necessary to provide the solubility of some heteroatoms. Large crystals (in terms of zeolite dimension) can be obtained and sometimes the fluoride route may be the only one for obtaining a specific zeolite framework. The solubility of the species and the effective supersaturation are lower when the fluoride route is used, determining higher temperatures and longer reaction time compared to the use of OH^-, but the importance of the presence of F^- in the reaction mixture is testified by the tendence of the products to contain structural F^-. F^- can be located in the double-4-ring (D4R) SBU and it plays an important role in stabilizing the structures.[2,30]

The chelating oxygen ligands (such as *ortho*-dihydroxy aromatic compounds and glycols, well known complexing agents for silicon) are another class of compounds that was explored as mineralizer.[2]

1.3.3. Organics compounds

The use of organic compounds is often necessary when the synthesis of specific frameworks must be achieved, especially for high-silica zeolites.[2,20] Usually a strong geometric match is observed between the organic molecule

and the obtained framework, but cases are known of organic molecules used to synthesize different zeolitic frameworks in different conditions (*e.g.* N,N,N-trimethyl-adamantly-ammonium hydroxide, TMAdaOH, used for the preparation of all-silica CHA and all-silica MWW). Davis and Lobo classified the organic molecules used in the synthesis of zeolites in three groups, considering the possibilities of the presence or absence of a specific match. (i) The "space fillers" are molecules used for synthesizing different framework; (ii) the "Structure Directing Agents" (SDA) are able to direct the formation of a specific product; and (iii) the "true templates" impose its geometric and electronic configurations to the formed framework. For simplicity in the following the organic molecules used in the synthesis will be called Organic SDAs (OSDAs), independently on their exact action.[20]

Studies on the structure-direction mechanism were conducted on the clathrasils.[2,20] Clathrasils are tectosilicates that contain in their cages small organic or inorganic molecules. Their synthesis was studied by varying the size of cyclic organic molecules and it was found that the size and the shape of the molecule determine the crystallized product. Hence, bigger molecules directed the synthesis of clathrates with bigger cages. The nature of the product was independent on the chemical properties (*e.g.* cyclopentane, tetrahydrofuran and pyrrolidine) but they were found to influence the crystallization rate: the stronger the basicity of the molecule, the higher the crystallization rate is. By continuing to increase the size of the OSDAs, the products were not clathrasils anymore, but large-pore zeolites. When linear molecules were used, medium pore zeolites were obtained (containing 10-MR channels) and by adopting branched molecules, 3D pore structures were obtained (*e.g.* the MFI framework).[2,20]

Tetraalkylammonium cations are often used as OSDAs, in hydroxide (OSDA-OH) or in halogenide (OSDA-X) form. In the former situation, the mineralizer OH^- is directly provided by the OSDA, while in the latter one, the use of a

strong base (such as NaOH or KOH) is necessary. The cations (both organic and inorganic) in the synthesis conditions assist the ordering of the TO_2 species because they induce the formation of a coordination sphere composed of oxy-species, around themselves. When the oxy-species are T-O-T or T-O^- or TO_2 small aggregates, the cations would originate preferred orientations during the assembly process of the final zeolite.[30]

1.3.4. Source of T atoms

The use of different T atom sources may affect the composition of the material and the nucleation equilibria.[2]

The composition can be affected by the degree of purity of the source; the typical situation where this happens involves the silica source. The commonly used sources are precipitated silica, colloidal silica, fumed silica and tetraalkylorthosilicates (prevalently tetraethylorthosilicate, TEOS). They could contain traces of Al^{3+}, but the amount of Al^{3+} decreases in the listed order. Therefore, zeolites with Si/Al ratios above 200, above 6000, above 10000 or purely siliceous zeolites can be obtained respectively, going from precipitated silica to TEOS. TEOS is the preferred reagent when purely siliceous materials should be obtained. However, the ethanol produced from its hydrolysis changes the medium of the synthesis. Its effect is slight, but it can determine the nucleation of undesired products, if not evaporated.[4]

The use of different T sources also influences the condensation equilibria reported above (eq. 1.1, 1.2 and 1.3), allow to approach them from different directions.[2] This may affect the nucleation kinetic of different phases, favoring or inhibiting the precipitation of the desired product, where in other condition mixtures could co-crystallize.[2] An example of this situation will be discussed in paragraph 4.3.5.

Since part of the present thesis work is focused on the synthesis of Ti-zeolites, a digression is worth regarding the Ti sources commonly used in the zeolite synthesis. As mentioned in paragraph 1.2, TS-1 is a Ti-zeolite where a low amount of Ti^{4+} is isomorphously substituted in the MFI framework. The tendency of Ti^{4+} to assume the octahedral coordination instead of the tetrahedral one makes the synthesis of Ti-zeolites particularly difficult.[4,42–44] When the traditional hydrothermal synthesis is used, TEOS was found to be the best choice for the Ti source.[42] The used sources of Ti are usually tetra-coordinated Ti compounds, such as tetraalkyl orthotitanates (tetraethylorthotitanate, TEOT, tetraisopropyl orthotitanate, TiPOT, or tetrabutyl orthotitanate, TBOT) or Ti-halides ($TiCl_4$, TiF_4,…).[4,23,42] They differ for the hydrolysis rate in synthesis conditions. The hydrolysis rate is a fundamental parameter, because comparable hydrolysis rates of the TEOS and the Ti^{4+} sources are reported to be necessary for the concurrent condensation of silicates with monomeric Ti-containing species.[42,44,45] Otherwise, the self-condensation of the Ti-containing species leads to the precipitation of insoluble TiO_2. This topic will be deepened in Chapter 3.

1.3.5. Nucleation and growth process

When Si- and metal-alkoxides (TEOS, TBOT, TEOT,…) are used as T atom sources and OH^- is used as mineralizer, the zeolite synthesis is often a three step-procedure. First, the alkoxides are hydrolyzed in basic medium, then a period of aging is conducted, in presence of the OSDA, followed by the hydrothermal treatment.[2,3] The nucleation and growth process that yield the desired zeolitic material occur through this whole procedure. Many studies were conducted to understand the synthesis mechanism of the zeolites and here the most probable mechanism of the zeolite formation is summarized, as reported by Cundy and Cox.[2] The process is divided macroscopically in two

moments: induction period and crystal growth (Figure 1.3.5.1a). The induction period is the time between the start of the synthesis reaction and the moment in which crystalline products are first detected and the crystal growth is the moment in which the growth of the detected crystalline products is observed. The induction period is further divided into three moments: the relaxation time, *i.e.* the time necessary to mix the reagents and to reach the desired temperature, the time necessary to form stable nuclei and the time for the nuclei to reach a detectable size. After the relaxation time, an amorphous gel frequently forms (primary amorphous phase, "initial gel" in Figure 1.3.5.1b). It can be a colloidal suspension, invisible to the naked eye ("clear solution" syntheses) or it can be a gel, visible to naked eye. The primary amorphous phase is probably heterogeneous and out of equilibrium.

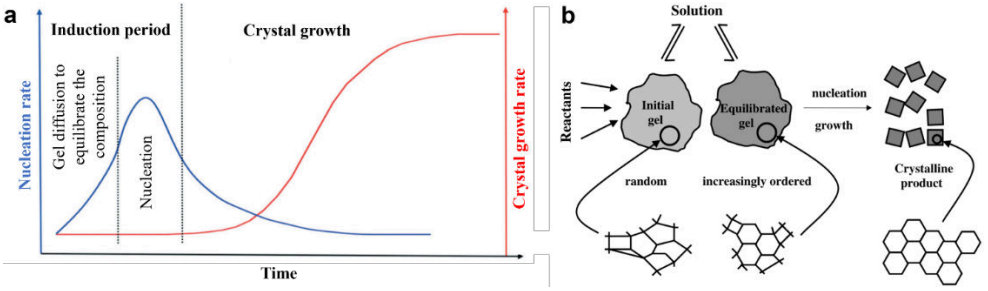

Figure 1.3.5.1. (a) Schematic representation of the nucleation rate (blue curve) and of the crystal growth rate (red curve). Adapted from Ref. 3 (b) Evolution of order from the primary amorphous phase (initial gel) to the secondary amorphous phase (equilibrated gel), through the solution, and final nucleation and growth leading to the crystalline product. Reproduced from Ref. 2.

Thank to equilibration reactions, the primary amorphous phase is converted into a secondary amorphous phase ("equilibrated gel" in Figure 1.3.5.1b). The secondary amorphous phase is a partially ordered phase formed by the

dissolution and reprecipitation of the primary amorphous phase. The partial ordering is regulated through the equilibria of condensation-dissolution catalyzed by the mineralizing agents (OH^- or F^-) and by the coordination effect of the cations (both organic and inorganic). The secondary amorphous phase is in a pseudo-steady-state and hence it is continuously evolving: the condensation and dissolution are obviously reversible, and the coordination effect of the cations is reversible as well. Regions called "island of order" or "proto-nuclei" can be formed in the secondary amorphous phase, and if they are stable enough to reach the critical radius (*i.e.* the minimum radius that a "proto-nucleus" should have so that its accretion is faster than its dissolution), the nucleation occurs.

After the nucleation, the crystals grow with the classical S-shaped curve (red curve in Figure 1.3.5.1a). The growth can occur by addition of small units or by aggregation of particles of comparable dimension. In the zeolites, the first one is the predominant mechanism that makes increase the crystals dimension.

1.4. Post-synthesis procedures

The post-synthesis modifications are a series of treatments applied to the zeolites after the hydrothermal crystallization, with the purpose of (i) maximizing the performances of the zeolite, by controlling properties, distribution and accessibility of the active sites, (ii) decreasing the impact of unfavorable properties and deactivation, (iii) shaping and (iv) regenerating the same. They include thermal (calcination) or chemical (oxidation) activations, functionalizations, modifications of framework composition (ion exchange, demetallation, acidity modification) or improving the accessibility, by a secondary porosity system or particle size modification.[4,46]

In this thesis work, particular attention was paid to the calcination procedures and to the use of acidic post-synthesis treatments. The effect of different calcination procedures was analyzed in Chapters 3 and 4 and the different consequences of the application of an HNO_3 washing were studied in Chapter 5.

The calcination is the procedure used to eliminate the OSDA from the pores and cavities of the zeolites. This is not the only effect it can have: it may affect the crystallinity, the condensation of silanol groups and the accessibility of the acid sites. In particular, the atmosphere used for the calcination is observed to affect the temperature at which the OSDA is oxidated, giving the opportunity of directing the other properties.[46]

Acid washings are an easy procedure used to oxidize and extract the occluded OSDAs in mesoporous materials. In the case of zeolites, the smaller pore openings and the stronger OSDA-wall interactions compared to mesoporous materials make necessary harsher conditions. Often the OSDA removal by acid treatments is reported to be incomplete in zeolites. When aluminosilicate zeolites are involved, the acid treatments are also used to extract framework aluminum cations to modify the framework composition, to insert an additional level of porosity or to operate an isomorphous substitution with a different heteroatom, in the remaining defective sites (silanol nests).[4,46] It will be shown later that in this thesis work (Chapter 5), the acid treatment will produce a combination of these and other effects.

1.5. Ti-doped zeolites for partial oxidation reactions

Ti-zeolites are zeolitic catalysts used for several partial oxidation reactions (*e.g.* phenol hydroxylation,[24,47–49] alkene epoxidation[12,50–54] or ketone ammoximation[55–58]), using hydrogen peroxide (H_2O_2) as oxidizing agent. [12,42] The isomorphous substitution of small percentages (2-3%) of Si by Ti atoms in the zeolite lattice provides Ti uncoordinated sites that are able to adsorb the H_2O_2.[59] Upon adsorption, the Ti-hydroperoxo (Ti-OOH) or Ti-peroxo (Ti-OO^-) complexes are formed. The complexes can be monodentate (η_1) or bidentate (η_2). The structure of the Ti-OO^- complex in Ti-zeolites is known to be η_2 by comparison with diffraction studies conducted on reference $(NH_4^+)_3(TiF_5O_2)^{3-}$ complex. Conversely, no Ti-OOH complex model compound is known, hence it is not possible to know its structure. It can be hypothesized that both are possible because the Ti-OO^- species can form by dehydration of both η_1 or η_2 Ti-OOH.[59] The investigations regarding the nature of the active species are still ongoing, but considering the Ti-OOH intermediate species active is the most accepted view.[12,59,60] The electrophilic transfer of an oxygen to the organic substrate closes the catalytic cycle, with the production of only a H_2O molecule as by-product.[12]

The TS-1, with MFI framework, is the best known and most studied Ti-zeolite. The MFI framework hosts a 3D network of interconnected 10 Member-Ring (MR) channels. The channels run straight along the *b* axis and sinusoidally along the *a* and *c* axes.[61,62] Figure 1.5.1 shows the projections of the MFI framework along the *a*, *b* and *c* axes.

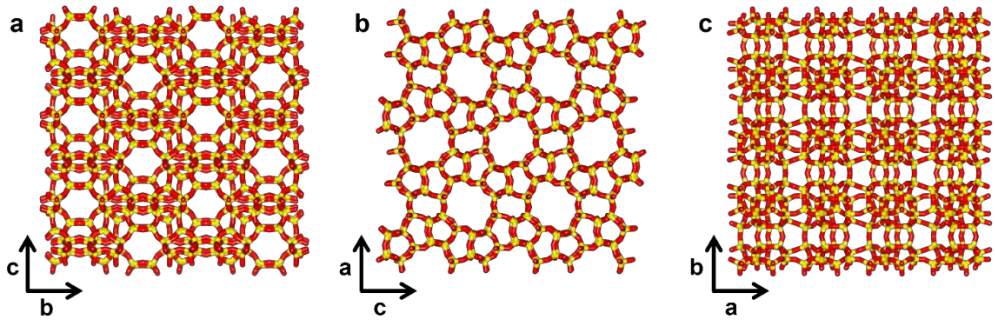

Figure 1.5.1. Projections of the MFI framework along the (a) *a*, (b) *b* and (c) *c* axes. The framework is represented with the stick model for the sake of clarity. Si atoms are depicted in yellow, O atoms are depicted in red.

The catalytic activity of TS-1 is strongly affected by the environment around the Ti(IV) center. Isolated Ti atoms in tetrahedral coordination with the surrounding O are commonly believed to be the most active sites for the partial oxidation reactions, even if some alternative situations have been proposed.[12,63–68] The real synthesized TS-1 samples often contain other species,[52,69–71] namely bulk titanium dioxide (TiO_2), in the anatase polymorph, where Ti is in octahedral coordination, and isolated Ti species with distorted or intermediate coordination between the tetrahedral and the octahedral (often referred as intermediate or amorphous sites in the following).[52,69–71] The catalytic activity of these sites is hardly debated (indeed the different interaction with the H_2O_2 may lead to modified catalytic cycles) and the presence of anatase is reported to lead to unfruitful decomposition of the H_2O_2.[42] Hence, their formation must be avoided during the synthetic process. The critical analysis of the literature regarding the TS-1 synthesis[43,45,72–78] reveals that the precise influence of the Si and Ti sources and of the synthesis conditions (time, temperature, stirring,…) on the Ti proper insertion in the zeolite framework are still unclear. For this reason, Chapter 3 of this thesis will be devoted to the optimization of the synthesis of TS-1.

A field where the academic literature put big efforts is proposing alternatives to solve the TS-1 limitations. Its limited pore dimension restricts its application to the oxidation of small substrates, making necessary the research for an alternative zeolitic framework with bigger pores.[42] Moreover, the geometry of the pores in form of channels imposes diffusion constraints, that may be solved by boosting the catalyst with an additional porosity level or by reducing the catalyst dimension.[13,34,79–81] Some alternatives were proposed regarding the choice for another zeolitic framework,[57,82–86] and among them, in this thesis work, the attention was focused on the MWW framework.[87,88] The MWW framework seems to overcome both the issues in one single solution. The zeolites with MWW framework crystallize with a nanosheets morphology, reducing the path necessary for the diffusion of reagents and products. Moreover, their peculiar pore system makes them catalytically behave as 12 MR zeolites.[89] Figure 1.5.2 shows the projections of the MWW framework in the three dimensions. The framework is layered and hosts two independent pore systems. The first one is composed of 10 MR sinusoidal channels running intralayer (their apertures are visible in Figure 1.5.2a, b). The second one is composed of internal super-cages with a 12 MR circumference and a height of 18.2 Å. At the external crystal surface, the super-cages are cut and expose hemi-cages, that are blind 12 MR channels, and hence they impose analogous size and shape selectivity that a 12 MR zeolite would do.[87,88] Moreover, the MWW framework opens many opportunities of structural modifications, by for example pillaring the layers and making the internal super-cages more accessible.[89–92]

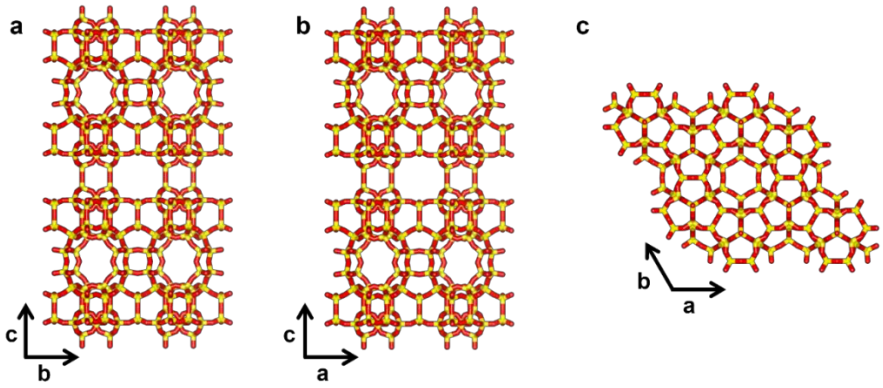

Figure 1.5.2. Projections of the MWW framework along the (a) *a*, (b) *b* and (c) *c* axes. The framework is represented with the stick model for the sake of clarity. Si atoms are depicted in yellow, O atoms are depicted in red.

Ti-MWW was first synthesized as titanium-boro-silicate (Ti-B-MWW) in 2001.[93] In this procedure, a deboronation by acid treatment was required to obtain the Ti-MWW catalyst. Even if the preparation of the Ti-B-MWW was done in a single batch, the authors identify in the acid treatment the moment when Ti was effectively inserted in the framework.[81,94] In the following years, a recipe to directly prepare the Ti-MWW catalyst was developed, in presence of two OSDAs: the TMAdaOH and the hexamethyleneimine (HMI).[57] The composition of the synthesis gel was obtained by the authors by modifying a recipe used to prepare the siliceous MWW zeolite, the ITQ-1.[95] The molar ratio between the reagents and the dilution of the gel were modified and potassium carbonate was added to the gel.[57,95] The acid treatment was however necessary to remove the extra-framework Ti species (amorphous and anatase) that precipitated during the hydrothermal crystallization. The reason why the recipe of the ITQ-1 needed modification for the aim of inserting Ti was not clear, hence a deep study of the differences between ITQ-1 samples synthesized using the original composition of the synthesis gel and with the composition used for inserting Ti, omitting the Ti source, was performed and exposed in Chapter 5 of this thesis. In this context, particular

attention was given to the as-synthesized, OSDA containing samples, and to the effect of different calcination procedures. This is the topic exposed in Chapter 4. Finally, the direct synthesis of the Ti-MWW sample was reproduced and the effect of the acid treatment was studied by comparison of a sample washed with acid and a directly calcined one.

Published results suggest that the Ti sites in Ti-MWW are slightly different respect to those ones in TS-1:[57,93,96] the vibrational fingerprint of tetrahedral Ti sites in TS-1 is a band at 960 cm^{-1} in the medium IR spectral region. In Ti-MWW two components, at 960 and at 930 cm^{-1}, are present in this region.[57,93] Computational studies indicate that the Ti atoms is Ti-MWW can be both in tetrahedral framework positions, *i.e.* $Ti(OSi)_4$, and in tetracoordinated $Ti(OSi)_3OH$ sites, probably explaining the splitting of the vibrational fingerprint.[96] Actually, a band at 930 cm^{-1} in the IR spectra of Ti-grafted MCM-41 and MCM-48 is was also found.[85,97] The behavior of the Ti sites in Ti-MWW in interaction with H_2O_2 and the acidic properties of Ti-MWW were not yet studied. Then, Chapter 5 was also devoted to the characterization of the acidic properties of the Ti-MWW sample and to the study of the interaction between Ti-MWW and the H_2O_2, by spectroscopic methods (IR and UV-Vis, in presence of probe molecules).

1.6. Optimization of the zeolite synthesis: Design of Experiment approach

The synthesis of the TS-1 zeolite exposed in Chapter 3 was performed with the Design of Experiments (DoE) approach and the application of the MultiVariate data Analysis (MVA). A digression is worth in this regard. The newcomer to the zeolite synthesis often feels that the optimization of a synthesis behind a published procedure is mainly based on the personal experience of a synthesizer and/or to serendipity. Often the unsuccessful

results (and sometimes also the successful ones) seem apparently unexplainable and/or irreproducible. The study of the conditions of the synthesis by the traditional One-Variable-At-Time (OVAT) method often gives, at best, unattainable good and, at worst, particularly unexplainable results. Despite the huge knowledge gained regarding the fundamental understanding of the zeolites crystallization mechanism, the necessary practical experience is difficult to transfer through written papers.

The DoE is a way to plan and conduct experiments in order to extract the maximum amount of information from the data collected, in presence of noise.[98,99] It was already applied to the synthesis of the zeolites, giving interesting results, both to explore the crystallization of different frameworks in a broad range of conditions[100,101] and to optimize the synthesis of a known material, by exploring small variables ranges.[102–106] In this context, it was applied to discern among the effects of multiple variables, used in a multi-stage synthesis procedure. Moreover, by repeating selected syntheses, it was possible to take into consideration the experimental variability on the properties of the catalyst obtained.

1.7. References

1 C. S. Cundy and P. A. Cox, *Chem. Rev.*, 2003, **103**, 663–701.

2 C. S. Cundy and P. A. Cox, *Microporous Mesoporous Mater.*, 2005, **82**, 1–78.

3 J. Grand, H. Awala and S. Mintova, *Cryst. Eng. Comm.*, 2016, **18**, 650–664.

4 S. Mintova, Alenka. Ristić, M. Rangus and Nataša. Novak Tušar, *Verified syntheses of zeolitic materials*, Synthesis Commission of the International Zeolite Association, 2016.

5 V. Van Speybroeck, K. Hemelsoet, L. Joos, M. Waroquier, R. G. Bell and C. R. A. Catlow, *Chem. Soc. Rev.*, 2015, 44, 7044–7111.

6 B. M. Weckhuysen and J. Yu, *Chem. Soc. Rev.*, 2015, 44, 7022–7024.

7 E. Pérez-Botella, S. Valencia and F. Rey, *Chem. Rev.*, 2022, **122**, 17647–17695.

8 D. G. Boer, J. Langerak and P. P. Pescarmona, *ACS Appl. Energy. Mater.*, 2023, **6**, 2634–2656.

9 A. Primo and H. Garcia, *Chem. Soc. Rev.*, 2014, **43**, 7548–7561.

10 W. Vermeiren and J. P. Gilson, *Top. Catal.*, 2009, **52**, 1131–1161.

11 C. Martínez and A. Corma, *Coord. Chem. Rev.*, 2011, **255**, 1558–1580.

12 V. Smeets, E. M. Gaigneaux and D. P. Debecker, *Chem. Cat. Chem.*, 2014, **14**, e202101132.

13 V. Smeets, E. M. Gaigneaux and D. P. Debecker, *Microporous Mesoporous Mater.*, 2020, **293**, 109801.

14 G. Berlier, V. Crocellà, M. Signorile, E. Borfecchia, F. Bonino and S. Bordiga, in *Struct. Bond.*, Springer International Publishing AG 2018, 2018, pp. 91–154.

15 B. M. Weckhuysen and J. Yu, *Chem. Soc. Rev.*, 2015, **44**, 7022–7024.

16 R. M. Barrer and C. Marcilly, *J. Chem. Soc. A Inorg. Phys. Theor.* 1970, 2735–2745.

17 R. M. Milton, US Patent 2,882,243, *Molecular Sieve Adsorbents* ,1959.

18 R. M. Milton, US Patent 2,882,244, *Molecular Sieve Adsorbents*, 1959.

19 R. M. Barrer and P. J. Denny, *J. Chem. Soc.*, 1961, 971–982.

20 R. F. Lobo, S. I. Zones and M. E. Davis, *J. Incl. Phenom. Mol. Recogn. Chem.*, 1995, **21**, 47–78.

21 R. J. Argauer and G. R. Landolt, US Patent 3,702,886, *Crystalline Zeolite ZSM-5 and Method for Preparing the Same*, 1972.

22 F. G. Dwyer and E. E. Jenkins, US Patent 3,941,871, *Crystalline Silicates and method of Preparing the Same*, 1976.

23 M. Taramasso, G. Perego and B. Notari, US Patent 4,410,501, *Preparation of Porpous Crystalline Synthetic Material Comprized of Silicon and Titanium Oxides*, 1983.

24 A. Esposito, M. Taramasso and C. Neri, US Patent 4,396,783, *Hydroxylating Aromatic Hydrocarbons*, 1983.

25 M. Taramasso, G. Perego and B. Notari, UK Patent 2,071,071A, *Titanium Modified Silica*, 1980.

26 V. Valtchev, G. Majano, S. Mintova and J. Pérez-Ramírez, *Chem. Soc. Rev.*, 2013, **42**, 263–290.

27 R. Von Bahmoos and W. M. Meier, *J. Phys. Chem.*, 1982, **86**, 2698–2700.

28 C. T. Kresge, J. C. Vartuli, W. J. Roth and M. E. Leonowicz, in *Stud. Surf. Sci. Catal.*, Elsevier, 2004, vol. 148, pp. 53–72.

29 A. Taguchi and F. Schüth, *Microporous Mesoporous Mater.*, 2005, **77**, 1–45.

30 A. Corma and M. E. Davis, *Chem. Phys. Chem.*, 2004, **5**, 304–313.

31 A. Corma, *J. Catal.*, 2003, **216**, 298–312.

32 J. Li, Z. Rei Gao, Q.-F. Lin, C. Liu, F. Gao, C. Lin, S. Zhang, H. Deng, A. Mayoral, W. Fan, S. Luo, X. Chen, H. He, M. A. Camblor, F.-J. Chen and J. Yu, *Science*, 2023, **379**, 283–287.

33 Q.-F. Lin, Z. R. Gao, C. Lin, S. Zhang, J. Chen, Z. Li, X. Liu, W. Fan, J. Li, X. Chen, M. A. Camblor and F.-J. Chen, *Science*, 2021, **374**, 1605–1608.

34 R. Bai, Y. Song, R. Bai and J. Yu, *Adv. Mater. Interfaces*, 2021, **8**, 2001095.

35 W. Schwieger, A. G. Machoke, T. Weissenberger, A. Inayat, T. Selvam, M. Klumpp and A. Inayat, *Chem. Soc. Rev.*, 2016, **45**, 3353–3376.

36 D. O'Hare, in *Encyclopedia of Materials: Science and Technology*, Elsevier, Second Edition, 2001, pp. 3989–3992.

37 K. Byrappa and M. Yoshimura, in *Handbook of Hydrothermal Technology*, eds. K. Byrappa and M. Yoshimura, Elsevier, Second Edition., 2013, pp. 1–49.

38 K. Byrappa and M. Yoshimura, in *Handbook of Hydrothermal Technology*, eds. K. Byrappa and M. Yoshimura, Elsevier, Second Edition., 2013, pp. 269–347.

39 D. Roizard, in *Encyclopedia of Membranes*, eds. E. Drioli and L. Giorno, Springer, Berlin, Heidelberg, 2014.

40 C. de la Calle-Arroyo, J. López-Fidalgo and L. J. Rodríguez-Aragón, *Chemometr. Intell. Lab. Syst.*, 2021, **214**, 104334.

41 C. J. Brinker and G. W. Scherer, *Sol-Gel Science: The Physics and Chemistry of Sol-Gel Processing*, Academic Press, INC, 1990.

42 G. Bellussi and R. Millini, in *Structure and Reactivity of Metals in Zeolite Materials,* 2017, pp. 1–52.

43 A. Tuel and Y. Ben Taârit, *Appl. Catal. A Gen.*, 1994, **110**, 137–151.

44 F. Rosso, A. Rizzetto, A. Airi, K. Khoma, M. Signorile, V. Crocellà, S. Bordiga, S. Galliano, C. Barolo, E. Alladio and F. Bonino, *Inorg. Chem. Front.*, 2022, **9**, 3372-3383.

45 A. Thangaraj, M. J. Eapen, S. Sivasanker and P. Ratnasamy, *Zeolites*, 1992, **12**, 943–950.

46 V. Valtchev, G. Majano, S. Mintova and J. Pérez-Ramírez, *Chem. Soc. Rev.*, 2013, **42**, 263–290.

47 A. Wróblewska, *React. Kinet. Mech. Catal.* 2013, **108**, 491–505.

48 R. Klaewkla, S. Kulprathipanja, P. Rangsunvigit, T. Rirksomboon and L. Nemeth, *Chem. Comm.*, 2003, **3**, 1500–1501.

49 H. Liu, G. Lu, Y. Guo and Y. Guo, *Appl. Catal. A Gen.*, 2005, **293**, 153–161.

50 X. Nie, X. Ji, Y. Chen, X. Guo and C. Song, *Mol. Catal.*, 2017, **441**, 150–167.

51 M. G. Clerici and P. Ingallina, *J. Catal.*, 1993, **140**, 71–83.

52 M. Signorile, V. Crocellà, A. Damin, B. Rossi, C. Lamberti, F. Bonino and S. Bordiga, *J. Phys. Chem. C*, 2018, **122**, 9021–9034.

53 J. Yin, H. Xu, B. Wang, W. Tian, J. Yin, J. Jiang and P. Wu, *Catal. Sci. Technol.*, 2020, **10**, 6050–6064.

54 H. Shima, T. Tatsumi and J. N. Kondo, *Microporous Mesoporous Mater.*, 2010, **135**, 13–20.

55 M. A. Mantegazza, G. Petrini, G. Spanò, R. Bagatin and F. Rivetti, *J. Mol. Catal. A Chem.*, 1999, **146**, 223–228.

56 G. Tozzola, M. A. Mantegazza, G. Ranghino, G. Petrini, S. Bordiga, G. Ricchiardi, C. Lamberti, R. Zulian and A. Zecchina, *J. Catal.*, 1998, **179**, 64–71.

57 H. Xu, Y. Guan, X. Lu, J. Yin, X. Li, D. Zhou and P. Wu, *ACS Catal.*, 2020, **10**, 4813–4819.

58 P. Yao, Y. Wang, T. Zhang, S. Wang and X. Wu, *Front. Chem. Sci. Eng.*, 2014, **8**, 149–155.

59 F. Bonino, A. Damin, G. Ricchiardi, M. Ricci, G. Spanò, R. D'Aloisio, A. Zecchina, C. Lamberti, C. Prestipino and S. Bordiga, *J. Phys. Chem. B*, 2004, **108**, 3573–3583.

60 T. Zhang, A. Solé-Daura, H. Fouilloux, J. M. Poblet, A. Proust, J. J. Carbó and G. Guillemot, *Chem. Cat. Chem.*, 2021, **13**, 1220–1229.

61 C. Baerlocher and L. McCusker, *Database of Zeolite Structures*, 1978.

62 R. Millini, G. Perego, D. Berti, W. O. P. Jr, A. Carati and G. Bellussi, *Microporous Mesoporous Mater.,* 2000, **35–36**, 387–403.

63 J. Přech, *Catal. Rev. Sci. Eng.*, 2018, **60**, 71–131.

64 T. Tatsumi, M. Nakamura, S. Negishi and H. o. Tominaga, *J. Chem. Soc. Chem. Commun.*, 1990, **202**, 476–477.

65 D. H. Wells, W. N. Delgass and K. T. Thomson, *J. Am. Chem. Soc.*, 2004, **126**, 2956–2962.

66 L. Wu, Z. Tang, Y. Yu, X. Yao, W. Liu, L. Li, B. Yan, Y. Liu and M. He, *Chem. Comm.*, 2018, **54**, 6384–6387.

67 C. P. Gordon, H. Engler, A. S. Tragl, M. Plodinec, T. Lunkenbein, A. Berkessel, J. H. Teles, A. N. Parvulescu and C. Copéret, *Nature*, 2020, **586**, 708–713.

68 Y. Yu, Z. Tang, J. Wang, R. Wang, Z. Chen, H. Liu, K. Shen, X. Huang, Y. Liu and M. He, *J. Catal.*, 2020, **381**, 96–107.

69 M. Signorile, L. Braglia, V. Crocellà, P. Torelli, E. Groppo, G. Ricchiardi, S. Bordiga and F. Bonino, *Angew. Chem. Int. Ed.*, 2020, **59**, 18145–18150.

70 J. Su, G. Xiong, J. Zhou, W. Liu, D. Zhou, G. Wang, X. Wang and H. Guo, *J. Catal.*, 2012, **288**, 1–7.

71 Y. Zuo, M. Liu, T. Zhang, L. Hong, X. Guo, C. Song, Y. Chen, P. Zhu, C. Jaye and D. Fischer, *RSC Adv.*, 2015, **5**, 17897–17904.

72 W. Fan, B. Fan, X. Shen, J. Li, P. Wu, Y. Kubota and T. Tatsumi, *Microporous Mesoporous Mater.*, 2009, **122**, 301–308.

73 D. Lin, Q. Zhang, Z. Qin, Q. Li, X. Feng, Z. Song, Z. Cai, Y. Liu, X. Chen, D. Chen, S. Mintova and C. Yang, *Angew. Chem. Int. Ed.*, 2021, **60**, 3443–3448.

74 J. Xing, D. Yuan, H. Liu, Y. Tong, Y. Xu and Z. Liu, *J. Mater. Chem. A Mater.*, 2021, **9**, 6205–6213.

75 M. Tamura, W. Chaikittisilp, T. Yokoi and T. Okubo, *Microporous Mesoporous Mater.*, 2008, **112**, 202–210.

76 Z. Shan, Z. Lu, L. Wang, C. Zhou, L. Ren, L. Zhang, X. Meng, S. Ma and F.-S. Xiao, *Chem. Cat. Chem.*, 2010, **2**, 407–412.

77 T. Ge, Z. Hua, J. Lv, J. Zhou, H. Guo, J. Zhou and J. Shi, *Cryst. Eng. Comm.*, 2017, **19**, 1370–1376.

78 G. J. Hutchings, D. F. Lee and A. R. Minihan, *Catal. Letters*, 1995, **33**, 369–385.

79 Z. Wu, B. Wang, J. Shi, P. Rui, X. Xie, W. Liao and X. Shu, *Microporous Mesoporous Mater.*, 2021, **327**, 111407.

80 Z. Kong, B. Yue, W. Deng, K. Zhu, M. Yan, Y. Peng and H. He, *Appl. Organomet. Chem.*, 2014, **28**, 239–243.

81 J. Zhang, S. Jin, D. Deng, W. Liu, G. Tao, Q. Luo, H. Sun and W. Yang, *Microporous Mesoporous Mater.* 2021, **314**, 110862.

82 M. L. Pena, V. Dellarocca, F. Rey, A. Corma, S. Coluccia and L. Marchese, *Microporous Mesoporous Mater.*, 2001, **44**, 345–356.

83 T. Blasco, M. A. Camblor, A. Corma, P. Esteve, J. M. Guil, A. Martínez, J. A. Perdigón-Melón and S. Valencia, *J. Phys. Chem. B*, 1998, **102**, 75–88.

84 U. Wilkenhöner, D. W. Gammon and E. Van Steen, *Stud. Surf. Sci. Catal.*, 2002, **142 A**, 619–626.

85 T. Blasco, A. Corma, T. Navarro and J. P. Pariente, *J. Catal.*, 1995, **156**, 65–74.

86 E. A. Eilertsen, S. Bordiga, C. Lamberti, A. Damin, F. Bonino, B. Arstad, S. Svelle, U. Olsbye and K. P. Lillerud, *Chem. Cat. Chem.*, 2011, **3**, 1869–1871.

87 M. E. Leonowicz, J. A. Lawton, S. L. Lawton and M. K. Rubin, *Science*, 1994, **264**, 1910–1913.

88 R. Millini, G. Perego, W. O. Parker, G. Bellussi and L. Carluccio, *Microporous Mater.*, 1995, **4**, 221–230.

89 V. A. Ostroumova and A. L. Maksimov, *Petrol. Chem.*, 2019, **59**, 788–801.

90 H. K. Beyer, H. G. Karge, I. Kiricsi, J. B. Nagy, W. J. Roth, C. T. Kresge, J. C. Vartuli, M. E. Leonowicz, A. S. Fung and S. B. Mccullen, in *Stud. Surf. Sci. Catal.*, 1995, vol. 94, pp. 301–308.

91 A. Corma, U. Diaz, V. Fornés, J. M. Guil, J. Martínez-Triguero and E. J. Creyghton, *J. Catal.*, 2000, **191**, 218–224.

92 G. G. Juttu and R. F. Lobo, *Microporous Mesoporous Mater.*, 2000, **40**, 9–23.

93 P. Wu, T. Tatsumi, T. Komatsu and T. Yashima, *J. Phys. Chem. B*, 2001, **105**, 2897–2905.

94 Z. Tang, Y. Yu, W. Liu, Z. Chen, R. Wang, H. Liu, H. Wu, Y. Liu and M. He, *Catal. Sci. Technol.*, 2020, **10**, 2905–2915.

95 M. A. Camblor, A. Corma, M. J. Díaz-Cabañas and C. Baerlocher, *J. Phys. Chem. B*, 1998, **102**, 44–51.

96 D. Zhou, H. Zhang, J. Zhang, X. Sun, H. Li, N. He and W. Zhang, *Microporous Mesoporous Mater.*, 2014, **195**, 216–226.

97 E. Gianotti, V. Dellarocca, L. Marchese, G. Martra, S. Coluccia and T. Maschmeyer, *Phys. Chem. Chem. Phys.*, 2002, **4**, 6109–6115.

98 T. Lundstedt, E. Seifert, L. Abramo, B. Thelin, A. Nystrom, J. Pettersen and R. Bergman, *Chemometr. Intell. Lab. Syst.*, 1998, **42**, 3–40.

99 R. Leardi, *Anal. Chim. Acta*, 2009, **652**, 161–172.

100 A. Corma, M. J. Díaz-Cabanas, M. Moliner and C. Martínez, *J. Catal.*, 2006, **241**, 312–318.

101 M. Moliner, M. J. Díaz-Cabañas, V. Fornés, C. Martínez and A. Corma, *J. Catal.*, 2008, **254**, 101–109.

102 A. De Lucas, L. Rodríguez and P. Sánchez, *Chem. Eng. Res. Des.*, 2000, **78**, 136–144.

103 M. Tagliabue, L. C. Carluccio, D. Ghisletti and C. Perego, *Catal. Today*, 2003, **81**, 405–412.

104 M. Balbaşi, *Mater. Res. Bull.*, 2013, **48**, 2908–2914.

105 N. Martín, M. Moliner and A. Corma, *Chem. Comm.*, 2015, **51**, 9965–9968.

106 C. F. Imbachi-Gamba and A. L. Villa, *Mater. Today Chem.*, 2021, **20**, 100442.

2. EXPERIMENTAL PROCEDURES

The chemicals and the synthesis procedures are reported separately in each chapter, for the sake of clarity. The description of the instruments used for the characterization of the synthesized samples are here reported, with the description of the procedures used throughout the whole PhD project. The specific characterization procedures for each topic will be discussed separately in the chapters.

2.1. Powder X-Ray Diffraction (PXRD)

PXRD patterns were obtained using a Cu K_α radiation, on a PANanalytical X'Pert diffractometer (Bragg-Brentano geometry), equipped with a X'celerator strip detector, in the range $5° \leq 2\theta \leq 45°$, with a step of 0.02° and 50 s/° of integration. Cu K_β was suppressed with a Ni filter.

2.2. Scanning Electron Microscopy (SEM)

The micrographs reported in chapter 3 and 5 were obtained with a Field Emission (FE) Scanning Electron Microscope (SEM) Tescan S9000G, on the metal sputtered samples (5 nm thick Cr layer). The micrographs reported in chapter 4 were obtained with a Mira\\Tescan SEM on the metal sputtered samples (2 nm thick film of a 70:30 Pt:Pd alloy).

2.3. N_2 physisorption at -196 °C

N_2 physisorption isotherms were recorded on a Micromeritics 3Flex instrument at -196 °C. The powders were pre-treated before the measurement, by outgassing overnight at 120 °C and at least 7 h at 400 °C. The Specific Surface Areas (SSAs) were determined with the Brunauer-Emmet-Teller (BET) and

Langmuir models, applied in pressure ranges suitable for obtaining a monolayer capacity included in the selected linearization range.[1] The cumulative pore volume, the pore size distribution and the total pore volume were obtained by applying the Non-Local Density Functional Theory (NL-DFT).

2.4. Elemental analysis

The Energy Dispersive X-ray (EDX) spectroscopy was performed on the Tescan S9000G FE-SEM, coupled with a EDX detector (Oxford – Detector equipped with an AZTEC software), for the sake of Ti quantification in the TS-1 and Ti-MWW synthesized samples.

CHNS elemental analysis was performed on the as-synthesized ITQ-1 samples by using a Thermo Nicolet FlashEA 1112 Series analyzer; the measurement was repeated three times and the results were averaged.

2.5. Activation procedure (for spectroscopic purposes)

The materials were pretreated (when specified) prior to the characterization by means of vibrational and electronic spectroscopy with a procedure named "activation" hereafter. The activation procedure foresees to insert the sample in a suitable cell to perform a thermal treatment and to be connected to a glass vacuum line to outgas the sample. The specific properties of the cell depend on the type of measurement needed and they will be specified in the following. The thermal treatment consists of a 5 °C/min ramp from Room Temperature (RT) to 500 °C, followed by 30 min of isothermal conditions at 500 °C while outgassing. Then, always at 500°C, 100 mbar of pure O_2 were dosed in the cell and left in contact with the sample for 30 min to oxidize organic residues. The sample was then outgassed at 500 °C until a final pressure of $< 10^{-3}$ mbar was reached.

2.6. Vibrational spectroscopies

2.6.1. InfraRed (IR) spectroscopy

IR spectra in transmission mode were recorded with a Bruker Vertex 70 spectrophotometer, equipped with a Mercury Cadmium Telluride (MCT) cryo-detector on self-supporting pellet of the pure sample, placed inside a home-made quartz cell with KBr windows. The pellet was mechanically protected by a gold envelope and activated before the spectroscopic measurement. The spectra were acquired under vacuum at *ca.* 40 °C (*i.e.* the temperature reached by the sample under the IR beam), by acquiring 32 scans (64 for the background) at 2 cm^{-1} of resolution. The spectra intensity was internally normalized (TS-1, ITQ-1 and Ti-MWW separately) to the overtone bands of bulk vibration modes (bands at 1990, 1877 and 1665 cm^{-1}).

IR spectra in Attenuated Total Reflection (ATR) mode were collected on the powdered samples. When the spectra were recorded in air, the Bruker Vertex 70 spectrophotometer was equipped with an ATR Platinum accessory, equipped with a single reflection diamond internal element, using a Deuterated TriGlycine Sulfate (DTGS) detector. 64 scans were accumulated for each spectrum (128 for the background), at 2 cm^{-1} of resolution. When the spectra were recorded after activation, a Bruker Alpha II spectrophotometer located inside a glove-box, equipped with a DTGS detector, was used. 64 scans were accumulated for each spectrum (128 for the background), at 2 cm^{-1} of resolution. The spectra were internally normalized at the 800 cm^{-1} band, assigned to the symmetric Si-O-Si stretching (ν_{sym}(Si-O-Si)) vibration.[2]

Temperature programmed oxidation/desorption measurements were performed using and AABSPEC CXX cell mounted in an IR spectrophotometer. A self-supporting pellet of the pure sample, mechanically protected by a gold envelope was inserted in the heating element of the AABSPEC CXX cell, equipped with two

thermocouples to control the temperature of the sample and to work under gas flow. IR spectra were recorded every 4 min accumulating 32 scans with a resolution of 4 cm^{-1}, on a Thermo Scientific Nicolet iS50 FTIR spectrophotometer, equipped with an MCT detector.

2.6.2. Raman spectroscopy

FT-Raman spectra reported in chapter 3 were acquired without activation with a Bruker Vertex 70 spectrophotometer, equipped with the RAMII accessory, with a resolution of 4 cm^{-1}. An excitation line at 1064 nm and a laser power of 460 mW were used. 1500 scans were accumulated for each sample. The spectra were internally normalized at the 800 cm^{-1} band, assigned to the ν_{sym}(Si-O-Si) vibration.[3]

Raman spectra reported in chapter 4 were measured without activation using the 244 nm excitation line (Coherent MotoFred 300C, frequency doubled Ar^+ laser) on a Renishaw inVia Raman microscope spectrometer, equipped with 3600 line/mm grating and UV-enhanced Change-Coupled-Device (CCD) detector. The laser was focused on the sample through a 15x objective. The spectra were internally normalized at the 800 cm^{-1} band, assigned to the ν_{sym}(Si-O-Si) vibration.[3]

2.7. Electronic spectroscopy

2.7.1. UltraViolet-Visible (UV-Vis) spectroscopy

UV-Vis-NIR spectra were acquired in Diffuse Reflectance (DR) mode on a Varian Cary5000 spectrophotometer, using Spectralon® as 100 % reflectance, in the 200-2500 nm spectral range. The samples were measured both in air and after activation.

2.8. Nuclear Magnetic Resonance (NMR) spectroscopy

NMR spectra of ITQ-1 samples were collected with One Pulse (OP) and Cross Polarization (CP) Magic-Angle Spinning (MAS) experiments on the nuclei of ^{29}Si and $^{29}Si\{^{1}H\}$, respectively, at 79.4 MHz on a Bruker Avance III-HD 400 (9.4 T), using a 4.0 mm outer diameter probe. For OP, a radiofrequency of 30 kHz and a recycle delay of 15 s was used. A recycle delay of 5 s and a contact time of 5 ms were used for ^{29}Si CP-MAS experiments. For ^{29}Si OP- and CP-MAS experiments, 4096 and 2048 transients were acquired respectively.

^{13}C OP-MAS-NMR spectra of the as-synthesized ITQ-1 samples were acquired at 100.6 MHz on a Bruker Avance III-HD 400 (9.4 T), using a 4.0 mm outer diameter probe. Radiofrequency pulses of 38.5 kHz and a recycle delay of 2 s were used. For each spectrum, 6144 transients were acquired.

2.9. Thermo-Gravimetric Analysis (TGA)

TGA was performed on the as-synthesized ITQ-1 samples with a STD Q600 analyzer by TA instrument, placing approximately 6 mg of sample inside an alumina pan. The flow was kept constant at 100 ml/min.

2.10. References

1 M. Thommes, K. Kaneko, A. V Neimark, J. P. Olivier, F. Rodriguez-Reinoso, J. Rouquerol and K. S. W. Sing, *Pure Appl. Chem.* 2015, **87**, 1051–1069.

2 E. Astorino, J. B. Peri, R. J. Willey and G. Busca, *J. Catal.* 1995, **157**, 482–500.

3 Y. Yu, G. Xiong, C. Li and F. S. Xiao, *Microporous Mesoporous Mater.* 2001, **46**, 23–34.

3. TITANIUM SILICALITE-1 (TS-1)

3.1. Scope of the work

The study about the synthesis of TS-1 was performed with multiple aims. Its synthesis was studied in detail for long times both in academic[1–15] and in industrial environments,[16–19] but the published results and the indication of the synthetic conditions leading to the formation of catalytically active species are sometimes not uniform and contradictory.

A newcomer to the synthesis of zeolites would experience difficulties and uncertainties in the interpretation of the quality and significancy of the results he/she is obtaining. In most cases, the optimization of the zeolite synthesis is performed by a trial-and-error process. This procedure could sometimes lead to outstanding results, but its success is mainly based on serendipity and/or by the personal experience of the synthesizer. The newcomer would be driven to optimize the zeolite synthesis by the One-Variable-At-Time (OVAT) method. This is often far from reality for the following reasons: (i) the multiple conditions adopted in each synthesis step can individually influence the final material, but the effect of each variable on the final material is often hardly distinguishable; and (ii) the fundamental understanding of the zeolite crystallization mechanism is rarely related to practical indications to be used to improve the synthetic method.

In this chapter, the use of the DoE and MVA, interchanged with the trial-and-error approach, will be used to optimize the synthesis of the TS-1 catalyst. The use of DoE and MVA allowed to discern the noise due to the experimental variability from the useful information. Furthermore, this approach allowed to get familiar with the zeolite synthesis in general, with the experimental setup and to discuss about basic phenomena that governs the hydrothermal crystallization of zeolites.

On the other hand, given the general topic of this PhD project, acquiring knowledge and experience dealing with the chemistry of the Ti insertion into a zeolite framework was of outstanding importance for the future development of the project.

3.2. Experimental procedure

3.2.1. Chemicals

Tetraethylorthosilicate (TEOS, reagent grade 98%, from Sigma Aldrich) was used as Si source. Tetrabutylorthotitanate (TBOT, reagent grade 97%, from Sigma Aldrich) and tetraethylorthotitanate (TEOT, from Sigma Aldrich) were used as Ti source and stored in a glove-box in N_2 atmosphere. Tetrapropylammonium hydroxide (TPAOH) was used as OSDA and was purchased by Sigma Aldrich (1 M aqueous solution) or by Thermo Scientific (40 wt% aqueous solution). Isopropyl alcohol (IPrOH) and absolute ethanol (EtOH) were used during the gel preparation. Milli-Q water (18.2 $M\Omega cm^{-1}$) was used for the preparation of all the synthesis gels and deionized or Milli-Q water were used for the washing of the samples.

3.2.2. Synthesis of TS-1 from Taramasso et al. (Patent 1983)

The study of the synthesis of TS-1 was first approached by reproducing the procedure reported in the Example 1 in US Patent 4,410,501 of 1983.[16] The procedure was adapted to fit the available experimental setup. A synthesis gel with the composition 1 SiO_2 : 0.0308 TiO_2 : 0.46 TPAOH : 15.59 H_2O was prepared by adding dropwise TBOT to TEOS under stirring in a round bottom flask, followed by the addition of the TPAOH aqueous solution. The solution was stirred at RT for 1 h with the sealed flask and 5 h at 80 °C with the open

flask to evaporate the ethanol produced from the hydrolysis. Finally, 26 ml of water were added, and the gel was transferred to a 45 ml Teflon lined Stainless Steel digestor. The hydrothermal treatment was conducted at 175 °C, for 10 days under tumbling conditions at 20 rpm The product was then separated and washed by centrifugation with deionized water, dried overnight at 65 °C and calcined in a muffle furnace at 550 °C for 7 h, with a heating ramp of 2 °C/min.

3.2.3. Synthesis of TS-1 with separated hydrolysis

3.2.3.1. Analysis of the Ti content in the synthesis gel

A set of materials with different Ti content were synthesized adapting a procedure reported in the literature.[9] This procedure involves the separate hydrolysis of the Si and Ti source. The rate of hydrolysis of transition metals alkoxides is faster than that of non-metallic elements, due to their electronic vacancies. It is also affected by the length of the organic chain; the longer the chain, the slower the hydrolysis is.[20] The separate hydrolysis allows to match them by performing both in their optimal conditions. In this procedure, the hydrolysis of the Si source must be speeded up and the one of the Ti source must be slowed down. In a typical synthesis, 6.25 g of TEOS are added dropwise to 23.53 g of TPAOH aqueous solution (from Sigma Aldrich) and stirred at 40 °C for 4 h under reflux conditions (solution A). Separately, the TBOT was added dropwise to 3.06 g of IPrOH and stirred at 0 °C for 4 h in a sealed round bottom flask (solution B). At the end of the 4 h, solution A was cooled down to 0 °C, added dropwise to solution B and stirred at 40 °C for 24 h under reflux conditions (aging). The obtained gel had the molar composition: 1 SiO_2 : x TiO_2 : 0.27 TPAOH : 2 IPrOH : 4 EtOH : 4x BuOH : 40.5 H_2O, where BuOH is the butanol produced during the TBOT hydrolysis, EtOH is produced during TEOS hydrolysis and x = 0.0072, 0.009, 0.0108,

0.0125, 0.0143 (for samples A20, A25, A30, A35 and A40 respectively). From this study on, the alcohols were not evaporated from the synthesis gel, because the process is hardly controlled and hence probably not reproducible. In this preliminary study, no particular attention was paid to avoid the evaporation, even if it is not performed by purpose. The gel undergoes hydrothermal treatment in a Teflon lined Stainless Steel digestor at 140 °C for 24 h under static conditions. The product was separated and washed by centrifugation with deionized water, dried overnight at 65 °C and calcined in a muffle furnace at 550 °C for 7 h, with a heating ramp of 2 °C/min.

3.2.3.2. MVA of the synthesis conditions (DoE 1)

The DoE approach was used to simultaneously screen the effects of the synthesis variables in the procedure described in paragraph 3.2.3.1. The explored variables are the time (t) and temperature (T) of (i) hydrolysis of TEOS (preparation of solution A: t(H-TEOS) and T(H-TEOS)), (ii) of the aging (t(A) and T(A)), (iii) of the hydrothermal treatment (t(Cry) and T(Cry)), and the time of hydrolysis of TBOT (preparation of solution B: t(H-TBOT)). The temperature of hydrolysis of TBOT was kept constant at 0 °C to ensure that the hydrolysis of the Ti source occurs slowly. The composition of the synthesis gel was 1 SiO_2 : 0.0143 TiO_2 : 0.27 TPAOH : 2 IPrOH : 4 EtOH : 0.0572 BuOH : 40.5 H_2O for each synthesis. From this study on, the evaporation of alcohols was accurately avoided, for the sake of reproducibility. Figure 3.2.3.2.1 shows schematically the synthesis procedure used in DoE 1.

The samples were selected following a D-optimal design at two levels, composed of 9 syntheses (N1-N9) and a center point (N10). N11, N12 and N13 were added as additional points since the used conditions are included in the experimental domain. The D-optimal design was produced with the MODDE® 13 software from Sartorius Stedim Data Analytics.[21] Table 3.2.3.2.1

lists the levels used for each variable and Table 3.2.3.2.2 lists the syntheses and the levels used for each synthesis.

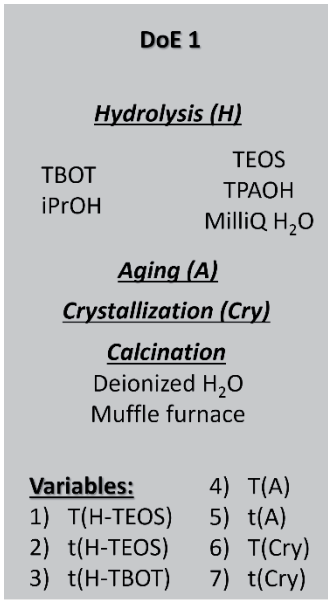

Figure 3.2.3.2.1. Schematic representation of the syntheses of DoE 1. In the section above of the scheme, the procedure is reported, in the section below the variables explored are listed.

Table 3.2.3.2.1. High (+1), intermediate (0) and low (-1) levels used for each variable.

Variable	+1	0	-1
t(H-TEOS)[1] (h)	24	14	4
t(H-TBOT)[2] (h)	24	14	4
T(H-TEOS)[3] (°C)	60	40	20
t(A)[4] (h)	48	36	24
T(A)[5] (°C)	60	40	20
t(Cry)[6] (h)	168	96	24
T(Cry)[7] (°C)	170	140	110

[1] t(H-TEOS): TEOS hydrolysis time.
[2] t(H-TBOT): TBOT hydrolysis time.
[3] T(H-TEOS): TEOS hydrolysis temperature.
[4] t(A): aging time.
[5] T(A): aging temperature.
[6] t(Cry): crystallization time.
[7] T(Cry): crystallization temperature.

Table 3.2.3.2.2. Syntheses and variable levels (high: +1; intermediate: 0; low: -1) used for each synthesis. Lines N1-N9: experimental matrix of the D-Optimal design. Line N10: center point. Lines N11-N13: additional syntheses in the experimental domain, included in the model. Line R: reproducibility samples.

Name	t(H-TEOS) [1]	t(H-TBOT) [2]	T(H-TEOS) [3]	t(A) [4]	T(A) [5]	t(Cry) [6]	T(Cry) [7]
N1	-1	+1	-1	-1	-1	-1	-1
N2	+1	+1	+1	+1	+1	-1	-1
N3	+1	-1	+1	-1	-1	+1	-1
N4	-1	-1	-1	+1	+1	+1	-1
N5	-1	-1	+1	+1	-1	-1	+1
N6	+1	-1	-1	-1	+1	-1	+1
N7	-1	+1	-1	+1	+1	-1	+1
N8	+1	+1	-1	+1	-1	+1	+1
N9	-1	+1	+1	-1	+1	+1	+1
N10	0	0	0	0	0	0	0
N11	-1	-1	-1	+1	-1	+1	-1
N12	+1	+1	+1	+1	+1	+1	-1
N13	-1	+1	0	+1	0	-1	+1
R [8]	-1	-1	0	-1	0	-1	0

[1] t(H-TEOS): TEOS hydrolysis time.
[2] t(H-TBOT): TBOT hydrolysis time.
[3] T(H-TEOS): TEOS hydrolysis temperature.
[4] t(A): aging time.
[6] t(Cry): crystallization time.
[7] T(Cry): crystallization temperature.
[8] Level used to synthesize 6 samples.

The reproducibility of the synthesis procedure was assessed to fruitfully apply the DoE. This was done by repeating three times the same synthesis before (R*i*-a, where *i* = 1, 2 or 3) and after (R*i*-b, where *i* = 1, 2 or 3) all the DoE set of samples. By comparing the results of the characterization of R*i*-a and R*i*-b samples, the absence of uncontrolled effects linked to the reagents aging was verified. To avoid the presence of uncontrolled parameters such as accidental seeding, the Teflon liners from this point on, were washed after each use with hydrofluoric acid (HF) at RT and with a 50 vol% of Milli-Q H_2O and acetone at 140 °C in hydrothermal conditions.

3.2.3.3. Screening syntheses after DoE 1

Following the direction suggested by DoE 1 four syntheses were performed using the same procedure, to improve the properties of the catalyst. The studied variables are t(Cry) and T(Cry), while all other variables were fixed at the -1 (for the times) and 0 (for the temperatures, to avoid the intrinsic irreproducibility of the -1 level of temperature, *i.e.* 20 °C, actually un-controlled RT), as reported in Table 3.2.3.3.1. Figure 3.2.3.3.1 shows schematically the comparison between the syntheses LL, LH, HL and HH with the DoE 1 syntheses.

Table 3.2.3.3.1. Syntheses and variable levels (high: +1; intermediate: 0; low: -1) used for each synthesis.

Name	t(H-TEOS) [1]	t(H-TBOT) [2]	T(H-TEOS) [3]	t(A) [4]	T(A) [5]	t(Cry) [6]	T(Cry) [7]
LL	-1	+1	0	-1	0	+0.66	+1
LH	-1	+1	0	-1	0	+0.66	+1
HL	-1	+1	0	-1	0	+1	+1.06
HH	-1	+1	0	-1	0	+1	+1.06

[1] t(H-TEOS): TEOS hydrolysis time, constant.
[2] t(H-TBOT): TBOT hydrolysis time, constant.
[3] T(H-TEOS): TEOS hydrolysis temperature, constant.
[4] t(A): aging time, constant.
[5] T(A): aging temperature, constant.
[6] t(Cry): crystallization time, variable.
[7] T(Cry): crystallization temperature, variable.

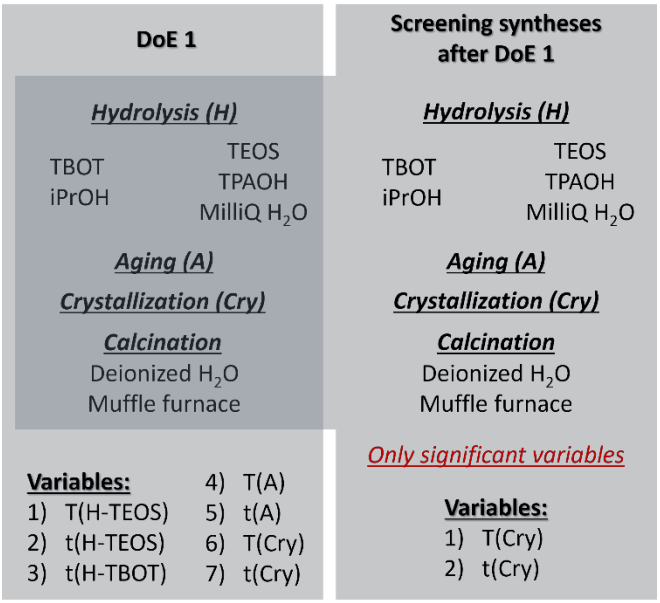

Figure 3.2.3.3.1. Schematic representation of the screening syntheses after DoE 1 compared to the syntheses of DoE 1. In the section above of the scheme, the procedure is reported, in the section below the variables explored are listed. The shadowed square highlights the parts of the DoE 1 procedure that were not modified. The italic red sentence highlights what was changed.

3.2.3.4. MVA of the hydrothermal crystallization conditions and Ti content (DoE 2)

A second DoE (DoE 2) was performed by changing the Ti source and the alcohol, with the aim to uniform the nature of the alcohols in the synthesis gel. TBOT and IPrOH were substituted with TEOT and EtOH, respectively. In this way, the transient formation of alkoxides of mixed alcohols due to the hydrolysis equilibrium of the Ti and Si sources is avoided. The following equations (eq. 3.1 and 3.2) reports an example of formation of alkoxides of mixed alcohols:

$$Ti(OBu)_4 + H_2O \rightleftarrows TiOH(OBu)_3 + BuOH \quad (3.1)$$

$$TiOH(OBu)_3 + IPrOH \rightleftarrows \boldsymbol{TiOIPr(OBu)_3} + H_2O \quad (3.2)$$

The formation of alkoxides of mixed alcohols must be avoided due to the low reproducibility and randomness of its occurrence. The source of Ti that undergoes hydrothermal crystallization could in principle be always different if mixed alkoxides can form, making the rational study of the synthesis useless. The substitution of TBOT with TEOT requires to reduce the time of hydrolysis of the Ti source from at least 4 h (4 to 24 h in DoE 1) to 20 min. This is due to the different hydrolysis ratios of the two alkoxides (as explained in paragraph 3.2.3.1). The formation of a white suspension in the alcohol was observed (probably TiO_2) for TEOT hydrolysis longer than 20 min.

An accurate analysis of the original patent[16] suggested to prepare the synthesis gel under N_2 atmosphere to avoid the presence of CO_2. The CO_2 can easily dissolve in strongly basic amine solutions, affecting the precise control of pH. The N_2 atmosphere is also needed for dosing TEOT without anatase formation, unavoidable when contacting with air moisture. The preparation of the gel was performed under N_2 flux with the help of a Schlenk glass line, equipped for performing reactions under vacuum conditions or in N_2 flux.

The patent[16] also suggested to operate in conditions free from alkaline metals. The presence of alkaline metals could lead to the formation of titanates, where Ti is in octahedral coordination. The alkaline metal detected in the final product was K. The formation of the titanates may occur virtually in each step of the synthesis, namely hydrolysis, aging, hydrothermal crystallization and calcination. The reversible condensation-hydrolyzation equilibria are responsible for providing Ti containing species that can react with K^+ in the first three steps of the synthesis. The extraction of Ti atoms in framework positions and the modification of the Ti speciation can occur

during the calcination. The calcination contemplates the heating of the sample in presence of moisture and K^+, and hence it behaves, *ipso facto*, as a second crystallization that can affect the Ti speciation. A common source of K^+ is the TPAOH, since it is synthesized by ion exchange from TPA^+ halogenide).[22] The presence of K^+ cations in the 1 M TPAOH aqueous solution from Sigma Aldrich was not reported in the information sheets and for this reason this source was excluded. However, subsequent analyses revealed that this TPAOH solution contained a relatively high amount of K^+. At this moment, K^+ was found in the homemade deionized water, used for washing the samples before the calcination. For this reason, the presence of extra-framework Ti species in the samples of DoE 1 was attributed to the calcination step. To avoid this, the washing of the samples of DoE 2 was performed with Milli-Q instead of deionized water to avoid the presence of K^+ during the calcination, and the calcination was performed in a tubular oven under dry air flux, to minimize the presence of moisture, CO_2 and NO_X produced upon combustion of the OSDA.

Three variables with two levels were explored in DoE 2. The variables are (i) the Ti content in the synthesis gel (the nominal Ti/Si ratio, Ti/Si_{nom}), (ii) t(Cry) and (iii) T(Cry), according to the levels in Table 3.2.3.4.1. The other variables (t(H-TEOS), T(H-TEOS), t(A) and T(A)) were fixed at the same levels used for the LL, LH, HL and HH samples (screening syntheses after DoE 1, paragraph 3.2.3.3). The syntheses of DoE 2 were chosen following a D-Optimal design produced by the MODDE® 13 software[21] and their levels are reported in Table 3.2.3.4.2. The selected D-Optimal design foresees the eight syntheses belonging to a full factorial design at 2 levels (N1-N8), the center point (R) and two additional syntheses added to evaluate the quadratic effects of t(Cry) and T(Cry) (N9-N10). Figure 3.2.3.4.1 shows schematically the comparison between DoE 2 with the DoE 1.

If the hydrolysis of both the Si and Ti source is assumed to be complete, the composition of the synthesis gels of DoE 2 is the following: 1 SiO_2 : x TiO_2 : 0.27 TPAOH : (6+4x) EtOH : 40.5 H_2O, where x = Ti/Si_{nom} reported in Table 3.2.3.4.1.

Table 3.2.3.4.1. High (+1), intermediate (0) and low (-1) levels used for each variable.

Variable	+1	0	-1
Ti/Si_{nom}[1]	0.014	0.017	0.020
t(Cry)[2] (h)	72	48	24
T(Cry)[3] (°C)	190	170	150

[1] Ti/Si_{nom}: nominal Ti content in the syntheses gel.
[2] t(Cry): crystallization time.
[3] T(Cry): crystallization temperature.

Table 3.2.3.4.2. Syntheses and variable levels (high: +1; intermediate: 0; low: -1) used for each synthesis. Lines N1-N10: experimental matrix of the D-Optimal design. Line R: center point and reproducibility samples.

Name	Ti/Si_{nom} [1]	t(Cry) [2]	T(Cry) [3]
N1	-1	-1	-1
N2	+1	-1	-1
N3	-1	+1	-1
N4	+1	+1	-1
N5	-1	-1	+1
N6	+1	-1	+1
N7	-1	+1	+1
N8	+1	+1	+1
N9	-1	+1	0
N10	-1	0	-1
R [4]	0	0	0

[1] Ti/Si_{nom}: nominal Ti content in the syntheses gel.
[2] t(Cry): crystallization time.
[3] T(Cry): crystallization temperature.
[4] Level used to synthesize 3 samples.

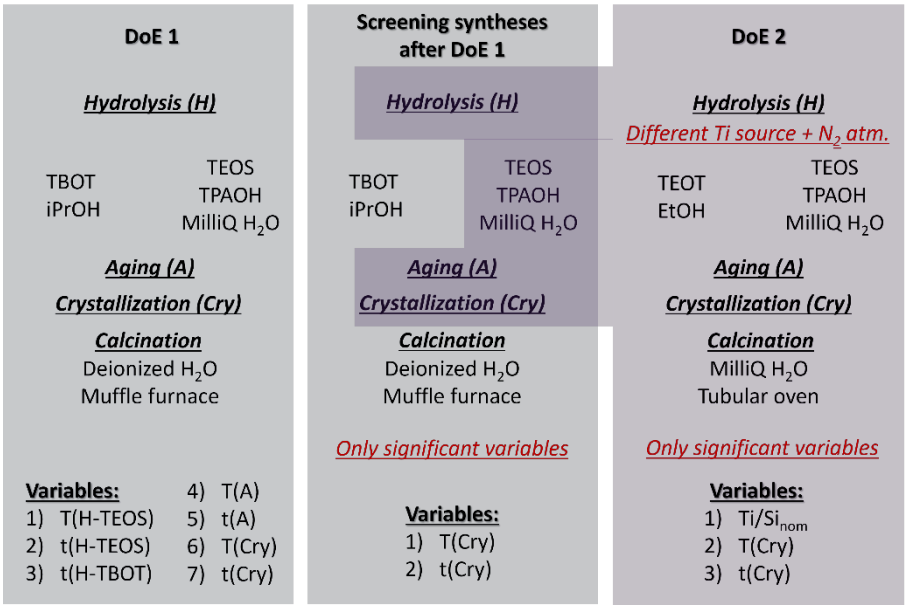

Figure 3.2.3.4.1. Schematic representation of the syntheses of DoE 2 compared to the syntheses of DoE 1 and of the screening syntheses after DoE 1. In the section above of the scheme, the procedure is reported, in the section below the variables explored are listed. The shadowed squares highlight the parts of the DoE 1 procedure that were not modified. The italics red sentences highlight what was changed.

3.2.3.5. Final synthesis after DoE 2

The results of DoE 2 suggested that probably a K source was still present in the gel. For this reason, aliquots of TPAOH solutions of different vendors were analyzed by ICP. The 1 M TPAOH aqueous solution from Sigma Aldrich is revealed to contain a high amount of K (1918 mg/l). The TPAOH source was changed from 1 M from Sigma Aldrich to 40 wt% from Thermo Scientific (the commercial solution with lower amount of K), to avoid any kind of K traces in the synthesis gel.

Following the direction suggested by DoE 2 regarding the hydrothermal conditions, *i.e.* the Ti/Si_{nom} to be used and the K-free TPAOH, a final synthesis

(F-TS-1) was performed. The procedure was slightly modified respect to the previous recipes. The analysis of the patent of Carati *et al.* in 2016[18] suggested that the amount of H_2O, that each TEOT molecule contacted during its hydrolysis, needs to be accurately controlled and that this could be done by using a gel with the following molar ratios: Si/Ti = 35 – 150, TPAOH/Si = 0.2 – 0.5, $H_2O/Si \geq 4 \wedge \leq 10$ and $H_2O/Ti \geq 320$, the EtOH being evaporated before the hydrothermal crystallization. The synthesis procedure used for F-TS-1 was adapted to fit the requirement of the $H_2O/Si = 10$, by reducing the amount of H_2O added to solution of TEOS in TPAOH. Hence, a gel with the following molar composition was prepared by the separated hydrolysis and combination of the two solutions: 1 SiO_2 : 0.008 TiO_2 : 0.27 TPAOH : 6.032 EtOH : 10 H_2O. Both the Ti/Si_{nom} and the H_2O/Si ratio were strongly reduced respect to those used in the previous TS-1 syntheses. This gel was aged for 2 h at 0 °C, to further slow-down the TEOT hydrolysis, followed by 22 h at 40 °C. A new aliquot of H_2O was added at the end of the aging, before transferring the gel to the Teflon liner, to obtain the same H_2O/Si used in the previous syntheses (namely $H_2O/Si = 40.5$). The final molar composition was: 1 SiO_2 : 0.008 TiO_2 : 0.27 TPAOH : 6.032 EtOH : 40.5 H_2O. The hydrothermal treatment was conducted at 190 °C for 24 h. Figure 3.2.3.4.1 reports schematically the procedure used to prepare F-TS-1 compared with the procedures used in the other TS-1 samples. The synthesis of F-TS-1 was a single point, hence no variables were explored. The study of the F-TS-1 synthesis is still ongoing, as it will be explained later.

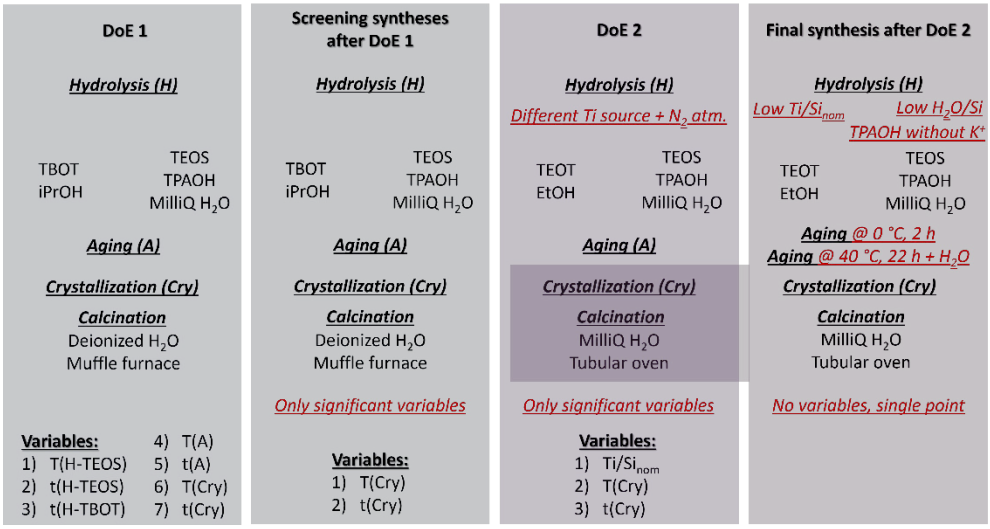

Figure 3.2.3.4.1. Schematic representation of the procedure used to prepare F-TS-1, compared with the procedure for the syntheses of DoE 2 DoE 1 and of the screening syntheses after DoE 1. In the section above of the scheme, the procedure is reported, in the section below the variables explored are listed. The shadowed squares highlight the parts of the DoE 2 procedure that were not modified. The italics red sentences highlight what was changed.

3.2.4. Characterization of the samples

All the samples were characterized by means of PXRD on the as-synthesized powders, by UV-Vis and ATR-IR spectroscopy on the activated calcined powders and by EDX-SEM for the Ti quantification. SEM images of P30 sample were recorded and the N7, N8 and N9 samples of DoE 2 and F-TS-1 the were analyzed by Raman spectroscopy (1064 nm laser).

The definition of numerical responses representative of the properties of the material are necessary to apply the MVA to the DoEs.[6,23,24] In the present work, four responses obtained from the characterization of the materials have been considered:

1) the yield of calcined material,
2) the total Ti content (Ti/Si_{EDX}), determined by EDX
3) the onset of the Ligand to Metal Charge Transfer (LMCT) electronic transition involving Ti (LMCT onset), as indication of the presence of extra-framework Ti species,
4) integrated area of the 960 cm^{-1} band in the ATR-IR spectrum, proportional to the amount of Ti in tetrahedral coordination.[25]

The four responses were analyzed with a MVA approach exploiting the MODDE® 13 software.[21] The responses of DoE 1 were fitted with the Partial Least Square (PLS) and the responses of DoE 2 were fitted with the Multiple Linear Regression (MLR) method. The choice was done to obtain the best fit for each DoE project. The linear effect of each variable on the responses was obtained in DoE 1, since the degrees of freedom of the models only allowed to determine linear terms. The degrees of freedom of the models of DoE 2 allowed to obtain all the linear terms and to estimate a couple of quadratic or interaction terms for each response.

It is important to specify that, in this context, the DoE and MVA approaches were used with the aim of qualitatively understand the system under investigation, and not for quantitative prediction purposes. The results of the MVA were used to make deductions and assumptions about what is happening during the different steps of the TS-1 synthesis.

A digression is worth on the LMCT onset response. It was determined as the wavelength value at 96 % of reflectance, after vertically shifting the spectrum to 100 % of reflectance at 400 nm (Figure 3.2.4.1a). Hence it has the dimension of wavelength, and it is unsuitable for the quantification of the Ti species with intermediate coordination. It is used as qualitative indicator of the coordination of the extra-framework species. The higher the onset, the higher the coordination would be. It was used both in DoE 1 and DoE 2 for

the sake of comparison. An accurate quantification of the Ti species in the samples belonging to DoE 1 was not possible, so the onset is the only indicator used for the extra-framework species. The validity of the LMCT response was evaluated by applying the Principal Component Analysis (PCA), as described elsewhere [6] (thanks to Dr. Eugenio Alladio). The application of the PCA to spectroscopic data allowed the determination of the variability between the spectra, by identifying the Principal Components (PCs). Typically, the PC1 is not informative, since dependent on the general shape of the spectrum. The PC2 and the PC3 are usually more instructive, and they enable to discern the differences between the spectra. The PC2 obtained by applying the PCA on the UV spectra of the TS-1 samples of DoE 1 was found to nicely correlate with the LMCT onset values. This was considered as an indication that the LMCT onset was representative of the variability among the UV spectra.

The quantification of the Ti species in DoE 2 samples was done as described elsewhere.[25] Briefly, a calibration line for the framework Ti and one for the anatase were constructed using TS-1 reference samples. The 960 cm^{-1} band in the ATR-IR spectra, assigned to the Si-O-Si asymmetric stretching (ν_{asym}(Si-O-Si)) perturbed by the presence of framework Ti, and the 144 cm^{-1} band in the Raman spectra, assigned to the intense E_g transition of anatase, were used for quantitative purposes. The amount of extra-framework Ti species with intermediate coordination was obtained by difference of the TiO_2 wt% determined by EDX and the amounts of framework Ti and anatase obtained by calibration.

This method could not be applied to the samples belonging to DoE 1 for the following reasons. (i) The bands at 960 cm^{-1} of TS-1 samples of DoE 1 present very low intensity, making necessary to extrapolate from the calibration line obtained with the available reference samples. Therefore, the uncertainty of the quantification would be extremely enhanced. (ii) An absorption band

assigned to the ν_{asym}(Si-O-Si) perturbed by the presence of defective groups (silanols, Si-OH) is found in the ATR-IR spectrum of S-1 samples at 960 cm^{-1}.[26] This hints that in TS-1 the bands assigned to ν_{asym}(Si-O-Si) perturbed by Si-OH and by framework Ti are probably overlapped, the intensity of the second being usually way higher. The amount of Si-OH groups in the synthesized sample was compared to the one in the samples used to construct the calibration lines by exploiting the bands assigned to the overtone and combination mode of the OH stretching ν(OH) of Si-OH groups in the NIR region of the UV-Vis-NIR spectra. The intensities of these bands in the spectra of DoE 1 samples are extremely low compared to those of the reference samples. This suggests that the amount of Si-OH in the two set of samples could be different, further increasing the uncertainty of the quantification.

On the other side, the samples belonging to DoE 2 shows prominent bands at 960 cm^{-1} in the ATR-IR spectra and prominent band of combination and overtone bands of the OH stretching in the UV-Vis-NIR spectra, making the quantification feasible.

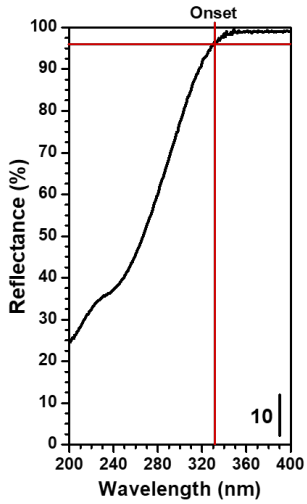

Figure 3.2.4.1. Schematic representation of the method used to determine the wavelength of the onset of the LMCT transition.

3.3. Results and discussion

3.3.1. Synthesis of TS-1 from Taramasso et al. (Patent 1983)

The PXRD pattern of P30 (Figure 3.3.1.1a) shows all and only the reflections typical of the MFI framework and it indicates the high crystallinity of the material. The SEM images reveal that the sample is composed of macro-aggregates of dimension in the order of magnitude of tens of μm and that the primary particles are nanometric sized hexagonal prisms with sharp edges. The EDX analysis (Table 3.3.1.1) reveals that the amount of incorporated TiO_2 is far higher than the limit amount that can be incorporated in isomorphous substitution (2.66 wt% of TiO_2).[25,27]

The UV-Vis-NIR spectra (Figure 3.3.1.2a) recorded both in air and after activation are shown. The as-such spectra are necessary as comparison to verify that no degradation of the sample occurred during the thermal treatment. In the UV wavelength region (200 – 400 nm), the LMCT electronic transition involving Ti is present. Its edge and maximum (visually the minimum when spectra are plotted in reflectance (%) scale) are sensitive to the environment around the Ti atoms in the sample. In fully dehydrated samples, maxima at 210 nm and 320 nm testify the presence of Ti sites in tetrahedral and octahedral coordination respectively (*i.e.* framework Ti and bulk anatase).[25] The presence of adsorbed H_2O determines the expansion of the coordination sphere of Ti, causing a broadening and upward shift of the maximum. It affects particularly the Ti in framework positions, the most prone to coordination expansion. The wavelength of the maximum of the LMCT transition is also affected by the nuclearity of Ti, *e.g.* isolated Ti atoms in octahedral coordination would generate an absorption with maximum downward shifted, compared to the one of bulk anatase, and by the possible intermediate coordination, *e.g.* five-coordinated species. The activated UV

spectrum of P30 presents a maximum at 210 nm, one at 270 nm and one at 320 nm. The maximum at 270 nm was assigned to hexacoordinated Ti sites inserted in the MFI framework, with a local symmetry approaching the octahedral one.[19]

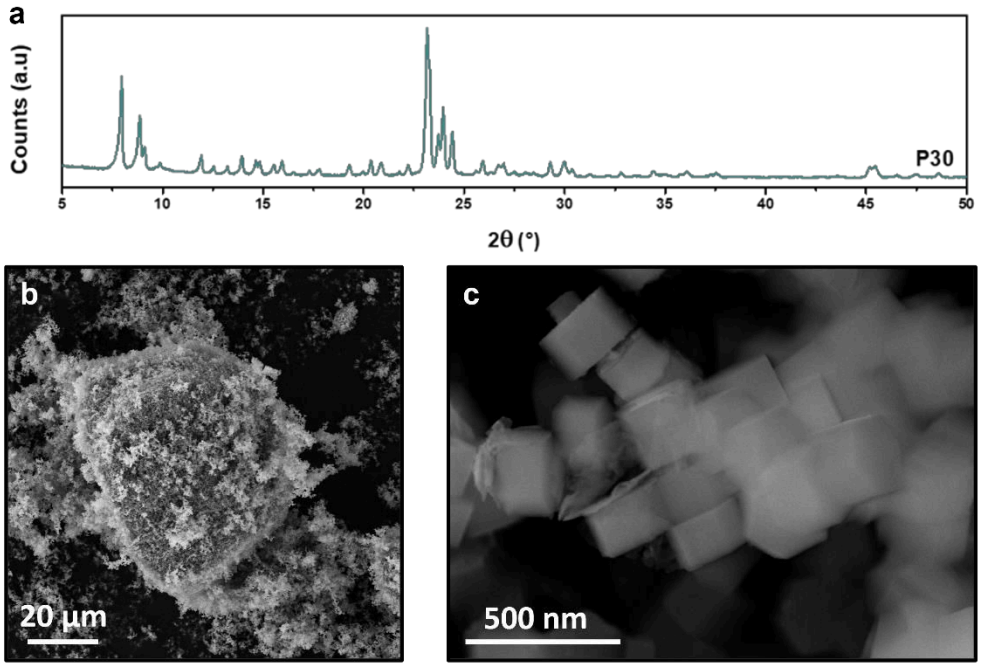

Figure 3.3.1.1. (a) PXRD pattern and (b,c) SEM images of P30.

Table 3.3.1.1. Total Ti content of P30, determined by EDX.

Name	Ti/Si_{nom}	Ti/Si_{EDX}	TiO_2 wt%	σ (TiO_2 wt%)
P30	0.0308	0.0306	4.08	0.17

The NIR wavelength region (750 – 2500 nm) of the activated spectrum hosts two bands, assigned to the overtone and combination mode of Si-OH groups, at 1369 and 2186 nm respectively.[25,28] In the spectra recorded in air, without activation, the presence of adsorbed water partially erodes these bands. The overtone and combination modes of the stretching and bending vibrations of H_2O are instead visible at 1400 and 1900 nm.[29] In the present work, the activation treatment never led to sample degradation, hence for the sake of

brevity, the Vis and NIR regions of the spectra and the UV spectra recorded in air will be omitted in the following.

The ATR-IR spectrum of P30 (Figure 3.3.1.2b) displays the signals typical of silicate materials, namely the bands at ≈1100 cm^{-1} and 800 cm^{-1}, assigned to ν_{asym}(Si-O-Si) and ν_{sym}(Si-O-Si) stretching modes respectively and the band at 450 cm^{-1}, assigned to the out-of-plane rocking vibration of the Si-O-Si units (ρ(Si-O-Si)). The signal at 550 cm^{-1} is typical of zeolites with MFI structure and it is ascribed to the pentasil unit collective mode.[26,30–34] At 960 cm^{-1}, the signal assigned to the ν_{asym}(Si-O-Si) perturbed by the presence of Ti in tetrahedral, framework positions[25,35] is visible.

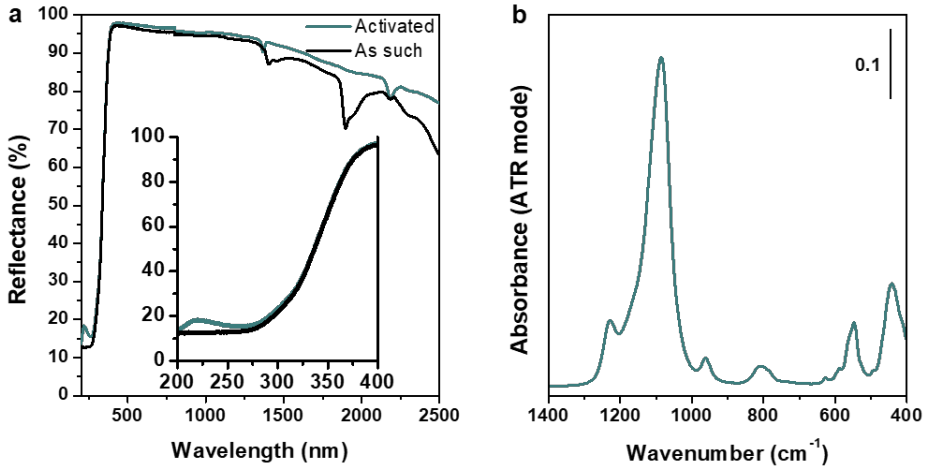

Figure 3.3.1.2. (a) UV-Vis and (b) ATR-IR spectra of P30, recorded as-such in air (black) and after activation (cyan).

The too high TiO_2 wt% in P30 explains the presence of amorphous Ti species and anatase. The presence of extra-framework species is unavoidable when the higher limit of TiO_2 loading is exceeded and for this reason, in the following, the Ti/Si_{nom} will be significantly reduced. To further avoid the formation of bulk anatase, following published procedures,[3,9] the dissolution of the Ti source in TEOS was substituted with the dissolution in alcohol (separate hydrolysis procedure).

3.3.2. Synthesis of TS-1 with separated hydrolysis

3.3.2.1. Analysis of the Ti content in the synthesis gel

A set of syntheses with different Ti/Si_{nom} were prepared to analyze its effect on the Ti speciation. Is it sufficient to reduce the Ti/Si_{nom} of the gel to avoid the formation of extra-framework species?

The PXRD patterns of A20-40 samples (Figure 3.3.2.1.1) are representative of a highly crystalline MFI phase. The crystallization of the framework appears not to be sensitive to the difference in autogenous pressure in the autoclave, consequence of avoiding alcohols evaporation.

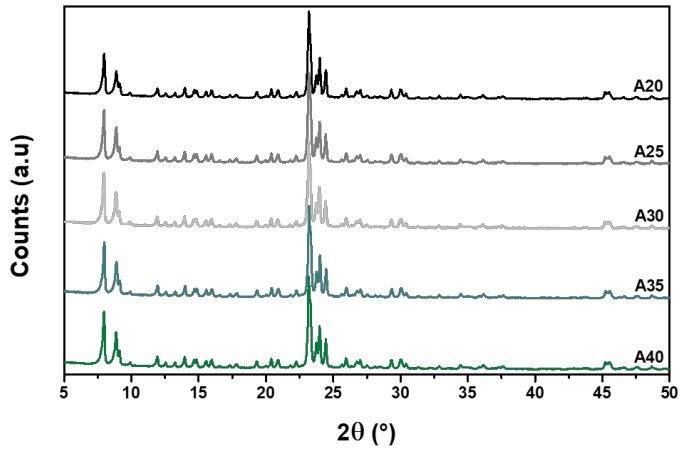

Figure 3.3.2.1.1. PXRD patterns of A20, A25, A30, A35 and A40 (from top to bottom).

The TiO_2 loading (wt%) (Table 3.3.2.1.1) is far below the limit value. The comparison of the Ti/Si_{nom} and Ti/Si_{EDX} highlights how the trend is not linear and both a Ti leaching and enrichment were observed depending on the sample analyzed. This is a weird result without clear explanation, that could be tentatively ascribed to errors of the operator, ageing of the reagents or nonlinear, co-variant effects.

The UV and ATR-IR (Figure 3.3.2.1.2) spectra of all the samples shows the presence of Ti in framework positions (LMCT absorption at 210 nm and

vibrational band at 960 cm^{-1}) and a Ti species absorbing at 235 nm. The band at 235 nm is ascribed here to "intermediate" Ti species because their exact geometry is unknown. They could be penta- or hexa-coordinated species with a strong distortion compared to the octahedral geometry. A weak shoulder at 320 nm in the spectrum of A20 suggests that possibly a very small fraction of anatase is present here.

Table 3.3.2.1.1. Total Ti content of A20, A25, A30, A35 and A40, determined by EDX.

Name	Ti/Si_{nom}	Ti/Si_{EDX}	TiO_2 wt%	σ (TiO_2 wt%)
A20	0.0072	0.0047	0.63	0.22
A25	0.0090	0.0066	0.88	0.05
A30	0.0108	0.0110	1.44	0.31
A35	0.0125	0.0055	0.73	0.10
A40	0.0143	0.0071	0.93	0.17

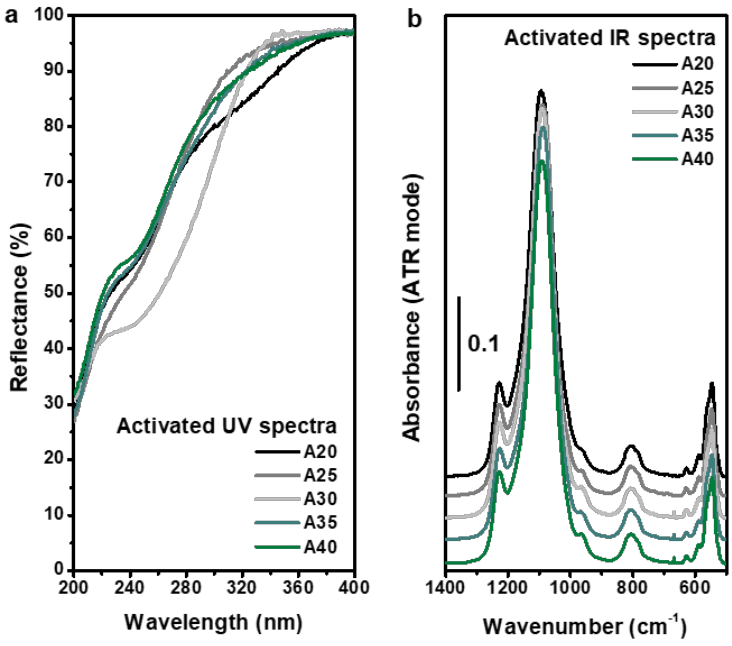

Figure 3.3.2.1.2. (a) UV-Vis and (b) ATR-IR spectra recorded after activation of A20, A25, A30, A35 and A40.

Reducing the Ti/Si_{nom} appears not to be an effective strategy to avoid the formation of extra-framework species. The presence of uncontrolled "hidden" variables seems evident. This highlights the necessity of a systematic study on the topic. The first part of the work must involve the evaluation of the reproducibility of the synthesis procedure, to evaluate if the observed differences occur randomly or are representative of a specific step of the synthesis. The second part involves the study of the effect of the experimental variables. Given the high number of experimental variables, this was conducted by using the DoE approach coupled with a MVA of the results obtained.

3.3.2.2. MVA of the synthesis conditions (DoE 1)

The work described as DoE 1 was published as an independent study.[6] Here the main points are reported.

The synthesis of the A40 sample was repeated three times (R1-a, R2-a and R3-a samples), to evaluate the reproducibility of the synthesis procedure before applying the DoE-MVA study. The higher Ti/Si_{nom} tested in the previous study was chosen, since it does not lead to anatase formation.

The PXRD patterns (Figure 3.3.2.2.1) show highly crystalline MFI phase. The yield and the TiO_2 loading (wt%) are reproducible among the samples (Table 3.3.2.2.1). The Ti speciation as it can be determined by the spectroscopical characterization (Figure 3.3.2.2.2), is qualitatively analog to the one of A40. The amount of framework Ti is comparable in the three syntheses, as it can be seen by the integrated areas of the 960 cm^{-1} bands (Table A1 of Appendix A). The LMCT band absorbing at 235 nm in the UV spectra, has comparable intensity in all the samples except than R3-a. R3-a contains a slightly lower amount of intermediate Ti species. The LMCT onset (Table A1) of the R1-3a sample is not in line with the other LMCT onsets. This was considered as

experimental variability and included in the MVA, given the reproducibility of the other responses.

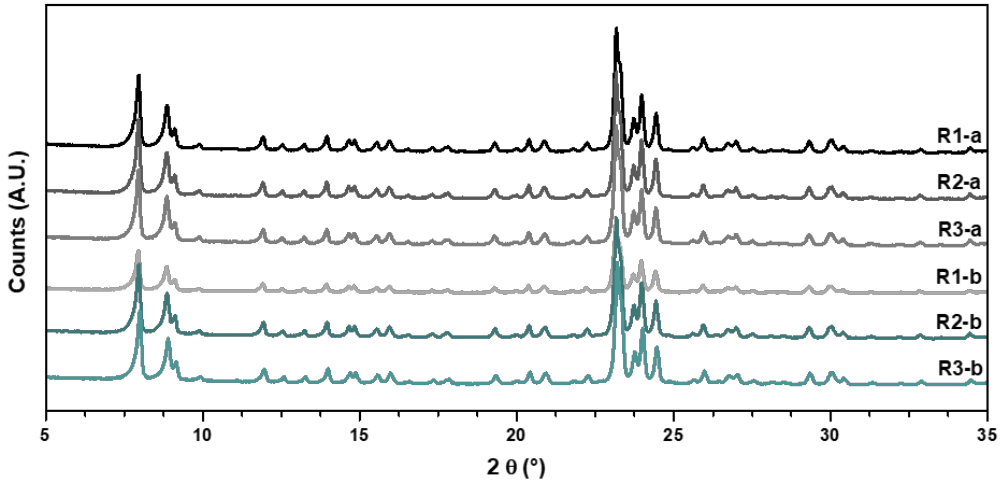

Figure 3.3.2.2.1. PXRD patterns of the reproduced samples of DoE 1.

Table 3.3.2.2.1. Yield and total Ti content of reproduced samples of DoE 1.

Name	Yield (%)	Ti/Si_{nom}	Ti/Si_{EDX}	TiO_2 wt%	σ (TiO_2 wt%)
R1-a	75.35	0.0143	0.0095	1.25	0.13
R2-a	72.82	0.0143	0.0090	1.18	0.19
R3-a	74.40	0.0143	0.0086	1.13	0.11
R1-b	76.85	0.0143	0.0097	1.28	0.08
R2-b	77.06	0.0143	0.0085	1.12	0.38
R3-b	76.97	0.0143	0.0097	1.28	0.30

The R*i*-b samples (synthesized after all the DoE 1) gave analogous results to those of the R*i*-a set. In the R*i*-b set, LMCT onset and the approximate amount of the Ti species with intermediate coordination are also reproducible. The coherence of the results of the R*i*-b with those of R*i*-a samples ensures that no uncontrolled variables involving the aging of the reagents or seeding in the liners are present.

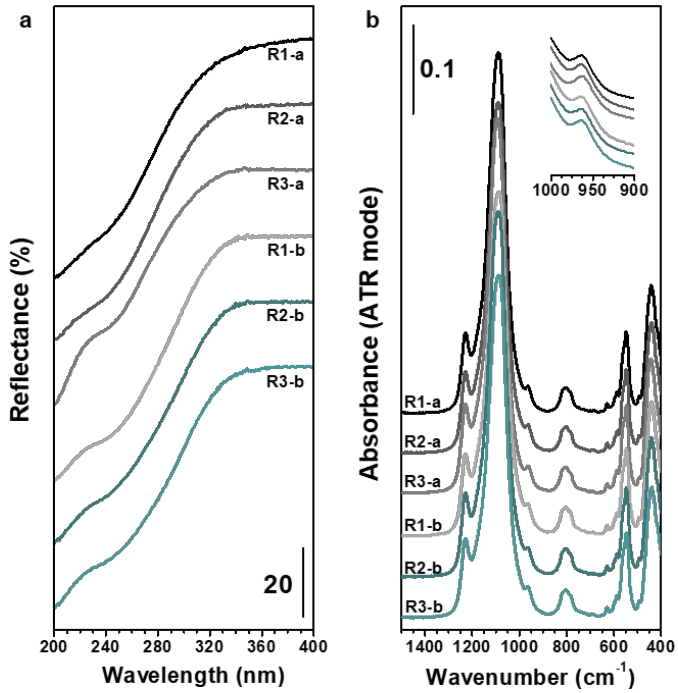

Figure 3.3.2.2.2. (a) UV-Vis and (b) ATR-IR activated spectra of reproduced samples of DoE 1.

The PXRD patterns (Figure 3.3.2.2.1) of the TS-1 samples belonging to DoE 1 shows that, in the experimental domain, highly crystalline MFI phase can be obtained, without nucleation of different phases. The TiO_2 content spreads from 0.91 to 2.40 wt%. The LMCT band in the UV spectra (Figure 3.3.2.2.4a) shows framework (210 nm) and intermediate Ti species (235 nm) in all the samples. None of the samples contain bulk anatase. The intensity of the 960 cm^{-1} band in the ATR-IR spectra (Figure 3.3.2.2.4) is difficult to visually compare; the differences can be better appreciated from the integrated areas in Table A1. The samples with higher integrated areas are N8, N9, N12 and N13. They are also those with higher LMCT onset (Table A1).

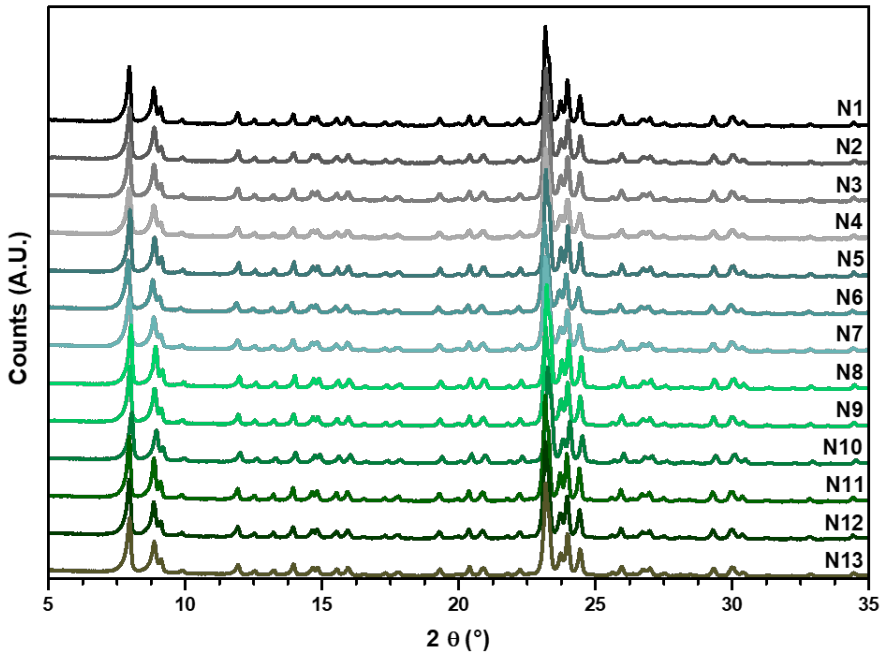

Figure 3.3.2.2.3. PXRD patterns of the samples of DoE 1.

Table 3.3.2.2.1. Yield and total Ti content of samples of DoE 1.

Name	Yield	Ti/Si_{nom}	Ti/Si_{EDX}	TiO_2 wt%	σ (TiO_2 wt%)
N1	75.32	0.0143	0.0122	1.60	0.37
N2	73.03	0.0143	0.0073	0.95	0.14
N3	74.88	0.0143	0.0059	0.78	0.15
N4	67.53	0.0143	0.0069	0.91	0.14
N5	79.71	0.0143	0.0116	1.53	0.14
N6	69.22	0.0143	0.0167	2.18	0.21
N7	66.82	0.0143	0.0120	1.57	0.31
N8	90.58	0.0143	0.0179	2.33	0.26
N9	94.94	0.0143	0.0166	2.16	0.39
N10	74.27	0.0143	0.0131	1.71	0.10
N11	89.66	0.0143	0.0148	1.93	0.10
N12	94.82	0.0143	0.0185	2.40	0.33
N13	78.46	0.0143	0.0163	2.12	0.31

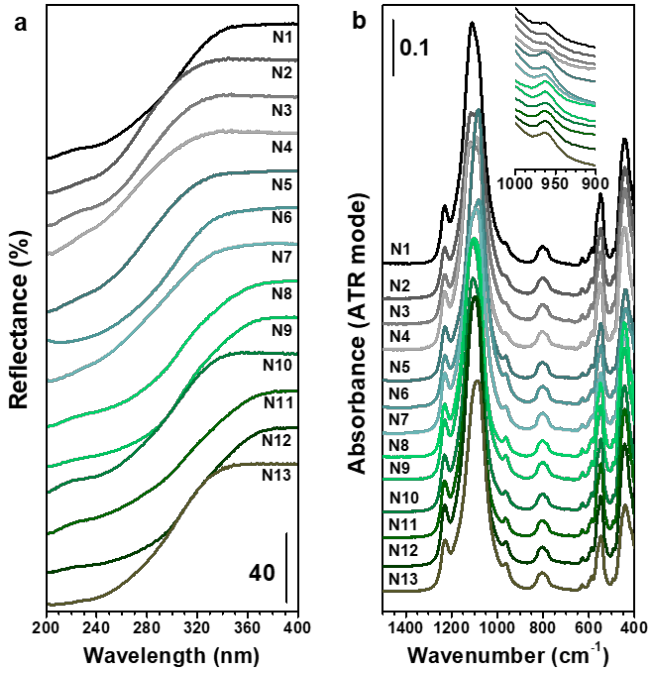

Figure 3.3.2.2.4. (a) UV-Vis and (b) ATR-IR spectra recorded after activation of samples of DoE 1.

The multivariate data analysis allowed to understand the positive or negative linear effect of the synthesis variables on the responses (yield, Ti/Si_{EDX}, LMCT onset and 960 cm^{-1} area). For each response, a coefficient plot was obtained (Figure 3.3.2.2.5). The coefficient plot is the column graph of the coefficients in equation 3.3:

$$y = C + a_1x_1 + a_2x_2 + a_3x_3 + a_4x_4 + a_5x_5 + a_6x_6 + a_7x_7 \qquad (3.3)$$

Where y is the response (yield, Ti/Si_{EDX}, LMCT onset or 960 cm^{-1} band) that can be obtained in a specific synthesis, x_i is the level used for the variable i (i = t(H-TEOS), T(H-TEOS), t(H-TBOT), t(A), T(A), t(Cry) or T(Cry)), a_i is the weight of the effect of the variable i on the response y and C is the constant term (namely the average value that the response y can assume in the experimental domain). When the coefficient a_i is positive, an increase of the level of the variable x_i determines an increase in the response y and *vice*

versa. In the coefficient plots, the height of each column numerically corresponds to the coefficients a_i and to the constant value C. The error bars of the columns were used to understand which term is significant and which one is not. If the error bar overpasses the zero level, *i.e.* it is not sure whether the effect is even positive or negative, the term is not significant. The design chosen in this work is a screening design, with the aim of discern which variable has a significant effect on which response, hence the obtained coefficients cannot be used for quantitative prediction of the result of a synthesis. Here the coefficients were used as an instrument for understanding the system under investigation.

The coefficient plot for the yield (Figure 3.3.2.2.5a) indicates that the time of crystallization is the only variable affecting it significantly. The time of the hydrothermal treatment probably affects the achievement of the equilibrium between the precipitation and the solubilization of the silicate species, responsible of most of the mass of the material and hence of the big part of the yield, the low TiO_2 loading given. Moreover, this result imply that the conditions used for the TEOS hydrolysis and for the aging do not significantly affect the yield, in the examined experimental domain.

The obtained coefficients for the Ti/Si_{EDX} (Figure 3.3.2.2.5b) evidence its correlation with the obtained yield. The Ti/Si_{EDX} is affected by the temperature of crystallization. The precipitation-solubilization equilibria of both the silicate and titanate species, and hence their relative solubility, are likely affected by the temperature used during the crystallization. The Ti/Si_{EDX} is also significantly affected by the time of hydrolysis of TBOT. This means that, in the used experimental conditions, the hydrolysis of TBOT needs more than 4 h to be complete. This suggests that long hydrolysis times are preferred to increase the Ti/Si_{EDX}.

The coefficient plot of the LMCT onset (Figure 3.3.2.2.5c) shows that it is slightly increased by increasing of the time and temperature of hydrothermal

crystallization. An abatement of the coordination of Ti could be achieved if time and temperature of crystallization could be lowered. The increase of the amount of Ti species in tetrahedral coordination could instead be obtained by increasing the temperature of crystallization (Figure 3.3.2.2.5d). It was also highlighted before that the total amount of Ti in the sample is increased by an increasing of the temperature of crystallization as well.

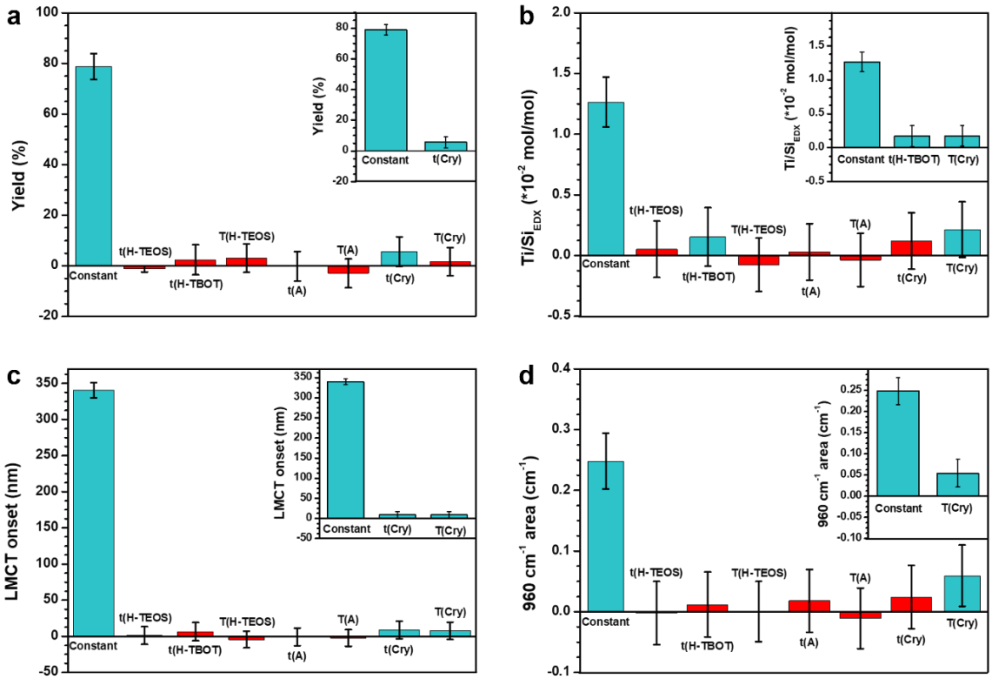

Figure 3.3.2.2.5. Coefficient plots for the responses studied in DoE 1. (a) Yield (%), (b) Ti/Si$_{EDX}$ (*10^{-2} mol/mol), (c) LMCT onset (nm) and (d) 960 cm^{-1} area (cm^{-1}). The labels identify the columns with the constant term C and the variables i in equation (1).

The temperature of crystallization proved to be a key parameter for determining the Ti content and speciation. The problem arises when noticing that its increase causes the increase of the total Ti/Si$_{EDX}$, the LMCT onset and the framework Ti species. Moreover, no variables were discovered that affects the LMCT onset and the framework Ti in opposite directions. This means that

with this synthetic procedure, reagents, and experimental domain, it is impossible to increase the amount of Ti in framework tetrahedral positions, avoiding the parallel formation of intermediate species. The relative amount between tetrahedral and intermediate Ti species is probably almost constant and the differences observed are determined by the difference in the total amount of Ti loaded. The Ti/Si_{EDX} can instead be controlled.

The variables that have a significant influence on the TS-1 synthesis in the explored experimental domain are the time and temperature of crystallization and the time of hydrolysis of TBOT. It is possible to represent the syntheses as points in the 3D space in Figure 3.3.2.2.6. By sectioning the 3D space parallelly to the faces of the cube, it is possible to obtain the so called "contour plots". The contour plots are iso-response plots that shows in a graphical way the effect of the significant variables and they are useful to see which direction should be followed to improve the result of the synthesis. They represent the projection on a plane of the value of the response y by varying the levels of two x_i.

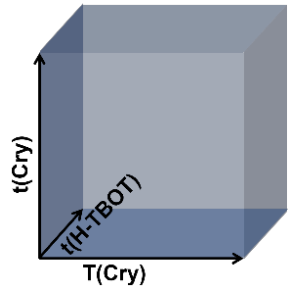

Figure 3.3.2.2.6. 3D experimental space analyzed with DoE 1. Only the significant variables were made explicit.

Figure 3.3.2.2.7 shows the contour plots of the responses involving Ti. The contour plots in panels b, c and d represents these responses as a function of the same variables (time and temperature of the hydrothermal crystallization). Their overlap indicates that the Ti speciation could be improved by moving at high temperature of crystallization and low

crystallization times, even if in the experimental domain it is not possible to completely avoid the formation of intermediate species upon increasing the Ti loading, as suggested by the interpretation of the previous coefficient plots. The next work was done following this direction.

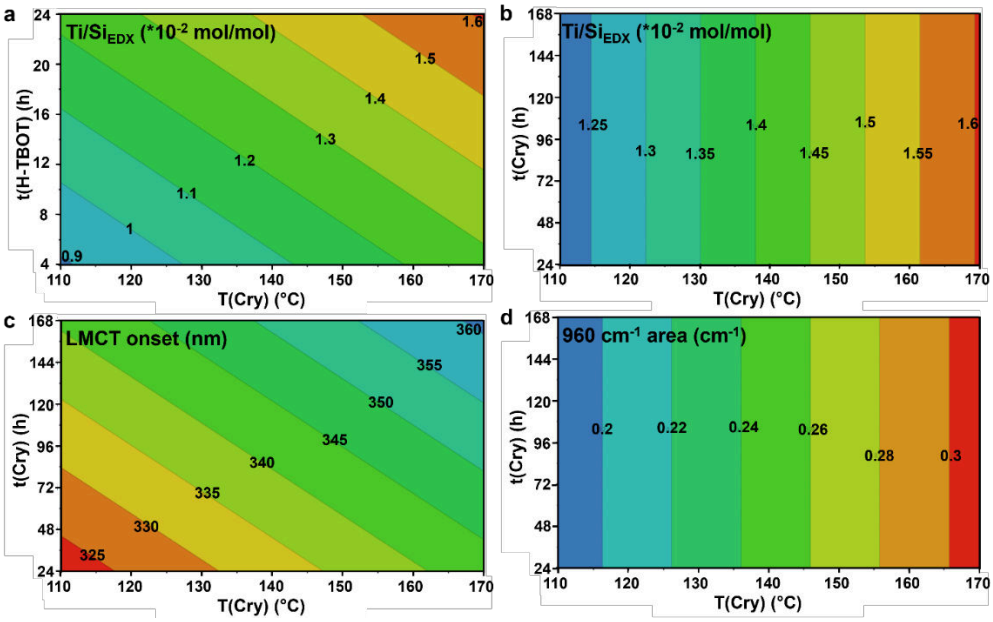

Figure 3.3.2.2.7. Contour plots for the responses involving Ti studied in DoE 1. (a) Ti/Si$_{EDX}$ (*10^{-2} mol/mol), (b) Ti/Si$_{EDX}$ (*10^{-2} mol/mol), expressed as a function of t(Cry) and T(Cry), for the sake of comparison with the other responses, (c) LMCT onset (nm) and (d) 960 cm^{-1} area (cm^{-1}).

3.3.2.3. Screening syntheses after DoE 1

Four syntheses were performed to explore the space outside the experimental domain of the DoE 1 for the time and temperature of the hydrothermal treatment. The insignificant variables were kept constant at the -1 level, for the times, or 0 level (*i.e.* 40 °C), for the temperatures, to avoid the intrinsic irreproducibility of the -1 level of temperature (*i.e.* 20 °C, actually uncontrolled RT). The time of hydrolysis of TBOT was kept constant at the

+1 level, due to its effect on the Ti/Si_{EDX} ratio. The four syntheses were designed to study the temperatures of 170 and 180 °C and the short times of 16 and 24 h for the hydrothermal treatment. Figure 3.3.2.3.1 shows schematically the position of the experimental domain of these syntheses compared with the 3D space constituted by the significant variables of DoE 1.

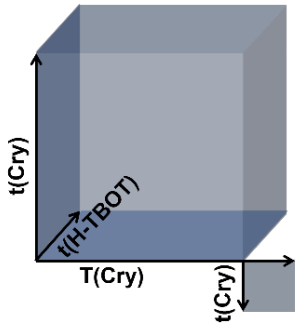

Figure 3.3.2.3.1. Representation of the position of the variables studied in the screening syntheses after DoE 1, compared to the 3D space constituted by the significant variables of DoE 1.

The PXRD patterns (Figure 3.3.2.3.2) show the presence of highly crystalline MFI phase, but the presence of hard, probably amorphous clots, not visible by PXRD but evident while milling the samples synthesized with a 16 h crystallization must be reported.

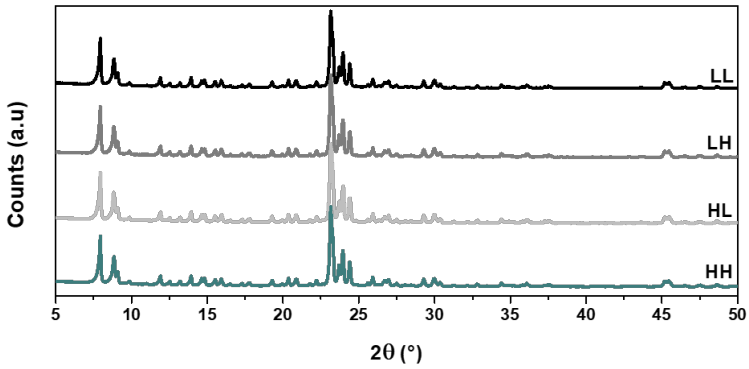

Figure 3.3.2.3.2. PXRD patterns of LL, LH, HL and HH.

The Ti/Si_{EDX} of the samples is in line with those found for the DoE 1 samples and the UV spectra (Figure 3.3.2.3.3a) do not show differences upon modification of the time and temperature of crystallization. The chosen ranges are probably too restricted to appreciate relevant differences among the samples. The integrated area of the 960 cm^{-1} band (Table A2, Figure 3.3.2.3.3b) of the LL sample, crystallized for 16 h at 170 °C, is significantly higher than those of the samples of DoE 1, and its LMCT onset is lower than the average on the DoE 1 samples with analogous integrated areas (see for example N8, N9, N12 and N13). This means that this would have been the correct direction to follow, but the presence of the (probably amorphous) clots makes it unattainable. For this reason, a new DoE was designed to study the effects of time and temperature of the hydrothermal treatment and the effect of the Ti/Si_{nom}, by slightly modifying the synthetic procedure.

Table 3.3.2.3.1. Total Ti content of TS-1 samples LL, LH, HL, HH.

Name	Ti/Si_{nom}	Ti/Si_{EDX}	TiO_2 (wt%)	σ (TiO_2 wt%)
LL	0.0143	0.0131	1.70	0.45
LH	0.0143	0.0097	1.28	0.13
HL	0.0143	0.0105	1.38	0.53
HH	0.0143	0.0115	1.51	0.25

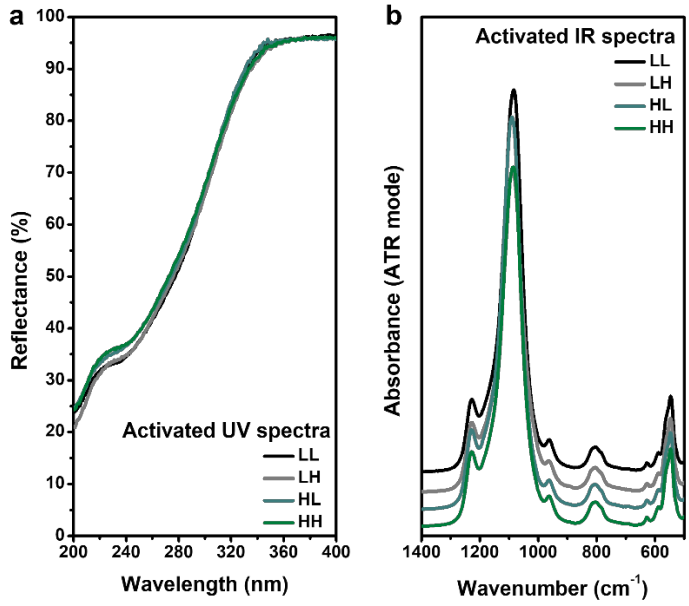

Figure 3.3.2.3.3. (a) UV-Vis and (b) ATR-IR spectra of LL, LH, HL and HH recorded after activation.

3.3.2.4. MVA of the hydrothermal crystallization conditions and Ti content (DoE 2)

The constant presence of the extra-framework species in the UV-Vis spectra absorbing at 235 nm highlights the necessity of modifying the synthesis procedure. The applied modifications were described in paragraph 3.2.3.4, and briefly summarized here: the synthesis was conducted under N_2 atmosphere to avoid the variation of the pH of the gel due to atmospheric CO_2, the samples were washed by centrifugation with alkali-free Milli-Q water and the Ti source was changed from TBOT to TEOT, dissolved in EtOH instead of IPrOH, to avoid the formation of Ti and Si alkoxides of mixed alcohols. The syntheses of DoE 2 were performed in the direction suggested by DoE 1. Figure 3.3.2.4.1 schematically represent the experimental domain of DoE 2 compared to the 3D space composed by the significant variables of DoE 1.

The Ti/Si_{nom} variable, added in DoE 2 is represented as coming toward the observer for graphical reasons.

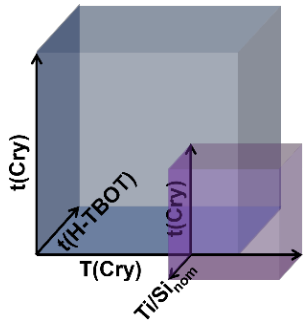

Figure 3.3.2.4.1. Schematical representation of the experimental domain of DoE 2 compared to the 3D space composed by the significant variables of DoE 1.

The PXRD patterns of the samples (Figure 3.3.2.4.2) show the presence of highly crystalline MFI phase. This testify that, as previously seen, the crystallization of the structure is not sensitive to the slight autogenous pressure variation, induced by the composition of the solvent (from a H_2O/EtOH/IPrOH/BuOH to a H_2O/EtOH mixture) or to the slight difference in the autogenous pressure due to the change in the solvent composition.
The yield (Table 3.3.2.4.1) was used for internal comparison since the % value was not calculated. Considering that the theoretical yield for the samples of DoE 1 was 1.85 g for an analogous volume of gel, N8 sample possibly approximates a 100 % yield.

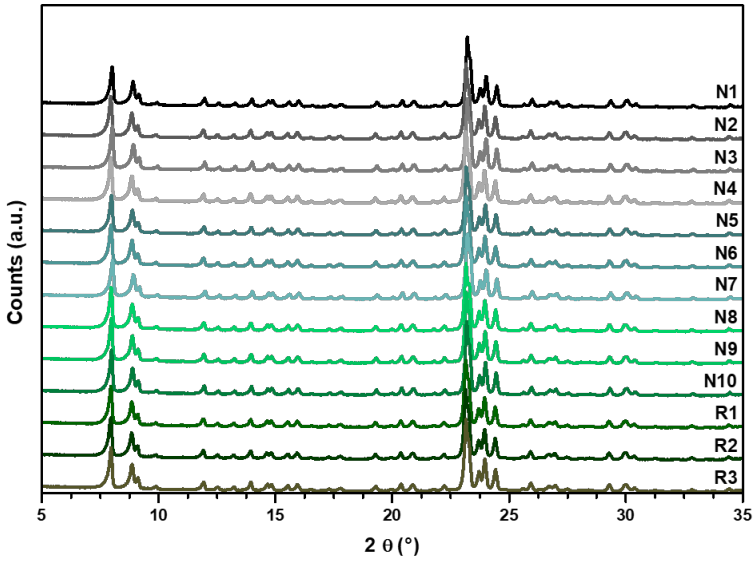

Figure 3.3.2.4.2. PXRD patterns of the samples of DoE 2 and of the reproduced samples of DoE 2.

The Ti/Si_{EDX} (Table 3.3.2.4.1) is higher than the Ti/Si_{nom} for all the samples of DoE 2. An enrichment of Ti, accompanied by a loss of silicate species occurs in the full examined experimental domain. The reduced time of TEOT hydrolysis to 20 min (from the 4 to 24 h used for TBOT) is enough to complete the hydrolysis, due to the different rate of the butoxy and the ethoxy derivate. For this reason, all the samples except for N2 have a TiO_2 loading (wt%) higher than the limit for the MFI framework. All the UV spectra reveals the presence of Ti species with intermediate coordination and possibly the presence of anatase in N7, N8 and N9 samples. It must be highlighted that the variability among the UV spectra of the samples of DoE 2 (Figure 3.3.2.4.3a) is higher respect to the variability among the UV spectra of DoE 1 (Figure 3.3.2.2.4a). This is probably because of the different washing and calcination of the samples. In DoE 1 the samples were washed with deionized water, found to contain traces of K^+ and were calcined in a muffle furnace. The combination of the presence of K^+ and of moisture during the calcination

probably leveled the Ti speciation of the samples of DoE 1. As observed for P30 sample, exceeding the limit of the TiO_2 loading makes the formation of extra-framework Ti species unavoidable. The ATR-IR spectra (Figure 3.3.2.4.3b) show that the bands at 960 cm^{-1} are more prominent than those of samples belonging to DoE 1 and the values of the integrated areas (Table A3) confirm this.

Table 3.3.2.4.1. Yield and total Ti content of the samples of DoE 2.

Name	Yield (g)[1]	Ti/Si_{nom}	Ti/Si_{EDX}	TiO_2 (wt%)	σ (TiO_2)
N1	1.47	0.014	0.0269	3.42	1.60
N2	1.55	0.014	0.0150	1.96	0.37
N3	1.75	0.014	0.0233	3.00	0.30
N4	1.70	0.014	0.0245	3.15	0.98
N5	1.48	0.020	0.0253	3.25	0.54
N6	1.50	0.020	0.0244	3.14	0.56
N7	1.79	0.020	0.0313	3.99	0.63
N8	1.83	0.020	0.0297	3.80	0.56
N9	1.75	0.017	0.0263	3.38	0.60
N10	1.67	0.014	0.0213	2.75	0.30
R1	1.73	0.017	0.0205	2.65	0.34
R2	1.74	0.017	0.0273	3.51	1.77
R3	1.65	0.017	0.0216	2.79	0.29

[1] The yield was expressed as grams of sample because in DoE 2 an excess of gel was prepared for each synthesis and exactly 30 ml of gel were dosed in the Teflon liner for the hydrothermal crystallization. The theorical yield necessary to calculate the % value is then unknown precisely.

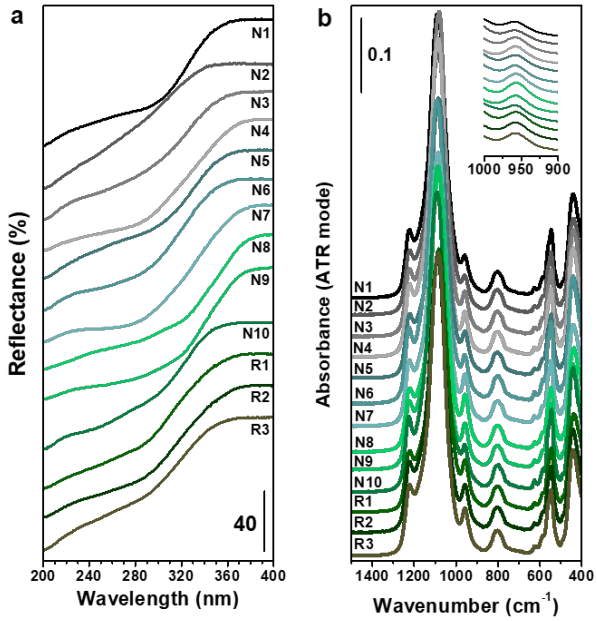

Figure 3.3.2.4.3. (a) UV-Vis and (b) ATR-IR spectra of the samples of DoE 2 and of the reproduced samples of DoE 2, recorded after activation.

The MVA of the results was performed to obtain the effect of the three explored variables. The lower number of variables in DoE 2 compared to those of DoE 1 allows to determine the effects with more details than with DoE 1.

The coefficient plot for the yield (Figure 3.3.2.4.4a) reveals that, as already obtained, it is affected by the temperature of the hydrothermal treatment (T(Cry)). Its effect is nonlinear, as demonstrated by the presence of a quadratic term ($T(Cry)^2$). The linear term is positive and the quadratic term is negative, hence the yield would increase by increasing the temperature of crystallization, approaching a plateau at high temperatures. The yield was also found to depend on the Ti/Si_{nom} and by the combination of Ti/Si_{nom} and temperature of crystallization (Ti/Si_{nom}*T(Cry)). This is consistent with the yield being affected by the solubilization/precipitation equilibria of both the silicate and titanate species, as previously observed.

The coefficient plot for the Ti/Si_{EDX} (Figure 3.3.2.4.4b) shows that it is affected by the temperature of the crystallization (as obtained in DoE 1) and by the Ti/Si_{nom}. This is coherent with the nature of the response. However, it must be noticed that a pronounced Ti enrichment is observed in every synthesis and that the limit value for the TiO_2 loading is overcome in every synthesis except for the N2 sample. This led to unavoidable formation of extra-framework Ti species. Hence, in this context, increasing the total Ti content of the material does not improve the properties of the material. The Ti/Si_{EDX} in DoE 2 should be minimized instead of maximized. The Ti/Si_{nom} is the parameter to act on to reduce the final Ti/Si_{EDX} in the sample, as it will be done in the final TS-1 synthesis (next paragraph). Even if the temperature of crystallization influences the Ti/Si_{EDX} as well, it affects also other responses and therefore, cannot be used.

Due to the too high Ti/Si_{EDX} in the samples, the reliability of the results obtained for the effect of the variables on the LMCT onset and the integrated area of the 960 cm^{-1} band must be considered with caution. The excess of Ti/Si_{EDX} surely affected the Ti speciation and hence could have forced the results toward a specific direction. The coefficient plot related to the LMCT onset (Figure 3.3.2.4.4c) shows that it is affected by the Ti/Si_{nom}, the temperature of crystallization and by a combination of the temperature and time of crystallization (T(Cry)*t(Cry)). The increase of the Ti/Si_{nom} causes an increase of the extra-framework species with intermediate coordination, probably because of the concomitant increment of the Ti/Si_{EDX}. The temperature and the time of crystallization affect the LMCT onset as described for DoE 1.

Similar deductions can be done when looking at the coefficient plot of the integrated area of the 960 cm^{-1} band (Figure 3.3.2.4.4d). In this case, a nonlinear dependence on the time of the hydrothermal treatment was detected. The amount of framework Ti species will increase upon increasing

the time of crystallization, approaching a plateau for elapsed times. The temperature of crystallization was found to have both an independent effect on the 960 cm^{-1} area and in combination with the time (t(Cry)*T(Cry)). This complex behavior could possibly be due to the overlap of the effect of the formation of tetrahedral Ti species ad of defective Si-OH species on the growth of the 960 cm^{-1} band. Actually, the variation of the Si-OH groups is probably affected by the temperature of crystallization because their presence is determined by the precipitation/solubilization equilibria and by the time because a pseudo steady-state level of the Si-OH content should be reached at long crystallization time. The temperature of crystallization appears again as a key factor in determining the TiO_2 content and speciation.

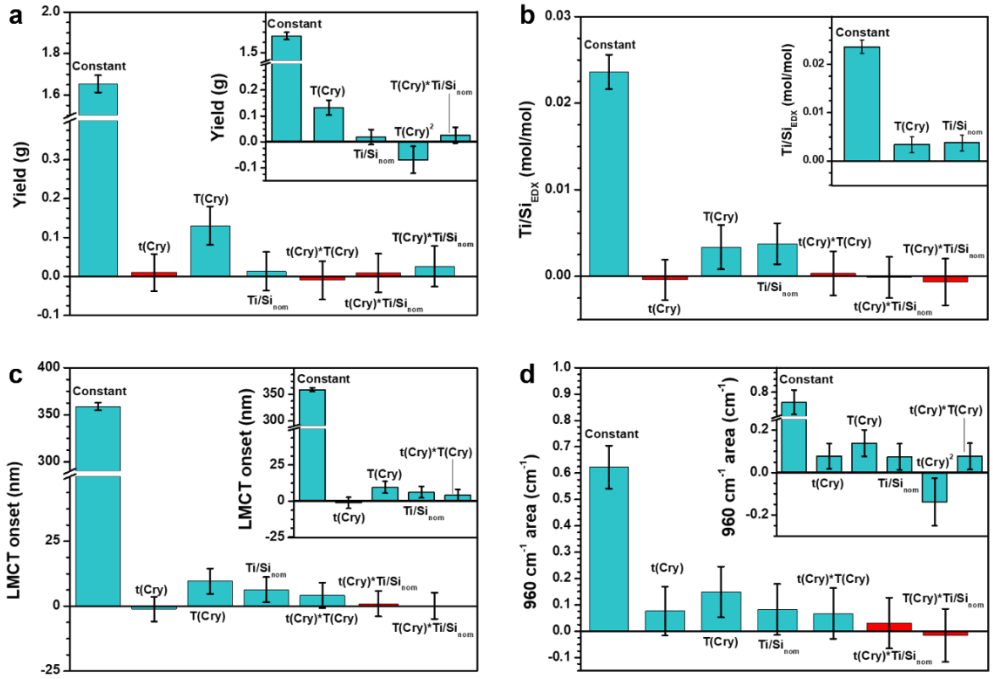

Figure 3.3.2.4.4. Coefficient plots for the responses studied in DoE 2. (a) Yield (%), (b) Ti/Si_{EDX} (mol/mol), (c) LMCT onset (nm) and (d) 960 cm^{-1} area (cm^{-1}).

The contour plots of the four responses of DoE 2 are reported in Figure 3.3.2.4.5. In each plot the temperature of crystallization is reported on the *x* axis and the Ti/Si_{nom} on the *y* axis. The contour plots of the LMCT onset and 960 cm^{-1} area are repeated three times, one for each level of time of crystallization, to represent the simultaneous effect of the three variables. The contour plots of the 960 cm^{-1} integrated area shows that the highest amount of framework Ti can be obtained with a Ti/Si_{nom} around 0.018 at 190 °C in 96 h of crystallization. The trend of the LMCT onset is analogous to the trend of increasing the Ti/Si_{EDX}, as obtained in DoE 1. Also in this experiment, the splitting of the formation of the tetrahedral and of the extra-framework species was not reached.

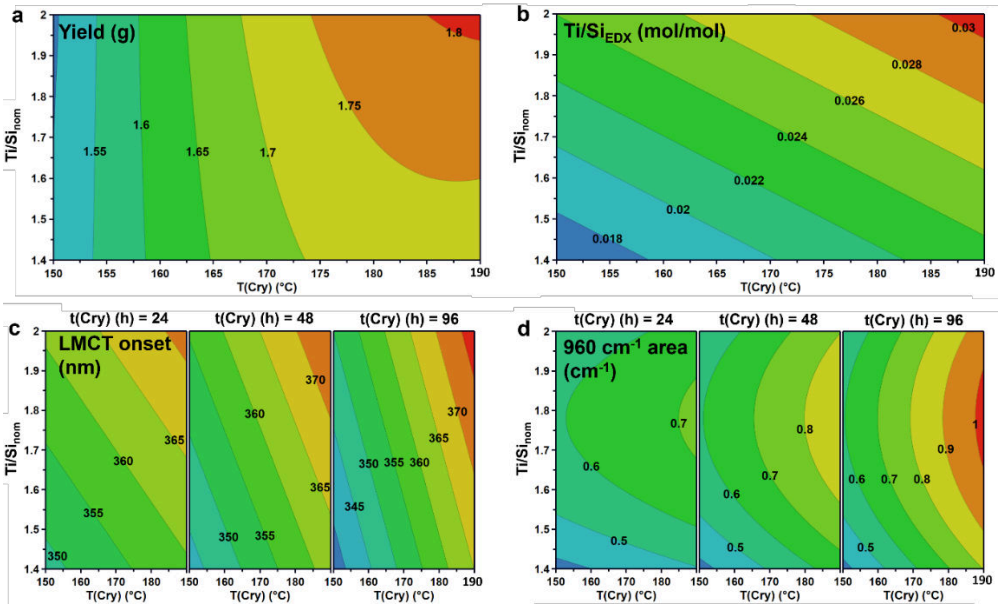

Figure 3.3.2.4.5. Contour plots of the responses studied in DoE 2. (a) Yield (g), (b) Ti/Si_{EDX} (mol/mol), (c) LMCT onset (nm) and (d) 960 cm^{-1} area (cm^{-1}).

The quantification of the Ti species in tetrahedral and intermediate coordination and of anatase was performed. Figure 3.3.2.4.6 shows the

spectra of the reference samples used for constructing the calibration lines and the Raman spectra of N7, N8 and N9 samples of DoE 2 suspected to contain anatase, based on the UV results. The Raman spectra reveals that N8 contains a relatively high amount of anatase and that N7 and N9 contain a very low amount of bulk oxide. Figure 3.3.2.4.7 shows the calibration lines for the framework Ti species (a) and for anatase (b).

The results of the quantification are reported in Table 3.3.2.4.2. The prevalent species of all the samples is the Ti with intermediate coordination. The amount of framework Ti in the samples is comprised between the 0.29 and the 1.43 wt%. The highest amount was obtained in N8, synthesized in 96 h at 190 °C, with a Ti/Si_{nom} of 0.02.

Table 3.3.2.4.2. Quantification of the framework and intermediate Ti species and of bulk anatase of TS-1 samples of DoE 2.

Name	TiO_2-fram.[1] (wt%)	TiO_2-an.[2] (wt%)	TiO_2-int.[3] (wt%)	TiO_2-fram./TiO_2 (%)
N1	0.29	-	3.16	8.5
N2	0.29	-	1.66	14.8
N3	0.71	-	2.30	23.7
N4	0.92	-	2.24	29.2
N5	0.61	-	2.65	18.8
N6	0.57	-	2.57	18.15
N7	0.57	0.01	3.42	14.28
N8	1.43	0.07	2.29	37.6
N9	0.92	0.03	2.43	27.2
N10	0.31	-	2.44	11.3
R1	0.85	-	1.81	32.1
R2	0.92	-	2.59	26.21
R3	0.88	-	1.91	31.54

[1] Ti in framework positions (tetrahedral coordination)
[2] Ti in bulk anatase (octahedral coordination)
[3] Ti in extra-framework positions with intermediate coordination

The last column of Table 3.3.2.4.2 reports the fraction of Ti in framework positions respect to the total amount of TiO_2. This value is low in all the

samples, comprised between the 8.5 to the 37.6%. The low fraction of framework species, the fact that the highest amount of tetrahedral species reached is still far below the limit amount of 2.66 wt%, and the prevalence of Ti species with intermediate coordination, absorbing at 235 nm in the UV spectra suggest that a hindrance to the insertion of Ti is still present in this synthesis procedure. To solve this issue, the synthesis procedure and the reagents were further modified as reported in paragraph 3.3.2.5.

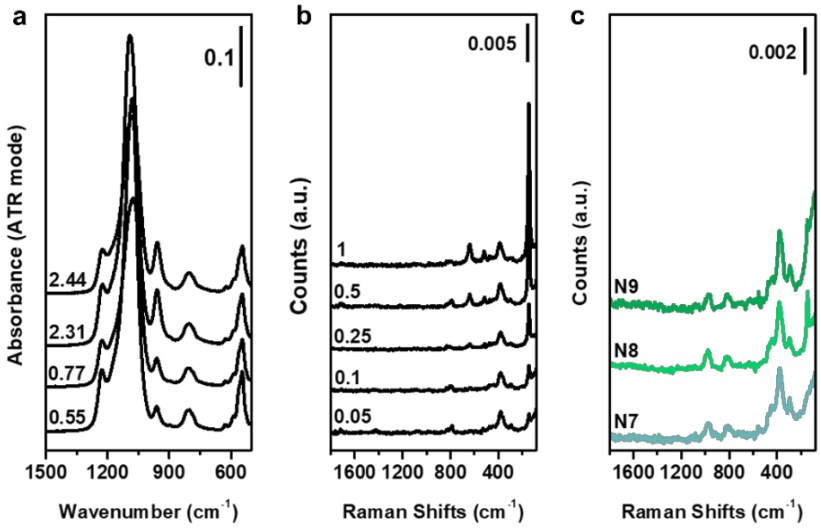

Figure 3.3.2.4.6. (a) ATR-IR activated spectra of the reference samples for Ti in tetrahedral coordination. (b) Raman spectra of the reference samples for anatase, recorded with a laser at 1064 nm. The labels in panels a and b indicate the wt% of TiO_2 in each sample, corresponding respectively to the amount of framework TiO_2 and the amount of anatase in the reference samples. (c) Raman spectra of the N7, N8 and N9 samples of DoE 2, recorded with a laser at 1046 nm.

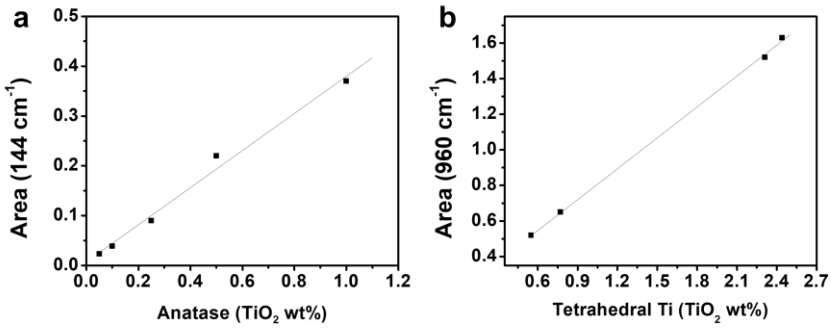

Figure 3.3.2.4.7. (a) Calibration line used for the quantification of anatase ($y = 0.3728x + 0.0072$) and (b) calibration line used for quantification of Ti in tetrahedral coordination ($y = 0.5791x + 0.1999$).

3.3.2.5. Final TS-1 synthesis after DoE 2

A final TS-1 synthesis (F-TS-1) was performed using a TPAOH source free from alkaline metals, adding a couple of hours of aging at 0 °C before heating up the gel for the usual aging at 40 °C and by reducing the H_2O/Si ratio in the gel undergoing hydrolysis and aging. The residual amount of water was added to the gel just before the hydrothermal treatment and the Ti/Si$_{nom}$ was substantially reduced, as suggested by DoE 2. Visually, the F-TS-1 synthesis can be represented as the cyan star in Figure 3.3.2.5.1. Compared to DoE 2, the Ti/Si$_{nom}$ is lower, the level of the time of crystallization is -1, *i.e.* 1 day and the level of the temperature of crystallization is +1, *i.e.* 190 °C. These levels correspond to those of N5 and N6 syntheses of DoE 2. The direction suggested by the MVA of DoE 2 is difficult to interpret, due to the Ti enrichment observed in the syntheses. N5 and N6 were the samples that manifested the lower degree of enrichment in the DoE 2 set of samples, calculated with eq. 3.4:

$$Degree\ of\ enrichment = \frac{Ti/Si_{EDX}}{Ti/Si_{nom}} * 100 \qquad (3.4)$$

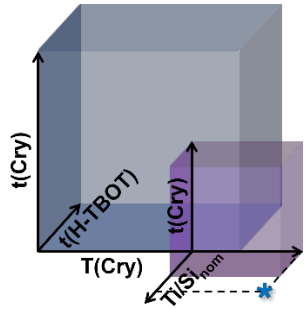

Figure 3.3.2.5.1. Schematic representation of the synthesis conditions of F-TS-1 compared to the experimental domain of DoE 2 and to the 3D space constituted by the significant variables of DoE 1. The cyan star indicates the point of the F-TS-1 synthesis.

The PXRD pattern (Figure 3.3.2.5.2) is typical of a highly crystalline MFI phase. The total TiO_2 content determined by EDX is still higher than the limit value. The UV spectrum plotted in reflectance mode (Figure 3.3.2.5.3a) shows a weak signal at 320 nm, but the plot in Kubelka Munk units (inset of Figure 3.3.2.5.3a) does not. The Kubelka Munk units are proportional to the concentration of the species and hence more reliable than the reflectance for the evaluation of the amount of anatase. The reflectance scale extremely enhances the intensity of a probably not quantifiable trace of oxide. This is confirmed by the absence of the peak at 144 cm^{-1} in the Raman spectrum (Figure 3.3.2.5.3c). The UV spectrum reveals that the formation of Ti species with intermediate coordination is totally avoided, and the only Ti species present in the sample is the tetrahedral one. The total Ti content of the F-TS-1 sample is reported in Table 3.3.2.5.1. The amount of the species in tetrahedral coordination determined by applying the calibration line in Figure 3.3.2.4.7b to the integration of the prominent band at 960 cm^{-1} in Figure 3.3.2.3b, is 2.64 wt% (Table 3.3.2.5.2). This value does not coincide with the total TiO_2 content determined by EDX (3.32 wt%). The difference between the quantification of the overall quantity of TiO_2 and the quantification of the

tetrahedral species determined with the calibration line could be due to the error of the quantification by EDX. The amount of sample used for quantification purposes in EDX is extremely low, and the statistical reliability of the measure is doubtful.

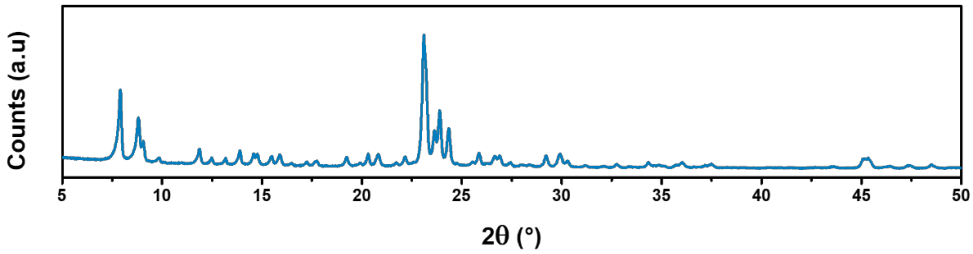

Figure 3.3.2.5.2. PXRD pattern of F-TS-1.

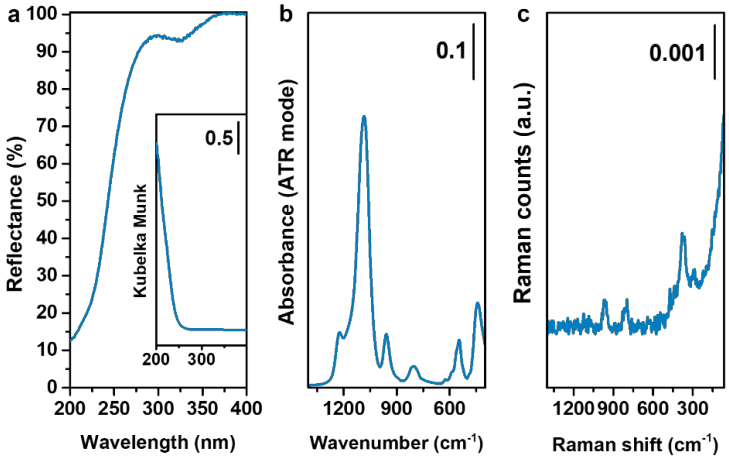

Figure 3.3.2.5.3. (a) UV activated spectrum in Reflectance (%) (main figure) and in Kubelka Munk units (inset), (b) ATR-IR activated spectrum and (c) Raman spectrum recorded with a laser at 1064 nm of F-TS-1.

Table 3.3.2.5.1. Total Ti content in F-TS-1 sample.

Name	Ti/Si_{nom}	Ti/Si_{EDX}	TiO_2 (wt%)	σ (TiO_2)
F-TS-1	0.008	0.026	3.32	0.9

Table 3.3.2.5.2. Quantification of the framework and intermediate Ti species and of bulk anatase in F-TS-1 sample.

Name	TiO_2-fram.[1] (wt%)	TiO_2-an.[2] (wt%)	TiO_2-int.[3] (wt%)	TiO_2-fram./TiO_2 (%)
F-TS-1	2.64	0	-	79.3

[1] Ti in framework positions (tetrahedral coordination)
[2] Ti in bulk anatase (octahedral coordination)
[3] Ti in extra-framework positions with intermediate coordination

3.4. Conclusions and open questions

The systematic work performed to study the synthesis of the TS-1 catalyst allowed to get familiar with the synthesis of Ti-zeolites and with the phenomena occurring during the hydrothermal treatment in general. The use of DoE efficiently helped in the identification and interpretation of the effects of the synthesis variables on the obtained results, clearly highlighting both the powerful and critical aspects of the adopted procedures. The coupling of the DoE approach and the accurate analysis of the published literature on the topic allowed to obtain a sample that contains exclusively Ti in tetrahedral, framework positions, qualitatively and quantitatively comparable with the industrial samples[25,36] and best results published in academic literature. [37–39]
The DoE 1 highlights how the conditions used during the hydrolysis and the aging steps of the synthesis are not significant compared to the effects of the time and temperature of the hydrothermal crystallization. In particular, the temperature of crystallization causes an increase of the total TiO_2 loading, both when inserted in framework and in extra-framework positions. The total TiO_2 loading is further affected by the Ti/Si_{nom} used in the gel and the coordination of the extra-framework species increases at elapsed times of crystallization. This highlighted how the total TiO_2 loading of the materials can be controlled but that the precipitation of extra-framework species cannot

be avoided, with the used experimental settings and in the explored range of variables. These are the main results published in Rosso et al.[6]

The syntheses performed after DoE 1 shows that the DoE approach is successful: actually, a sample having the 960 cm^{-1} band more intense that anyone obtained in DoE 1 was synthesized. However, this direction was not further explored because of the presence of amorphous clots in the sample with the intense 960 cm^{-1}, probably due to the short crystallization time (16 h).

The DoE 2 allowed to evaluate the effects of the change in Ti source, from TBOT to TEOT. The hydrolysis rate of TEOT was extremely fast compared to the TBOT one, hence its hydrolysis was complete in every synthesis performed in DoE 2. This determined the observation of a strong Ti enrichment and TiO_2 loading too high to allow the complete insertion in the framework. The high percentage of species with intermediate compared to the Ti species in tetrahedral coordination also suggested that a hinder to the Ti insertion is still present.

With the F-TS-1 synthesis, the effect of the absence of any trance of K^+ in the gel was observed. All the Ti inserted in tetrahedral positions, except for an unquantifiable trace of anatase. In particular, the formation of Ti species with intermediate coordination was completely avoided.

However, the reproducibility of the synthesis procedure adopted to prepare F-TS-1 sample is not yet fully established. The presence or absence of the weak band ascribable to bulk anatase, visible only in reflectance scale, is not reproducible, and in some batches, the precipitation of enough anatase to be detected by Raman is observed. A study on the reproducibility of the synthesis is on-going and a third DoE is already programmed, to study the effects of the temperature and time of the hydrothermal treatment and the effect of slight changes in the Ti/Si_{nom}.

The complete absence of TiO_2 species with intermediate coordination appears as the most important result achieved with F-TS-1 and is observed to be fully reproducible. It can be ascribed to (i) the complete absence of K^+ cations or (ii) the modified H_2O/Si (and consequent H_2O/Ti) ratio in the synthesis gel. Results shown in Chapter 6 would suggest the first hypothesis as the most probable, but this still need a confirmation, and a cooperative effect of the two parameters is not excluded. In any case, the formation of TiO_2 species with intermediate coordination likely hindered the formation of bulk anatase in the DoE 1 and DoE 2 samples. Actually, bulk anatase was never observed in DoE 1 and rarely in DoE 2 samples. The elimination of the origin of the intermediate TiO_2 species leads to an easier precipitation of bulk anatase. Whether one situation or the other is preferred is still controversial.[5,14,25,40–42] The extreme Ti enrichment experimented when TEOT is used as Ti source is another point that needs clarification. The Ti enrichment is rarely reported in published procedures and a Ti leaching more frequently occurs in literature reported data.[3,6,8–10,14,43] In this thesis, both leaching and enrichment were observed when TBOT is used (DoE 1, LL, LH, HL and HH) and only enrichment when TEOT is used as Ti source (DoE 2 and F-TS-1), in the syntheses where the separate hydrolysis was performed. The Ti/Si_{nom} and the Ti/Si_{EDX} were coincident in the P30 sample, prepared using TBOT, instead. This point needs further studies to be clarified, but an important difference must be noted between P30 (and the majority of the published syntheses) and the procedure involving the separate hydrolysis used in this work: the evaporation of the alcohols. The alcohols produced upon hydrolysis of the Si and Ti precursors were evaporated only during the preparation of P30. The lack of evaporation surely affects the hydrolysis equilibria, pushing it toward the reagents. This is particularly important when TEOS is involved, because its hydrolysis rate is the slower among the precursors.[20] When the EtOH is not evaporated, the leaching of Si-containing species is probably increased, determining the Ti

enrichment observed in some of the samples of DoE 1, in all the samples of DoE 2 and in F-TS-1. When TEOT is involved, both the hydrolysis and the condensation of the Ti-containing species are so fast that the presence of the excess of EtOH has no effect on the recombination of the TEOT molecule, after its hydrolysis. When TBOT is used as Ti source, the situation is intermediate. This is the reason why both Ti leaching and enrichment were observed in the samples of DoE 1, depending on the influence of the reaction conditions on the condensation/solubilization equilibria of the Ti- and Si-containing species.

3.5. References

1 G. J. Hutchings, D. F. Lee and A. R. Minihan, *Catal. Letters*, 1995, **33**, 369–385.

2 R. Bai, Y. Song, R. Bai and J. Yu, *Adv. Mater. Interfaces*, 2021, **8**, 2001095.

3 A. Thangaraj, M. J. Eapen, S. Sivasanker and P. Ratnasamy, *Zeolites*, 1992, **12**, 943–950.

4 G. Zhang, J. Sterte and B. J. Schoeman, *Chem. Mater.* 1997, **9**, 210–217.

5 T. Tatsumi, K. A. Koyano and Y. Shimizu, *Appl. Catal. A Gen.* 2000, **200**, 125–134.

6 F. Rosso, A. Rizzetto, A. Airi, K. Khoma, M. Signorile, V. Crocellà, S. Bordiga, S. Galliano, C. Barolo, E. Alladio and F. Bonino, *Inorg. Chem. Front.* 2022, **9**, 3372–3383.

7 Y. Wang, M. Lin and A. Tuel, *Microporous Mesoporous Mater.* 2007, **102**, 80–85.

8 J. Xing, D. Yuan, H. Liu, Y. Tong, Y. Xu and Z. Liu, *J. Mater. Chem. A Mater.*, 2021, **9**, 6205–6213.

9 T. Ge, Z. Hua, J. Lv, J. Zhou, H. Guo, J. Zhou and J. Shi, *CrystEngComm*, 2017, **19**, 1370–1376.

10 W. Fan, B. Fan, X. Shen, J. Li, P. Wu, Y. Kubota and T. Tatsumi, *Microporous Mesoporous Mater.* 2009, **122**, 301–308.

11 V. Smeets, E. M. Gaigneaux and D. P. Debecker, *Microporous Mesoporous Mater.* 2020, **293**, 109801.

12 J. F. Bengoa, N. G. Gallegos, S. G. Marchetti, A. M. Alvarez, M. V Cagnoli and A. A. Yeramián, *Microporous Mesoporous Mater.* 1998, **24**, 163–172.

13 Q. Guo, Z. Feng, G. Li, F. Fan and C. Li, *J. Phys. Chem. C*, 2013, **117**, 2844–2848.

14 W. Fan, R. G. Duan, T. Yokoi, P. Wu, Y. Kubota and T. Tatsumi, *J. Am. Chem. Soc.* 2008, **130**, 10150–10164.

15 A. Tuel and Y. Ben Taârit, *Appl. Catal. A Gen.* 1994, **110**, 137–151.

16 M. Taramasso, G. Perego and B. Notari, US Patent 4,410,501, 1983.

17 A. Esposito, M. Taramasso and C. Neri, US Patent 4,396,783, 1983.

18 A. Carati, D. Berti, R. Millini, F. Rivetti, M. A. Mantegazza and G. Girotti, US Patent 9,358,531, 2016.

19 M. Signorile, L. Braglia, V. Crocellà, P. Torelli, E. Groppo, G. Ricchiardi, S. Bordiga and F. Bonino, *Angew. Chem. Int. Ed.* 2020, **59**, 18145–18150.

20 J. Blanchard, S. Barboux-Doeuff, J. Maquet and C. Sanchez, *New J. Chem.* 1995, **19**, 929–941.

21 MODDE® 13 Software; Umeå, Sweden, 2020, Available Online: https://www.sartorius.com/en/products/process-analyticaltechnology/data-analytics-software/doe-software/modde?gclid=CjwKCAjwiuuRBhBvEiwAFXKaNM5XdB5p1oonkutonEjqk72uuSniQRNaZNqpIKZe3pQs0t2VRutWkRoCNvYQAvD_BwE (accessed 23 March 2022).

22 T. Kavitha, P. Attri, P. Venkatesu, R. S. R. Devi and T. Hofman, *J. Phys. Chem. B*, 2012, **116**, 4561–4574.

23 T. Lundstedt, E. Seifert, L. Abramo, B. Thelin, A. Nystrom, J. Pettersen and R. Bergman, *Chemometr. Intell. Lab. Syst.* 1998, **42**, 3–40.

24 R. Leardi, *Anal. Chim. Acta*, 2009, **652**, 161–172.

25 M. Signorile, V. Crocellà, A. Damin, B. Rossi, C. Lamberti, F. Bonino and S. Bordiga, *J. Phys. Chem. C*, 2018, **122**, 9021–9034.

26 D. Scarano, A. Zecchina, S. Bordiga, F. Geobaldo, G. Spoto, G. Petrini, G. Leofanti, M. Padovan and G. Tozzola, *J. Chem. Soc., Faraday Trans.* 1993, **89**, 4123–4130.

27 R. Millini, E. P. Massara, G. Perego and G. Bellussi, *J. Catal.* 1992, **137**, 497–503.

28 E. Gianotti, V. Dellarocca, L. Marchese, G. Martra, S. Coluccia and T. Maschmeyer, *Phys. Chem. Chem. Phys.* 2002, **4**, 6109–6115.

29 F. Bonino, A. Damin, G. Ricchiardi, M. Ricci, G. Spanò, R. D'Aloisio, A. Zecchina, C. Lamberti, C. Prestipino and S. Bordiga, *J. Phys. Chem. B*, 2004, **108**, 3573–3583.

30 T. Armaroli, M. Trombetta, A. Gutièrrez Alejandre, J. R. Solis and G. Busca, *Phys. Chem. Chem. Phys.* 2000, **2**, 3341–3348.

31 G. Coudurier, C. Naccache and J. C. Verdine, *J. Chem. Soc. Chem. Commun.* 1982, 1413–1415.

32 E. Astorino, J. B. Peri, R. J. Willey and G. Busca, *J. Catal.* 1995, **157**, 482–500.

33 A. Airi, M. Signorile, F. Bonino, P. Quagliotto, S. Bordiga, J. A. Martens and V. Crocellà, *ACS Appl. Mater. Interfaces*, 2021, **13**, 49114–49127.

34 R. Ravishankar, C. Kirschhock, B. J. Schoeman, P. Vanoppen, P. J. Grobet, S. Storck, W. F. Maier, J. A. Martens, F. C. De Schryver and P. A. Jacobs, *J. Phys. Chem. B*, 1998, **102**, 2633–2639.

35 G. Ricchiardi, A. Damin, S. Bordiga, C. Lamberti, G. Spanò, F. Rivetti and A. Zecchina, *J. Am. Chem. Soc.* 2001, **123**, 11409–11419.

36 A. Carati, C. Flego, E. P. Massara, R. Millini, L. Carluccio, W. O. Parker and G. Bellussi, *Microporous Mesoporous Mater.* 1999, **30**, 137–144.

37 X. Zhang, Z. Zhang, J. Suo and S. Li, *Catal. Letters*, 2000, **66**, 175–179.

38 V. Hulea and E. Dumitriu, *Appl. Catal. A Gen*. 2004, **277**, 99–106.

39 Z. Shan, Z. Lu, L. Wang, C. Zhou, L. Ren, L. Zhang, X. Meng, S. Ma and F.-S. Xiao, *ChemCatChem*, 2010, **2**, 407–412.

40 P. Yao, Y. Wang, T. Zhang, S. Wang and X. Wu, *Front. Chem. Sci. Eng.* 2014, **8**, 149–155.

41 D. H. Wells, A. M. Joshi, W. N. Delgass and K. T. Thomson, *J. Phys. Chem. B*, 2006, **110**, 14627–14639.

42 H. Xu, Y. Guan, X. Lu, J. Yin, X. Li, D. Zhou and P. Wu, *ACS Catal*. 2020, **10**, 4813–4819.

43 G. Bellussi and R. Millini, in Struct. Bond. 2017, pp. 1–52.

4. SILICEOUS ZEOLITES WITH MWW FRAMEWORK

4.1. Scope of the work

The work shown in this chapter is a preparatory study needed to synthesize a Ti-MWW catalyst. The synthesis of the Ti-zeolites is only possible if the framework is crystalline and stable in its purely siliceous form. The siliceous analogous of Ti-MWW is the ITQ-1 zeolite and in this chapter, it was synthesized and calcined with different procedures. Both the calcined and as-synthesized samples were characterized in depth to understand the role played by the OSDAs and the H_2O during the synthesis.

The Aerosil® 200 was used to prepare the ITQ-1 samples, as reported in the literature on the topic. In Chapter 3 it was shown that the best conditions to synthesize a Ti-zeolite consist in the use of Ti and Si alkoxides, in complete absence of K, and, for this reason, some attempts of preparing ITQ-1 using TEOS as Si source were made.

4.2. Experimental procedures

4.2.1. Chemicals

Aerosil® 200 (from Evonik Industries), N,N,N-trimethyl adamantil ammonium hydroxide (TMAdaOH, 25 wt% in water, from TCI), hexamethyleneimine (HMI, 99 % from Sigma Aldrich), potassium carbonate (K_2CO_3, anhydrous, ACS reagent, from Sigma Aldrich) and Milli-Q water (18.2 MΩ cm) were used for the synthesis of ITQ-1 samples. All the reagents were used without further purification.

4.2.2. Synthesis of ITQ-1 samples

4.2.2.1. Preliminary syntheses

The synthesis of ITQ-1 was approached by reproducing two procedures reported in the literature.[1,2] They differ for the composition of the synthesis gel and the ratio between the volume of gel and the volume of the Teflon liner used for the hydrothermal treatment (namely, the degree of filling, 25 or 66 vol%). Here, the four combinations of gel composition and volume ratio in the liner were tested (Table 4.2.2.1.1).

The first composition is the following: 1 SiO_2 : 0.2 TMAdaOH : 0.3 HMI : 0.07 K_2CO_3 : 30 H_2O.[1] In a typical procedure, 8.45 g of TMAdaOH solution, 1.49 g of HMI and 0.4837 g of K_2CO_3 were added in this order to 20.68 g of Milli-Q H_2O. 3.004 g of Aerosil® were added portion-wise to the above solution after 30 min stirring at RT. The stirring was continued until a homogeneous gel was obtained. The listed quantities were used for a gel filling approximately the 66 vol% of the liner. When a degree of filling the 25 vol% of the liner was needed, the composition was scaled. The molar composition of the second gel was: 1 : SiO_2 : 0.25 TMAdaOH : 0.31 HMI : 44 H_2O.[2] In a typical procedure (for a 66 vol% degree of filling), 7.29 g of TMAdaOH solution and 1.06 g of HMI were added to 21.86 g of Milli-Q H_2O. 2.0728 g of SiO_2 were then added to the above solution under vigorous stirring, until a homogeneous gel was obtained. The composition was scaled when a 25 vol% degree of filling was needed.

Each gel was transferred to a 45 ml Teflon lined stainless steel digestor and crystallized in tumbling conditions at 60 rpm at 150 °C for 5 days. The obtained samples were called: rose-ITQ-1-66-HS and rose-ITQ-1-25-HS when obtained with the first composition and sf-ITQ-1-66-HS and sf-ITQ-1-25-HS when obtained with the second composition (Table 4.2.2.1.1).

A portion of each sample was calcined in a tubular oven under dry air flow, with a heating ramp of 1 °C/min, up to 580 °C, followed by 3 h of isotherm (*procedure A580*). Additional calcination procedures were tested on rose-ITQ-1-66-HS: a heating ramp of 1 °C/min under pure N_2 flow up to 580 °C followed by 3 h of isotherm under pure O_2 flow (*procedure B580*) and heating ramp of 1 °C/min up to 550 °C under dry air, followed by 7 h of isotherm under the same flow (*procedure A550*).

Table 4.2.2.1.1. List of ITQ-1 preliminary samples synthesized from different precursor gels, exploiting different calcination procedures.

Name	Degree of filling	Gel molar composition	Calcination procedure
rose-ITQ-1-66-HS	66 vol%	1 SiO_2 : 0.2 TMAdaOH : 0.3 HMI : 0.07 K_2CO_3 : 30 H_2O	None
rose-ITQ-1-25-HS	25 vol%	1 SiO_2 : 0.2 TMAdaOH : 0.3 HMI : 0.07 K_2CO_3 : 30 H_2O	None
sf-ITQ-1-66-HS	66 vol%	1 SiO_2 : 0.25 TMAdaOH : 0.31 HMI : 44 H_2O	None
sf-ITQ-1-25-HS	25 vol%	1 SiO_2 : 0.25 TMAdaOH : 0.31 HMI : 44 H_2O	None
rose-ITQ-1-66-calcA580	66 vol%	1 SiO_2 : 0.2 TMAdaOH : 0.3 HMI : 0.07 K_2CO_3 : 30 H_2O	A580
rose-ITQ-1-25-calcA580	25 vol%	1 SiO_2 : 0.2 TMAdaOH : 0.3 HMI : 0.07 K_2CO_3 : 30 H_2O	A580
sf-ITQ-1-66-calcA580	66 vol%	1 SiO_2 : 0.25 TMAdaOH : 0.31 HMI : 44 H_2O	A580
sf-ITQ-1-25-calcA580	25 vol%	1 SiO_2 : 0.25 TMAdaOH : 0.31 HMI : 44 H_2O	A580
rose-ITQ-1-66-calcA550	66 vol%	1 SiO_2 : 0.2 TMAdaOH : 0.3 HMI : 0.07 K_2CO_3 : 30 H_2O	A550
rose-ITQ-1-66-calcB580	25 vol%	1 SiO_2 : 0.2 TMAdaOH : 0.3 HMI : 0.07 K_2CO_3 : 30 H_2O	A580

4.2.2.2. Systematic study of the synthesis and calcination conditions

Based on the preliminary results, the 66 vol% was chosen as the most convenient degree of filling of the liner, and the syntheses with the two different gel compositions were reproduced. Each as-synthesized sample was

divided in three portions. One was characterized without calcination (rose-ITQ-1-HS and sf-ITQ-1-HS samples); the second was calcined with *procedure A550*, in the following called *procedure A* (rose-ITQ-1-calcA and sf-ITQ-1-calcA samples); the third fraction was calcined with *procedure B580*, in the following called *procedure B*, (rose-ITQ-1-calcB and sf-ITQ-1-calcB). The choice of temperatures (580 or 550 °C) and the length (7 or 3 h) of the isotherms, coupled with every atmosphere was done to obtain samples with the more divergent properties.

Table 4.2.2.1. List of ITQ-1 samples synthesized from different precursor gels, exploiting different calcination procedures.

Name	Gel molar composition	Calcination procedure
rose-ITQ-1-HS	1 SiO_2 : 0.2 TMAdaOH : 0.3 HMI : 0.07 K_2CO_3 : 30 H_2O	None
rose-ITQ-1-calcA	1 SiO_2 : 0.2 TMAdaOH : 0.3 HMI : 0.07 K_2CO_3 : 30 H_2O	A
rose-ITQ-1-calcB	1 SiO_2 : 0.2 TMAdaOH : 0.3 HMI : 0.07 K_2CO_3 : 30 H_2O	B
sf-ITQ-1-HS	1 SiO_2 : 0.25 TMAdaOH : 0.31 HMI : 44 H_2O	None
sf-ITQ-1-calcA	1 SiO_2 : 0.25 TMAdaOH : 0.31 HMI : 44 H_2O	A
sf-ITQ-1-calcB	1 SiO_2 : 0.25 TMAdaOH : 0.31 HMI : 44 H_2O	B

4.2.2.3. Attempts of synthesizing ITQ-1 from TEOS

The study of the synthesis of TS-1 (reported in Chapter 3) revealed how the best conditions to insert Ti in the zeolite framework is realized when alkoxides of Si and Ti were hydrolyzed separately and when alkoxides of the same alcohol are used. For this reason, some attempts of preparing an ITQ-1 sample using TEOS instead of Aerosil® 200 as Si source were done (Table 4.2.2.3.1). The attempts are almost all unsuccessful, but they are worth to be reported due to the room for improvement they open.

A first synthesis was performed using a special apparatus for the hydrothermal treatment, composed of a home-made DrySyn, specifically built for the 45 ml digestor sold by Parr. The stirring was ensured through a

magnetic bar in the liner and the DrySyn was used on a magnetic stirrer and heating plate, equipped with a thermocouple for the temperature control. A gel with the following molar composition was prepared: 1 SiO_2 : 0.2 TMAdaOH : 0.3 HMI : 30 H_2O. Specifically, 5.92 g of TMAdaOH solution and 2.22 g of HMI were added in this order to 14.48 g of Milli-Q H_2O. After 30 min of stirring at RT, 7.29 g of TEOS were added dropwise. The molar composition is the one used to prepare rose-ITQ-1 samples except for the presence of K_2CO_3. The presence of K_2CO_3 was avoided because a white precipitate was immediately observed by dropping the TEOS in the K_2CO_3 containing solution of the OSDAs. The gel was hydrolyzed at RT for 3 h and then was transferred to a 45 ml Teflon liner placed inside a stainless steel digestor for the hydrothermal crystallization. Due to technical issues, the crystallization was conducted for 1 day at ≈ 100 °C, followed by 7 days at 140 °C. The as-synthesized sample was named ITQ-1-TEOS-A-HS. The sample was calcined with procedure A to obtain ITQ-1-TEOS-A-calc.

This synthesis was repeated using the tumbling agitation of the digestor during the hydrothermal treatment (7 days at 140 °C, 60 rpm). The as-synthesized sample was named ITQ-1-TEOS-B-HS and the calcined one ITQ-1-TEOS-B-calc.

Some attempts to prepare ITQ-1 in presence of K_2CO_3 even if the white precipitate is observed were performed. The molar composition used was 1 SiO_2 : 0.2 TMAdaOH : 0.3 HMI : 0.07 K_2CO_3 : 30 H_2O. The TEOS was hydrolyzed at RT and at 60 °C for 3 h (to obtain ITQ-1-TEOS-C-RT-HS and ITQ-1-TEOS-C-60-HS respectively). An intermediate K_2CO_3/SiO_2 molar ratio was also tested, by preparing a gel with the molar composition: 1 SiO_2 : 0.2 TMAdaOH : 0.3 HMI : 0.035 K_2CO_3 : 30 H_2O and hydrolyzing it at 80 °C for 4 h (ITQ-1-TEOS-C-HS). ITQ-1-TEOS-C-60-HS and ITQ-1-TEOS-C-HS were calcined with procedure A to obtain ITQ-1-TEOS-C-60-calc and ITQ-1-TEOS-C-calc.

Table 4.2.2.3.1. List of ITQ-1 samples synthesized using TEOS as Si source, using different precursors gels and different experimental setups.

Name	Experim. setup	Hydrolysis	Gel molar composition	Calcination procedure
ITQ-1-TEOS-A-HS	DrySyn	3 h, RT	1 SiO_2 : 0.2 TMAdaOH : 0.3 HMI : 30 H_2O	None
ITQ-1-TEOS-A-calc	DrySyn	3 h, RT	1 SiO_2 : 0.2 TMAdaOH : 0.3 HMI : 30 H_2O	A
ITQ-1-TEOS-B-HS	Tumbling	3 h, RT	1 SiO_2 : 0.2 TMAdaOH : 0.3 HMI : 30 H_2O	None
ITQ-1-TEOS-B-calc	Tumbling	3 h, RT	1 SiO_2 : 0.2 TMAdaOH : 0.3 HMI : 30 H_2O	A
ITQ-1-TEOS-C-RT-HS	Tumbling	3 h, RT	1 SiO_2 : 0.2 TMAdaOH : 0.3 HMI : 0.07 K_2CO_3 : 30 H_2O	None
ITQ-1-TEOT-C-60-HS	Tumbling	3 h, 60 °C	1 SiO_2 : 0.2 TMAdaOH : 0.3 HMI : 0.07 K_2CO_3 : 30 H_2O	None
ITQ-1-TEOT-C-60-calc	Tumbling	3 h, 60 °C	1 SiO_2 : 0.2 TMAdaOH : 0.3 HMI : 0.07 K_2CO_3 : 30 H_2O	A
ITQ-1-TEOT-C-HS	Tumbling	4 h, 80 °C	1 SiO_2 : 0.2 TMAdaOH : 0.3 HMI : 0.035 K_2CO_3 : 30 H_2O	None
ITQ-1-TEOT-C-calc	Tumbling	4 h, 80 °C	1 SiO_2 : 0.2 TMAdaOH : 0.3 HMI : 0.035 K_2CO_3 : 30 H_2O	A

4.2.3. Characterization of ITQ-1 samples

The as-synthesized and calcined samples were analyzed by means of PXRD, SEM and ^{29}Si-MAS-NMR spectroscopy. The calcined samples were characterized by N_2 physisorption at – 196 °C, Hg porosimetry (sf-ITQ-1-calcA and sf-ITQ-1-calcB only) and vibrational spectroscopies (IR in ATR and in transmission mode and Raman with a 244 nm excitation laser). The as-synthesized samples were further analyzed by ^{13}C-MAS-NMR spectroscopy, CHNS elemental analysis, TGA and IR spectroscopy upon temperature variation.

The ^{29}Si-OP-MAS spectra of the rose-ITQ-1-HS, rose-ITQ-1-calcA and rose-ITQ-1-calcB samples were deconvoluted as Lorentzian peaks, using the program Fityk. The deconvolution of the spectra of the calcined samples was

performed by considering the theorical chemical shifts computed with equation 4.1:[3]

$$\delta_{iso} = 11.531\langle r_{SiO}\rangle + 27.280\sigma(r_{SiO}) + 83.7430\cos(\langle\theta_{SiOSi}\rangle) + 0.20246\sigma(\theta_{SiOSi}) - 59.999 \qquad (4.1)$$

Where δ_{iso} is the chemical shift (ppm), $\langle r_{SiO}\rangle$ is the average Si-O distance, $\sigma(r_{SiO})$ is its standard deviation, $\langle\theta_{SiOSi}\rangle$ is the average Si-O-Si angle and $\sigma(\theta_{SiOSi})$ is its standard deviation. The structure of the MWW framework was used to calculate the r_{SiO} and the θ_{SiOSi}, as obtained from the cif file downloaded from the Database of Zeolite Structures present on the website of the International Zeolite Association (IZA)[4].

The raw results of the CHNS elemental analyses were used to calculate the molar fraction of each ODSA in the rose-ITQ-1-HS and sf-ITQ-1-HS samples, by solving the following equation system.

$$a + b = 1 \qquad (4.2)$$

$$a * \left(\frac{C}{N}\right)_{HMI} + b * \left(\frac{C}{N}\right)_{TMAdaOH} = \left(\frac{C}{N}\right)_{exp} \qquad (4.3)$$

Where a is the HMI molar fraction, b is the TMAdaOH molar fraction, $\left(\frac{C}{N}\right)_{HMI}$ is equal to 6, $\left(\frac{C}{N}\right)_{TMAdaOH}$ is equal to 13 and $\left(\frac{C}{N}\right)_{exp}$ is the experimental molar ratio.

The molar fractions were calculated as in the following:

$$b = \frac{\left(\frac{C}{N}\right)_{exp} - \left(\frac{C}{N}\right)_{HMI}}{\left(\frac{C}{N}\right)_{TMAdaOH} - \left(\frac{C}{N}\right)_{HMI}} \qquad (4.4)$$

$$a = 1 - b \qquad (4.5)$$

The molar amounts of the OSDAs in the as-synthesized samples were calculated as follows:

$$wt\% = \frac{mass_x(g)}{U} \qquad (4.6)$$

$$\frac{mol_N}{U} = \frac{1}{MW_N} * \frac{mass_N(g)}{U} \quad (4.7)$$

$$\frac{mol_N}{U} = \frac{mol_{HMI} + mol_{TMAdaOH}}{U} \quad (4.8)$$

$$\frac{mol_{HMI}}{U} = a * \frac{mol_N}{U} \quad (4.9)$$

$$\frac{mol_{TMAdaOH}}{U} = b * \frac{mol_N}{U} \quad (4.10)$$

Where x is the component in the sample (N, C, H, TMAdaOH, HMI, SiO_2 or H_2O), U is considered equal to 100 g of sample (arbitrary unit), MW_N in the molar weight of N.

The calcination procedure was studied by TGA and transmission IR spectroscopy. For each as-synthesized sample, the following procedures are used for the TGA. *Procedure A*: heating ramp of 1 °C/min to 550 °C under dry air flow, followed by a 3 h isotherm under the same flow. *Procedure B*: heating ramp of 1 °C/min to 580 °C under N_2 flow, followed by a 3 h isotherm under dry air flow. The isotherm was stopped after 3 h because a plateau was already achieved. The protocol followed for the calcination monitored with IR spectroscopy (IR experiment upon variation of the temperature) was analogous, but Ar was used instead of N_2 (air was simulated as 20 vol% of O_2 in Ar).

4.3. Results and discussion

4.3.1. PXRD characterization of the preliminary samples

The PXRD patterns of the as-synthesized and calcined ITQ-1 samples are shown in Figure 4.3.1.1. The MWW phase can be identified by the presence of some sharp reflections, having Miller indexes *hk*0 (*e.g.* 100, 220 and 310)[1,2,5–7] in the patterns of the as-synthesized samples (Figure 4.3.1.1a). Other reflections, having *hkl* with *l* ≠ 0 (*e.g.* 002, 101, 102 and 201) [1,2,5–7] appear broad, sometimes not resolved and slightly shifted in the different

samples. The patterns of the calcined samples (Figure 4.3.1.1b) show that the position of the peaks belonging to the family *hk*0 is not affected by the calcination. The position, resolution and broadness of the peaks having *hkl* with $l \neq 0$ are slightly affected in rose-ITQ-1-66-calcA580 and increasingly modified in the other samples, such that the 101 and 102 reflections are not distinguishable in sf-ITQ-1-25-calcA580. These properties can be explained by the peculiar structure and morphology of many of the zeolites with MWW framework. The ITQ-1 zeolite crystallizes as separated single layers during the hydrothermal treatment. [5,7–10] The single layers develop along the *ab* crystallographic plane, perpendicular to the *c* axis of the unit cell. Hence, the reflections free from component along the *c* directions are fully formed in the patterns of the as-synthesized samples. The calcination causes the condensation of the single layers to yield the 3D zeolite and a consequent contraction of the *c* dimension of the unit cell. [1,5,7] The contraction determines the shift of the reflections with a component along the *c* axis of the unit cell. The crystallization of separated single layers under hydrothermal conditions is reported in literature for zeolites with MWW framework free from Al (as ITQ-1) and with Al, depending on the Si/Al ratio and gel composition (as for the aluminosilicate MCM-22 and its layered precursor MCM-22(P)).[5,7–10]

The differences observed between the PXRD patterns of the samples has a different origin. The stacking of the layers, probably governed by the balance between dispersion forces and hydrogen bonds with the OSDAs molecules,[9] can occur in an uneven way in aluminosilicate zeolites with MWW framework, depending on the composition of the synthesis gel.[6,11,12] The uneven stacking determines a diminished long-range order in the direction perpendicular to the *c* axis, generating the difference observed among the samples. The PXRD calcined patterns of rose-ITQ-1-66-calcA580 and sf-ITQ-1-25-calcA580 (Figure 4.3.1.1b) are representative of the two limit samples, analogous to the fully ordered aluminosilicate MCM-22[6,7,9,10] and to the fully disordered

aluminosilicate MCM-56,[6,9,11,13,14] respectively. The other patterns show intermediate situations. It is hard to say if an intermediate level of disorder is present in rose-ITQ-1-25-calcA580 and sf-ITQ-1-66-calcA580 or if they are composed of a mixture of the two limit phases.

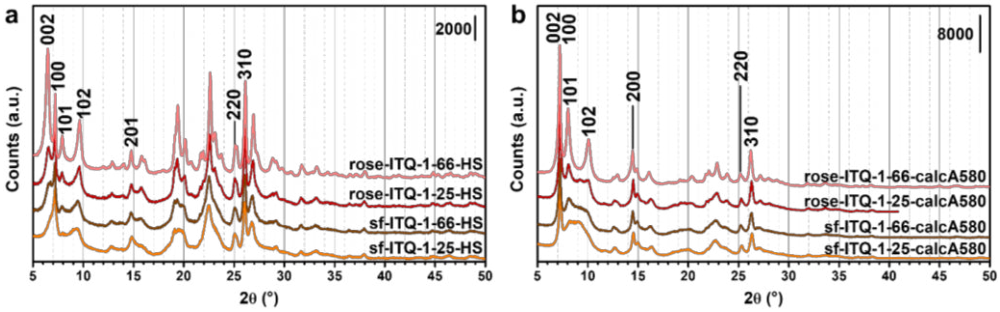

Figure 4.3.1.1. PXRD patterns of the ITQ-1 preliminary samples (a) before and (b) after the calcination.

The fact that the degree of order seems to increase gradually from sf-ITQ-1-25-calcA580, sf-ITQ-1-66-calcA580, rose-ITQ-1-25-calcA580 to rose-ITQ-1-66-calcA580 could suggest that both the degree of filling of the liner and the composition of the synthesis gel could affect the degree of order. Actually, the syntheses of rose-ITQ-1-25-calcA580, sf-ITQ-1-66-calcA580 and sf-ITQ-1-25-calcA580 were never reproduced successfully. In particular, many attempts were made to reproduce sf-ITQ-1-25-calcA580, purely siliceous analogous of MCM-56, but it was one of a kind.

The autogenous pressure in the liner was calculated and it was used to evaluate the possible effect of the vapor to liquid ratio of H_2O in the liner during the hydrothermal treatment (Table 4.3.1.1). The autogenous pressure of pure H_2O was considered as only responsible for the internal pressure. This is a good approximation when H_2O is the only solvent used in the synthesis, as for the preparation of ITQ-1. The Antoine Equation[15,16] (eq. 4.11) was used to calculate the pressure.

$$\log_{10} p(mmHg) = A - \frac{B}{C+T\ (°C)} \qquad (4.11)$$

In eq. 4.11, T is the temperature and A (8.140191),[17] B (1810.94)[17] and C (244.485)[17] are the Antoine coefficients when the temperature is ≥ 100 °C. The specific volumes in the vapor and liquid phases depending on the temperature[17] were then used to calculate the vapor to liquid mass ratio at the two different degree of filling, with the following equations (eq. 4.12 – 4.14):

$$m_{vapor}(g) = \frac{m_x(kg) * \left(\frac{V(m^3)}{m_x(kg)} - v_{liquid}\left(\frac{m^3}{kg}\right)\right)}{(v_{vapor} - v_{liquid})} * 1000 \qquad (4.12)$$

$$m_{liquid}(g) = m_x(kg) * 1000 - m_{vapor}(g) \qquad (4.13)$$

$$R(m)_{v/l}@x\ vol\% = \frac{m_{vapor}(g)}{m_{liquid}(g)} \qquad (4.14)$$

Where m_x is the mass of H_2O in the liner at the degree of filling x, with x = 25 or 66 vol%, V is the volume of the liner (45 ml), v_{vapor} and v_{liquid} are the specific volumes of the vapor and the liquid respectively, depending on the temperature, and m_{vapor} and m_{liquid} are the mass of H_2O in vapor and liquid phase in the liner.

Table 4.3.1.1 shows that the difference between the vapor to liquid ratio calculated for the two compositions of the gel is negligible when the degree of filling is the same. The degree of filling of 25 or 66 vol% of the liner determines, instead, a slight difference in the vapor to liquid ratio. The significancy of this difference must be considered with caution. The crystal growth occurs through solid phases in pseudo-steady state with the liquid phase. The vapor pressure is not involved in the crystal growth. The calculations in Table 4.3.1.1 revealed that more of the 99 wt% of the H_2O would be in the liquid phase both when the degree of filling is 25 and 66

vol%. For this reason, it is unlikely that it could have a significant influence on the result.

Table 4.3.1.1. Autogenous pressure, specific volume of the liquid (v_{liquid}) and vapor (v_{vapor}) H_2O, volume/liquid mass ratio ($R(m)_{v/l}$) when degree of filling of 25 and 66 vol% of the liner, depending on the temperature of the hydrothermal treatment, between 100 and 200 °C. The temperature of 150 °C is highlighted in bold, since it is the one used in the ITQ-1 synthesis.

T (°C)	Pressure (bar)	v_{liquid} (m^3/kg)	v_{vapor} (m^3/kg)	$R(m)_{v/l}$ rose@25 vol% (g/l)	$R(m)_{v/l}$ rose@66 vol% (g/l)	$R(m)_{v/l}$ sf@25 vol% (g/l)	$R(m)_{v/l}$ sf@66 vol% (g/l)
100	1.02	0.00104	1.6718	0.0020	0.0004	0.0020	0.0004
110	1.43	0.00105	1.2093	0.0028	0.0005	0.0028	0.0005
120	1.98	0.00106	0.8912	0.0037	0.0007	0.0038	0.0007
130	2.69	0.00107	0.6680	0.0050	0.0009	0.0050	0.0009
140	3.59	0.00108	0.50845	0.0066	0.0012	0.0066	0.0011
150	**4.73**	**0.00109**	**0.39245**	**0.0085**	**0.0015**	**0.0085**	**0.0014**
160	6.14	0.00110	0.30678	0.0109	0.0019	0.0109	0.0018
170	7.87	0.00111	0.24259	0.0137	0.0023	0.0138	0.0022
180	9.97	0.00113	0.19384	0.0172	0.0028	0.0173	0.0027
190	12.50	0.00114	0.15636	0.0213	0.0034	0.0215	0.0033
200	15.52	0.00116	0.12721	0.0262	0.0040	0.0264	0.0039

The uneven stacking of the layers observed in the synthesized samples could instead be ascribed to slight differences in the preparation procedure of which the operator is not aware, or to the formation of seeds in the internal walls of the liner. In this work, the presence of seeds was accurately avoided by washing the liners with HF after each use, such that the liners were used without distinction for the preparation of zeolites with MWW and MFI frameworks, without observing the formation of contaminant phases. Since this is the second episode where the reproducibility of the syntheses is ensured only with liners used and washed many times, the possible presence of residues of CBU, that do not discriminate between the frameworks, but

that favor the nucleation of both, cannot be excluded. Otherwise, a possible rugosity of the liners induced by the repeated use could play the role of a nucleation center.

Some calcination procedures were tested on the rose-ITQ-1-66-HS sample (Figure 4.3.1.2). No differences are observed between the PXRD patterns calcined in air, while a lower resolution of the Bragg peaks when the sample is calcined with the *procedure B580* is evident. In the following, a deep characterization of the as-synthesized and calcined samples is exposed, and the A550 and B580 procedures were selected for this purpose, in order to obtain the more divergent properties.

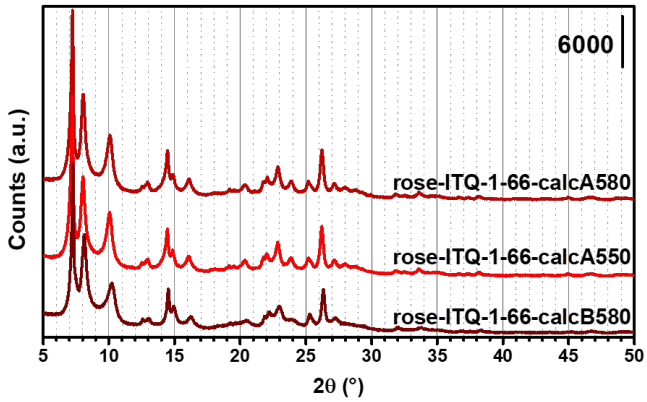

Figure 4.3.1.2. PXRD patterns of rose-ITQ-1-66 sample calcined with different procedures.

4.3.2. Characterization of crystalline structure and morphology

Most of the characterization of the as-synthesized and calcined samples presented in paragraphs from 4.3.2 to 4.3.4 was published as independent paper[18] and will be summarized here.

The PXRD patterns of the as-synthesized and calcined ITQ-1 samples are shown in Figure 4.3.2.1. The patterns show highly crystalline MWW phase.[1,2,5]

The differences observed between the calcined and as-synthesized samples are related to the contraction of the unit cell along the *c* axis, upon condensation of the layers, as previously observed.[1,5,7–10]

The reflections with a component along the *c* direction (e.g. 002, 101, 102) appears broader than those without it. Moreover, the broadening of sf-ITQ-1 is more severe than the one in rose-ITQ-1 samples. This could be due to a lower crystalline domain dimension along the *c* axis respect to the other dimensions of the crystals or to a slight lack of long-range order in the same direction. To clarify this point, SEM images of the samples were recorded.

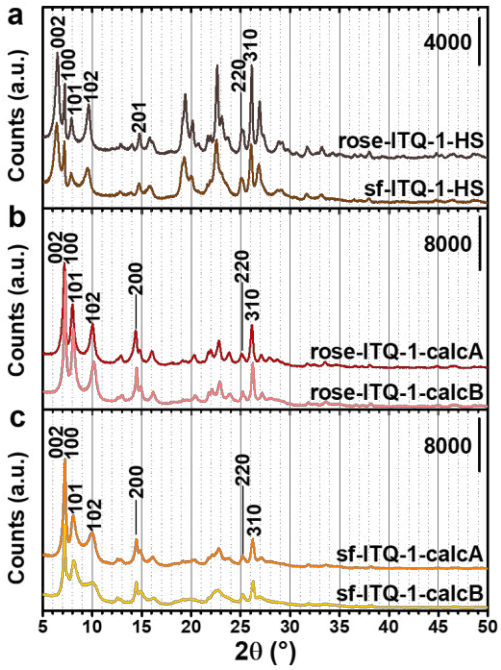

Figure 4.3.2.1. PXRD patterns of (a) the as-synthesized rose-ITQ-1-HS and sf-ITQ-1-HS, (b) calcined rose-ITQ-1-calcA and rose-ITQ-1-calcB and (c) calcined sf-ITQ-1-calcA and sf-ITQ-1-calcB.

The SEM images (Figure 4.3.2.2) show that all the ITQ-1 samples are composed of nanosheets of approximate hexagonal morphology. The strong asymmetricity of the particles visible with SEM reflects the asymmetricity of

the crystalline domain, explaining the broadening of the PXRD peaks. However, the possibility of the contribution of a slight disorder along the *c* axis on the broadening cannot be excluded. The thickness of the nanosheets was measured and the thickness size distribution plots are reported in Figure 4.3.2.3 (average values in Table 4.3.2.1, number of measured particles in Table 4.3.2.2). The maximum of each distribution is clearly distinguishable and shifted for each sample, even if the thickness size distribution plots are quite superimposed. The sf-ITQ-1-HS, -calcA and -calcB samples show slightly thinner particles respect to rose-ITQ-1-HS, -calcA and -calcB samples (Table 4.3.2.1 and Figure 4.3.2.3) and both rose-ITQ-1-calcA and sf-ITQ-1-calcA show slightly thicker particles than their analogous, -calcB.

The differences in the nanosheets thickness can be associated with the variation in the PXRD peaks broadening. This is correct if the following assumptions are considered: (i) the size of the hexagonal nanosheets visible with SEM could be resembled with the size of the crystallite domain and (ii) the broadening of the PXRD peaks is the manifestation of the average crystallite domain dimension, mediated on the bulk of the material (represented by the slight shift of the thickness size distribution). If the layers stack is not perfectly even during the hydrothermal treatment, the growth of the crystal would probably be more frequently interrupted, resulting in a thinner crystal, as probably occurring in sf-ITQ-1 samples. In this context, it can be hypothesized that in rose-ITQ-1 samples the asymmetricity is the only origin of the PXRD peaks broadening, while in sf-ITQ samples a slight disorder could also be involved.

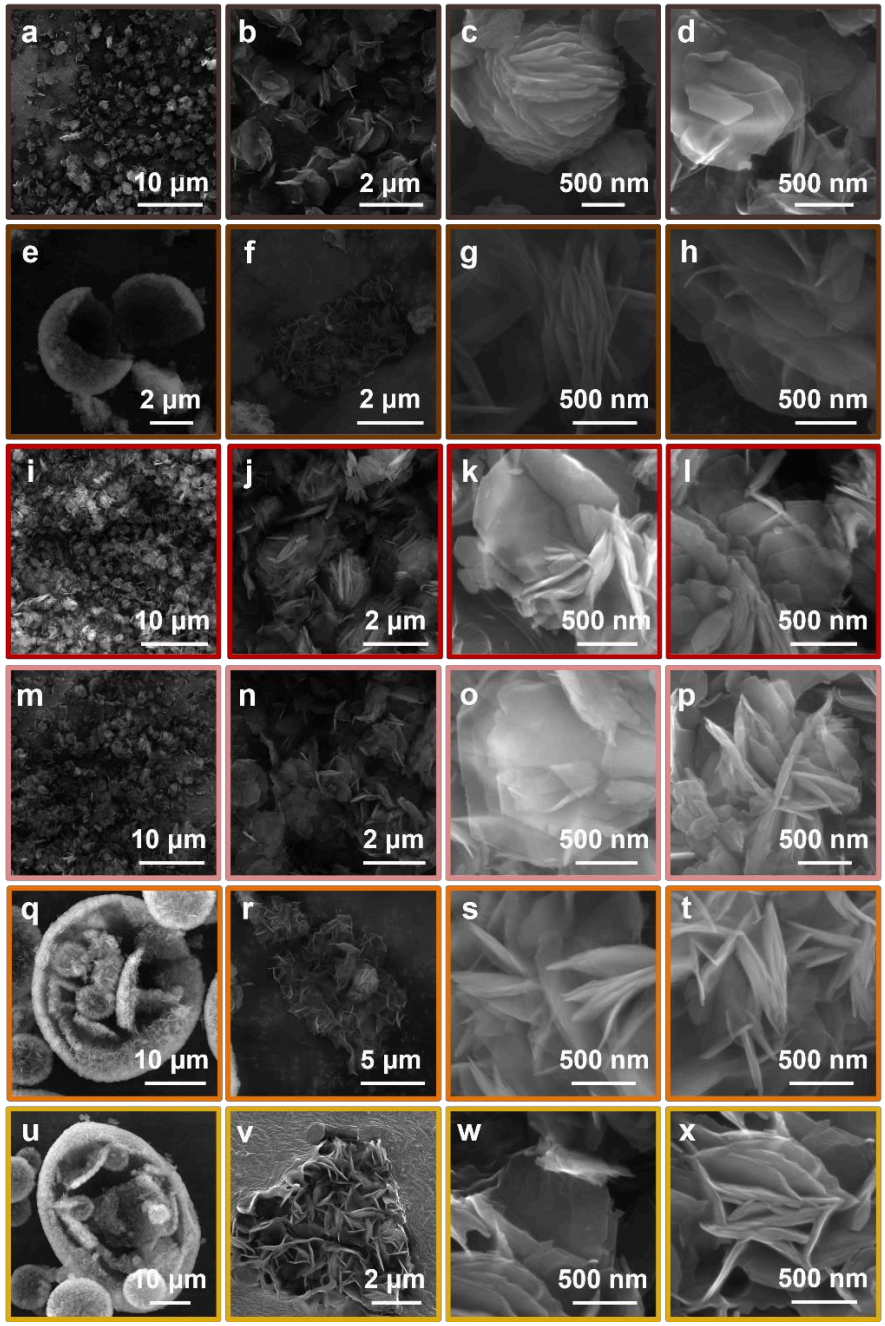

Figure 4.3.2.2. SEM images at different magnifications of (a-d – dark brown) rose-ITQ-1-HS, (e-h – brown) sf-ITQ-1-HS, (i-l – red) rose-ITQ-1-calcA, (m-p – pink) rose-ITQ-1-calcB, (q-t – orange) sf-ITQ-1-calcA and (u-x – yellow) sf-ITQ-1-calcB.

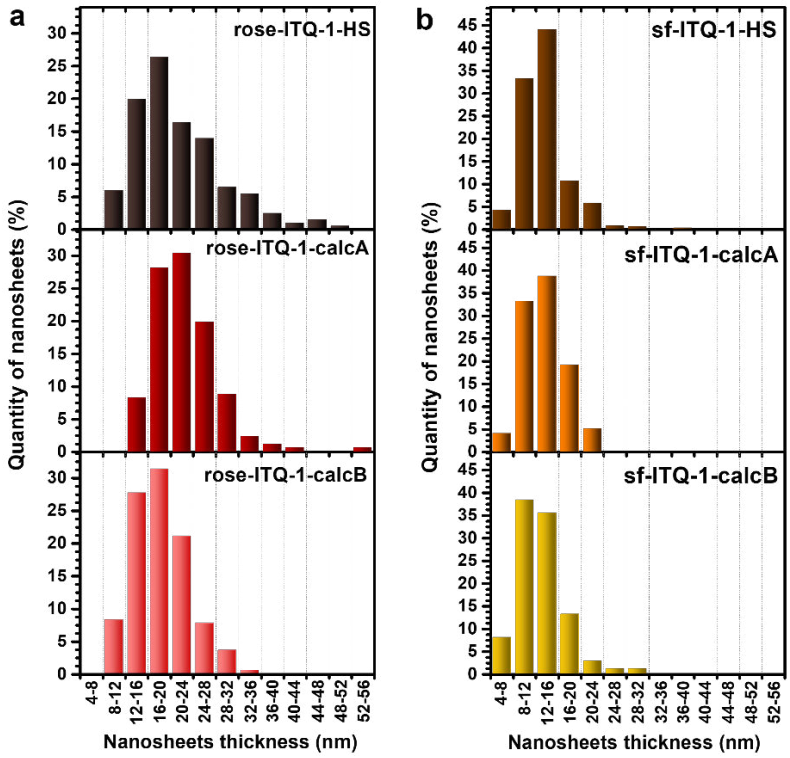

Figure 4.3.2.3. Thickness size distribution plots of the (a) rose-ITQ-1 and (b) sf-ITQ-1 samples.

Table 4.3.2.1. Average nanosheets thickness (particle dimension along the *c* axis) of all the samples and sphere diameters of sf-ITQ-1 samples.

Sample	Particle thickness (nm)	Spheres diameter (μm)
rose-ITQ-1-HS	21 ± 1	-
rose-ITQ-1-calcA	23 ± 1	-
rose-ITQ-1-calcB	18 ± 1	-
sf-ITQ-1-HS	14 ± 2	14 ± 1
sf-ITQ-1-calcA	14 ± 1	13 ± 1
sf-ITQ-1-calcB	13 ± 1	11 ± 1

Table 4.3.2.2. Number of particles/spheres measured for preparing the thickness size distribution and the diameter size distribution plots, respectively.

Sample	Number of particles	Number of spheres
rose-ITQ-1-HS	201	-
rose-ITQ-1-calcA	171	-
rose-ITQ-1-calcB	195	-
sf-ITQ-1-HS	327	176
sf-ITQ-1-calcA	199	244
sf-ITQ-1-calcB	175	200

The SEM images (4.3.2.2) at low magnifications show a difference in the aggregation way of the samples prepared with different gel compositions. The rose-ITQ-1 samples form rose-like small aggregates, uniform in shape and size, while sf-ITQ-1 samples agglomerate in macro-sized hollow spheres (Figure 4.3.2.4). The reason why this difference occurs is not studied yet, but the formation of spheric aggregates in zeolites with MWW framework was already observed in the literature.[19–21] In these cases, additional SDA were added to this purpose, *e.g.* carbon black[19] or BP 2000[20] as hard templates, or di-quaternary ammonium surfactants[21] as soft templates were used in the synthesis of MCM-22. In the present work, no organic or inorganic SDA was deliberately added in the synthesis gel, but it is possible that the higher TMAdaOH/SiO_2 and HMI/SiO_2 ratios in the synthesis gel of sf-ITQ-1, respect to the one of rose-ITQ-1, could have caused the formation of hollow spherical aggregates. This point needs further studies for clarification.

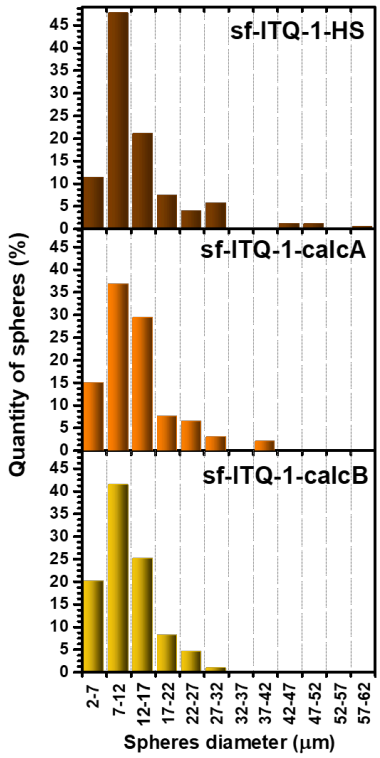

Figure 4.3.2.4. Diameter size distribution plot for the spheres in sf-ITQ-1 samples.

The properties of the hollow spheres were investigated by measuring the average particle diameter (Table 4.3.2.1), the corresponding size distribution (Figure 4.3.2.4) and by Hg porosimetry (Figures 4.3.2.5 and 4.3.2.6). The aggregation of the particles occurs during the hydrothermal crystallization, because the hollow spheres are already present in the as-synthesized sf-ITQ-1-HS sample and they do not collapse upon calcination. The diameter size distribution for the hollow spheres (Figure 4.3.2.4) was computed by measuring more than 170 spheres per sample (Table 4.3.2.2). The average diameter seems slight lower in the calcined samples respect to the one in the as-synthesized sample, suggesting that the biggest spheres could partially collapse upon calcination.

The Hg porosimetry measurement (Figures 4.3.2.4 and 4.3.2.5) was performed on the calcined sf-ITQ-1-calcA and sf-ITQ-1-calcB samples to understand whether these materials could behave as macroporous materials. The intrusion-extrusion cycle (Figure 4.3.2.4) was repeated twice for each sample to evaluate the reversibility of the process. The intrusion curves plotted in semi-logarithmic scale show a moderate steep due to the rearrangement of particles within the powder bed, at low pressure (below 2 bar), then, the interparticle filling occurs, with a sharp steep (below 5 bar). This phenomenon is the origin of the peak at 5.0 μm in the dV/d(log d) vs pore diameter plot.

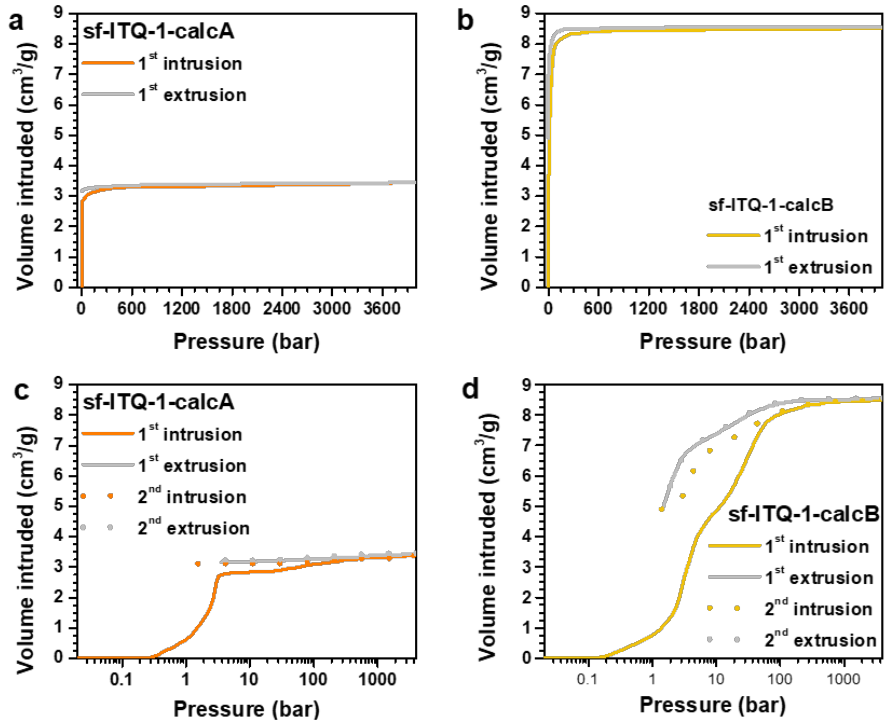

Figure 4.3.2.4. Hg porosimetry intrusion-extrusion curves of the sf-ITQ-1-calcA (a, c) and sf-ITQ-1-calcB (b, d) samples in linear (a, b) and in logarithmic (c, d) scale.

At higher pressure the pores filling takes place.[22,23] The intruded volume due to the filling of the pores in the sf-ITQ-1-calcA sample is lower than that of sf-ITQ-1-calcB sample. The macro-voids to be filled should be the voids inside the spheres. It is unlikely that Hg could penetrate inside the spheres through the interparticle voids of mesopore dimension, present in the sphere walls, so the filled macro-voids are probably the voids inside broken spheres. Hence, the high intruded volume of sf-ITQ-1-calcB can be a symptom of a higher fraction of broken spheres in sf-ITQ-1-calcB respect to sf-ITQ-1-calcA.

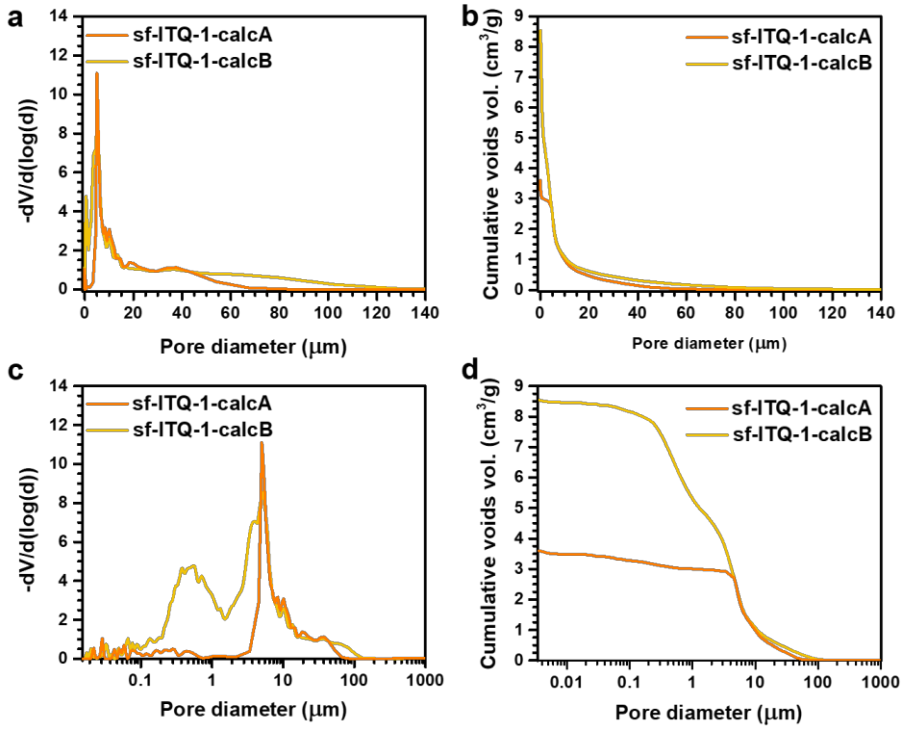

Figure 4.3.2.5. Incremental voids volume (a, c) and cumulative voids volume (b, d) of sf-ITQ-1-calcA and sf-ITQ-1-calcB samples, plotted in linear (a, b) and logarithmic (c, d) scales. The Washburn equation was used to calculate the voids volume.

The textural properties of the calcined samples were studied also by N_2 physisorption at -196 °C. The isotherms (Figure 4.3.2.6a,b) are of type I,

typical of microporous materials, with an H3 hysteresis loop at high relative pressure, arising from the filling of interparticle voids between plate-like particles.

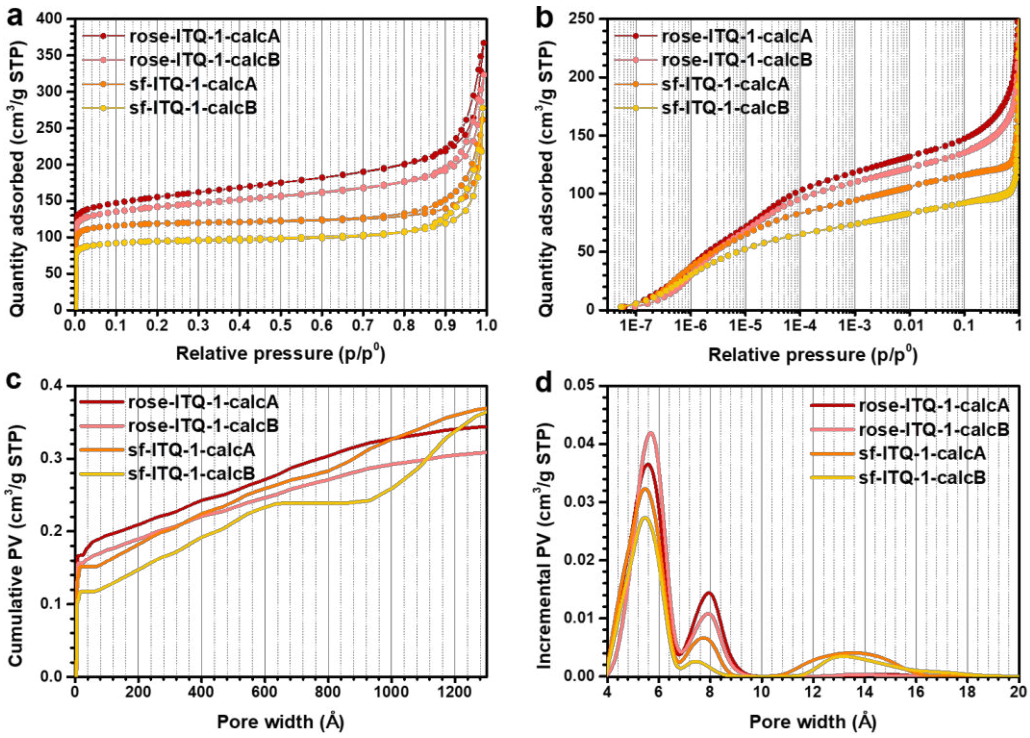

Figure 4.3.2.6. Volumetric N_2 adsorption/desorption isotherms at -196 °C in the whole relative pressure range, plotted in (a) linear and (b) semi-logarithmic scale. (c) Cumulative pore volume plot in the 0 – 1300 Å pore size range and (d) pore size distribution in the micropore size range (< 20 Å, points connected by a B-spline function), computed by NL-DFT method applied to the N_2 adsorption isotherms in the whole relative pressure range.

The calculated SSAs and micropore volumes (Table 4.3.2.3) are coherent with what reported in literature for the MWW framework type.[1,4,6,11,19,20] rose-ITQ-1-calcB and sf-ITQ-1-calcB present a slight lower micropore volume and SSA (Table 4.3.2.3 and Figure 4.3.2.6c,d) than their analogous calcined with *procedure A*, probably due to a partial occlusion of the pores during the

heating ramp under inert flow. This is particularly evident for sf-ITQ-1-calcB. An additional family of voids of micropore dimension (10 – 20 Å) is present in the sf-ITQ-1 samples, that is not related with the MWW structure. This is tentatively ascribed to the presence of random voids in the interlayer space when the layers slightly mismatch.

Table 4.3.2.3. SSAs calculated with the BET and Langmuir models and micropore (V_{micro}) and interparticle voids (V_{ipv}) volume computed using the NL-DFT method.

Sample	BET SSA[1] (m^2/g)	Langmuir SSA[2] (m^2/g)	V_{micro}[3] (cm^3/g STP)	V_{ipv}[4] (cm^3/g STP)
rose-ITQ-1-calcA	586 ± 1	676 ± 5	0.17	0.03
rose-ITQ-1-calcB	538 ± 1	616 ± 4	0.16	0.03
sf-ITQ-1-calcA	465 ± 2	525 ± 1	0.15	0.03
sf-ITQ-1-calcB	368 ± 1	417 ± 2	0.12	0.03

[1] Calculated in the 0.008 – 0.08 p/p^0 range.
[2] Calculated in the 15 – 200 mbar pressure range.
[3] Calculated from the Cumulative pore volume plot for pore size < 20 Å.
[4] Calculated form the Cumulative pore volume plot by difference of the total pore volume by V_{micro}.

4.3.3. Spectroscopic characterization

The spectroscopic characterization was used to reveal the differences between the ITQ-1 samples at an atomic scale. The ATR-IR spectra (Figure 4.3.3.1a) in the low frequency region host the collective bending modes of groups of atoms that have specific positions. The broadening of these bands is an indication of the structural order of the crystal under investigation.[12,24,25] In fact, bands assigned to the stretching of double-6-ring (D6R) units are present[14,26,27] in the ATR-IR spectra of zeolites with MWW topology, at 611 and 562 cm^{-1}. They appear sharper and more intense in rose-ITQ-1 respect to sf-ITQ-1 samples, probably due to their lower defectivity, similarly to what observed by means of

PXRD. Analogous information is provided by the Raman spectra in the low frequency region (Figure 4.3.3.1b). Here, bands assigned to collective vibrations of a ring of tetrahedra are present at 522, 483 and 345 cm^{-1}, that can be ascribed to the vibrations of 4-, 5- and 6-MR respectively.[28,29] The intensity of these bands is lower for sf-ITQ-1-calcA and sf-ITQ-1-calcB samples respect to rose-ITQ-1-calcA and rose-ITQ-1-calcB. This is a further confirmation of the higher defectivity of sf-ITQ-1 samples.

Detailed information about the presence of defects can be obtained from the analysis of the ATR-IR spectra in the high frequency region (Figure 4.3.3.1a, 1300 – 700 cm^{-1}) and the region where the hydroxyl (OH) stretching absorbs in the IR spectra recorded in transmission mode (Figure 4.3.3.2, 3800 – 2900 cm^{-1}). In the ATR-IR spectra, a broad band at 960 cm^{-1} is present, covering almost the whole transparency window between the ν_{asym}(SiOSi) (1300-900 cm^{-1}) and the ν_{sym}(SiOSi) (850-750 cm^{-1}) bands.[25] It is assigned to a localized stretching mode of a $Si(OSi)_3OH$ group in siliceous zeolites.[25] The presence of $Si(OSi)_3OH$ is an irregularity in the crystalline order and hence it is considered as a "point defect". The band at 960 cm^{-1} in the ATR-IR spectra does not discriminate among different kind of $Si(OSi)_3OH$ groups, while the IR spectra in transmission mode are more informative (Figure 4.3.3.2).

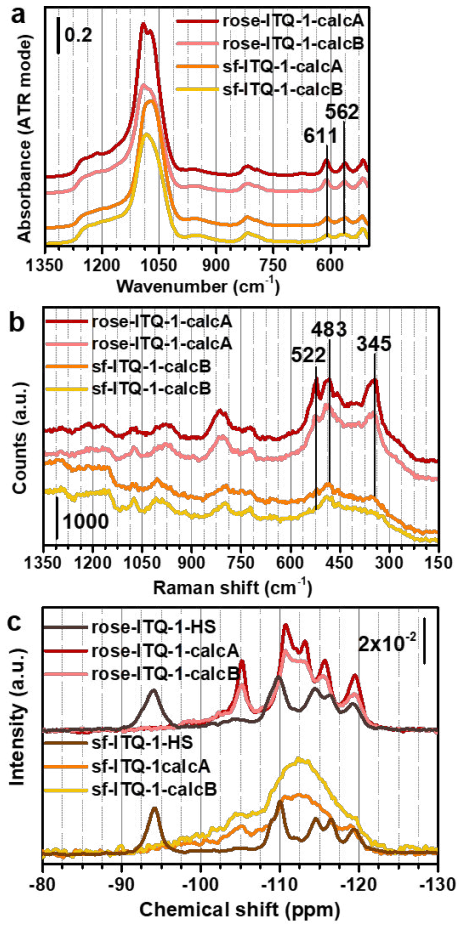

Figure 4.3.3.1. (a) ATR-IR spectra in the 1350 – 500 cm^{-1} range and (b) Raman spectra in the 1350 – 150 cm^{-1} range, of the calcined rose-ITQ-1-calcA, rose-ITQ-1-calcB, sf-ITQ-1-calcA and sf-ITQ-1-calcB samples, and (c) ^{29}Si-OP-NMR spectra of the as-synthesized rose-ITQ-1-HS and sf-ITQ-1-HS and calcined rose-ITQ-1-calcA, rose-ITQ-1-calcB, sf-ITQ-1-calcA and sf-ITQ-1-calcB samples. The ATR-IR and Raman spectra are normalized to the band at 800 cm^{-1} and the NMR spectra are normalized to the mass of sample in the rotor.

The higher frequency component (3745 cm^{-1}) of the signal associated to the stretching vibration of OH groups (ν(OH)), is associated to external isolated $Si(OSi)_3OH$ groups. The band at 3740 cm^{-1} in rose-

ITQ-1 and at 3730 cm^{-1} in sf-ITQ-1 samples is ascribed to the vibration of OH groups located at the end of a chain of hydrogen bonds. The frequency of this band is related to the length of the chain: the longer the chain, the stronger the interaction and the lower the frequency of the signal will be. [30–33] The vibration of the H-bonded OH present in the chain is visible in the 3650-3500 cm^{-1} region as a broad shoulder. The chains of hydrogen bonded OH are probably located in the space between adjacent nanosheets. A band ascribed to the vibration of $Si(OSi)_3OH$ groups in a nest of $Si(OSi)_3OH$ can be found at low frequencies, centered at about 3500 cm^{-1}. Its intensity is different among the samples, suggesting the presence of lower amounts of "point defects" in rose-ITQ-1 respect to sf-ITQ-1 samples. Additionally, a slight effect of the calcination procedure can be noted: the samples calcined with *procedure B* show a slight lower amount of defects respect to those calcined with *procedure A*. The reasons of the differences in the defectivity of the samples will be explained later.

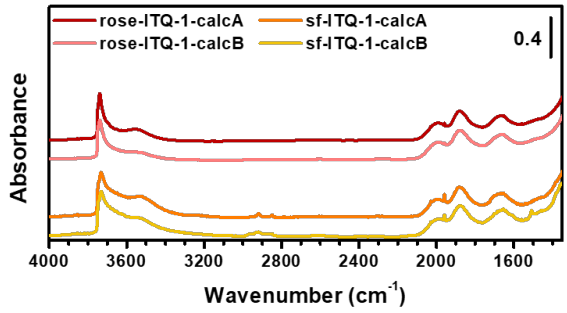

Figure 4.3.3.2. Transmission IR spectra of the activated calcined samples, in the 4000 – 1350 cm^{-1} range. The spectra are normalized to the overtones in the region 2100 – 1500 cm^{-1}.

The ^{29}Si MAS-NMR spectra recorded with OP experiments are reported in Figure 4.3.3.1c. A loss of resolution of the signals of sf-ITQ-1-calcA and sf-ITQ-1-calcB upon calcination is observed. The rose-ITQ-1-calcA

and rose-ITQ-1-calcB samples maintain the signal resolution instead. The loss of resolution could be due to a higher local disorder (wider angular distribution) or to a higher amount of structural defects, in accordance with what observed in the IR transmission spectra (Figure 4.3.3.2).[3,18,34] The NMR spectra of the as-synthesized samples show a peculiar intense signal at -94 ppm. In this region, the Q^3 (tetrahedral Si site connected to three Si atoms and an atom different from Si) or Q^2 (tetrahedral Si site connected to two Si atoms and two atoms different from Si) sites are usually located. The presence of Q^3 sites in the calcined materials can be appreciated from the signal at -96 ppm in the ^{29}Si MAS-NMR spectra obtained with a {^{1}H-^{29}Si} CP (Figure 4.5.3.4); the signal at -96 ppm is broad and it is representative of a statistical distribution of $Si(OSi)_3OH$ sites. The comparison of the peak at -94 ppm in the spectra of the as-synthesized samples with the one at -96 ppm in the {^{1}H-^{29}Si} CP spectra of the calcined materials suggests that the first could be ascribed to a specific crystallographic position, instead of a statistical distribution of $Si(OSi)_3OH$ sites. This is an indication of a significant structural change occurring upon calcination, together with the condensation of the layers.

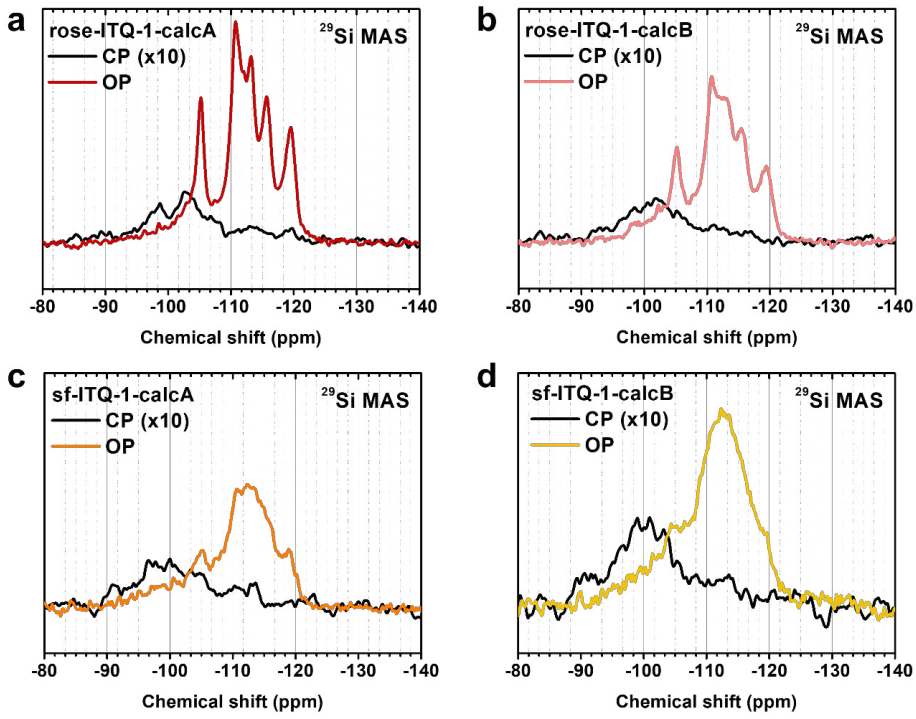

Figure 4.3.3.4. ^{29}Si-NMR spectra obtained with a {^{1}H-^{29}Si} CP experiment on the calcined samples (black spectra in all the panels), compared with the OP spectra: (a) rose-ITQ-1-calcA, (b) rose-ITQ-1-calcB, (c) sf-ITQ-1-calcA and (d) sf-ITQ-1-calcB.

The deconvolution of the ^{29}Si OP-MAS-NMR spectra of rose-ITQ-1-calcA and rose-ITQ-1-calcB calcined samples (Figure 4.3.3.5 top and center) was performed taking into account the eight crystallographic sites of the MWW framework as reported in the Database of Zeolites Structure in the IZA website).[4] The deconvolution of the spectrum of the rose-ITQ-1-HS as-synthesized sample (Figure 4.3.3.5 bottom) was done assuming that no modification of the hexagonal symmetry system occurs upon calcination, save the contraction of the *c* cell parameter.[35,36] This is a rough approximation, because the Si(OSi)$_3$OH groups at the surface of the single layers in rose-ITQ-1-HS are in principle 4 over 72

Si atoms per unit cell, that is to say ≈5% of the T sites. The relative integrated intensity of the signal at -94 ppm, far higher than the 5% of the sum of the integrated areas, suggests that crystallographic sites other than those undergoing condensation are Q^3 before the calcination. In this regard, it must be noted that the structure refinement of the as-synthesized form of a zeolite with MWW framework has never been published.[5,36] The calculation of the initial peak positions is performed using eq. 4.1. The integrated area of the deconvoluted peaks in the calcined samples spectra (Table 4.3.3.1 and 4.3.3.2) is consistent with the multiplicity of the crystallographic sites (three sites with a multiplicity of four and five peaks with a multiplicity of twelve). Two components (at -94 and -93 ppm) in the spectrum of the as-synthesized rose-ITQ-1-HS sample, were considered to contribute to the signal at -94 ppm (see the integrated areas in Table 4.3.3.3). An exceptionally high amount of Q^3 sites ($Si(OSi)_3OH$ groups) is present in the as-synthesized material (≈22%), as already reported in the literature.[36,37] The crystallinity of the as-synthesized rose-ITQ-1-HS and sf-ITQ-1-HS samples is guaranteed by the presence of the coordinated OSDAs molecules, despite the high amount of $Si(OSi)_3OH$ groups. The condensation of the $Si(OSi)_3OH$ groups upon H_2O removal would lead to the formation of the 3D zeolite,[5,35,37] but the fraction of $Si(OSi)_3OH$ groups in the rose-ITQ-1-HS and sf-ITQ-1-HS samples is too high to be ascribed to the condensation of completely formed separated layers (as it occurs *e.g.* in the borosilicate analogous),[35] suggesting the possibility of a more complex phase transition.

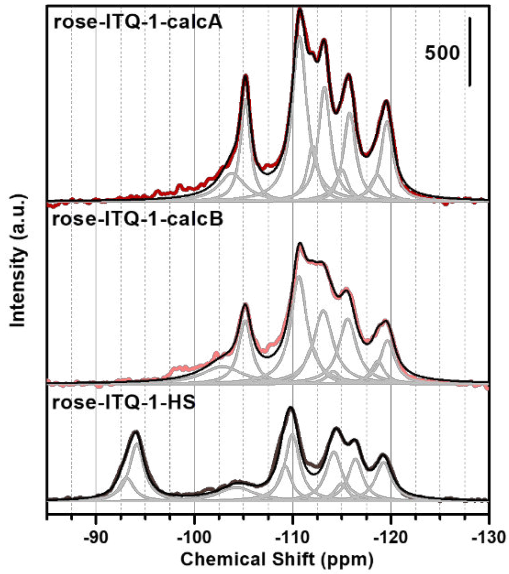

Figure 4.3.3.5. Deconvolution of the ^{29}Si-OP-NMR spectra of (from the top to the bottom) the rose-ITQ-1-calcA, rose-ITQ-1-calcB and rose-ITQ-1-HS samples. The colored traces correspond to the experimental spectra, the black traces to the simulated spectra and the gray traces to the deconvoluted peaks.

Table 4.3.3.1. Deconvoluted peaks of the calcined rose-ITQ-1-calcA sample, the site assignation, integrated area values, obtained with the program Fityk, percentage integrated area (the percentage of the Q^4 sites is calculated relatively to the sum of Q^4 sites, the percentage of the Q^3 site was calculated relatively to the sum of all Q^4 and the Q^3 sites).

Maximum of deconvoluted peaks (ppm)	Site	Integrated area	Area (%)
-105.2	Q^4	1483.3	12.1
-110.7	Q^4	3581.5	29.2
-112.0	Q^4	3581.5	29.2
-112.0	Q^4	916.4	7.5
-113.2	Q^4	534.1	4.4
-115.8	Q^4	1608.9	13.1
-118.6	Q^4	575.6	4.7
-119.6	Q^4	1481.2	12.1
-103.8	Q^3	1093.0	8.2

Table 4.3.3.2. Deconvoluted peaks of the calcined rose-ITQ-1-calcB sample, the site assignation, integrated area values, obtained with the program Fityk, percentage integrated area (the percentage of the Q^4 sites is calculated relatively to the sum of Q^4 sites, the percentage of the Q^3 sites was calculated relatively to the sum of all Q^4 and the Q^3 sites).

Maximum of deconvoluted peaks (ppm)	Site	Integrated area	Area (%)
-105.2	Q^4	1223.1	12.1
-110.6	Q^4	2592.5	25.7
-112.0	Q^4	788.6	7.8
-113.1	Q^4	2121.9	21.0
-114.1	Q^4	248.6	2.5
-115.6	Q^4	1727.9	17.1
-118.6	Q^4	442.8	4.4
-119.6	Q^4	944.4	9.4
-102.8	Q^3	1050.3	9.4

Table 4.3.3.3. Deconvoluted peaks of the as-synthesized rose-ITQ-1-HS sample, the site assignation, integrated area values, obtained with the program Fityk, percentage integrated area (the percentage of the Q^4 sites is calculated relatively to the sum of Q^4 sites and Q^3 sites peaked at -93.1 and -94.1 ppm, the percentage of the Q^3 sites was calculated relatively to the sum of all Q^4 and the Q^3 sites).

Maximum of deconvoluted peaks (ppm)	Site	Integrated area	Area (%)
-93.1	Q^3	2051.4	7.0
-94.1	Q^3	4974.0	17.1
-109.2	Q^4	2724.5	9.4
-110.0	Q^4	5816.1	20.0
-114.2	Q^4	4764.8	16.4
-114.9	Q^4	1359.9	4.7
-116.4	Q^4	3688.9	12.7
-119.2	Q^4	3755.9	12.9
-104.3	Q^3	2963.4	9.2

4.3.4. Role of the OSDAs in the ITQ-1 synthesis

The properties of the ITQ-1 samples here synthesized (macroscopical aggregation, primary particle thickness, long-range crystalline order and amount of defective sites) seem to be affected by both the composition of the synthesis gel and by the calcination procedure. The study of the organic fraction in the as-synthesized material and the presence of alkali cations in the framework were used to analyze the effect of the gel composition, while TGA and variable temperature IR experiments were used to study the effect of the calcination procedure.

The ^{13}C OP-MAS-NMR spectra of the as-synthesized rose-ITQ-1-HS and sf-ITQ-1-HS, together with the liquid phase ^{13}C-NMR spectra of the two OSDA (HMI and TMAdaOH) are shown in Figure 4.3.4.1. The signals of the pure OSDA molecules should appear in the spectra of the as-synthesized samples, shifted, depending on the interaction of the organic molecules with the walls of the zeolite cavities. The MWW framework hosts two cavity systems (the sinusoidal channel and the internal super-cages), so, in principle, the signal of each molecule should appear twice, one for each location. The spectra of rose-ITQ-1-HS and sf-ITQ-1-HS contains similar signals, hence the two cavities should host the same kind of molecules. HMI is reported to locate both in the sinusoidal channels and in the super-cages in MCM-22, while $TMAda^+$ is found only in the internal supercages.[2,36,37] Here, no clear evidence of the presence of HMI in the internal super-cages is present. The relative intensity of the signals is the main difference between the spectrum of rose-ITQ-1-HS and sf-ITQ-1-HS, suggesting that the amount of organic molecules is different in the two samples. A complete assignment of the spectra is ventured due to the overlapping of chemical shifts.[37,38]

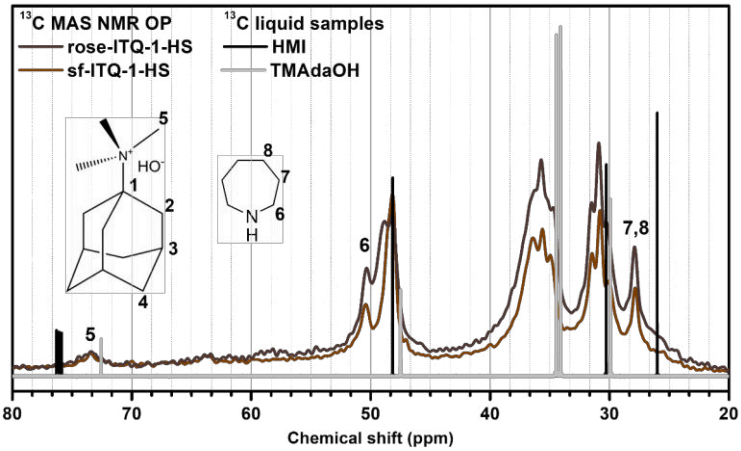

Figure 4.3.4.1. ^{13}C-NMR spectra of as-synthesized rose-ITQ-1-HS and sf-ITQ-1-HS samples, compared with the liquid spectra of the pure OSDAs (HMI and TMAdaOH). The zeolite spectra are normalized by the mass of sample in the rotor.

CHNS elemental analysis was performed to quantitatively evaluate the amount of OSDA in the as-synthesized samples (Table 4.3.4.1). The molar ratio between the two OSDAs ($TMAda^+$/HMI) is analogous in the two samples but rose-ITQ-1-HS shows a higher $TMAda^+$/unit cell and HMI/unit cell than sf-ITQ-1-HS, indicating a higher total amount of organics. The stronger dilution of the gel of sf-ITQ-1-HS respect to rose-ITQ-1-HS sample could be the reason of the reduced incorporation of organic molecules during the hydrothermal treatment. The reduced incorporation of $TMAda^+$, located in the interlayer space, may be the reason behind the slightly uneven stacking of the layers of sf-ITQ-1-HS, -calcA and -calcB samples respect to their analogous rose-ITQ-1 samples. Considering that its theoretical amount should be 4 cations/unit cell,[36] this number is perfectly respected in sample rose-ITQ-1-HS, and it is in slight shortage for sf-ITQ-1-HS sample. This could be responsible for the layer mismatch and for the presence of defective sites in the interlayer space for sf-ITQ-1 samples. The shortage of HMI

(respect to the theorical amount of 3 molecules/unit cell), located in the sinusoidal channels, makes impossible for it to supply for the lack of $TMAda^+$ in sf-ITQ-1-HS sample and it justifies the high amount of defects in the sf-ITQ-1-calcA and -calcB samples. The slight excess of HMI in rose-ITQ-1-HS sample may be the responsible for the low amount of defects ($Si(OSi)_3OH$ nests) visible in the transmission IR spectra in Figure 4.3.3.2.

The excess of H_2O molecules is considered to supply for the lack of OSDAs in sf-ITQ-1-HS sample, making its crystallization possible.

Table 4.3.4.1. C/N ratio, OSDAs per unit cell and OSDAs ratio for the rose-ITQ-1 and sf-ITQ-1 synthesis gels and for the as-synthesized samples determined by CHNS elemental analysis. 72 Si atoms are used to calculate the $TMAda^+$, HMI and H_2O molar ratio per unit cell in the synthesis gel.

	Synthesis gel		**As-synthesized samples**	
	rose-ITQ-1-HS	sf-ITQ-1-HS	rose-ITQ-1-HS	sf-ITQ-1-HS
C/N	8.80	9.13	9.91	9.92
$TMAda^+$/HMI	0.67	0.81	1.27	1.27
$TMAda^+$/unit cell	14.4	18.00	3.95	3.60
HMI/unit cell	21.6	22.32	3.11	2.83
$TMAda^+/H_2O$ ($*10^{-3}$)	6.67	5.68	-	-
HMI/H_2O ($*10^{-3}$)	10.00	7.05	-	-
H_2O/SiO_2	30	44	-	-

The correct stacking of the layers could be hindered also by the higher OH/SiO_2 ratio in the gel of sf-ITQ-1 in respect to the one of rose-ITQ-1 samples, due to the influence of the OH/SiO_2 ratio on the surface charge of the layers. The low amount of $Si(OSi)_3OH$ nests visible in the transmission IR spectra of rose-ITQ-1-calcA and -calcB samples could also be influenced by the presence of K^+ cations in the synthesis gel. It

sometimes acts as inorganic SDA, but it was not detected in the synthesized materials by chemical analysis. It is not retained in the structure, hence it is improbable it could act as inorganic SDA in this context.

The effect of the *A* and *B* calcination procedures was also studied by TGA and variable temperature IR spectroscopy, to understand the reason behind the slight difference in the defectivity of the samples when they are prepared with the same synthesis gel and calcined with different procedures, as visible by the intensity of the band assigned to the $Si(OSi)_3OH$ nests in the transmission IR spectra (Figure 4.3.3.2).

The weight losses of the TG curves (Figure 4.3.4.2) were tentatively explained by using the DTG curves and the IR experiments. The HMI, $TMAda^+$ and the H_2O produced upon condensation are the species expected to degrade/leave the sample during the calcination. The TG and DTG curves of the calcination performed with the same procedure looks similar (comparison of panels a and b with c and d respectively), suggesting that the degradation of the organic molecules occurs with the same mechanism. When *procedure A* is used, four peaks are present in the DTG curves, indicating a degradation in several steps. When *procedure B* is used, the DTG curves show three broad and one sharp signal, the last being due to the sudden oxidation of any organic residuals that occurs by switching from N_2 to air flow. The H_2O is tentatively assigned to a moderately sharp signal visible at around 200 °C in the DTG of all the samples, consistently with previously reported results on phase transition between separated single layers and calcined zeolite phases.[35]

The combination of the TGA and the results of the CHNS elemental analysis allowed to justify the exceptionally high amount of $Si(OSi)_3OH$ groups visible in the ^{29}Si OP-MAS-NMR spectra of the as-synthesized

samples (Figure 4.3.3.1c). From the difference between the quantification of the H_2O by TGA and the one calculated from the CHNS analysis, the amount of H_2O produced upon condensation was calculated. It is found to be coherent with the equivalent number of H_2O molecules generated during the condensation of the $Si(OSi)_3OH$ groups present in the as-synthesized sample, as determined by the ^{29}Si OP-NMR spectra shown in Figure 4.3.3.5 and Table 4.3.3.3. This means that the totality of the exceptionally high amount of $Si(OSi)_3OH$ groups in the as-synthesized material (≈22%) undergoes condensation during the phase transition between the 2D precursor to the 3D calcined zeolite.[18]

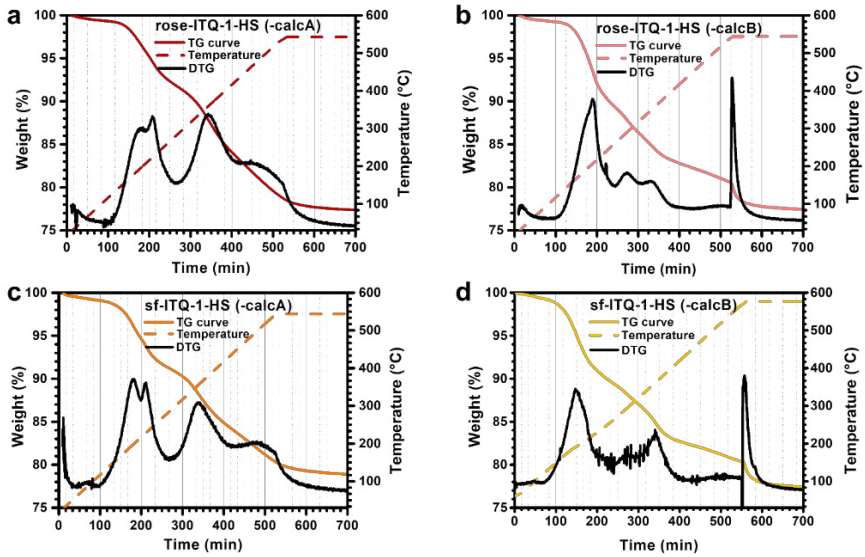

Figure 4.3.4.2. TG analysis of (a) rose-ITQ-1-HS sample calcined with *procedure A*, (b) rose-ITQ-1-HS sample calcined with *procedure B*, (c) sf-ITQ-1-HS sample calcined with *procedure A* and (d) sf-ITQ-1-HS sample calcined with *procedure B*. *Procedure A*: 1 °C/min up to 550 °C under dry air, followed by 3 h in isothermal conditions under the same flow. *Procedure B*: 1 °C/min up to 580 °C under N_2 flow, followed by 3 h in isothermal conditions under dry air.

The IR experiments performed to simulate the calcination procedure were used to try to identify the several degradation steps of the OSDA molecules. Figure 4.3.4.3 shows the IR spectra recorded during the heating ramp in oxidant (for rose-ITQ-1-HS (a) and sf-ITQ-1-HS (c)) and inert (for rose-ITQ-1-HS (b) and sf-ITQ-1-HS (d)) atmosphere. The degradation pathway of the OSDA molecules is revealed by the diminishing of the intensity of the IR bands (both stretching, 3050 – 2800 cm^{-1} and bending, 1500 – 1250 cm^{-1} modes). Below 300 °C, a similar degradation path is followed by heating in an oxidant or inert atmosphere (spectra from blue to green in Figure 4.3.4.3). The $TMAda^+$ may fragment in trimethylamine (TMA) and adamantane (Ada) during the hydrothermal treatment or during the calcination. In both the cases, the thermal degradation of trimethylamine (TMA) is observed first, from the diminishing of the signals at 3050, 2825 and 2753 cm^{-1}. At 300 °C, the full degradation of the TMA is gone (green spectrum in each panel). The degradation of HMI is testified by the signals at 1453 and 2944 cm^{-1}, assigned to a deformation of the CH_2 groups next to the N in HMI ($\delta(CH_2)$) and to the asymmetric stretching of CH_2 ($\nu_{asym}(CH_2)$) and of the signals between 1570 and 1300 cm^{-1} (deformations of the CH_2 group in aliphatic chains). It occurs between 200 °C (light cyan spectra) and 400 °C (brown spectrum in each panel). Above 300 °C, the degradation pathway is different depending on the used procedure (A or B). The degradation of Ada can be followed by observing the CH stretching region of the spectra, where signals at 2913 and 2855 cm^{-1} are preserved, and by the CH_2 deformation range (band at 1455 cm^{-1}). When *procedure A* is used, the oxidation of the Ada appears to be almost finished at 550 °C. On the other hand, when *procedure B* is used, a significant amount of Ada is preserved till the end of the heating ramp (red spectrum in b and d panels). Ada is probably trapped into

the internal super-cages of the framework, due to its large size (6.8 x 7.6 x 7.4 Å),[39] bigger than the 10-MR apertures. It is, however, immediately burned when O_2 was sent in the flow, as shown by TGA. The presence of the OSDA at such a high temperature probably originates a partial healing of the defects, determining the slightly lower amount of nests visible in the transmission IR spectra of rose-ITQ-1-calcB and sf-ITQ-1-calcB respect to their analogous rose-ITQ-1-calcA and sf-ITQ-1-calcA.

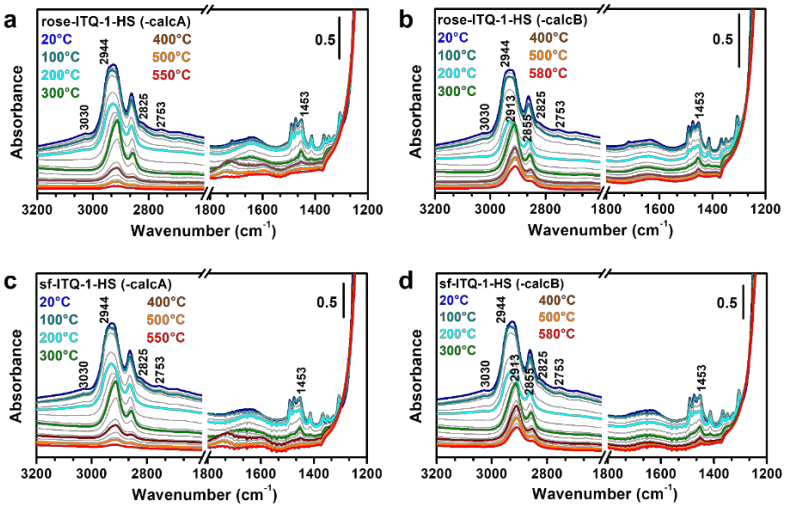

Figure 4.3.4.3. Transmission IR spectra of (a) rose-ITQ-1-HS sample calcined with *procedure A*, (b) rose-ITQ-1-HS sample calcined with *procedure B*, (c) sf-ITQ-1-HS sample calcined with *procedure A* and (d) sf-ITQ-1-HS sample calcined with *procedure B*. The grey spectra shown are recorded every 20 min. The colored spectra corresponds to the temperature: 20 °C blue, 100 °C dark cyan, 200 °C light cyan, 300 °C green, 400 °C brown, 500 °C orange and 550 °C (a, c) or 580 °C (b, d) red. *Procedure A*: 1 °C/min up to 550 °C under 20 vol% O_2 in Ar, followed by 3 h in isothermal conditions under the same flow. *Procedure B*: 1 °C/min up to 580 °C under pure Ar flow, followed by 3 h in isothermal conditions under 20 vol% O_2 in Ar. The spectra recorded during the isotherm are not shown.

4.3.5. Attempts to prepare ITQ-1 from TEOS as Si source: PXRD characterization

The PXRD pattern of ITQ-1-TEOS-A-HS sample, compared with the reference sf-ITQ-1-HS sample (Figure 4.3.5.1a) reveals the formation of the MWW framework. All the reflections are present and their relative intensity is almost respected, even if a loss of resolution is observed, probably due to a partial disorder at short range scale, or to a reduced crystal dimension. The presence of amorphous domain can be inferred by the increase of the baseline around the 20° to 25° 2θ range. Similar conclusions can be made observing the PXRD pattern of the calcined ITQ-1-TEOS-A-calc sample, compared with the reference sf-ITQ-1-calcA sample (Figure 4.3.5.1b).

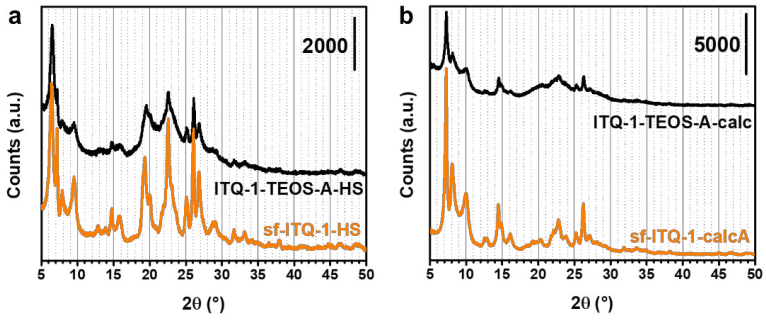

Figure 4.3.5.1. PXRD patterns of (a) as-synthesized ITQ-1-TEOS-A-HS and sf-ITQ-1-HS reference sample and (b) calcined ITQ-1-TEOS-A-calc and sf-ITQ-1-calcA reference sample in the 5° to 50° 2θ range.

However, the inhomogeneity of the slurry recovered from the digestor must be reported. The OSDAs degraded to different extent at different height in the liner, as testified by the presence of white, light brown and brown portions of slurry. This could be due to temperature gradients in the digestor, due to the heating from the lower part of the autoclave, or to inhomogeneity caused by the stirring conducted at the bottom of the liner (with a magnetic stir bar) and hence possibly not uniform along the height of the liner. Moreover, it is

not possible to ensure the persistence of the stirring along the whole 8 days of the hydrothermal crystallization, due to the precipitation of the solid silicate. For this reason, the synthesis was repeated in tumbling conditions.

The Figure 4.3.5.2a shows the PXRD patterns of the ITQ-1-TEOS-B-HS sample, compared with the sf-ITQ-1-HS reference sample. The pattern is unknown and the MWW phase does not seem to be present even mixed with other ones. The sample was calcined to see if the possible presence of MWW phase undetected in the as-synthesized sample could be found after calcination (Figure 4.3.5.2b). This did not happen and the unknown phase(s) present in the as-synthesized sample proved to be unstable to calcination. Few diffraction peaks of really low intensity are present in ITQ-1-TEOS-B-calc sample. The nucleation of the MWW phase occurred upon hydrothermal treatment on the heating plate with the DrySyn for digestors but it did not at 140 °C in tumbling conditions. This could be due to the first day of hydrothermal treatment conducted at ≈ 100 °C, prior to the treatment at 140 °C for ITQ-1-TEOS-A-HS sample, absent for ITQ-1-TEOS-B-HS. An effect of the different agitation method (mechanical stirring by a magnetic system or tumbling conditions) could also have affected the nucleation of the MWW phase.

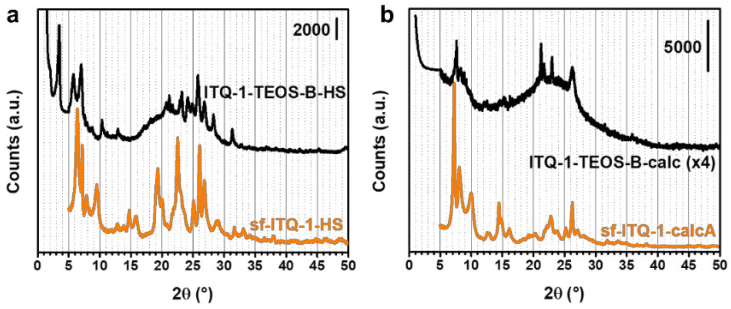

Figure 4.3.5.2. PXRD patterns of (a) as-synthesized ITQ-1-TEOS-B-HS and sf-ITQ-1-HS reference sample and (b) calcined ITQ-1-TEOS-B-calc (intensity multiplied by a factor 4 for the sake of clarity) and sf-ITQ-1-calcA reference sample in the 0° to 50° 2θ range.

The inhomogeneity of the slurry observed during the preparation of ITQ-1-TEOS-A-HS and the many problems connected to the use of a DrySyn for digestors made unworthy further attempts with that setup. The synthesis of ITQ-1 from TEOS was then approached by reproducing the procedure to obtain the rose-ITQ-1 samples with the different Si source. A period of hydrolysis prior to the hydrothermal treatment was added. Figure 4.3.5.3 shows the PXRD patterns of the as-synthesized (a) and calcined (b) ITQ-1-TEOS-C samples, compared with the reference sf-ITQ-1-HS and sf-ITQ-1-calcA respectively. The MWW phase did not nucleates in these experimental conditions and the obtained phase is unknown. N_2 physisorption at -196 °C was performed on ITQ-1-TEOS-C-60-calc to see if the PXRD pattern could be ascribed to a non-dense unknown crystalline phase, but its SSA was considered too low for being worth of further studies at this moment.

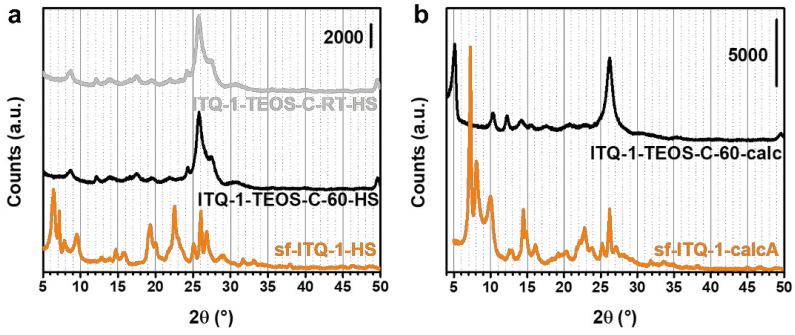

Figure 4.3.5.3. PXRD patterns of (a) as-synthesized ITQ-1-TEOS-C-RT-HS, ITQ-1-TEOS-C-60-HS and sf-ITQ-1-HS reference sample in the 5° to 50° 2θ range and (b) calcined ITQ-1-TEOS-C-60-calc and sf-ITQ-1-calcA reference sample in the 4° to 50° 2θ range.

4.4. Conclusions and open questions

In this work, the composition of the synthesis gel and calcination procedure for obtaining the ITQ-1 zeolite were studied. Samples with different particle thickness and crystalline order along the *c* axis were obtained and a relation between the two properties was found. If the layers stack in a partially disordered way, the crystal growth was more frequently interrupted and the particles were thinner. The amount of OSDA incorporated in the crystalline framework during the hydrothermal treatment was found to be at the origin of the different stack of the layers. When an excess amount of OSDA molecules was incorporated, the layers were perfectly ordered, while if a shortage of OSDA occurs, a partially disordered crystal was obtained. When a lack of OSDA occurs, the presence of an excess of H_2O helped in the crystallization of the material, acting as space filler, even if a material containing more defects was produced. The slight effect of the calcination procedure on the defectivity was also studied and it was understood that by calcining the sample under inert atmosphere, a fraction of the OSDA was preserved till high temperatures, helping in the healing of defects. The most relevant role on the defectivity is however played by the composition of the synthesis gel. Finally, the spontaneous aggregation of sf-ITQ-1 samples in macro-hollow spheres was observed. This property must surely be further investigated.

The results obtained from the summarized published study[18] can be used to try to reproduce the synthesis of the first rose-ITQ-1-25-calcB580 sample. Actually, a slight increase of the H_2O/SiO_2 ratio, coupled with a decrease of the HMI/SiO_2 ratio should lead to the desired direction. The effect of the $TMAdaOH/SiO_2$ is critical, since the increase of the $TMAda^+$ should help the correct stacking of the layers, while the OH^- could affect the surface charge, enhancing the disordered orientation.

Parallelly, some sporadic attempts of preparing an ITQ-1 sample using TEOS instead of Aerosil® 200 as Si source were done. They were all unsuccessful (because a systematic study of the synthesis conditions was not performed yet), but some hypotheses can however be proposed. The crystallization of the MWW phase is strongly affected by the temperature (and probably by the pressure) and by the speed of rotation in tumbling conditions used during the hydrothermal treatment. When Aerosil® 200 is used as Si source, slight variation of the temperature (± 5 °C) or the use of less of 60 rpm causes the formation of amorphous aggregates not visible by PXRD, that, upon calcination, trap the OSDA molecules, hindering their combustion and leading to the formation of coke residues. This could suggest that, when TEOS is used as Si source, the strong increase of the autogenous pressure due to the presence of EtOH (produced upon the TEOS hydrolysis) could hinder the nucleation of the MWW phase, if the same hydrothermal treatment conditions are used. Moreover, the possible incomplete hydrolysis of TEOS could affect the molar ratio of the OSDAs and K_2CO_3 respect to SiO_2 available species. Surely, the EtOH evaporation could help in bridging the gap between the use of Aerosil® 200 and TEOS. Further investigation is needed to clarify this point.

4.5. References

1 H. Xu, Y. Guan, X. Lu, J. Yin, X. Li, D. Zhou and P. Wu, *ACS Catal.*, 2020, **10**, 4813–4819.

2 M. A. Camblor, A. Corma, M. J. Díaz-Cabañas and C. Baerlocher, *J. Phys. Chem. B*, 1998, **102**, 44–51.

3 D. M. Dawson, R. F. Moran and S. E. Ashbrook, *J. Phys. Chem. C*, 2017, **121**, 15198–15210.

4 C. Baerlocher and L. B. McCusker, *Database of Zeolite Structures*, 1997.

5 M. Fabbiani, A. Morsli, G. Confalonieri, T. Cacciaguerra, F. Fajula, J. Haines, A. Bengueddach, R. Arletti and F. Di Renzo, *Microporous Mesoporous Mater.* 2022, **332**, 111678–111685.

6 V. A. Ostroumova and A. L. Maksimov, *Petrol. Chem.* 2019, **59**, 788–801.

7 M. E. Leonowicz, J. A. Lawton, S. L. Lawton and M. K. Rubin, *Science*, 1994, **264**, 1910–1913.

8 S. L. Lawton, A. S. Fung, G. J. Kennedy, L. B. Alemany, C. D. Chang, G. H. Hatzikos, D. N. Lissy, M. K. Rubin, H. K. C. Timken, S. Steuernagel and D. E. Woessner, *J. Phys. Chem.* 1996, **100**, 3788–3798.

9 M. Položij, H. V. Thang, M. Rubeš, P. Eliášová, J. Čejka and P. Nachtigall, *Dalton Trans.* 2014, **43**, 10443–10450.

10 A. Corma, C. Corell and J. Pérez-Pariente, *Zeolites*, 1995, **15**, 2–8.

11 G. G. Juttu and R. F. Lobo, *Microporous Mesoporous Mater.* 2000, **40**, 9–23.

12 B. Gil, W. J. Roth, W. Makowski, B. Marszalek, D. Majda, Z. Olejniczak and P. Michorczyk, *Catal. Today*, 2015, **243**, 39–45.

13 A. S. Fung, S. L. Lawton and W. J. Roth, US Patent 5,362,697, 1994.

14 B. Gil, W. Makowski, B. Marszalek, W. J. Roth, M. Kubu, J. Čejka and Z. Olejniczak, *J. Chem. Soc., Dalton Trans.* 2014, **43**, 10501–10511.

15 D. Roizard, in *Encyclopedia of Membranes*, eds. E. Drioli and L. Giorno, Springer, Berlin, Heidelberg, 2014.

16 C. de la Calle-Arroyo, J. López-Fidalgo and L. J. Rodríguez-Aragón, *Chemom. Intell. Lab. Syst.* 2021, **214**, 104334.

17 Water, NIST WebBook, https://webbook.nist.gov/cgi/cbook.cgi?ID=C7732185 (accessed on 8 december 2023).

18 F. Rosso, A. Airi, M. Signorile, E. Dib, S. Bordiga, V. Crocellà, S. Mintova and F. Bonino, accepted to *Microporous Mesoporous Mater.* 2023.

19 N. Chu, J. Wang, Y. Zhang, J. Yang, J. Lu and D. Yin, *Chem. Mater.* 2010, **22**, 2757–2763.

20 A. Schwanke, J. Villarroel-Rocha, K. Sapag, U. Díaz, A. Corma and S. Pergher, *ACS Omega*, 2018, **3**, 6217–6223.

21 S. Cao, Y. Shang, Y. Liu, J. Wang, Y. Sun, Y. Gong, G. Mo, Z. Li and P. Liu, *Microporous Mesoporous Mater.*, 2021, **315**, 110910–110921.

22 H. Giesche, *Part. Part. Syst. Charact.* 2006, **23**, 9–19.

23 S. P. Rigby, D. Barwick, R. S. Fletcher and S. N. Riley, *Appl. Catal. A Gen.*, 2003, **238**, 303–318.

24 M. Król, W. Mozgawa, W. Jastrzbski and K. Barczyk, *Microporous Mesoporous Mater.* 2012, **156**, 181–188.

25 D. Scarano, A. Zecchina, S. Bordiga, F. Geobaldo, G. Spoto, G. Petrini, G. Leofanti, M. Padovan and G. Tozzola, *J. Chem. Soc., Faraday Trans.* 1993, **89**, 4123–4130.

26 K. Ogorzały, B. Gil, M. Mazur, W. Makowski and W. J. Roth, *Microporous Mesoporous Mater.* 2021, **324**, 111300–111307.

27 W. Mozgawa, W. Jastrzębski and M. Handke, in *J. Mol. Struct.* 2005, vol. 744–747, pp. 663–670.

28 Y. Yu, G. Xiong, C. Li and F.-S. Xiao, *Microporous Mesoporous Mater.* 2001, **46**, 23–34.

29 F. Fengtao, F. Zhaochi and L. Can, *Chem. Soc. Rev.* 2010, **39**, 4794–4801.

30 M. Signorile, V. Crocellà, A. Damin, B. Rossi, C. Lamberti, F. Bonino and S. Bordiga, *J. Phys. Chem. C*, 2018, **122**, 9021–9034.

31 S. Bordiga, I. Roggero, P. Ugliengo, A. Zecchina, V. Bolis, G. Artioli, R. Buzzoni, G. Marra, F. Rivetti, G. Spano and C. Lamberti, *J. Chem. Soc., Dalton Trans.*, 2000, 3921–3929.

32 S. Bordiga, P. Ugliengo, A. Damin, C. Lamberti, G. Spoto, A. Zecchina, G. Spanò, R. Buzzoni, L. Dalloro and F. Rivetti, *Top. Catal.*, 2001, **15**, 43–52.

33 F. Pascale, P. Ugliengo, B. Civalleri, R. Orlando, P. D'Arco and R. Dovesi, *J. Chem. Phys.* 2002, **117**, 5337–5346.

34 G. J. Kennedy, S. L. Lawton and M. K. Rubin, *J. Am. Chem. Soc.* 1994, **116**, 11000–11003.

35 R. Millini, G. Perego, W. O. Parker, G. Bellussi and L. Carluccio, *Microporous Mater.* 1995, **4**, 221–230.

36 S. L. Njo, H. Van Konigsveld, B. Van De Graaf, C. Barelocher and L. B. Mccusker, in *12th International Zeolite Conference*, eds. M. M. J. Treacy, B. K. Marcus, B. M. E and J. B. Higgins, 1999, 2519–2524.

37 P. Lu, L. Gómez-Hortigüela and M. A. Camblor, *Chem. Eur. J.* 2019, **25**, 1561–1572.

38 S. Sabnis, V. A. Tanna, J. Gulbinski, J. Zhu, S. S. Nonnenmann, G. Sheng, Z. Lai, H. H. Winter and W. Fan, *Microporous Mesoporous Mater.* 2021, **315**, 110883–110890.

39 F. Jiménez-Cruz and J. L. García-Gutiérrez, *Arab. J. Chem.* 2020, **13**, 8592–8599.

5. Ti-DOPED ZEOLITES WITH MWW FRAMEWORK

5.1. Scope of the work

In this chapter, a Ti-MWW sample was synthesized by slightly modifying a procedure reported in the literature. The procedure involved the use of Aerosil® 200 as Si source and a post-hydrothermal treatment washing with HNO_3, to remove the extra-framework species. The Ti-MWW properties were characterized in depth to understand the role of the HNO_3 washing. The synthesis and characterization of a Ti-MWW catalyst prepared modifying a synthesis reported in the literature allowed to get familiar with the behavior of the MWW framework when Ti is inserted as heteroatom.

5.2. Experimental procedures

5.2.1. Chemicals

Aerosil® 200 (from Evonik Industries), tetrabuthyl orthotitanate (TBOT, reagent grade 97% from Sigma Aldrich), N,N,N-trimethyl-adamantil-ammonium hydroxide (TMAdaOH, 25 wt% in water, from TCI), hexamethyleneimine (HMI, 99% from Sigma Aldrich), potassium carbonate (K_2CO_3, anhydrous, ACS reagent, from Sigma Aldrich), nitric acid (HNO_3, 65% for analysis-ISO, from Carlo Erba Reagents) and Milli-Q water were used for the synthesis of the Ti-MWW samples. Hydrogen peroxide (H_2O_2) aqueous solution (≥ 30 wt%, for trace analysis, from Sigma Aldrich) was used as oxidizing agent.

5.2.2. Synthesis

5.2.2.1. Preliminary synthesis of Ti-MWW samples

The preparation of a Ti-MWW sample was reproduced from the literature.[1] The procedure is analogous to that used for rose-ITQ-1 samples, with the addition of a TiO_2 source. A gel with the composition 1 SiO_2 : 0.02 TiO_2 : 0.2 TMAdaOH : 0.3 HMI : 0.07 K_2CO_3 : 30 H_2O was prepared by adding 8.45 g of TMAdaOH aqueous solution, 1.49 g of HMI and 0.4837 g of K_2CO_3 to 20.68 g of Milli-Q H_2O in this order. After the complete dissolution of K_2CO_3, 0.34 g of TBOT were added drop-wise under vigorous stirring. After 30 min of stirring at RT, 3.004 g of Aerosil® 200 were added portion-wise to the solution and the gel was stirred until it was fully homogeneous. The gel was transferred to a 45 ml Teflon lined stainless steel digestor (ratio between the volume of gel and volume of liner ≈ 66%) and it was crystallized under autogenous pressure at 150 °C and under tumbling conditions at 60 rpm. The gel was filtered, washed with H_2O until a pH ≈ 8 was reached and dried overnight at 65 °C. The same procedure was repeated using a gel with the following molar composition: 1 SiO_2 : 0.02 TiO_2 : 0.2 TMAdaOH : 0.3 HMI : 0.035 K_2CO_3 : 30 H_2O, to test the appropriate K_2CO_3/SiO_2 ratio. Actually, the authors were contacted upon repeated unsuccessful syntheses. They indicated the K_2CO_3/SiO_2 as a key parameter for the successful and complete crystallization of the Ti-MWW and they realized that the K_2CO_3/SiO_2 = 0.07 written in the paper was instead K_2CO_3/SiO_2 = 0.035. The hydrothermally synthesized samples were called Ti-MWW-0.07-HS and Ti-MWW-0.035-HS, where 0.07 and 0.035 are the used K_2CO_3/SiO_2 molar ratios.

Ti-free references were also prepared with the following molar compositions: 1 SiO_2 : 0.2 TMAdaOH : 0.3 HMI : 0.07 K_2CO_3 : 30 H_2O and 1 SiO_2 : 0.2 TMAdaOH : 0.3 HMI : 0.035 K_2CO_3 : 30 H_2O. The two samples were called

rose-ITQ-0.07-HS (namely rose-ITQ-1-HS in Chapter 4) and rose-ITQ-1-0.035-HS.

Ti-MWW-0.07-HS, Ti-MWW-0.035-HS, rose-ITQ-1-0.07-HS and rose-ITQ-1-0.035-HS were washed with a 2 M aqueous solution of HNO_3 for 20 h at 100 °C under reflux, with a solid to liquid ratio of 1 g : 50 ml. The obtained samples were named Ti-MWW-0.07-HNO_3-HS, Ti-MWW-0.035-HNO_3-HS, rose-ITQ-1-0.07-HNO_3-HS and rose-ITQ-1-0.035-HNO_3-HS. The acid washing is reported to be necessary to remove the extra-framework anatase, formed during the hydrothermal crystallization.[1] The HNO_3 washed Ti-free reference is useful to highlight the effect of the acid treatment on the other properties of the material, such as the crystallinity and defectivity.

5.2.2.2. Synthesis of Ti-MWW samples

Based on the results of the preliminary synthesis, the preparation of Ti-MWW-0.035-HS was reproduced, and the obtained sample will be called Ti-MWW-HS in the following, for the sake of brevity. A portion of Ti-MWW-HS was washed with the 2 M aqueous solution of HNO_3 to obtain Ti-MWW-HNO_3-HS, as previously described. Ti-MWW-HS and Ti-MWW-HNO_3-HS were calcined with procedure A (described in Chapter 4, namely, a heating ramp of 1 °C/min up to 550 °C under dry air flow, followed by 7 h of isotherm under the same flow). The calcined samples were called Ti-MWW-calc and Ti-MWW-HNO_3-calc. sf-ITQ-1-calcA was used as Ti-free reference sample for the characterization of the acidic properties of Ti-MWW-HNO_3-calc, based on the crystallinity (PXRD) and defectivity (transmission IR) properties, considering that a HNO_3 washed Ti-free sample without presence of additional phases was not obtained.

5.2.3. Characterization of Ti-MWW samples

All the preliminary and final Ti-MWW samples were characterized by means of PXRD. The TiO_2 loading in Ti-MWW-HS, Ti-MWW-calc, Ti-MWW-HNO_3-HS and Ti-MWW-HNO_3-calc was determined by EDX. Ti-MWW-calc and Ti-MWW-HNO_3-calc were analyzed by means of N_2 physisorption at -196 °C and IR spectroscopy in ATR and transmission mode.

The acidic properties of Ti-MWW-HNO_3-calc and of the sf-ITQ-1-calcA reference were studied by transmission IR spectroscopy, dosing basic probe molecules on the sample under acquisition. The home-made quartz cell described in Chapter 2 was equipped with KBr or CaF_2 windows depending on the used probe molecule. Carbon monoxide (CO),[2,3] deuterated acetonitrile (CD_3CN),[4] pyridine (Py)[4] and ammonia (NH_3)[5] were used as probe molecules. The specific experimental settings are reported elsewhere.[2–5]

In situ UV-Vis-NIR spectroscopy in Diffuse Reflectance (DR) mode was used to study the interaction of the Ti sites in Ti-MWW-HNO_3-calc with H_2O_2. The sample was contacted with the H_2O_2 aqueous solution, dried for ≈ 25 min in air by continuously milling until a pale orange powder was obtained. The degradation of the complexes was studied by drying the sample for 4, 24 and 96 h in air at RT. The effect of the addition of H_2O was tested on the samples dried for 4 and 96 h. After 96 h of drying, the pale ocher powder was contacted again with H_2O_2 and further dried for 24 h. The sample contacted twice with H_2O_2 was regenerated by calcination in a tubular oven, using a heating ramp of 1 °C/min up to 550 °C, followed by a 4 h isotherm, under dry air flow. UV-Vis spectra were recorded in air after each step.

In situ transmission IR spectroscopy was used to study the interaction between H_2O_2 and the Ti sites in Ti-MWW-HNO_3-calc sample by wetting a pellet with a drop of H_2O_2, drying it in air till no residue of solution was visible by naked eye and inserting it in a home-made quartz cell equipped with KBr

windows. The sample was quickly outgassed to remove the air and the excess of H_2O and H_2O_2. The catalytic behavior of Ti-MWW-HNO_3-calc was tested on the target reaction: Hydrogen Peroxide to Propylene Oxide (HPPO). This was done by dosing 60 mbar of pure propylene on the H_2O_2 soaked/outgassed sample, to observe the formation of propylene oxide. Reference spectra of pure propylene and pure propylene oxide dosed on the RT outgassed sample, in absence of H_2O_2, were also recorded.

5.3. Results and discussion

5.3.1. Crystalline structure analysis of the preliminary Ti-MWW samples

The preliminary syntheses exposed in the present paragraph are aimed at evaluating the best K_2CO_3/SiO_2 ratio to be used to prepare a Ti-MWW sample and at exploring the effect of the HNO_3 washing on the crystallinity of the Ti-MWW and Ti-free ITQ-1 reference samples.

The PXRD patterns of the as-synthesized samples (Figure 5.3.1.1a) show highly crystalline MWW phase. The diffractograms of the HNO_3 washed Ti-MWW-0.07-HNO_3-HS, rose-ITQ-1-0.07-HNO_3-HS and rose-ITQ-1-0.035-HNO_3-HS samples (Figure 5.3.1.1b) show the presence of a single broad peak in the 7.5° to 10° 2θ range and the growth of a peak at 15°. This could suggest that the MWW single layers are completely delaminated and disordered, but the identification of a delaminated phase is not straightforward from at the PXRD. The diffractogram of Ti-MWW-0.035-HNO_3-HS is coherent with the presence of partially disordered layers, still organized in a 3D structure. It appears to be the only sample preserving the crystalline structure upon the acid treatment. Hence, this sample was chosen as the one worth of further studies, and it will be calcined and fully characterized in the following.

Since a Ti-free HNO_3 washed sample cannot be obtained by simply removing the Ti source from the gel used to prepare the Ti-MWW sample, sf-ITQ-1-HS and sf-ITQ-1-calcA samples were used as Ti-free reference, due to its similarities with Ti-MWW, based on PXRD and transmission IR characterization.

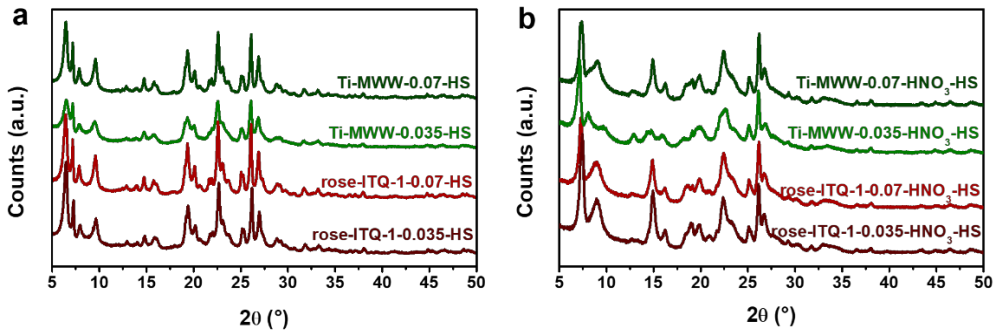

Figure 5.3.1.1. PXRD patterns in the 5° to 45° 2θ range. (a) as-synthesized samples: Ti-MWW-0.07-HS (dark olive), Ti-MWW-0.035-HS (olive), rose-ITQ-1-0.07-HS (red) and rose-ITQ-1-0.035-HS (dark red). (b) HNO_3 washed samples: Ti-MWW-0.07-HNO_3-HS (dark olive), Ti-MWW-0.035-HNO_3-HS (olive), rose-ITQ-1-0.07-HNO_3-HS (red) and rose-ITQ-1-0.035-HNO_3-HS (dark red).

5.3.2. Crystalline structure and defects analysis of Ti-MWW samples

The work reported in paragraphs from 5.3.2 to 5.3.5 was submitted as original paper to the Special Collection "Oxygen Activation and Oxidation Catalysis", that will be published jointly in *ChemCatChem* and in the *European Journal of Inorganic Chemistry* (*EurJIC*). Here, the results will be summarized and commented by considering the viewpoint of the full thesis manuscript.

Figure 5.3.2.1 shows the PXRD patterns of the as-synthesized sf-ITQ-1-HS, Ti-MWW-HS and Ti-MWW-HNO_3-HS samples (a) and of the calcined sf-ITQ-

1-calcA, Ti-MWW-calc and Ti-MWW-HNO_3-calc samples (b). The diffractogram of Ti-MWW-HS is typical of the as-synthesized MWW phase [1,6–8] and those of Ti-MWW-calc and of Ti-MWW-HNO_3-calc are typical of the calcined MWW phase, [1,6–8] as can be seen by the comparison with the references sf-ITQ-1-HS and sf-ITQ-1-calcA respectively. The PXRD pattern of the as-synthesized, acid washed Ti-MWW-HNO_3-HS sample represents an intermediate situation between the as-synthesized and the calcined materials. This is due to the partial elimination of the OSDA molecules that occurs during the acid treatment, conducted in presence of an oxidizing acid (HNO_3).[9] The slight broadening of the peaks displayed by the calcined, acid washed Ti-MWW-HNO_3-calc compared to the not washed Ti-MWW-calc suggest a possible etching of the crystals or a reduced crystallite dimension caused by the HNO_3 treatment. The presence of anatase and of different zeolitic frameworks in detectable amounts is excluded.

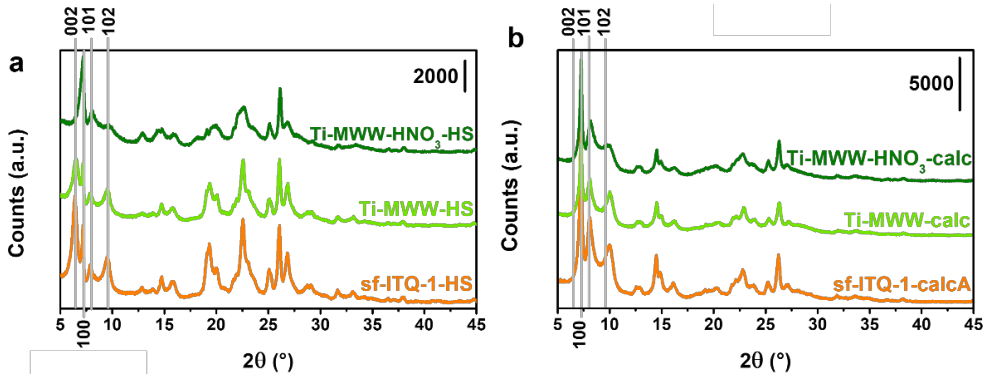

Figure 5.3.2.1. PXRD patterns in the 5° to 45° 2θ range. (a) As-synthesized samples: Ti-MWW-HNO_3-HS (olive), Ti-MWW-HS (light green) and sf-ITQ-1-HS (orange). (b) Calcined samples: Ti-MWW-HNO_3-calc (olive), Ti-MWW-calc (light green) and sf-ITQ-1-calcA (orange).

The N_2 physisorption isotherms recorded at -196 °C are reported in Figure 5.3.2.2a. The isotherms are type I, typical of microporous materials. The micropore volume (Figure 5.3.2.2b and Table 5.3.2.1) and the SSA (Table

5.3.2.1) of Ti-MWW-calc are lower than those of Ti-MWW-HNO_3-calc, as also visible from the low knee of the isotherm of Ti-MWW-calc. This suggests a possible partial occlusion of the channels of Ti-MWW-calc sample, possibly due to the presence of coke residuals from the OSDAs removal by calcination. In Ti-MWW-HNO_3-calc, the formation of coke residual should be avoided thanks to the fraction of organic molecules already oxidized during the HNO_3 washing.

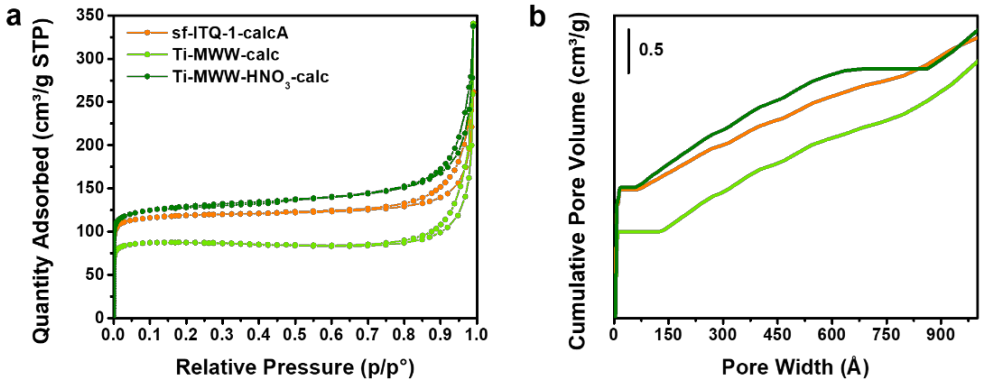

Figure 5.3.2.2. (a) Volumetric N_2 adsorption/desorption isotherms at -196 °C in the whole relative pressure range and (b) cumulative pore volume plot in the 0 – 1000 Å pore size range, obtained applying the NL-DFT model, of sf-ITQ-1-calcA (orange), Ti-MWW-calc (light green) and Ti-MWW-HNO_3-calc (olive).

Table 5.3.2.1. SSAs calculated with the BET and Langmuir models and micropore volume (V_{micro}), computed using the NL-DFT method.

Sample	BET SSA[1] (m^2/g)	Langmuir SSA[2] (m^2/g)	V_{micro}[3] (cm^3/g STP)
Ti-MWW-HNO_3-calc	498 ± 1	581 ± 2	0.15
Ti-MWW-calc	350 ± 2	384 ± 1	0.10
sf-ITQ-1-calcA	465 ± 2	525 ± 1	0.15

[1] Calculated in the 0.008 – 0.08 p/p^0 range.
[2] Calculated in the 15 – 200 mbar pressure range.
[3] Calculated from the cumulative pore volume plot for pore size < 20 Å.

Figure 5.3.2.3 shows the IR spectra of the activated Ti-MWW-calc and Ti-MWW-HNO_3-calc samples in the hydroxyls (OH) stretching region, compared with the reference sf-ITQ-1-calcA. The signals assigned to the OH stretching could be due to the presence of both $Si(OSi)_3OH$ and $Ti(OSi)_3OH$ species, but discerning among them is a hard task due to their very similar stretching frequency.[10] The spectrum of Ti-MWW-HNO_3-calc displays signals similar to the reference ones, namely isolated and chain terminal $Si(OSi)_3OH$ and $Si(OSi)_3OH$ nests. [2,10–12] sf-ITQ-1-calcA was chosen as reference thanks to its very similar amount of $Si(OSi)_3OH$ nests with Ti-MWW-HNO_3-calc. A new signal is present at 3688 cm^{-1} in the spectrum of Ti-MWW-HNO_3-calc sample. We will see in the following that the assignment of this component is not straightforward.

The spectrum of the directly calcined, not HNO_3 washed Ti-MWW-calc sample, curiously shows only the signal assigned to isolated $Si(Ti)(OSi)_3OH$ species, probably due to a defect healing phenomenon occurring upon direct calcination.

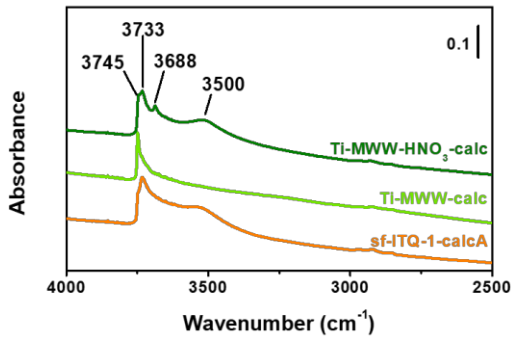

Figure 5.3.2.3. Transmission IR spectra of sf-ITQ-1-calcA (orange), Ti-MWW-calc (light green) and Ti-MWW-HNO_3-calc (olive) in the 4000-2500 cm^{-1} spectral range. The spectra are recorded after activation, internally normalized at the Si-O-Si stretching overtone absorptions and vertically shifted for the sake of comparison.

5.3.3. Ti active site characterization

One of the main issues in the preparation of Ti zeolites is the low amount of active site that can be inserted in the framework. The TiO_2 loading and the uniformity of the element distribution was analyzed by EDX-SEM (EDX maps reported in Figures 5.3.3.1 and 5.3.3.2 and quantification reported in Table 5.3.3.1). The maps show that the distribution of the Ti atoms is uniform in both the samples. The presence of potassium (K) was detected in Ti-MWW-calc sample, probably originating from the K_2CO_3 used in the hydrothermal treatment and retained in the structure. In Chapter 4 the K was shown not to be retained in rose-ITQ-1 samples, suggesting that the presence of K in Ti-MWW-calc could be related to the Ti containing species. K is not detected any more in the HNO_3 washed Ti-MWW-HNO_3-calc sample (Figure 5.3.3.2). The TiO_2 loading of Ti-MWW-HNO_3-calc sample (2.91 wt%) is higher than the one of Ti-MWW-calc (1.75 wt%). The high TiO_2 content in Ti-MWW-HNO_3-calc is an intriguing result, since the limit amount of TiO_2 in TS-1 is 2.76 wt%. This value was obtained at an industrial scale[10,13,14] and rarely replicated at laboratory scale, without the compromise of extra-framework species.[15–21] Obtaining in Ti-MWW-HNO_3-calc a TiO_2 loading higher than that of TS-1 opens the possibility of even higher loadings, considering that the limit for the MWW framework was not determined yet.

The variation of the TiO_2 content observed between Ti-MWW-calc and Ti-MWW-HNO_3-calc samples can be explained. The Ti/Si ratio in the synthesis gel is 0.02, hence a loss of silicate species occurs during the hydrothermal treatment (Ti/Si = 0.0134 in Ti-MWW-calc). The loss could be due to an incomplete hydrolysis of the Ti source, possibly occurring at the temperature used during the hydrothermal crystallization (150 °C), based on the results showed in Chapter 3 (DoE 1). A steep increase in the Ti/Si ratio is observed because of the acid treatment. The Ti enrichment could be due to a loss of

silicate species or to the solubilization-recrystallization of Ti-rich aggregates possibly present in the as-synthesized sample. The loss of silicate species in highly unlikely because silicates are not soluble in acidic conditions and because the yield of Ti-MWW-HNO_3-calc was 93.7% respect to the reagents. Such a high yield is not consistent with a significant silicate loss. It is instead probable that Ti-rich aggregates are present in the hydrothermally synthesized sample (Ti-MWW-HS), that may be dissolved during the HNO_3 washing providing available Ti species. The nature and composition of such aggregates cannot be defined, since they are not detected by SEM, but they could be related with the presence of K in Ti-MWW-calc and eliminated during the HNO_3 washing.

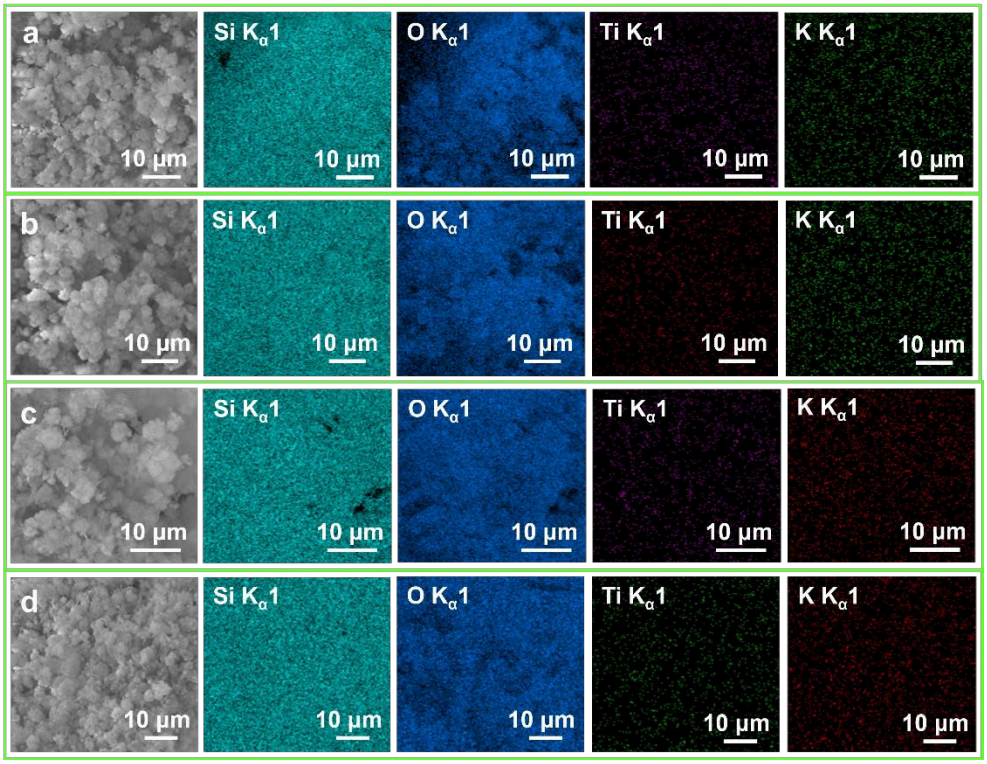

Figure 5.3.3.1. EDX-SEM maps of the four sites used to quantify the Ti/Si of Ti-MWW-calc. For each site (a, b, c and d), the SEM image and the Si, O, Ti and K distribution are reported (from left to right).

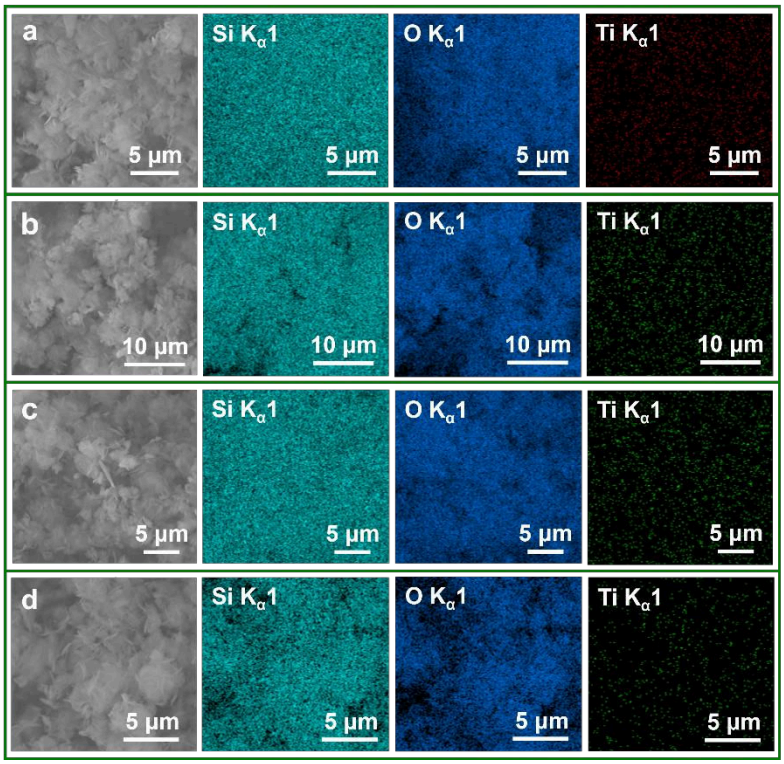

Figure 5.3.3.2. EDX-SEM maps of the four sites used to quantify the Ti/Si of Ti-MWW-HNO_3-calc. For each site (a, b, c and d) the SEM image and the Si, O and Ti distribution are reported from left to right. K is not detected in the sample.

Table 5.3.3.1. Quantification of the total TiO_2 content determined by EDX-SEM.

Sample	Ti/Si[1]	TiO_2 (wt%)[1]	σ[2]
Ti-MWW-calc	0.0134	1.75	0.17
Ti-MWW-HNO_3-calc	0.0226	2.91	0.52

[1] Average on 4 points
[2] Standard deviation referred to the TiO_2 (wt%)

Figure 5.3.3.3 shows the UV (a) and ATR-IR (b) spectroscopies characterization of the Ti-MWW-calc and Ti-MWW-HNO_3-calc. The interpretation is analogous to what reported in Chapter 3 regarding TS-1. The

band edge and maximum (minimum in reflectance (%) scale) of the LMCT electronic transition involving Ti is sensitive to the environment around the Ti atoms, and in the transparency window between the v_{asym}(SiOSi) (at 1100 cm^{-1}) and the v_{sym}(SiOSi) (at 800 cm^{-1}) stretching bands, the vibrational band associated to the presence of Ti in framework positions is present. The UV spectrum of Ti-MWW-HNO_3-calc shows a single band at 205 nm, doubtless ascribed to Ti species in framework, tetrahedral positions. The spectrum of Ti-MWW-calc does not present any clear maximum at 210 nm; it displays instead a broad absorption at 235 nm with a shoulder at 280 nm. The frequency of the band at 235 nm is reported to be compatible with the LMCT involving $Ti(OSi)_3OH$ species,[22] but computational studies revealed that the $Ti(OSi)_4$ and the $Ti(OSi)_3OH$ species (among others) cannot be discriminated based on their UV spectrum.[23] The presence of a shoulder at 235 nm was also observed in TS-1 samples synthesized using a K containing TPAOH (Chapter 3). This suggests that this signal could be associated to Ti and K containing species, *e.g.* K titanates.

The possible presence of K titanates in the PXRD pattern of Ti-MWW-calc (Figure 5.3.2.1) is not detected, but they could be amorphous or well dispersed in the sample (as suggested by the homogeneous distribution of Ti and K in Figure 5.3.3.1). Assuming all the Ti and K were involved in the formation of K titanates, it is possible to give a rough estimation of the nuclearity of Ti atoms in the titanates. The Ti/K obtained ratios (Table 5.3.3.2) are consistent with the K_2TiO_3 (a and c sites) and $K_2Ti_2O_5$ (b and d sites) stoichiometries.

The ATR-IR spectra of the activated Ti-MWW-HNO_3-calc and Ti-MWW-calc, compared with sf-ITQ-1-calcA are shown in Figure 5.3.3.3b. It is worth noticing that the broad band centered at 960 cm^{-1} observed in the ATR-IR spectrum of sf-ITQ-1-calcA recorded in air[24] (Figure 4.3.3.1a in Chapter 4) is not present in the activated spectrum due to the temporary defect healing

effect of the thermal treatment. Ti-MWW-calc does not show signals in the transparency window, verifying the absence of Ti in framework positions when the acid treatment is not performed. Ti-MWW-HNO_3-calc spectrum shows two bands at 965 and 930 cm^{-1}. The first one can be considered an analogous of the 960 cm^{-1} band in TS-1,[25–29] while the component at 930 cm^{-1} [1] is typical of the Ti-MWW catalyst [1,30] and of some amorphous mesoporous silicates, depending on the synthetic procedure, *e.g.* Ti-MCM-41. [31,32] In Ti-MWW catalyst, it was assigned to a defective $Ti(OSi)_3OH$ site, located at the T1 crystallographic site.[1] The Ti sites involved in the $Ti(OSi)_3OH$ species are probably in a distorted tetrahedral coordination, due to the presence of the hydroxyl ligand, conferming that they cannot be discerned from the $Ti(OSi)_4$ species, based on their LMCT electronic transition in the UV spectrum.

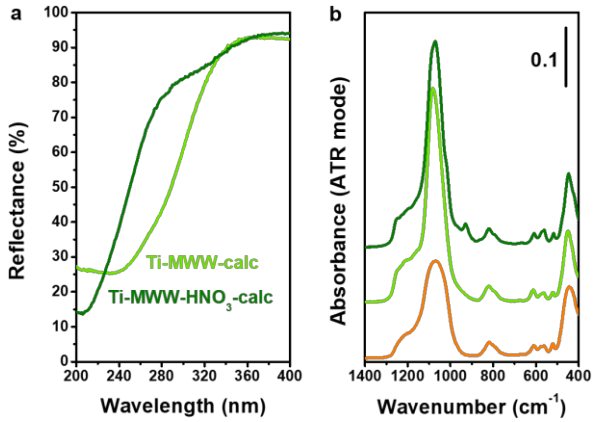

Figure 5.3.3.3. (a) UV-Vis spectra of activated samples: Ti-MWW-HNO_3-calc (olive) and Ti-MWW-calc (light green). (b) Vertically shifted ATR-IR spectra of activated samples: (from top to bottom) Ti-MWW-HNO_3-calc (olive), Ti-MWW-calc (light green) and sf-ITQ-1-calc (orange).

Table 5.3.3.2. Ti and K atomic % determined by EDX-SEM in Ti-MWW-calc sample and consequent Ti/K atomic ratio. The a, b, c and d site are referred to the a, b, c and d panel of Figure 5.3.3.1.

Site	Ti (atomic %)	K (atomic %)	Ti/K
a	0.19	0.39	0.49
b	0.38	0.38	1.00
c	0.25	0.43	0.58
d	0.70	0.51	1.37

The absence of bands ascribed to Ti in framework positions in Ti-MWW-calc suggests that the HNO_3 washing is the only responsible for the Ti insertion in the zeolitic framework and supports the hypothesis of the predominant presence of inactive K titanate species in Ti-MWW-calc. For this reason, the characterization of the acidic properties will be performed only on the Ti-MWW-HNO_3-calc sample and on the sf-ITQ-1-calcA reference sample.

5.3.4. Study of acid sites and hydroxyls group using probe molecules

The Ti-zeolites contains different acidic sites: the Ti(IV) atoms in tetrahedral coordination are Lewis centers and the OH groups belonging to $Si(OSi)_3OH$ and $Ti(OSi)_3OH$ constitute weak Brønsted sites. The IR spectroscopy coupled with the use of basic probe molecules is an effective tool to study the strength and location of the acid sites.[27,33]

The use of probe molecules with different protonic affinity, namely CO, CD_3CN, Py and NH_3, were used to compare the acidic properties of Ti-MWW-HNO_3-calc with those of the Ti-free reference sf-ITQ-1-calcA.

In each figure, the effect of the maximum coverage is reported in bold (olive for Ti-MWW-HNO_3-calc and orange for sf-ITQ-1-calcA samples respectively), the spectra collected after progressive outgassing are reported in grey and

the last spectrum is reported with the thin olive or orange trace for Ti-MWW-HNO_3-calc and sf-ITQ-1-calcA respectively.

Figure 5.3.4.1 shows the background subtracted spectra of CO dosed on Ti-MWW-HNO_3-calc (a and b) and sf-ITQ-1-calcA (c and d) at -173 °C. The low proton affinity of CO (141.9 kcal/mol) [27,33] makes it unable to interact with Ti(IV) sites in tetrahedral coordination.

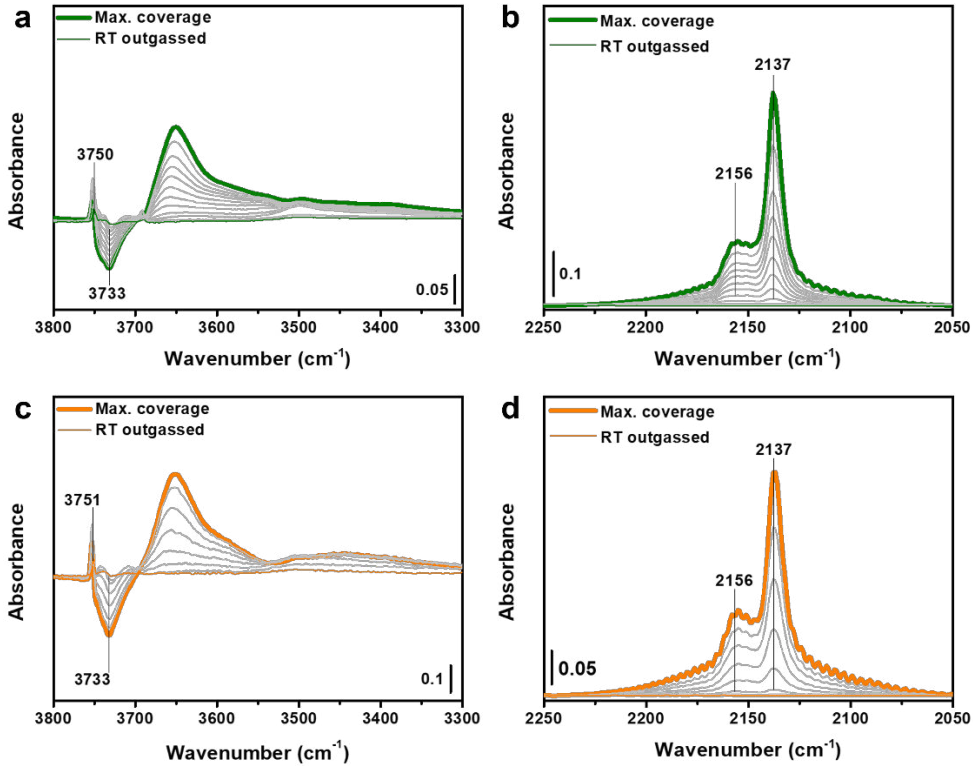

Figure 5.3.4.1. Background subtracted IR spectra of (a, b) Ti-MWW-HNO_3-calc, and (c, d) sf-ITQ-1-calcA after contact with CO at -173 °C in the (a, c) 3800-3300 cm^{-1} and (b, d) 2250-2050 cm^{-1} spectral regions. The spectrum of the activated sample was used as background.

This experiment was conducted to possibly detect differences between the hydroxyl population of the Ti-containing and free samples. The discrimination of $Si(OSi)_3OH$ and the $Ti(OSi)_3OH$ species based on spectroscopic results is

hindered by their very similar stretching frequency,[10] hence no clear differences can be appreciated from the comparison of the experiment conducted on Ti-MWW-HNO_3-calc and sf-ITQ-1-calcA. In both cases, the erosion of the signals of isolated (3750 cm^{-1}) and chain terminal (3733 cm^{-1}) OH and the corresponding growth of the signal of OH in interaction with CO (broad signal around 3650 cm^{-1}) are observed in the hydroxyls stretching region. [33]

The CO stretching region hosts two bands, centered at 2137 and 2156 cm^{-1}, assigned to weakly physisorbed and H-bonded CO molecules, respectively. The fate of the new band centered at 3688 cm^{-1} in Ti-MWW-HNO_3-calc spectrum is unclear, because no specific band is observed to grow distinguishable from the broad envelope centered at 3650 cm^{-1}(see Figure 5.3.4.2). The adsorption of CO on Ti-MWW-HNO_3-calc and sf-ITQ-1-calcA is totally reversible at the temperature of the experiment.

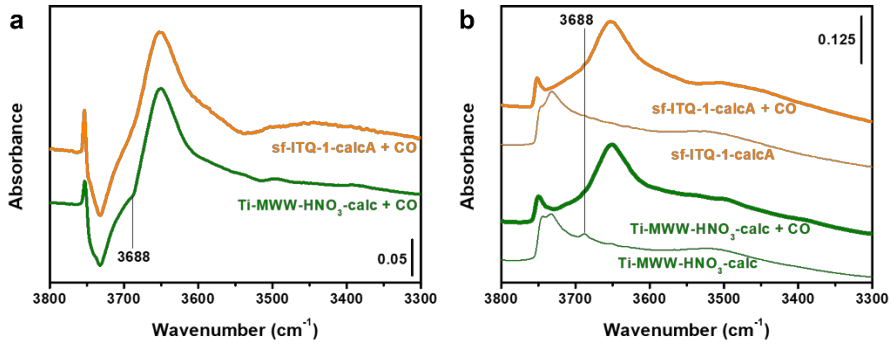

Figure 5.3.4.2. (a) background subtracted IR spectra of (from bottom to top) Ti-MWW-HNO_3-calc (olive) and sf-ITQ-1-calcA (orange) after dosing CO (activated spectra used as background). (b) vertically shifted IR spectra of (from bottom to top) activated Ti-MWW-HNO_3-calc (olive), Ti-MWW-HNO_3-calc after CO dosing (bold olive), activated sf-ITQ-1-calcA (orange) and sf-ITQ-1-calcA after CO dosing (bold orange), in the 3800-3300 cm^{-1} spectral region.

Figure 5.3.4.3 shows the background subtracted spectra in the hydroxyls (a and d) and CN (b and e) stretching regions and the spectra in the framework vibration region (c and f) of CD_3CN adsorbed on Ti-MWW-HNO_3-calc (a, b and c) and sf-ITQ-1-calcA (d, e and f). CD_3CN is a base stronger than CO and it is able to interact with Ti(IV) in tetrahedral coordination.[4] In the hydroxyl stretching region, the erosion of the bands associated to the surface hydroxyls and the parallel growth of a broad band at 3400 cm^{-1} ascribed to the stretching of OH groups in interaction with CD_3CN ($Si(OSi)_3OH$---$NCCD_3$ or $Ti(OSi)_3OH$---$NCCD_3$ complexes) are observed. The CN stretching region displays the band of the physisorbed, basically unperturbed CD_3CN (at 2264 and 2263 cm^{-1} in Ti-MWW-HNO_3-calc and sf-ITQ-1-calcA, respectively), a band due to the CN stretching when CD_3CN is involved in the formation of the $Si(OSi)_3OH$---$NCCD_3$ or $Ti(OSi)_3OH$---$NCCD_3$ complex (at 2274 cm^{-1} in both Ti-MWW-HNO_3-calc and sf-ITQ-1-calcA) and a band at 2307 cm^{-1} in Ti-MWW-HNO_3-calc, assigned to the CN stretching when CD_3CN forms the Ti(IV)---$NCCD_3$ complex.[4] The shift of the absorption frequency, respect to the frequency of the CN stretching in physisorbed CD_3CN, is representative of the strength of the Lewis acid site. In TS-1, an analogous signal is present, but the shift is lower respect to that of Ti in Ti-MWW-HNO_3-calc, suggesting that the Ti Lewis acidic sites in Ti-MWW are stronger than those in TS-1. This is a very important result, because CD_3CN allowed to directly compare the Lewis acidity of metal centers in different frameworks. The observed strength of the Ti Lewis sites is coherent with the presence of $Ti(OSi)_3OH$ species in the framework, proved to be more acidic than the fully coordinated $Ti(OSi)_4$ tetrahedral sites.[22,34]

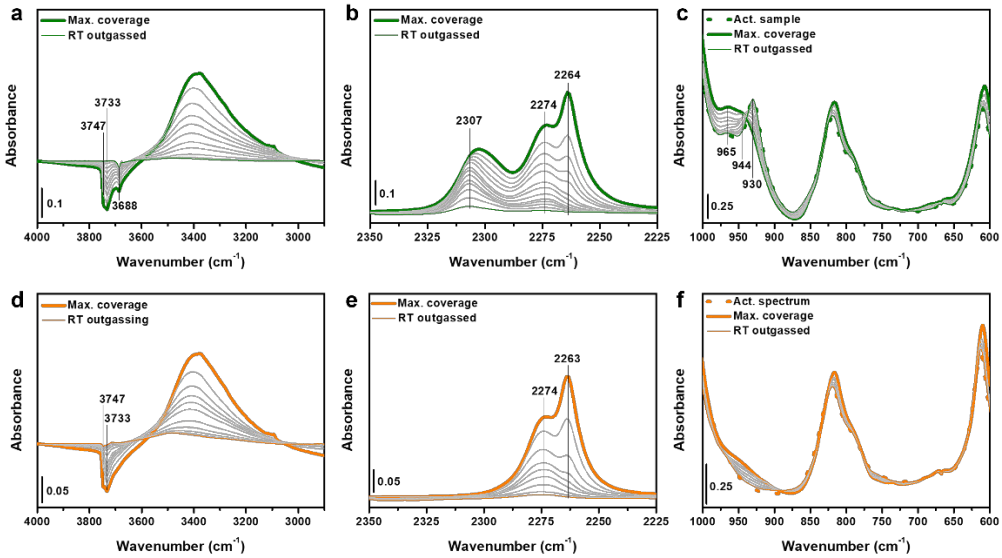

Figure 5.3.4.3. Background subtracted IR spectra of (a, b) Ti-MWW-HNO_3-calc and (d, e) sf-ITQ-1-calcA after contact with CD_3CN at RT, in the (a, d) 4000-2900 cm^{-1} and (b, e) 2350-2225 cm^{-1} spectral regions. The spectra of the activated samples were used as background. IR spectra of (c) Ti-MWW-HNO_3-calc and (f) sf-ITQ-1-calcA after contact with CD_3CN in the framework vibration region (1000-600 cm^{-1}).

In the framework vibration region (Figure 5.3.4.3c, f), the modification of the bands associated with the presence of Ti in framework positions upon interaction with CD_3CN can be appreciated. The band at 930 cm^{-1} upward shifts to 944 cm^{-1} (the presence of a transient species seems to occur), while the band at 965 cm^{-1} increases in intensity and broadens, without shifting.

Figure 5.3.4.4 shows the background subtracted spectra of recorded upon adsorption of Py on Ti-MWW-HNO_3-calc (a and b) and sf-ITQ-1-calcA (c and d), in the hydroxyl (4000-2600 cm^{-1}) and ring deformation (1650-1350 cm^{-1}) spectroscopical regions. The erosion of the band related to OH groups is observed, but, interestingly, not all the hydroxyl nests interact with Py (Figure 5.3.4.5). Probably due to its kinetic diameter (0.57), Py cannot interact with all the OH groups present in the defective sites, but only with a fraction of

them. The interpretation of the Py CH stretching region is complicated by the overlap with the broad signal growth as a consequence of the Py interaction with $Si(OSi)_3OH$ or $Ti(OSi)_3OH$ groups. In the 1650-1350 cm^{-1} range, the signals assigned to the 8a, 8b, 19a and 19b ring modes of Py are present.[4] Their absorption frequency shifts as a consequence of the interaction with the $Si(OSi)_3OH$ or $Ti(OSi)_3OH$ and with the Ti(IV) Lewis acid sites. Table 5.3.4.1 summarizes the frequencies of the spectral modes when Py is physisorbed, in interaction with OH groups or with Ti(IV) in tetrahedral coordination. No bands associated to the presence of Brønsted sites strong enough to protonate Py are present (around 1550 cm^{-1}).[35]

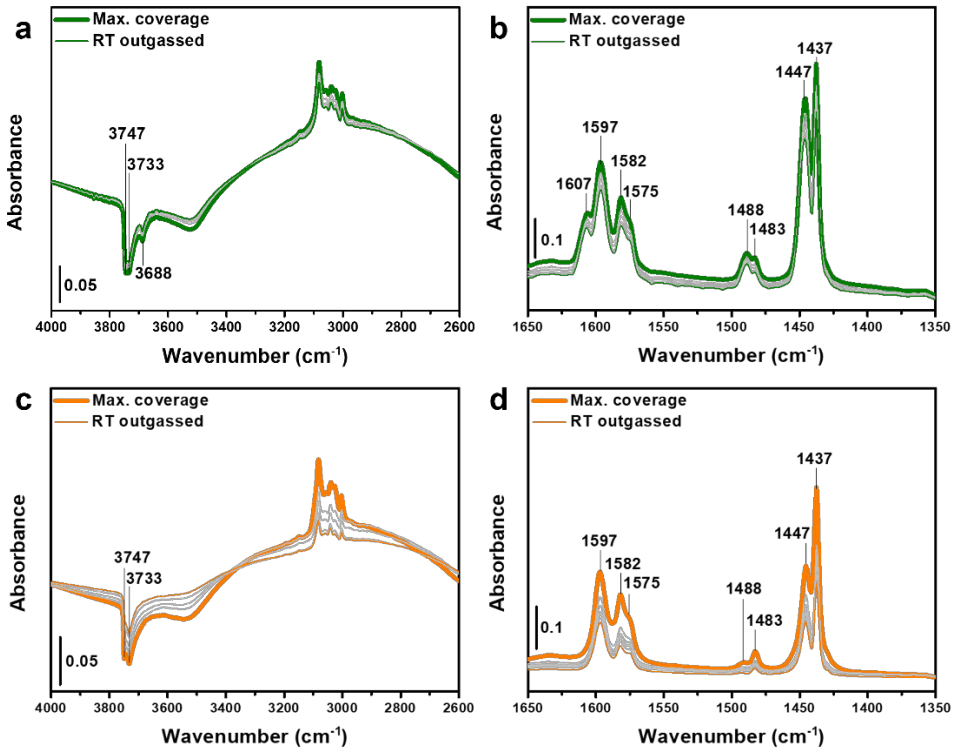

Figure 5.3.4.4. Background subtracted IR spectra of (a, b) Ti-MWW-HNO_3-calc and (c, d) sf-ITQ-1-calcA after contact with Py in the regions (a, c) 4000-2600 cm^{-1} and (b, d) 1650-1350 cm^{-1}. The spectra of the activated samples were used as background.

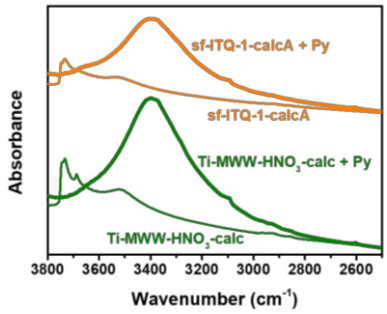

Figure 5.3.4.5. Vertically shifted IR spectra of (from bottom to top) activated Ti-MWW-HNO_3-calc, Ti-MWW-HNO_3-calc after Py dosing, activated sf-ITQ-1-calcA and sf-ITQ-1-calcA after Py dosing, in the 3800-2500 cm^{-1} spectral range. The spectra are vertically shifted for the sake of comparison.

Table 5.3.4.1. Vibrational frequencies and assignment of the Py vibrational modes highlighted in Figure 5.3.4.4b.

Wavenumber (cm^{-1})	Specie	Vibrational mode	Reference
1597	$Si(Ti)(SiO)_3OH$---Py	8a	[4,36]
1582	$Si(Ti)(SiO)_3OH$---Py	8b	[4,36]
1483	$Si(Ti)(SiO)_3OH$---Py	19a	[4,36]
1447	$Si(Ti)(SiO)_3OH$---Py	19b	[4,36]
1607	Ti(IV)---Py	8a	[4]
1575	Ti(IV)---Py	8b	[4]
1488	Ti(IV)---Py	19a	[4]
1437	Ti(IV)---Py	19b	[4]
1582	Physisorbed Py	8b	[4,36]
1483	Physisorbed Py	19a	[4,37]
1437	Physisorbed Py	19b	[4]

NH_3 is the last probe molecule used in this work and the one showing the stronger basicity,[27,33] with the aim of detecting the presence of medium strength Brønsted acid sites. Figure 5.3.4.6 shows the background subtracted (a and c) and the spectra (b and d) of Ti-MWW-HNO_3-calc (a and b) and sf-ITQ-1-calcA (c and d) recorded upon adsorption and progressive outgassing of NH_3 on the activated samples. In the hydroxyl stretching region is it possible to appreciate the erosion of the OH stretching bands and the growth

of a very broad band centered around 2880 or 2845 cm^{-1} in Ti-MWW-HNO_3-calc or sf-ITQ-1-calcA respectively. In the NH stretching region, the ν_{sym}(NH) and the ν_{asym}(NH) are present (Table 5.3.4.2 summarizes the frequencies).

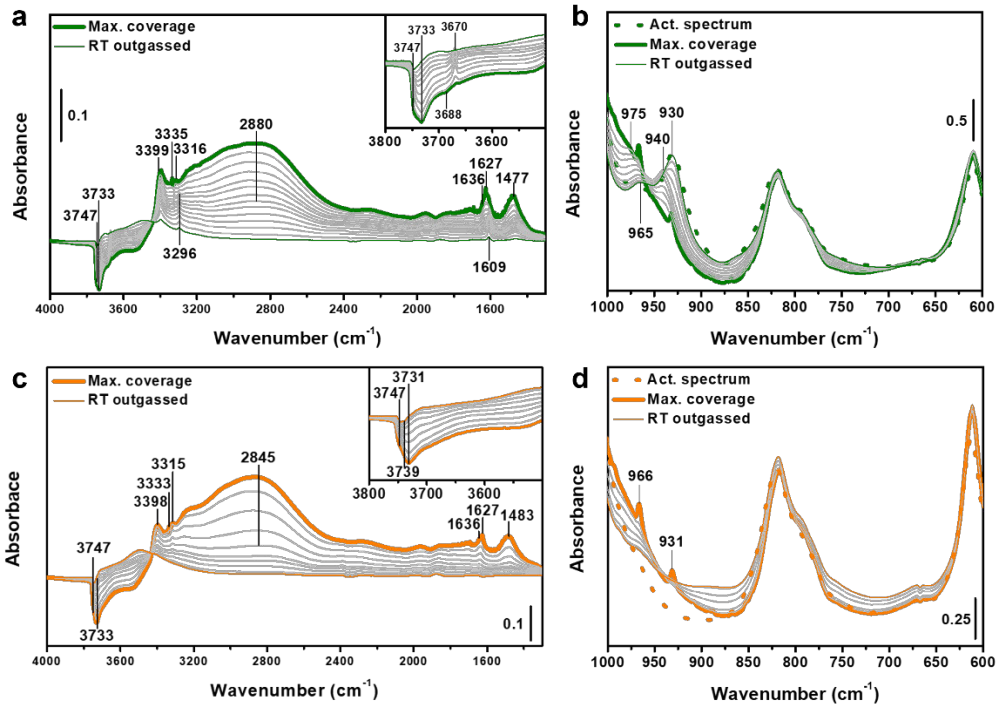

Figure 5.3.4.6. Background subtracted IR spectra of (a) Ti-MWW-HNO_3-calc and (c) sf-ITQ-1-calcA after contact with NH_3 at RT, in the 4000-1300 cm^{-1} spectral region. The spectra of the activated samples were used as background. IR spectra of (b) Ti-MWW-HNO_3-calc and (d) sf-ITQ-1-calcA after contact with HN_3 in the framework vibration region (1000-600 cm^{-1}).

Table 5.3.4.1. Vibrational frequencies and assignment of the bands ascribed to the NH stretching modes of NH_3 in interaction with Ti-MWW-HNO_3-calc.

Wavenumber (cm^{-1})	Specie	Vibrational mode	Reference
3316	$Si(Ti)(SiO)_3OH$---NH_3	$\nu_{sym}(NH)$	[32,38,39]
3399	$Si(Ti)(SiO)_3OH$---NH_3	$\nu_{asym}(NH)$	[32,38,39]
3296	Ti(IV)---NH_3	$\nu_{sym}(NH)$	[40–42]
3399	Ti(IV)---NH_3	$\nu_{asym}(NH)$	[40–42]
3335	Gas phase NH_3	$\nu_{sym}(NH)$	[32,38,39]
3444[1]	Gas phase NH_3	$\nu_{asym}(NH)$	[32,38,39]

[1] Probably superimposed to the broad band at 3399 cm^{-1}

In the hydroxyls stretching spectral region of Ti-MWW-HNO_3-calc sample, the formation of a transient band upon NH_3 desorption is observed (inset in Figure 5.3.4.6a), while it is not in sf-ITQ-1-calcA (inset in Figure 5.3.4.6c). The band is found at 3670 cm^{-1} and it is completely eroded at the end of the RT outgassing. Further studies are needed to clarify the nature of this band. In the NH_3 bending region, the band assigned to the asymmetric bending of NH_3 in interaction with the Ti(IV) Lewis acid sites is present. A peculiar absorption found at 1477 and 1483 cm^{-1} in Ti-MWW-HNO_3-calc and sf-ITQ-1-calcA respectively is detected upon NH_3 adsorption and was tentatively assigned to the bending mode of NH_4^+ cation (usually found in the 1500-1350 cm^{-1} range). [43–45] This signal is present independently on the presence or absence of Ti in the framework and it is completely eroded upon NH_3 outgassing at RT (contrarily to what occurs when NH_3 is protonated by strong Brønsted acid sites, as in H-ZSM-5). This spectral behavior was already reported for other heteroatom free zeolites.[25,32]

5.3.5. Study of the interaction with H_2O_2

The interaction among the Ti(IV) sites and the H_2O_2 was studied by means of UV-Vis-NIR in DR mode and by IR in transmission mode spectroscopies. The olive full curve in Figure 5.3.5.1 is the UV-Vis-NIR spectrum of Ti-MWW-HNO_3-calc. It is slightly different from the one shown in Figure 5.3.3.3 due to the presence of adsorbed H_2O molecules coming from the atmospheric moisture. The signals at 1900 and 1400 nm in the NIR region, assigned to combination and overtone modes of the H_2O molecule [46] are visible. When H_2O is coordinated to the Ti sites, the Ti coordination sphere is expanded and for this reason, a broadening and redshift of the LMCT absorption band is observed (the minimum shifts from 205 to 220 nm). [46]

When the powder is soaked with the H_2O_2 aqueous solution, a strong intensification of the signals ascribed to combination and overtone of the H_2O molecule, a further broadening of the LMCT band at 220 nm[39,47] and a lowering of the scattering baseline are observed (dark yellow full curve in Figure 5.3.5.1), due to the presence of liquid solution in the interparticle spaces. The interaction between the Ti sites and the H_2O_2 causes the formation of an evident shoulder, around 385 nm, assigned to the LMCT involving Ti, when a "side-on" peroxo ligand is coordinated to the Ti site (Ti-OO^- complex). This complex confers to the material the typical pale orange color. [46]

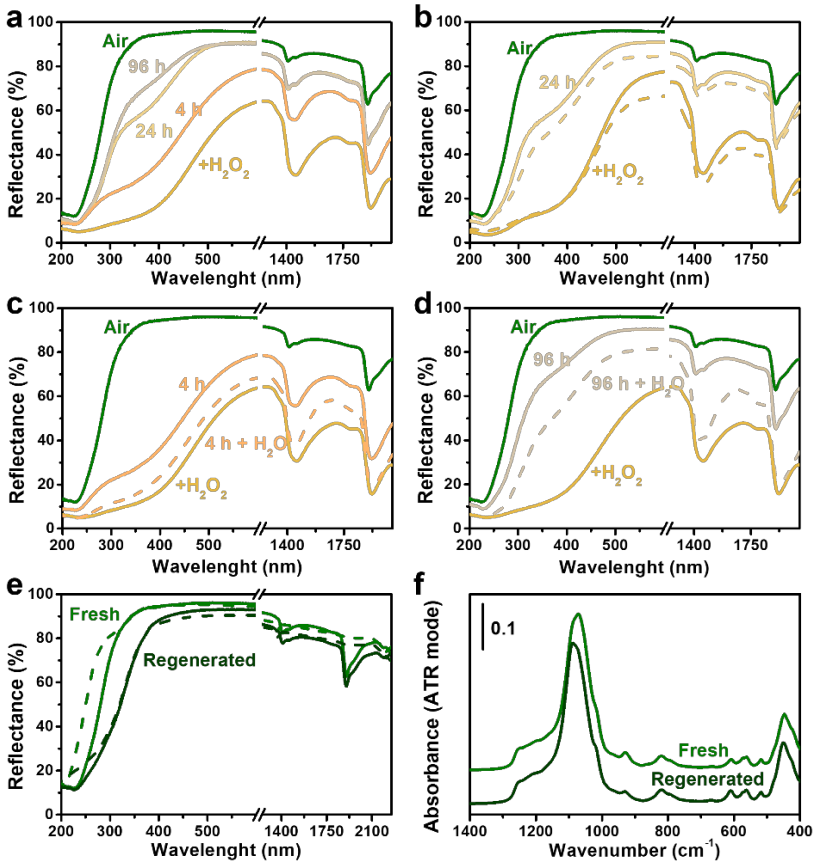

Figure 5.3.5.1. (a) UV-Vis-NIR spectra of Ti-MWW-HNO_3-calc in air (full olive), contacted with H_2O_2 (full dark yellow), dried for 4 h (full light salmon), for 24 h (full yellow) and for 96 h (full ocher). (b) UV-Vis-NIR spectra of Ti-MWW-HNO_3-calc in air (full olive), contacted with H_2O_2 (full dark yellow) dried for 24 h (full yellow), dried for 96 h (not shown, the same as in panel a), further contacted with H_2O_2 (dashed dark yellow) and further dried for 24 h (dashed yellow). (c) UV-Vis-NIR spectra of Ti-MWW-HNO_3-calc in air (full olive), contacted with H_2O_2 (full dark yellow), dried for 4 h (full light salmon) and further contacted with H_2O (dashed light salmon). (d) UV-Vis-NIR spectra of Ti-MWW-HNO_3-calc in air (full olive), contacted with H_2O_2 (full dark yellow), dried for 96 h (full ocher) and further contacted with H_2O (dashed ocher). (e) UV-Vis-NIR spectra of Ti-MWW-HNO_3-calc in air (full olive), after activation

(dashed olive) and regenerated by calcination after two cycles with H_2O_2 (namely after dashed yellow curve in panel b) in air (full dark olive) and after activation (dashed dark olive). (f) ATR-IR spectra of activated Ti-MWW-HNO_3-calc (full olive) and of the regenerated (the same as in panel e) (full dark olive).

Upon dehydration (drying), the stable Ti-hydroperoxo (Ti-OOH) complex forms, [46] following the equilibrium: $Ti-OOH+nH_2O \rightleftarrows [Ti-OO]^- + H_3O^+(H_2O)_{n-1}$. In Figure 5.3.5.1a the effect of drying the powder in air for different times is evident. The scattering baseline increases and approaches that of the fresh sample (from dark yellow to ocher curves), the intensity of the overtone and combination modes of H_2O decreases and the LMCT absorption band at 220 nm becomes less broad than that of the soaked sample. Figure 5.3.5.1b shows that the formation of the Ti-OO^- and Ti-OOH complexes is reversible. The powder dried for 96 h was contacted again with the H_2O_2 solution further dried for 24 h. The formation of the Ti-OO^- and Ti-OOH occurred in the same way as the first time.

The equilibrium between the Ti-OO^- and Ti-OOH complexes governed by the level of hydration can be influenced by the adding H_2O to the dried sample. Figures 5.3.5.1c and d shows the effect of contacting H_2O after 4 and 96 h of drying. The Ti-OO^- complex is formed again from the Ti-OOH complex when the powder is dried for 4 h but it is not after 96 h. The degradation in air of the Ti-OOH complexes after 96 h is probably too advanced to allow the formation of the Ti-OO^- species.

The comparison of the data collected in this work with literature data [46] suggests that the degradation in air of the Ti-OO^- and Ti-OOH complexes in Ti-MWW-HNO_3-calc occurs faster than what happens in TS-1. The Ti-OO^- and Ti-OOH complexes in Ti-MWW-HNO_3-calc seem to be more labile at RT and ambient pressure respect to that formed in TS-1. The Ti atoms in $Ti(OSi)_3OH$

species are less constrained and less bound to the framework respect to fully coordinated $Ti(OSi)_4$ species and consequently the formed complexes are less stable in time.

The regeneration of the sample was tested by calcining the sample contacted twice with H_2O_2 (namely dashed yellow curve in Figure 5.3.5.1b, further dried for 24 h). The TiO_2 content and speciation of the regenerated sample were determined by EDX, UV-Vis and ATR-IR spectroscopies (Figure 5.3.5.1e and f). The TiO_2 loading after regeneration was slightly lower than that of the fresh sample (2.35 wt% of TiO_2, σ=0.37, compared to 2.91 wt% of TiO_2, σ=0.52, respectively). The UV-Vis spectrum (dark olive full and dashed curves in Figure 5.3.5.1e) shows a broadened LMCT absorption band and the ATR-IR spectrum (dark olive curve in Figure 5.3.1f) shows a decrease of the band at 930 cm^{-1}, ascribed to Ti in framework positions. These facts indicate that a fraction of Ti has come out of the framework, forming extra-framework, probably amorphous species, but most of the Ti species are still in framework positions.

The interaction of H_2O_2 with Ti atoms in Ti-MWW-HNO_3-calc was also studied by *in situ* IR spectroscopy (Figure 5.3.5.2). H_2O_2 cannot be dosed in vapor phase, hence the use of IR spectroscopy is complicated by the presence of the excess of liquid H_2O_2 and H_2O upon soaking of the pellet. It was used because it allowed to observe *in situ* the formation of the reaction product, in the HPPO epoxidation reaction.[10] After soaking a pellet of Ti-MWW-HNO_3-calc with H_2O_2 aqueous solution, the excess of H_2O_2 and H_2O was rapidly outgassed (Figure 5.3.5.2a). The molecularly adsorbed H_2O must be removed, to avoid overlapping of the intense bending mode of H_2O at with the signals of propylene and propylene oxide. During the outgassing, the band assigned to the bending vibration of OH group of H_2O_2 shifts from 1360 to 1328 cm^{-1} and first increases and then decreases in intensity. This is an indication of the removal of the excess of H_2O_2. The spectra recorded during

the outgassing of the not soaked Ti-MWW-HNO_3-calc sample are reported in Figure 5.3.5.3 for reference. The stretching mode of the O-O group in H_2O_2 falls at 879 cm^{-1} and it is overlapped to the O-O stretching of Ti-OO^- and Ti-OOH complexes (Figure 5.3.5.2a). [48] In the framework vibration region in Figure 5.3.5.3, the growth of bands at 933 and 955 cm^{-1} is observed, the slight shift respect to the values of 930 and 965 cm^{-1} observed in Figure 5.3.3.3b being due to the presence of strongly adsorbed H_2O molecules that are not removed by outgassing at RT. When the same region is observed while outgassing the H_2O_2 aqueous solution (Figure 5.3.5.2a), a similar phenomenon occurs, but the signals are still slightly shifted, at 936 and 965 cm^{-1}, due to the formation of the Ti-OO^- and/or the Ti-OOH complexes.

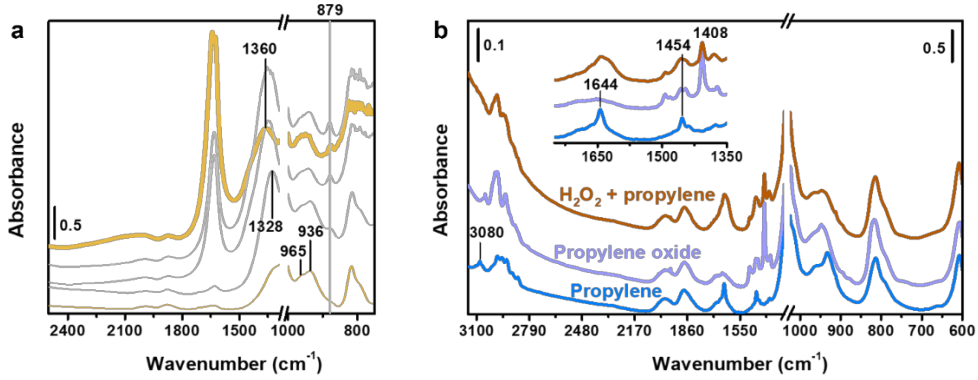

Figure 5.3.5.2. IR spectra in the 2500-600 cm^{-1} spectral range of (a) Ti-MWW-HNO_3-calc recorded after soaking the pellet with a H_2O_2/H_2O 30 wt% solution (bold dark yellow), during the outgassing of the H_2O_2/H_2O excess (top to bottom, grey to dark yellow). The spectra are vertically shifted for the sake of clarity. (b) IR spectrum recorded after 5 min from the dosing of 60 mbar of propylene on the H_2O_2 soaked/outgassed sample (light brown) and on the RT outgassed sample (blue) and after dosing propylene oxide on the RT outgassed sample (light purple); the spectra are vertically shifted for the sake of clarity.

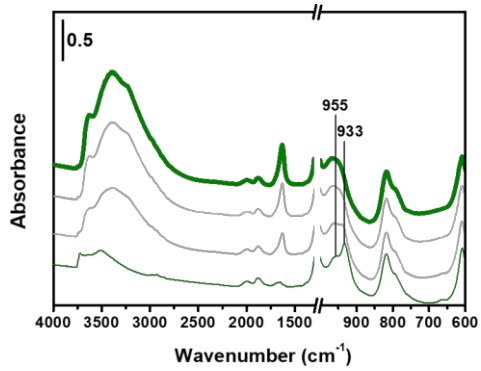

Figure 5.3.5.3. Transmission IR spectra of Ti-MWW-HNO_3-calc recorded during the outgassing at RT: progressive outgassing from top (bold olive) to bottom (olive). The spectra are vertically shifted for the sake of clarity.

The result of pure propylene dosage on the dark yellow spectrum in Figure 5.3.5.2a is showed in Figure 5.3.5.2b (light brown curve). The comparison with the reference spectra of pure propylene (blue) and pure propylene oxide (light purple) dosed on the RT outgassed sample free from H_2O_2 (namely the sample with the olive spectrum in Figure 5.3.5.3) revealed that the desired product is formed, according to the reaction $propylene + H_2O_2 \rightarrow propylene\ oxide + H_2O$. The sharp band at 1408 cm^{-1} [49] is assigned to a CH_3 deformation mode typical of propylene oxide. In propylene, the band due to the CH_3 deformation mode is found at 1454 cm^{-1}, [50] as highlighted in the inset of Figure 5.3.5.2b. The absence of the CH ν_{asym} of CH_2 vinyl groups of propylene at 3080 cm^{-1},[50] is considered an indication that after 5 min from the propylene dosage, all the available propylene reacted to give propylene oxide. The fate of the intense signal at 1644 cm^{-1} in the propylene spectrum, assigned to the C=C stretching vibration of the vinyl group [50] is difficult to foresee, due to the growth of the broad band due to the bending mode of H_2O molecules (the only by-product of the reaction). Similarly, the breathing mode of the epoxide ring (in the 1290-1235 cm^{-1} range) [49,50] is completely covered by the out-of-scale Si-O-Si ν_{asym}.

5.4. Conclusions and open questions

In this chapter, the synthesis of a Ti-MWW catalyst containing unprecedentedly high TiO_2 loadings, almost entirely in tetrahedral coordination, both $Ti(OSi)_4$ and $Ti(OSi)_3OH$ species, was performed (Ti-MWW-HNO_3-calc sample).

Under the synthetic point of view, the HNO_3 washing was shown to be the only responsible for the Ti insertion in framework positions and hence it is demonstrated to be an essential step of this synthesis procedure. The presence of potassium residues is observed when the HNO_3 washing was not performed and its presence seems to be related to the Ti speciation in the not acid washed Ti-MWW-calc sample, possibly forming potassium titanate species. The residues of potassium are due to the use of K_2CO_3 in the synthesis gel, whose use cannot be avoided. Actually, if a Ti source (TBOT) is added, the MWW framework is not able to crystallize in absence of K_2CO_3. This could be related to the variation of the autogenous pressure induced by the presence of butanol in the gel, produced upon hydrolysis of TBOT. Following what reported for the synthesis of an ITQ-1 sample using TEOS as Si source, the optimization of a procedure or evaporating the alcohol produced upon hydrolysis, is probably fundamental to improve the synthesis of the Ti-MWW, possibly removing the use of K_2CO_3 and hence the necessity of the HNO_3 washing. Many further studies are needed to explore this possibility. The removal of the acid washing from the synthesis procedure of the Ti-MWW can surely paved the way for a possible industrial applicability.

The use of IR spectroscopy in presence of targeted probe molecules allowed to reveal that the Lewis acidity of the Ti sites in Ti-MWW are stronger than the corresponding ones in TS-1, due to the prevalent presence of $Ti(OSi)_3OH$ in Ti-MWW. The study of the interaction of the Ti sites with H_2O_2 was performed by means of IR and UV-Vis spectroscopies. The Ti-OO^- and Ti-

OOH complexes formed on Ti-MWW appear to be more labile than in TS-1, their formation is reversible and after two cycles of contact with H_2O_2, the sample can be regenerated with only a slight leaching of framework Ti species.

5.5. References

1 H. Xu, Y. Guan, X. Lu, J. Yin, X. Li, D. Zhou and P. Wu, *ACS Catal.*, 2020, **10**, 4813–4819.

2 S. Bordiga, I. Roggero, P. Ugliengo, A. Zecchina, V. Bolis, G. Artioli, R. Buzzoni, G. Marra, F. Rivetti, G. Spano and C. Lamberti, *J. Chem. Soc., Dalton Trans.* 2000, 3921–3929.

3 A. Zecchina, S. Bordiga, G. Spoto, L. Marchese, G. Petrini, G. Leofanti and M. Padovan, *J. Phys. Chem.* 1992, **96**, 4985–4990.

4 F. Bonino, A. Damin, S. Bordiga, C. Lamberti and A. Zecchina, *Langmuir*, 2003, **19**, 2155–2161.

5 S. Bordiga, A. Damin, F. Bonino, G. Ricchiardi, A. Zecchina, R. Tagliapietra and C. Lamberti, *Phys. Chem. Chem. Phys.* 2003, **5**, 4390–4393.

6 M. A. Camblor, A. Corma, M. J. Díaz-Cabañas and C. Baerlocher, *J. Phys. Chem. B*, 1998, **102**, 44–51.

7 M. E. Leonowicz, J. A. Lawton, S. L. Lawton and M. K. Rubin, *Science*, 1994, **264**, 1910–1913.

8 C. H. L. Tempelman, M. T. Portilla, M. E. Martínez-Armero, B. Mezari, N. G. R. De Caluwé, C. Martínez and E. J. M. Hensen, *Microporous Mesoporous Mater.* 2016, **220**, 28–38.

9 M. Fabbiani, A. Morsli, G. Confalonieri, T. Cacciaguerra, F. Fajula, J. Haines, A. Benguedach, R. Arletti and F. Di Renzo, *Microporous Mesoporous Mater.* 2022, **332**, 111678–111685.

10 M. Signorile, V. Crocellà, A. Damin, B. Rossi, C. Lamberti, F. Bonino and S. Bordiga, *J. Phys. Chem. C*, 2018, **122**, 9021–9034.

11 S. Bordiga, P. Ugliengo, A. Damin, C. Lamberti, G. Spoto, A. Zecchina, G. Spanò, R. Buzzoni, L. Dalloro and F. Rivetti, *Top. Catal.* 2001, **15**, 43–52.

12 F. Pascale, P. Ugliengo, B. Civalleri, R. Orlando, P. D'Arco and R. Dovesi, *J. Chem. Phys.* 2002, **117**, 5337–5346.

13 G. Bellussi, A. Carati, M. G. Clerici, G. Maddinelli and R. Millini, *J. Catal.* 1992, **133**, 220–230.

14 R. Millini, E. P. Massara, G. Perego and G. Bellussi, *J. Catal.* 1992, **137**, 497–503.

15 D. Lin, Q. Zhang, Z. Qin, Q. Li, X. Feng, Z. Song, Z. Cai, Y. Liu, X. Chen, D. Chen, S. Mintova and C. Yang, *Angew. Chem. Int. Ed.* 2021, **60**, 3443–3448.

16 A. Thangaraj, M. J. Eapen, S. Sivasanker and P. Ratnasamy, *Zeolites*, 1992, **12**, 943–950.

17 J. Xing, D. Yuan, H. Liu, Y. Tong, Y. Xu and Z. Liu, *J. Mater. Chem. A Mater.* 2021, **9**, 6205–6213.

18 M. Tamura, W. Chaikittisilp, T. Yokoi and T. Okubo, *Microporous Mesoporous Mater.* 2008, **112**, 202–210.

19 Q. Guo, Z. Feng, G. Li, F. Fan and C. Li, *J. Phys. Chem. C*, 2013, **117**, 2844–2848.

20 Z. Shan, Z. Lu, L. Wang, C. Zhou, L. Ren, L. Zhang, X. Meng, S. Ma and F.-S. Xiao, *ChemCatChem*, 2010, **2**, 407–412.

21 F. Rosso, A. Rizzetto, A. Airi, K. Khoma, M. Signorile, V. Crocellà, S. Bordiga, S. Galliano, C. Barolo, E. Alladio and F. Bonino, *Inorg. Chem. Front.* 2022, 9, 3372–3383.

22 L. Wu, Z. Tang, Y. Yu, X. Yao, W. Liu, L. Li, B. Yan, Y. Liu and M. He, *Chem. Comm.* 2018, **54**, 6384–6387.

23 M. Signorile, L. Braglia, V. Crocellà, P. Torelli, E. Groppo, G. Ricchiardi, S. Bordiga and F. Bonino, *Angew. Chem. Int. Ed.* 2020, **59**, 18145–18150.

24 D. Scarano, A. Zecchina, S. Bordiga, F. Geobaldo, G. Spoto, G. Petrini, G. Leofanti, M. Padovan and G. Tozzola, *J. Chem. Soc., Faraday Trans.* 1993, **89**, 4123–4130.

25 E. Astorino, J. B. Peri, R. J. Willey and G. Busca, *J. Catal.* 1995, **157**, 482–500.

26 Y. Liu, F. Wang, X. Zhang, Q. Zhang, Y. Zhai, G. Lv, M. Li and M. Li, *Microporous Mesoporous Mater.* 2022, **331**, 111676.

27 S. Bordiga, C. Lamberti, F. Bonino, A. Travert and F. Thibault-Starzyk, *Chem. Soc. Rev.* 2015, **44**, 7262–7341.

28 T. Blasco, M. A. Camblor, A. Corma, P. Esteve, J. M. Guil, A. Martínez, J. A. Perdigón-Melón and S. Valencia, *J. Phys. Chem. B*, 1998, **102**, 75–88.

29 E. A. Eilertsen, S. Bordiga, C. Lamberti, A. Damin, F. Bonino, B. Arstad, S. Svelle, U. Olsbye and K. P. Lillerud, *ChemCatChem*, 2011, **3**, 1869–1871.

30 P. Wu, T. Tatsumi, T. Komatsu and T. Yashima, *J. Phys. Chem. B*, 2001, **105**, 2897–2905.

31 T. Blasco, A. Corma, T. Navarro and J. P. Pariente, *J. Catal.* 1995, **156**, 65–74.

32 E. Gianotti, V. Dellarocca, L. Marchese, G. Martra, S. Coluccia and T. Maschmeyer, *Phys. Chem. Chem. Phys.* 2002, **4**, 6109–6115.

33 G. Busca, *Microporous Mesoporous Mater.* 2017, **254**, 3–16.

34 Y. Yu, Z. Tang, J. Wang, R. Wang, Z. Chen, H. Liu, K. Shen, X. Huang, Y. Liu and M. He, *J. Catal.* 2020, **381**, 96–107.

35 A. Airi, M. Signorile, F. Bonino, P. Quagliotto, S. Bordiga, J. A. Martens and V. Crocellà, *ACS Appl. Mater. Interfaces*, 2021, **13**, 49114–49127.

36 R. Buzzoni, S. Bordiga, G. Ricchiardi, C. Lamberti, A. Zecchina and G. Bellussi, *Langmuir*, 1996, **12**, 930–940.

37 C. Morterra, G. Cerrato, M. Visca and D. M. Lenti, *Chem. Mater.* 1991, **3**, 132–142.

38 V. Bolis, S. Bordiga, C. Lamberti, A. Zecchina, A. Carati, F. Rivetti, G. Spanò and G. Petrini, *Microporous and Mesoporous Materials*, 1999, **30**, 67–76.

39 S. Bordiga, A. Damin, F. Bonino, A. Zecchina, G. Spanò, F. Rivetti, V. Bolis, C. Prestipino and C. Lamberti, *J. Phys. Chem. B*, 2002, **106**, 9892–9905.

40 S. Bordiga, A. Damin, F. Bonino, A. Zecchina, G. Spanò, F. Rivetti, V. Bolis, C. Prestipino and C. Lamberti, *J. Phys. Chem. B*, 2002, **106**, 9892–9905.

41 V. Bolis, S. Bordiga, C. Lamberti, A. Zecchina, A. Carati, F. Rivetti, G. Spanò and G. Petrini, *Langmuir*, 1999, **15**, 5753–5764.

42 E. Gianotti, V. Dellarocca, L. Marchese, G. Martra, S. Coluccia and T. Maschmeyer, *Phys. Chem. Chem. Phys.* 2002, **4**, 6109–6115.

43 A. Zecchina, L. Marchese, S. Bordiga, C. Pazè and E. Gianotti, *J. Phys. Chem. B*, 1997, **101**, 10128–10135.

44 F. Giordanino, E. Borfecchia, K. A. Lomachenko, A. Lazzarini, G. Agostini, E. Gallo, A. V Soldatov, P. Beato, S. Bordiga and C. Lamberti, *J. Phys. Chem. Letters*, 2014, **5**, 1552–1559.

45 J. Datka and K. Góra-Marek, *Catal. Today*, 2006, **114**, 205–210.

46 F. Bonino, A. Damin, G. Ricchiardi, M. Ricci, G. Spanò, R. D'Aloisio, A. Zecchina, C. Lamberti, C. Prestipino and S. Bordiga, *J. Phys. Chem. B*, 2004, **108**, 3573–3583.

47 M. Signorile, A. Damin, F. Bonino, V. Crocellà, C. Lamberti and S. Bordiga, *J. Comput. Chem*. 2016, **37**, 2659–2666.

48 G. Tozzola, M. A. Mantegazza, G. Ranghino, G. Petrini, S. Bordiga, G. Ricchiardi, C. Lamberti, R. Zulian and A. Zecchina, *J. Catal.* 1998, **179**, 64–71.

49 R. L. Hudson, M. J. Loeffler and K. M. Yocum, *Astrophys. J.* 2017, **835**, 225.

50 N. B. Colthup, L. H. Daly and S. E. Wiberley, in *Introduction to Infrared and Raman Spectroscopy*, Elsevier, 1990, pp. 327–337.

6. CONCLUSIONS

This thesis work was focused on the synthesis and characterization of Ti-containing and purely siliceous zeolitic materials. In particular, the objective was the study of the synthesis of Ti-zeolites. First, the synthesis of the TS-1, with MFI framework, was optimized exploiting the DoE approach, to get familiar with the Ti chemistry in the zeolite synthesis. Then, the attention was moved to the synthesis of another framework, the MWW. Purely siliceous zeolite with MWW framework (the ITQ-1) and the Ti-containing analogous (Ti-MWW) were prepared and characterized. The MWW framework was chosen as promising alternative to TS-1, thanks to its potential application in the partial oxidation of bulky alkenes. The ITQ-1 was synthesized with different procedures and the effect of the calcination conditions was evaluated. The synthesis of Ti-MWW was also reproduced from the literature and the properties of the Ti sites in the obtained sample were examined. Separated conclusions and perspective are reported for each topic, but some cross-sectoral conclusions can be drawn.

The choice of the T atom source turned out to be relevant in the successful outcome of a synthesis. The modification of the Ti source from the TBOT to the TEOT, in Chapter 3, allowed to reach a complete hydrolysis of the Ti source in every synthesis condition, increasing sensibly the TiO_2 loading of the samples.[1] Moreover, it was shown that the best results can be obtained when a coherent coupling of the sources is implemented: when TEOS, TBOT and iPrOH were used for the separate hydrolysis, the formation of different and mixed Ti and Si alkoxides complicated the system under investigation, and it made it difficult to rationalize. Hence, the use of TEOT and EtOH with TEOS is preferred to avoid the *in situ* formation of mixed alkoxides, and actually gave the best results. On the MWW side, the synthesis of ITQ-1 is shown to be successful when Aerosil® 200 is used[2] and mostly unsuccessful

when TEOS is used as Si source, surely due to differences in the kinetic of nucleation.

The role of the OSDA used in the syntheses of both the MFI and the MWW samples was not analyzed in detail throughout the thesis, but a consideration can be done. Taking into account the classification of the OSDAs proposed by Davies and Lobo (paragraph 1.3.3), the TPAOH belongs to the second group, "structure-directing agent", since it is able to direct specifically the formation of the MFI framework. The HMI and the TMAdaOH in the MWW framework are instead "space fillers". Actually, zeolites with MWW framework were synthesized also using other cyclic amines as OSDA and the TMAdaOH is used to prepare also other zeolitic frameworks. The lower ability of directions of the OSDAs used for the MWW framework strongly reduced the possibility of adjusting the properties of the materials by modification of the crystallization conditions. Literature procedures for preparing highly siliceous MWW zeolites always indicate 150 °C for at least 3 days in tumbling conditions to crystallize the material. On the other side, the synthesis of TS-1 is reported in literature to occur in a wider range of conditions, from around 140 to 210 °C, in a time range comprised between few hours to 10 days. In this work, TS-1 was synthesized even at 110 °C. This is an important point that should be taken into account when the synthesis of a Ti-zeolite is involved, because the presence of Ti does not support the crystallization of the framework, due to its too large atomic radius. A strong directing power from the side of the OSDA would dictate a big advantage in the successful crystallization of a Ti-zeolite.

In this work attention was also paid to the post-synthesis treatments of the samples. The calcination procedure is shown to be important in the preparation of Ti-zeolites because the used conditions can negatively affect the speciation of Ti. The combustion of the OSDA gave H_2O and CO_2 as products. If alkaline metals are deposited on the sample during the washing

step of the synthesis, during the calcination, the heating in presence of alkaline metals and H_2O is able to extract Ti atoms from framework positions yielding alkaline metal titanate species. On the other side, when zeolites with MWW framework are involved, the calcination was shown to have an impact on the defectivity of the samples.[2] The other used post-synthesis treatment is the HNO_3 washing applied to the Ti-MWW sample.[3] It is demonstrated to have a dual function. It partially removed the OSDA from the framework, reducing the amount of OSDAs that must be eliminated through calcination and hence making the calcination more effective.[3] Moreover, the acid treatment eliminates the K present on the material, encouraging the Ti insertion in framework positions.[3] It would be interesting to see if an analoguous behavior is also observed when a TS-1 sample containing Ti species with intermediate coordination is washed with HNO_3.

6.1. References

1 F. Rosso, A. Rizzetto, A. Airi, K. Khoma, M. Signorile, V. Crocellà, S. Bordiga, S. Galliano, C. Barolo, E. Alladio and F. Bonino, *Inorg. Chem. Front.* 2022, 9, 3372–3383.

2 F. Rosso, A. Airi, M. Signorile, E. Dib, S. Bordiga, V. Crocellà, S. Mintova and F. Bonino, *Microporous Mesoporous Mater.* 2024, **366**, 112924.

3 F. Rosso, A. Airi, M. Signorile, S. Bordiga, V. Crocellà, F. Bonino, submitted to the Special Collection "Oxygen Activation and Oxidation Catalysis" that will be published jointly in *ChemCatChem* and the *European Journal of Inorganic Chemistry* (*EurJIC*).

Acknowledgements

During my PhD project I had the honor of meeting many people, all of them extraordinary. The work and the preparation of this thesis would not have been possible without all of them.

I would like to express my sincere gratitude to my supervisor Francesca for all her scientific and professional teaching and for her invaluable personal guidance. I would like to extend my thanks to Alessia, Valentina, Matteo and Silvia for their support and for the fruitful discussion.

My sincere thanks go also to Prof. Svetlana Mintova and Dr. Eddy Dib, who welcomed me in their beautiful city and taught me so much in such a short time.

My thanks go to Sauro Passeri and Matteo Dellapasqua from CFS Camlin company for the fruitful discussion and for the ongoing catalytic tests.

A special thank goes to Andrea Rizzetto, Laura Gastaudo and Andrea Lugas because their master's thesis work helped me to develop my own project. Working with you has made me better under the professional and personal point of view.

Finally, my dearest and heartfelt thanks go to all the past and present colleagues and friends from Via Quarello and Via Giuria. You made me feel part of a family.

I acknowledge support from the Project CH4.0 under the MUR program "Dipartimenti di Eccellenza 2023-2027" (CUP: D13C22003520001).

Appendix A

Table A1. LMCT onsets and integrated areas of the 960 cm^{-1} band of the ATR-IR spectra of TS-1 samples belonging to DoE 1.

Sample	LMCT onset (nm)	960 cm^{-1} area (cm^{-1})
R1-a	340	0.22
R2-a	322	0.23
R3-a	316	0.26
R1-b	328	0.21
R2-b	330	0.20
R3-b	333	0.22
N1	341	0.16
N2	314	0.12
N3	312	0.10
N4	309	0.11
N5	332	0.31
N6	353	0.30
N7	341	0.27
N8	368	0.35
N9	365	0.34
N10	335	0.29
N11	367	0.32
N12	370	0.35
N13	337	0.33

Table A2. LMCT onsets and integrated areas of the 960 cm^{-1} band of the ATR-IR spectra of TS-1 LL, LH, HL and HH samples.

Sample	LMCT onset (nm)	960 cm^{-1} area (cm^{-1})
LL	338	0.40
LH	341	0.28
HL	334	0.35
HH	339	0.36

Table A3. LMCT onsets and integrated areas of the 960 cm^{-1} band of the ATR-IR spectra of TS-1 samples belonging to DoE 2.

Sample	LMCT onset (nm)	960 cm^{-1} area (cm^{-1})
R1	358	0.69
R2	361	0.73
R3	352	0.71
N1	355	0.37
N2	335	0.37
N3	357	0.61
N4	367	0.73
N5	358	0.55
N6	354	0.53
N7	370	0.53
N8	377	1.03
N9	373	0.73
N10	349	0.38

Appendix B

Appendix B contains the papers published during the PhD, related to the topic of the project.

Volume 9 | Number 14 | 21 July 2022

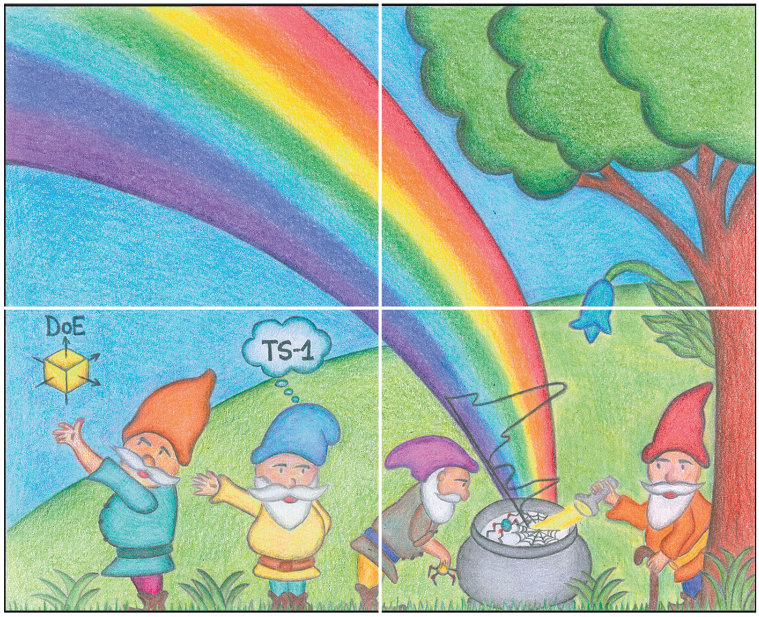

INORGANIC CHEMISTRY

FRONTIERS

CCS 中国化学会 CHINESE CHEMICAL SOCIETY
PEKING UNIVERSITY 1898
ROYAL SOCIETY OF CHEMISTRY
rsc.li/frontiers-inorganic

INORGANIC CHEMISTRY
FRONTIERS

RESEARCH ARTICLE

View Article Online
View Journal | View Issue

Cite this: *Inorg. Chem. Front.*, 2022, **9**, 3372

Rationalization of TS-1 synthesis through the design of experiments†

Francesca Rosso, Andrea Rizzetto, ‡ Alessia Airi, Khrystyna Khoma, ‡ Matteo Signorile, Valentina Crocellà, Silvia Bordiga, Simone Galliano, Claudia Barolo, Eugenio Alladio * and Francesca Bonino *

Received 28th March 2022,
Accepted 29th April 2022

DOI: 10.1039/d2qi00643j

rsc.li/frontiers-inorganic

Titanium Silicalite-1 (TS-1) is a zeolite used as a catalyst in partial oxidation reactions, whose synthesis is often performed under hydrothermal conditions by exploiting alkoxides as Ti and Si precursors. A rational study of the synthesis procedure of TS-1 using the experimental design approach was performed. Seven variables (*i.e.* times and temperatures of the various synthesis steps) were explored, by fixing the reagents ratio to establish which of them could affect the Ti incorporation and speciation. The syntheses were chosen following a D-optimal experimental design strategy, and each variable was explored at two levels and one center point. The responses monitored were: the yield of the synthesis; the total Ti content of the catalyst; the wavelength for the onset of the Ligand-to-Metal Charge Transfer (LMCT) transition involving Ti; and the vibrational fingerprint of tetrahedral Ti (centred at 960 cm^{-1} in the IR spectra). It was found that a few variables affect the Ti content and speciation (time and temperature of the hydrothermal treatment and the time of hydrolysis of the Ti precursor), whereas the yield is determined by the time of crystallization.

Introduction

Zeolites are crystalline microporous (alumino)silicates that can have both natural and synthetic origin. The most used procedure to synthesize zeolites is the hydrothermal treatment inside autoclaves or digestors, which aims at emulating the conditions occurring during their natural formation (burial metamorphic environments, saline alkaline lakes, geothermal environments, *etc.*).[1] Si- and metal-alkoxides are commonly used as the elemental source, and the synthetic procedure is usually based on three steps: (i) hydrolysis of the alkoxides; (ii) aging, possibly in the presence of an Organic Structure Directing Agent (OSDA), when the polymerization and the nucleation begin; and (iii) the hydrothermal crystallization step.[2] The conditions used in each step may affect the thermodynamics and the kinetics of the zeolite formation; therefore, many efforts were devoted to study the zeolite crystallization mechanism under hydrothermal conditions,[3–7] and particular attention was delivered to the synthesis of highly or purely siliceous materials.[8–14]

In most of the cases the optimization of the zeolite synthetic procedure is still carried on by the trial-and-error process; this procedure may sometimes lead to outstanding results, but its success is mainly based on serendipity and/or the personal experience of the synthesizer, and therefore it is complex to teach or transfer to other experimenters. Moreover, many attempts to rationalise the zeolite syntheses are done by the One-Variable-At-Time method (OVAT), which is often far from reality, especially when the system under investigation is complex as the formation of a zeolite is.

The multiple conditions adopted in each synthesis step can individually influence the final material, and the singular effects are, in most cases, hardly distinguishable. The determination of the factors affecting the synthesis of zeolites is a very challenging issue, since the investigation of the final result of the synthesis leads to the overlap of all the effects. For this purpose, many literature studies involve the interruption of the synthesis for the characterization of every step product,[15,16] but this procedure may strongly modify the material itself. The modification is unavoidable when studying the hydrothermal treatment because the step-by-step analysis implies the quenching of the autoclaves for separating the intermediate material during the crystal formation. On the contrary, the most interesting results in the study of the crystallization mechanism were obtained without isolating the intermediates

Department of Chemistry, NIS and INSTM Reference Centre, Università di Torino, Via G. Quarello 15, 10135 and Via P. Giuria 7, 10125, Torino, Italy.
E-mail: eugenio.alladio@unito.it, francesca.bonino@unito.it

†Electronic supplementary information (ESI) available. See DOI: https://doi.org/10.1039/d2qi00643j

‡Present address: Department of Applied Sciences and Technology, Politecnico di Torino, Corso Duca degli Abruzzi 24, 10129, Torino, Italy

from the autoclaves, by studying colloidal systems[17–19] and by *in situ* studies of the crystallization.[20] For this reason, the development of non-invasive and easily applicable techniques to study the zeolite synthesis and the parameters affecting their formation, avoiding the separation of intermediates, is needed.

Despite the importance of the fundamental understanding of the crystallization mechanism of zeolites, it is often difficult to correlate its results with practical indications that can be used to improve the synthetic method, and when a new catalyst has to be designed, a (semi)empirical optimization step is always required.

An approach that could overcome both these issues is the use of the Design of Experiments (DoE)[21,22] and the Multivariate Data Analysis (MDA).[23,24] The DoE is a way to plan and conduct experiments to extract the maximum amount of information from the data collected, even in the presence of noise. It can screen the influence of the experimental variables and their interactions on the result and/or optimize a procedure. The DoE approach was already used to study the synthesis of zeolites, both to explore all the frameworks that can be obtained in a broad range of conditions[25–27] and to optimize the synthesis conditions for an already discovered material, in a smaller range of variables.[28–32] Nevertheless, it was never applied to the synthesis of Titanium Silicalite-1 (TS-1), a zeolite whose preparation features many synthetic difficulties, still not unequivocally clarified, beyond the wide literature on the field.[33–43] The possibility to control and direct the speciation of Ti(IV) represents the most challenging aspect in the TS-1 synthesis and, at the same time, the most relevant feature for the catalyst, since the coordination of the Ti(IV) centres in the TS-1 framework directly influences the catalytic properties of the material. The introduction of heteroatoms in highly or purely siliceous frameworks allows obtaining functional materials with tuneable catalytic properties and, in particular, the isomorphous substitution of Si by Ti into a purely siliceous framework produces a material able to catalyse partial oxidation reactions under mild conditions, using hydrogen peroxide (H_2O_2) as the oxidizing agent.[44–50,33,34] The TS-1 was originally patented by Taramasso *et al.* in 1983. It presents the MFI framework of Silicalite-1 in which a little percentage of Ti(IV) cations partially replaces Si.[33] Afterwards, TS-1 has been successfully used at an industrial scale to produce, *e.g.*, pyrocatechol and hydroquinone from phenol and cresols from toluene.[51] Epoxidation reactions of propylene and bulkier olefines to produce epoxides were also extensively studied, both at an academic and at an industrial scale.[45–50,52–55] The applicability of TS-1 as partial oxidation catalyst is strictly dependent on the steric limitations imposed by the dimensions of the MFI pores, that imply diffusional constrictions to bulky substrates and easy deactivation of the catalyst by coke formation. The efforts devoted in trying to resolve the diffusional problems are various, some examples are the hierarchization of TS-1,[56,46,47] the production of nanosized TS-1[57,58] or the formation of hollows into bulk TS-1.[59,60] These and other attempts to modify the TS-1 for varying its catalytic properties are reported in Scheme S1.†

On the other hand, the activity of the TS-1 is determined by the nature of the active site represented by the framework Ti(IV) centres and it is affected by the not optimal Ti coordination. The activity of TS-1 in presence of H_2O_2 depends on the geometry of the interaction of the Ti(IV) site with H_2O_2. When tetrahedral Ti is involved, Ti-peroxo or Ti-hydroperoxo active species are formed upon adsorption of a H_2O_2 molecule and hydrolysis of a Ti–O–Si bond.[45,53–55] When Ti sites present distorted coordination from tetra- to octahedral, the different interaction with H_2O_2 may lead to a different catalytic cycle and the catalytic activity of these sites is hardly debated.[61,49,50] For this reason, their formation should be avoided during synthesis to improve the control over the catalytic process.

The efforts made to improve the Ti insertion and speciation are aimed at avoiding the formation of the less active bulk titanium dioxide (TiO_2). The patented TS-1 synthetic procedure involves the hydrolysis of Si and Ti alkoxides (the tetraethylorthosilicate, TEOS, and the tetraethylorthotitanate, TEOT, respectively), followed by the crystallization in an aqueous solution of tetrapropylammonium hydroxide (TPAOH) as OSDA. This synthesis should produce a zeolite in which some Si atoms are isomorphously substituted by Ti ones, in tetrahedral coordination. Nevertheless, real samples often deviate from this sharp definition, presenting Ti(IV) species at coordination different from the tetrahedral one. The commonly adopted syntheses suffer from a poor control over the correct insertion of Ti into the framework (leading to a lower and/or not optimized catalytic activity) and from a low reproducibility of the products. The critical analysis of the literature[37–44,62–64,35,36] on the topic shows that the precise influence of the Ti and Si sources and other synthetic parameters on the Ti(IV) insertion and speciation is still unclear and that no attention is usually paid on the control of accidental seeding occurring inside the Teflon liners. These parameters seem to be hardly operator dependent. The general rule about the alkoxide hydrolysis is that the hydrolysis rate of the alkoxides increases upon decreasing the length of the organic chain and the hydrolysis of the transition metals alkoxides is always faster than that of non-metallic elements, due to their electronic vacancies.[65] As a consequence, the precipitation of the more stable TiO_2 instead of the formation of the less stable tetrahedral coordinated Ti is favoured by the TEOT hydrolysis being much faster than TEOS one and by the approaching of the intrinsic incorporation limit of ≈2.7 wt% TiO_2 for tetrahedral Ti in the MFI framework.[62] To overcome, at least partially, this issue, TEOT was progressively substituted at a laboratory scale by Ti alkoxides with longer organic chains,[65] such as tetrapropylorthotitanate (TPOT) or tetrabutylorthotitanate (TBOT). Nevertheless, this strategy is insufficient to completely avoid the TiO_2 formation.[36–38] To further surmount this problem, some research focused on the use of additives, called crystallization mediating agents, coupled with the use of TBOT. Among them, it is worth mentioning: (i) H_2O_2,[39–41,66] as already suggested in the original patent,[33] which coordinates to Ti and forms water-soluble complexes, thus avoiding the precipitation of TiO_2; (ii) isopropyl alcohol

(IPA),[42,36,41] as solvent for the Ti alkoxide hydrolysis, which slows its hydrolysis and physically separates the TiO_4^{4-} hydrolysed units; and (iii) ammonium carbonate ($(NH_4)_2CO_3$),[43,35] which buffers the increasing pH during TEOS hydrolysis and favours the gelation of the solution.

In particular, the hydrolysis of TBOT in IPA is a widely used approach,[39,41,36,37] but the published results regarding Ti incorporation and speciation obtained are contrasting,[36,62–64] and it is hardly distinguishable if a specific "good result" arises from the overall synthetic procedure or the use of IPA as crystallization mediating agent. For this reason, the study with the DoE approach of the TS-1 synthesis by TBOT hydrolysis in IPA may help to shed light on the incorporation of Ti into the MFI framework with this synthetic strategy. The parameters of all the steps of the synthesis were explored, using the DoE approach and the work was supported by the MDA on the obtained results. An accurate evaluation of the reproducibility of the synthetic procedure and the control over the accidental seeding inside the liners, by hydrofluoric acid (HF) washings, was also performed.

Consequently, we present herein a rational study of the TS-1 synthesis, where the separate hydrolysis of TEOS (in the aqueous solution of the OSDA) and TBOT (in IPA at low temperature) were employed and where the times and temperatures of hydrolysis, aging and hydrothermal crystallization were explored with a D-optimal design. Besides the yield of the synthesized materials, the Ti content and speciation, using a multi-technique approach, were evaluated. These outcomes were then used as responses for the DoE,[22] fitted with the Partial Least Squares (PLS)[67] method and further explored by the Principal Component Analysis (PCA)[24] in order to identify trends and correlations among the synthetic conditions and the properties of the obtained catalysts. Moreover, significant and insignificant effects were discerned thanks to a careful evaluation of the experimental variability by repeating the same synthesis several times (for reproducibility assessment). The catalytic activity of the samples was not evaluated, since it falls out of the scope of the present work and it calls for a dedicated study. In this work, the total Ti amount was determined by Energy Dispersive X-rays spectroscopy (EDX), the tetrahedral Ti content was evaluated by the integrated area of 960 cm^{-1} signal in the infrared (IR) spectra[69,45,68] and the presence of Ti species of coordination different from the tetrahedral one was determined using the onset wavelength for the Ligand to Metal Charge Transfer (LMCT) electronic transition associated to Ti, in the ultraviolet (UV) range.[71,45,70]

Experimental

Chemicals

For the TS-1 syntheses, tetraethylorthosilicate (TEOS, reagent grade 98%, from Sigma Aldrich), tetrabutylorthotitanate (TBOT, reagent grade 97% from Sigma Aldrich), tetrapropylammonium hydroxide solution (TPAOH, 1.0 M in H_2O from Sigma Aldrich), isopropyl alcohol (IPA, ACS reagent, ≥99.8% from Sigma Aldrich) and Milli-Q water (18.2 MΩ cm^{-1}) were used. All the reagents were used without further purification.

Synthesis of TS-1 samples

Synthesis procedure. Six reproduced samples and thirteen DoE samples were prepared using a fixed stoichiometry (1 SiO_2 : 0.014 TiO_2 : 0.27 TPAOH : 2 IPA : 4 EtOH : 0.056 BuOH 40.5 H_2O) and varying the times (t) and temperatures (T) of the different steps of the synthesis.

In a typical procedure: (i) Solution A was prepared by adding 6.25 g of TEOS dropwise to 8.20 g of TPAOH diluted in 15.33 g of Milli-Q water; this solution was hydrolysed at a temperature T(H-TEOS) for a time t(H-TEOS) under reflux conditions. Solution B was prepared by adding 0.15 g of TBOT dropwise to 3.06 g of IPA and it was hydrolysed at 0 °C for a time t(H-TBOT). (ii) At the end of both the hydrolysis, solution A was cooled down to 0 °C and added dropwise to solution B under vigorous stirring; the resultant was aged at a temperature T(A) for a time t(A) under reflux conditions for gelification. (iii) The gel was crystallized at a temperature T(Cry) for a time t(Cry) in a Teflon lined stainless steel digestor of 45 ml volume, under static conditions.

At the end of the crystallization, each sample was recovered by centrifugation, washed with abundant deionized water and dried at 60 °C for 24 h. The resulting powder was then calcined in air at 550 °C for 7 h, under static conditions in a muffle furnace. After each use, the liners were washed with HF to avoid accidental seeding. Alcohols (*i.e.* ethanol (EtOH) from TEOS hydrolysis, butanol (BuOH) from TBOT hydrolysis and IPA) elimination from the synthesis mixture was avoided, since the separation by rotary evaporation resulted scarcely reproducible and did not allow for the precise control of the stoichiometry of the synthesis. Table S1† summarises the conditions used for all the synthesized samples.

Reproducibility assessment. The reproducibility of this procedure was assessed by repeating three times the same synthesis, before (Ei-a samples,) and after (Ei-b,) all the DoE set of samples, for verifying the absence of any uncontrolled variables influencing the results, such as the aging of the reagents.

D-optimal design. The DoE was used to simultaneously screen the effect of the seven variables on the Ti insertion and speciation. The samples were selected following a D-optimal design at two levels, composed of 9 syntheses (N1–N9 samples) and a centre point (N10). The syntheses N11–N13 were added to the set of DoE samples, since the conditions used are included in the experimental domain. The levels used for each variable are reported in Table 1, and the list of the syntheses and the levels used for each synthesis is reported in Table 2.

TS-1 characterization

A brief description on the methodologies used to obtain the responses adopted in DoE follows. Full details are available in the Section S2 of the ESI.†

Table 1 High (+1), intermediate (0) and low (−1) levels used for each variable

Name	+1	0	−1
t(H-TEOS)[a] (h)	24	14	4
t(H-TBOT)[b] (h)	24	14	4
T(H-TEOS)[c] (°C)	60	40	20
t(A)[d] (h)	48	36	24
T(A)[e] (°C)	60	40	20
t(Cry)[f] (h)	168	96	24
T(Cry)[g] (°C)	170	140	110

[a] t(H-TEOS): TEOS hydrolysis time. [b] t(H-TBOT): TBOT hydrolysis time. [c] T(H-TEOS): TEOS hydrolysis temperature. [d] t(A): Aging time. [e] T(A): Aging temperature. [f] t(Cry): Crystallization time. [g] T(Cry): Crystallization temperature.

Yield and crystallinity. The yield (%) of the calcined materials was used as a response for the DoE. X-Rays Diffraction (XRD) patterns were collected on the as-synthesized samples with a Cu Kα radiation on a PANalytical X'Pert diffractometer (Bragg-Brentano geometry), in the range $5° \leq 2\theta \leq 50°$, with a step of 0.02° and 50 s of integration per step.

Ti characterization. The total Ti content (defined as "Ti/Si × 100") was determined by an EDX detector (Oxford – Detector with an AZTEC software) set on a Field Emission Scanning Electron Microscope (Tescan S9000G with a Scottky FEG source) and it was used as a response for the DoE.

The speciation of Ti was assessed using UV spectroscopy in Diffuse Reflectance (DR) mode and Fourier Transform (FT) IR spectroscopy in Attenuated Total Reflectance (ATR) mode. DR-UV spectra were collected on a Varian Cary5000 spectrophotometer, equipped with a DR sphere, on the pure samples (Spectralon® was used as 100% reflectance reference). All the samples were measured as such and after the following activation procedure, aiming at eliminating the influence of water on the Ti coordination, as well as that from possible organic pollutants: the samples were heated to 500 °C with a ramp of 5° per min under dynamic vacuum (residual pressure < 10^{-3} mbar), outgassed for 1 h at 500 °C and then exposed to 100 mbar of pure oxygen (O_2) for 30 min; the samples were finally further outgassed for 1 h prior cooling.[45] After the activation, the samples were transferred from the activation cell to the measurement holder inside a glovebox (H_2O < 0.5 ppm), in order to avoid any rehydration or contamination. The onset wavelength for the LMCT electronic transitions involving Ti (hereafter "LMCT onset"), was used as a response for the DoE (calculated as shown in Fig. S1†), as indication of the presence of non-tetrahedral Ti species; in detail, an LMCT onset value larger than 335 nm (Fig. S2†) is representative for the presence of Ti species with a coordination number higher than for the perfect tetrahedral sites (*i.e.* > 4). ATR-IR spectra were recorded on a Bruker Alpha II spectrophotometer located inside the glovebox, on the same samples pre-activated for the sake of DR-UV measurements. The spectra were recorded with a DTGS detector by accumulating 32 scans (64 for the background spectrum), with a resolution of 2 cm^{-1}. The integrated area of the 960 cm^{-1} signal (hereafter "960 cm^{-1} area"), quantitatively correlated to the amount of tetrahedrally coordinated Ti inserted in the MFI framework,[45,68] was used as a response for the DoE.

Analysis of data. The MDA was performed with the PLS regression[67] using the MODDE® 13 software by Sartorius Stedim Data Analytics.[72] The chosen D-optimal design allows the determination of only linear terms so that, for each response, a straight line in the following form was obtained (eqn (1))

$$y = C + a_1x_1 + a_2x_2 + a_3x_3 + a_4x_4 + a_5x_5 + a_6x_6 + a_7x_7 \quad (1)$$

where y is the response, x_n are the levels centred and scaled for the seven variables n (high: + 1; intermediate: 0; low: −1), C is the constant term (intercept), and a_n are the coefficients of the model, centred and scaled. When the coefficients are centred and scaled, their value is proportional to the positive or negative effect that a given variable n has on the response y, thus

Table 2 List of the syntheses and levels (high: +1; intermediate: 0; low: −1) used for each variable. Lines N1–N9: experimental matrix of the D-optimal design. Line N10: centre point. Lines N11–N13: additional syntheses in the experimental domain, included in the model. Line E: reproducibility samples

Name	t(H-TEOS)[a]	t(H-TBOT)[b]	T(H-TEOS)[c]	t(A)[d]	T(A)[e]	t(Cry)[f]	T(Cry)[g]
N1	−1	+1	−1	−1	−1	−1	−1
N2	+1	+1	+1	+1	+1	−1	−1
N3	+1	−1	+1	−1	−1	+1	−1
N4	−1	−1	−1	+1	+1	+1	−1
N5	−1	−1	+1	+1	−1	−1	+1
N6	+1	−1	−1	−1	+1	−1	+1
N7	−1	+1	−1	+1	+1	−1	+1
N8	+1	+1	−1	+1	−1	+1	+1
N9	−1	+1	+1	−1	+1	+1	+1
N10	0	0	0	0	0	0	0
N11	−1	−1	−1	+1	−1	+1	−1
N12	+1	+1	+1	+1	+1	+1	−1
N13	−1	+1	0	+1	0	−1	+1
E[h]	−1	−1	0	−1	0	−1	0

[a] t(H-TEOS): TEOS hydrolysis time. [b] t(H-TBOT): TBOT hydrolysis time. [c] T(H-TEOS): TEOS hydrolysis temperature. [d] t(A): Aging time. [e] T(A): Aging temperature. [f] t(Cry): Crystallization time. [g] T(Cry): Crystallization temperature. [h] Level used to synthesize 6 samples.

allow the comparison among the effect of different variables n. The error bar (calculated at 90% of confidence) of the coefficients can be used to determine the significance of each term in the eqn (1). The coefficients can consequently be used to identify which variable n has a significant influence on the response y, and if the effect is positive or negative (*i.e.*, if the increase of the variable causes an increase or a decrease in the response, respectively). The PLS regression was performed by including the responses of samples from N1 to N13 and the series Ei-b.

Subsequently, R software (version 4.0.2)[73] was employed to compute PCA models on datasets involving DR-UV and ATR-IR measurements (in the 200–350 nm and 1000–900 cm^{-1} ranges, respectively). The data were pre-processed by using the Standard Normal Variate (SNV) algorithm before calculating models.[74] The PCA models were used to evaluate the correlation among the responses LMCT onset and 960 cm^{-1} area with the actual variability among DR-UV and ATR-IR spectra, and to individuate correlations among the responses.

Results and discussion

TS-1 samples characterization

The experimental variability was evaluated, and the results are reported in Section S3 of the ESI.† The repeated syntheses were judge sufficiently coherent to allow the DoE approach to study the Ti insertion (Table S2 and Fig. S3†). Moreover, the comparison between the Ei-a and Ei-b series is necessary to exclude the presence of uncontrolled, variable in time parameters, that could influence the result of the syntheses (such as the aging of reagents or the adsorption of organic pollutant on the Teflon liners): such effects were eventually excluded.

Fig. 1 shows the XRD patterns (panel a), ATR-IR spectra (panel b) and DR-UV spectra (panel c) of the DoE set of samples. All the samples are highly crystalline as testified by their XRD patterns, synthesized with yields between 67% and 95% (Table 3).

Regarding the Ti speciation of the DoE set of samples, the Ti/Si × 100 is comprised between 0.59 of N3 and 1.85 of N12 (Table 3). The ATR-IR spectra of all the samples (Fig. 1b) show the typical signals of silicate materials, such as the asymmetric and symmetric Si–O–Si stretching (bands centred at ≈1100 cm^{-1} and 800 cm^{-1}, respectively) and the pentasil unit collective modes of MFI structure, peaked at 550 cm^{-1}.[75] The band centred at 960 cm^{-1} is assigned to the antisymmetric Ti–O–Si vibrations, caused by the insertion of Ti in a tetrahedral framework position.[69,45,68] The signal is visible in all the reported spectra. The integrated areas of the band at 960 cm^{-1} for each sample spectrum are listed in Table 3, and represent a quantitative indicator of the tetrahedral Ti incorporated in the MFI framework.[69,45,68]

The DR-UV spectrum of each sample (Fig. 1c) presents the LMCT electronic transition involving Ti. When only tetrahedral Ti is present in the sample, this band is peaked at approximately 200 nm and consists of a monodispersed signal (LMCT

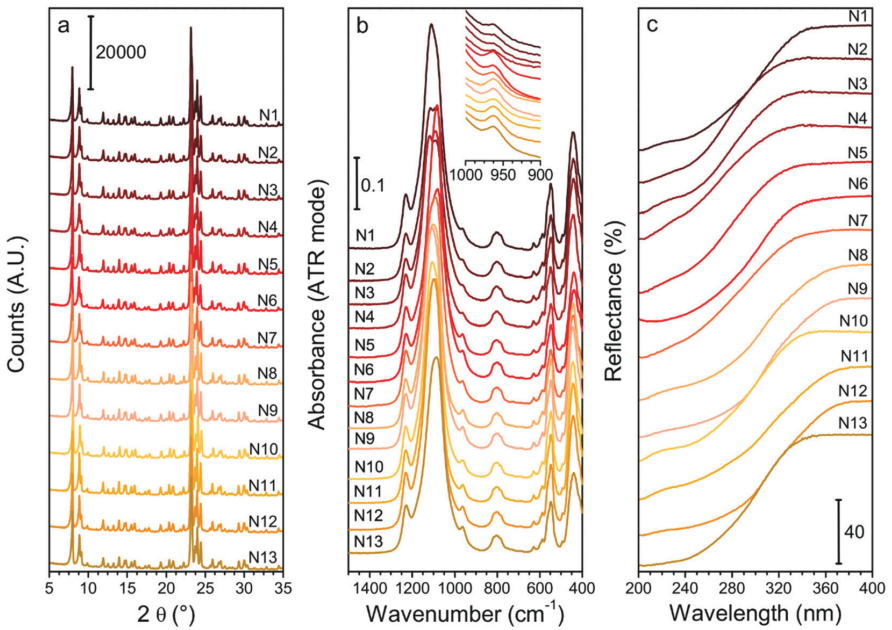

Fig. 1 (a) XRD patterns of the as synthesized full set of DoE samples; (b) ATR-IR spectra of the activated DoE samples; the inset reports the magnification of 960 cm^{-1} signal. (c) DR-UV spectra of the activated DoE samples.

Table 3 List of the responses obtained for each synthesis. Lines N1–N9: syntheses belonging to the D-optimal design. Line N10: centre point. Lines N11–N13: additional syntheses in the experimental domain, included in the model

Name	Yield (%)	Ti/Si × 100 (mol/mol)	LMCT onset (nm)	960 cm^{-1} area (cm^{-1})
N1	75.32	1.22	341	0.157
N2	73.03	0.73	314	0.122
N3	74.88	0.59	312	0.104
N4	67.53	0.69	309	0.114
N5	79.71	1.17	332	0.313
N6	69.22	1.68	353	0.298
N7	66.82	1.20	341	0.265
N8	90.58	1.79	368	0.345
N9	94.94	1.66	365	0.336
N10	74.27	1.31	335	0.286
N11	89.66	1.48	367	0.315
N12	94.82	1.85	370	0.352
N13	78.46	1.71	337	0.334

onset at about 335 nm, see Fig. S2†). The signal does not present shoulders when all the Ti is tetrahedrally coordinated. Conversely, it shifts downward and broadens progressively when intermediate pentacoordinated or hexacoordinated TiO_x species are present, or upon increasing the nuclearity of Ti centre (from isolated to multimeric centres), until reaching the wavelength of the octahedral Ti in bulk TiO_2 (peaked at ≈320 nm, with an LMCT onset at 380 nm, Fig. S2†).[76,45,70] When intermediate defective sites among the bulk TiO_2 and the tetrahedral Ti are present, additional components peaked between 260–280 nm arises[45,76] (with onset around 360 nm in the case octahedral species are the dominant class of defects, Fig. S2†). However, the relative intensity of those components cannot be used for a quantitative purpose since the extinction coefficient for each component is unknown.[45] For these reasons, in this work, the intermediate Ti sites were not quantified, but their presence was qualitatively evaluated using the wavelength at which the LMCT signal starts (LMCT onset in Table 3). All the samples present the spectral component due to tetrahedral Ti (accordingly to the presence of the 960 cm^{-1} signal in the IR range of frequencies), and none of them presents the component assigned to bulk TiO_2. This result implies that the slow hydrolysis of TBOT at 0 °C in IPA is effective in avoiding the TiO_2 formation in the whole experimental domain. The presence of intermediate non-tetrahedral Ti species is testified in the majority of the samples by the LMCT band broadening and, occasionally, by the presence of defined shoulders, highlighting distinct additional maxima (*e.g.*, in the samples N3 and N9).

Analysis of the responses through the DoE

The effect of each variable (listed in the Synthesis procedure section) on the yield of the synthesis, the Ti/Si × 100 or the Ti speciation (LMCT onset and 960 cm^{-1} area) was screened with a limited number of experiments (19 synthesis including both the DoE and the reproducibility samples). For each response, the positive or negative linear effect of each variable was calculated, as expressed by the coefficient plots in Fig. 2.

The coefficient plot shows a column reporting the average value of the response (constant term) obtained with the synthesis procedure and other columns reporting the effects of the synthesis variables. The constant term was obtained by the intercept of eqn (1) and the other columns correspond to terms a_n of the same equation. Therefore, the columns of the synthesis variables show the margin of improvement of the response into the experimental domain upon changing the variable, to add (if positive) or subtract (if negative) to the constant term. The significant and insignificant terms can be discerned by evaluating the error bars of the columns: an effect is insignificant negligible when its error bar overpasses the zero level (*i.e.* when it is not sure if the effect is positive or negative). For this reason, Fig. 2 shows the coefficient plots for each response, before (main plot) and after (inset) the exclusion of insignificant terms. As it can be seen, the variables significantly influencing the responses are few. This outcome implies the possibility of excluding all the insignificant variables in the investigated experimental domain from further studies.

The yield coefficient plot analysis (Fig. 2a) shows that the yield of the synthesis depends only on t(Cry). The predicted confidence interval for the response are reported in Tables S3 and S4.† This result highlights how, with this synthetic procedure, the TEOS hydrolysis conditions (which supply the SiO_2 units, that give the major contribution to the yield) do not significantly affect the yield. Consequently, the yield is determined during the hydrothermal crystallization step, possibly by the equilibrium among precipitation and solubilization of silicate species, even if we do not know if the TEOS hydrolysis is quantitative during the hydrolysis step.

The Ti/Si × 100 coefficient plot analysis (Fig. 2b) indicates that the Ti/Si × 100 is significantly affected by t(H-TBOT) and T(Cry). This suggests that at 0 °C, in 4 h (the low level) the TBOT hydrolysis is not completed; therefore, the number of available TiO_4^{4-} units in SiO_4^{4-} units medium affects the Ti incorporation. Conversely, t(H-TEOS) and T(H-TEOS) do not affect Ti/Si × 100. We can deduce that the hydrolysis degree of TEOS, when it contacts the TiO_4^{4-} units, is sufficient to start and support the co-polymerization during the aging step. The insignificance of t(A) and T(A) indicates that the rate of polymerization of the SiO_4^{4-} units and the nucleation of the MFI framework (possibly influenced by t(A) and T(A)) does not significantly affect Ti/Si × 100 when the same hydrolysis conditions and T(Cry) are used. Moreover, the significant effect of T(Cry) on Ti/Si × 100 can be explained considering the common theory for which the crystal growth of the highly siliceous MFI framework occurs by addition of solubilized units from the liquid phase, when alkoxides are used as starting materials.[77,78] Therefore, the increasing of T(Cry) facilitates the incorporation of TiO_4^{4-} units from the liquid phase into the growing crystals, thus influencing the final Ti/Si × 100.

The LMCT onset coefficient plot (Fig. 2c) demonstrates as the LMCT onset is significantly affected by t(Cry) and T(Cry),

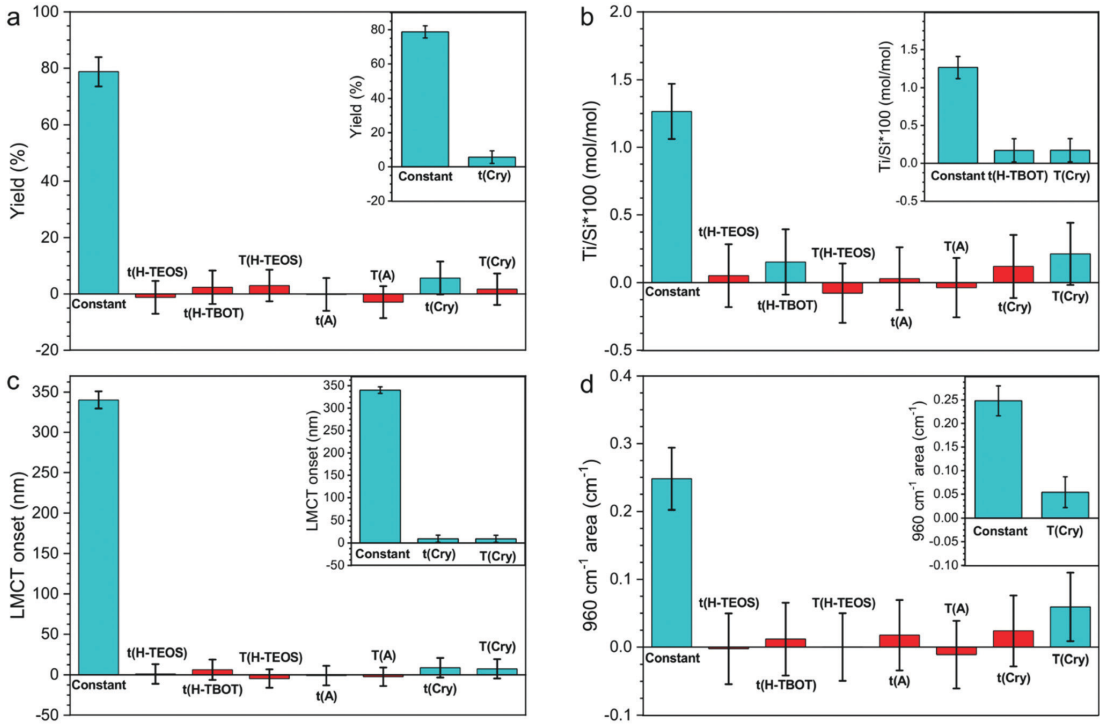

Fig. 2 Coefficient plot for each response: (a) Yield (%), (b) Ti/Si × 100 (mol mol^{-1}), (c) LMCT onset (nm) and (d) 960 cm^{-1} area (cm^{-1}). For each panel, the main plot shows the coefficient of all the variables with their error bars and the inset shows only the coefficients that have a significant influence on the response, with their error bars. For clarity, the insignificant effect columns were coloured in red and the significant effect columns were coloured in light blue.

even if their effect is small (as shown in Table S3 and S4†). This observation is coherent with the onset of the LMCT transition of the experimental DR-UV spectra (Fig. 1c and Fig. S3†), that moderately varies in the range 309–370 nm (Table 3). This result suggests that the Ti speciation is therefore influenced mainly by the synthesis procedure with slight modifications occurring during the crystal growth.

The 960 cm^{-1} area coefficient plot analysis (Fig. 2d) shows as the band's area, proportional to the concentration of the tetrahedrally coordinated Ti, is the response that more strongly varies into the experimental domain, as it can be seen by the ratio between the column of the significant variable and the column of the constant term in Fig. 2d. The variable significantly affecting the 960 cm^{-1} area is T(Cry), in accordance with the fact that the same variable affects the LMCT onset response. Considering the synthesis procedure and experimental domain chosen for this work, the marked increase of the 960 cm^{-1} area is associated to the increase of total Ti content. Since the Ti/Si × 100 experimentally obtained are all far under the theorical limit, it is plausible that an increase in the Ti/Si × 100 will proportionally lead to a rise of the tetrahedral Ti content, therefore of the 960 cm^{-1} area. Moreover, T(Cry) has also the effect of increasing the LMCT onset, *i.e.*, to increase the content of non-tetrahedral species. From these observations, it can be excluded that the increase in the temperature of crystallization might cause the transformation of non-tetrahedral Ti sites to tetrahedral ones, thus it is more reasonable to assume that the Ti is directly incorporated in the tetrahedral centres.

The general deduction is that using the synthetic procedure descripted and, within this experimental domain, the Ti/Si × 100 could be controlled, and the inserted Ti will be principally tetrahedral, but it is not possible entirely excluding the formation of non-tetrahedral species. Instead, the formation of bulk TiO_2 is totally avoided.

The contour plots (Fig. 3) show in a graphical way the effect of the significant variables (reported on the axes) and the desired direction to follow for improving the synthesis results (indicated by the warm colours). The graph in Fig. 3 reports the responses regarding Ti (Ti/Si × 100: Fig. 3a and b, LMCT: Fig. 3c, 960 cm^{-1} area: Fig. 3d). The comparison among panels b, c and d (expressed *versus* the same variable) evidenced how, with this synthesis procedure and within this experimental domain, the Ti/Si × 100 and Ti speciation (LMCT onset and

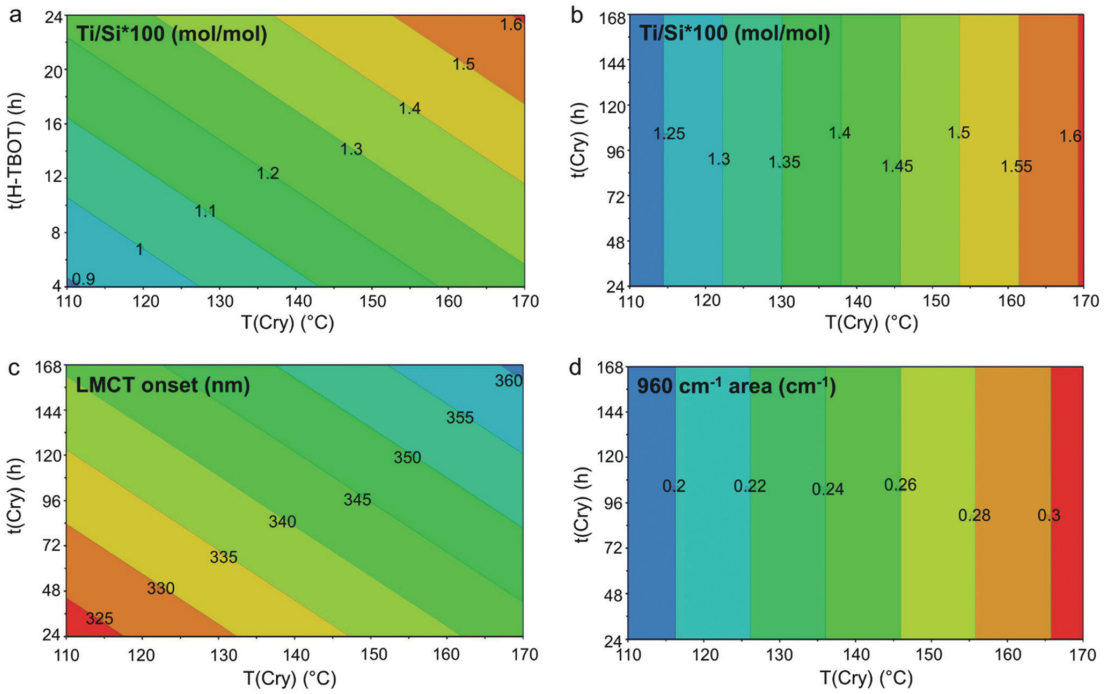

Fig. 3 Contour plots for the responses regarding Ti content (Ti/Si × 100 in panels a and b) and speciation (LMCT onset in panel c and 960 cm^{-1} area in panel d). Panels a and c report the contour plots involving the significant variables for the responses Ti/Si × 100 and LMCT onset, while panels b is included to compare the total Ti content with the LMCT onset and the 960 cm^{-1} area varying the same variables (time and temperature of crystallization). The askew bands are iso-response regions, delimited by lines which corresponding response is reported in the labels (the label have the dimension of the response).

960 cm^{-1} area) can be simultaneously improved until a specific limit, with the compromise of a fraction of Ti unavoidably incorporated as non-tetrahedral.

Finally, a digression is worth regarding the choice not to evaporate the alcohols from the synthesis mixture to favour the reproducibility of the synthesis procedure and facilitates the use of the DoE approach. Indeed, DoE requires as precise as possible knowledge of the synthesis parameters, in order to avoid the attribution to explored variables of response variations instead ascribable to uncontrolled parameters. For this reason, the evaporation of alcohols has been avoided. However, it must be considered that the addition of alcohols to hydrolysed solutions of TEOS is reported to favour the immediate polymerization and precipitation of silicate species.[79,17,63] The precipitation could have influenced the overall Ti/Si × 100 as this response is affected by the t(H-TBOT) (Fig. 2b). The t(H-TBOT) determines the number of TiO_4^{4-} units present in the TBOT/IPA solution when the TEOS/TPAOH/H_2O solution was added. The already hydrolysed TiO_4^{4-} units will probably be easily incorporated into the polymerised silicate framework, without leaving further time for the TBOT hydrolysis.

PCA of ATR-FT-IR and DR-UV data

Finally, the developed PCA models on ATR-IR and DR-UV measurements showed clear trends in the data, since they correlate with Ti/Si × 100. Fig. 4 and 5 show the PCA scores and loadings plots from the 2nd and 3rd components of the PCA models developed on ATR-IR and DR-UV data, respectively. In particular, panels 4a and 5a show the scores plots as obtained from the model, panels 4b and 5b show the same plots, where the colours of the sample spots were scaled according to the Ti/Si × 100, and panels 4c and 5c reports the loadings plots. PCA scores plots (Fig. 4 and 5, a-b) show PC2 and PC3 values since PC1, mostly representative for the overall spectral shape, did not turn to be informative when looking at the measurements monitored in the study. On the other hand, Ti/Si × 100 variability (as well as LMCT onset and the area of the 960 cm^{-1} signal, showed in Fig. S4 and S5 of the ESI†) is mainly represented by PC2 for the ATR-IR data and by PC2 and PC3 by the DR-UV data. In both the cases, the PCA scores plots showed that the samples N8, N9, N11 and N12 provided the highest values of Ti/Si × 100, in correlation with the intensity of the signal within the 950–975 cm^{-1} range for ATR-IR

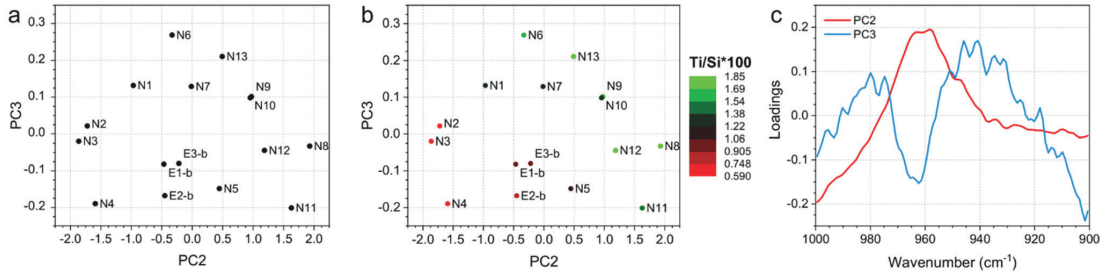

Fig. 4 (a) PC2 and PC3 scores plot, (b) PC2 and PC3 scores plot, in which the sample spots were scaled according to the Ti/Si × 100 and (c) loadings plot of the PCA model developed on ATR-IR data.

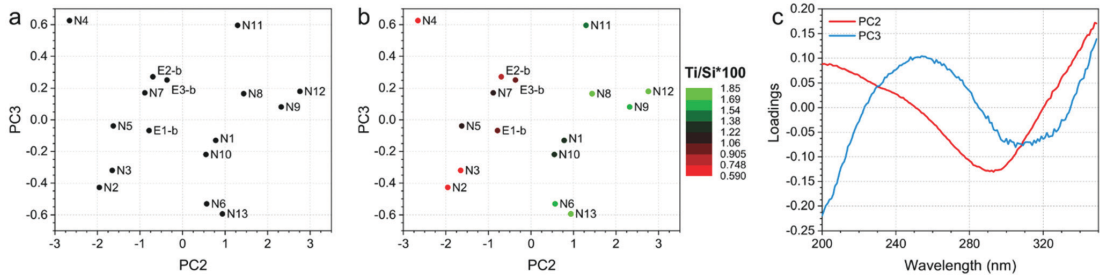

Fig. 5 (a) PC2 and PC3 scores plot, (b) PC2 and PC3 scores plot, in which the sample spots were scaled according to the Ti/Si × 100 and (c) loadings plots of the PCA model developed on DR-UV data.

measurements, and the 250–300 nm range for DR-UV measurements. These results further confirm that the increase of Ti/Si × 100 is correlated with the insertion of tetrahedrally coordinated Ti (PCA on ATR-IR data). Conversely, the content of non-tetrahedral species will also increase by raising the value of Ti/Si × 100, as can be seen by the PC2 of DR-UV data in the 250–300 nm range. The PCA analysis of ATR-IR and DR-UV spectra thus fully supports the evidences from DoE as previously commented.

Conclusions

The rational study of the synthesis of TS-1 zeolite using the DoE approach was reported to discern the synthesis parameters that significantly impact the catalyst properties. It was established that the Ti insertion and speciation is mainly determined during the hydrothermal step of the synthesis. In particular, the total Ti content (Ti/Si × 100) is increased by the time of hydrolysis of the Ti source (t(H-TBOT)) and by higher temperatures of crystallization (T(Cry)). On the other hand, Ti speciation can be controlled by varying the time of crystallization (t(Cry)) and the temperature of crystallization (T(Cry)). Regarding the variability of the responses in the explored experimental domain, the total Ti content and the area of the 960 cm^{-1} band (correlated to the concentration of the tetrahedral Ti) are determined in a certain amount by the procedure itself, but they can be heavily modified by regulating the variables. On the other hand, the LMCT onset is basically determined by the synthesis procedure and it can only be modified slightly by these variables in the experimental domain. This framework is entirely in agreement with the independent PCA analysis of the spectroscopic results.

Although the presented DoE project does not lead to the synthesis of a TS-1 sample with an elevated quantity of Ti, entirely inserted in tetrahedral framework position, this work allowed investigating the direct correlation of the synthesis variables with the results, net of the experimental variability of the procedure, using a limited number of experiments and resources. In a more general conception, DoE is a practical approach that helps identifying the issues of the procedure and their causes, leading to an exceptional improvement in the knowledge on this vast field, impossible to reach with the trial-and-error or with the OVAT approaches.

The application of this work methodology to the optimization of the present synthesis, by excluding the insignificant variables and by adding other parameters (such as different precursors or varying composition of the synthesis gel), could lead to the preparation of a “perfect” TS-1 sample, featuring Ti in the only tetrahedral positions with a concentration reaching

the theoretical insertion limit. Moreover, the same approach could be applied, in the future, to the study of Ti insertion into different zeolitic frameworks and to disclose the relation of Ti speciation with catalytic performances in partial oxidation reactions.

Author contributions

All the authors contributed in the conceptualization of the project. Francesca Rosso contributed to conceptualization, formal analysis, investigation, methodology, validation, visualization, writing – original draft. Andrea Rizzetto contributed to formal analysis, investigation, validation, visualization, writing -review and editing. Alessia Airi contributed to conceptualization, investigation, supervision, writing -review and editing. Khrystyna Khoma contributed to investigation, writing -review and editing. Matteo Signorile contributed to conceptualization, supervision, writing -review and editing. Valentina Crocellà contributed to conceptualization, supervision, writing -review and editing. Silvia Bordiga contributed to conceptualization, funding acquisition, resources, writing -review and editing. Simone Galliano contributed to conceptualization, formal analysis, methodology, validation, writing -review and editing. Claudia Barolo contributed to conceptualization, supervision, writing -review and editing. Eugenio Alladio contributed to conceptualization, formal analysis, methodology, supervision, validation, writing – original draft. Francesca Bonino contributed to conceptualization, funding acquisition, project administration, resources, supervision, writing -review and editing.

Conflicts of interest

There are no conflicts to declare.

Notes and references

1 I. Marantos, G. G. Christidis and M. Ulmanu, in *Handbook of Natural Zeolites*, ed. V. J. Inglezakis and A. A. Zorpas, Bentham E Books, 2012, pp. 28–51.
2 *Handbook of Zeolite Science and Technology*, ed. S. M. Auerchach, K. A. Carrado and P. K. Dutta, Marcel Dekker, Inc., New York, 2003.
3 S. I. Zones and Y. Nakagawa, Use of Modified Zeolites as Reagents Influencing Nucleation in Zeolite Synthesis, *Stud. Surf. Sci. Catal.*, 1995, **97**, 45–52.
4 S. Mintova, N. H. Olson, V. Valtchev and T. Bein, Mechanism of Zeolite A Nanocrystal Growth from Colloids at Room Temperature, *Science*, 1999, **283**, 958–960.
5 P. S. Singh, Complexity of silicate/aluminosilicate polymerization: some insights using a small-angle X-ray scattering study, *J. Appl. Crystallogr.*, 2007, **40**, 590–593.
6 A. Deneyer, Q. Ke, J. Devos and M. Dusselier, Zeolite Synthesis Under Nonconventional Conditions: Reagents, Reactors, and *Modi Operandi*, *Chem. Mater.*, 2020, **32**, 4884–4919.
7 A. Corma and M. E. Davis, Issues in the Synthesis of Crystalline Molecular Sieves: Towards the Crystallization of Low Framework Density Structures, *ChemPhysChem*, 2004, **5**, 304–313.
8 S. L. Burkett and M. E. Davis, Mechanism of Structure Direction in the Synthesis of Si-ZSM-5: an Investigation by Intermolecular ^{1}H ^{29}Si CP MAS NMR, *J. Phys. Chem.*, 1994, **98**, 4647–4653.
9 S. L. Burkett and M. E. Davis, Mechanism of Structure Direction in the Synthesis of Pure-Silica Zeolites. 2. Hydrophobic Hydration and Structural Specificity, *Chem. Mater.*, 1995, **7**, 920–928.
10 M. A. Camblor, A. Corma, M. J. Díaz-Cabañas and C. Baerlocher, Synthesis and Structural Characterization of MWW Type Zeolite ITQ-1, the Pure Silica Analog of MCM-22 and SSZ-25, *J. Phys. Chem. B*, 1998, **102**, 44–51.
11 C. S. Cundy, J. O. Forrest and R. J. Plaisted, Some observations on the preparation and properties of colloidal silicalites. Part I: Synthesis of colloidal silicalite-1 and titanosilicalite-1 (TS-1), *Microporous Mesoporous Mater.*, 2003, **66**, 143–156.
12 Á. Cantín, A. Corma, M. J. Díaz-Cabañas, J. L. Jordá, M. Moliner and F. Rey, Synthesis and Characterization of the All-Silica Pure Polymorph C and and Enriched Polymorph B Intergrowth of Zeolite Beta, *Angew. Chem., Int. Ed.*, 2006, **45**, 8013–8015.
13 J. Grand, H. Awala and S. Mintova, Mechanism of zeolite crystal growth: new findings and open questions, *CrystEngComm*, 2016, **18**, 650–664.
14 R. Bai, Y. Song, R. Bai and J. Yu, Creation of Hierarchical Titanosilicate TS-1 Zeolite, *Adv. Mater. Interfaces*, 2021, **8**, 2001095–2001095.
15 R. J. Francis and D. O. Hare, The kinetics and mechanism of the crystallization of microporous materials, *J. Chem. Soc. Trans.*, 1998, 3133–3148.
16 F. Fengtao, F. Zhaochi and L. Can, UV Raman spectroscopic study on the synthesis mechanism and assembly of molecular sieves, *Chem. Soc. Rev.*, 2010, **39**, 4794–4801.
17 G. Zhang, J. Sterte and B. J. Schoeman, Discrete Colloidal Crystals of Titanium Silicalite-1, *J. Chem. Soc., Chem. Commun.*, 1995, 2259–2260.
18 G. Zhang, J. Sterte and B. J. Schoeman, Preparation of Colloidal Suspensions of Discrete TS-1 Crystals, *Chem. Mater.*, 1997, **9**, 210–217.
19 A. Aerts, C. E. A. Kirschhock and J. A. Martens, Methods for *in situ* spectroscopic probing of the synthesis of a zeolite, *Chem. Soc. Rev.*, 2010, **39**, 4626–4642.
20 D. Grandjean, A. M. Beale, A. V. Petukhov and B. M. Weckhuysen, Unraveling the Crystallization Mechanism of CoAPO-5 Molecular Sieves Under Hydrothermal Conditions, *J. Am. Chem. Soc.*, 2005, **127**, 14454–14465.
21 T. Lundstedt, E. Seifert, L. Abramo, B. Thelin, A. Nystrom, J. Pettersen and R. Bergman, Experimental design and optimization, *Chemom. Intell. Lab. Syst.*, 1998, **42**, 3–40.

22 R. Leardi, Experimental Design in Chemistry: A Tutorial, *Anal. Chim. Acta*, 2009, **652**, 161–172.
23 K. Héberger, Chemoinformatics – multivariate mathematical-statistical methods for data evaluation, in *Medical Applications of Mass Spectrometry*, ed. K. Vekey, A. Telekes and A. Vertes, Elsevier B.V., 2008, pp. 141–169.
24 R. Bro and A. K. Smilde, Principal component analysis, *Anal. Methods*, 2014, **6**, 2812–2831.
25 A. Corma, M. J. Díaz-Cabanas, M. Moliner and C. Martínez, Discovery of a new catalytically active and selective zeolite (ITQ-30) by high-throughput synthesis techniques, *J. Catal.*, 2006, **241**, 312–318.
26 M. Moliner, M. J. Díaz-Cabañas, V. Fornés, C. Martínez and A. Corma, Synthesis methodology, stability, acidity and catalytic behavior of the 18 × 10 member ring pores ITQ-33 zeolite, *J. Catal.*, 2008, **254**, 101–109.
27 Z. Liu, A. Chokkalingam, S. Miyagi, M. Yoshioka, T. Ishikawa, H. Yamada, K. Ohara, N. Tsunoji, Y. Naraki, T. Sano, T. Okubo and T. Wakihara, Revealing scenarios of interzeolite conversion from FAU to AEI through the variation of starting materials, *Phys. Chem. Chem. Phys.*, 2022, **24**, 4136–4146.
28 A. De Lucas, L. Rodríguez and P. Sánchez, Optimization of the Molar Composition of the Gel in the Synthesis of Titanium Silicalite-2 TS-2, *Chem. Eng. Res. Des.*, 2000, **78**, 136–144.
29 M. Tagliabue, L. C. Carluccio, D. Ghisletti and C. Perego, Multivariate approach to zeolite synthesis, *Catal. Today*, 2003, **81**, 405–412.
30 M. Balbaşi, Application of full factorial design method to silicalite synthesis, *Mater. Res. Bull.*, 2013, **48**, 2908–2914.
31 N. Martín, M. Moliner and A. Corma, High yield synthesis of high-silica chabazite by combining the role of zeolite precursors and tetraethylammonium: SCR of NO_X, *Chem. Commun.*, 2015, **51**, 9965–9968.
32 C. F. Imbachi-Gamba and A. L. Villa, Statistical analisys of the influence of the synthesis conditions on the properties of hierarchical zeolite Y, *Mater. Today Chem.*, 2021, **20**, 100442.
33 M. Taramasso, G. Perego and B. Notari, *US Pat*, 4410501, 1983.
34 J. Přech, Catalytic performance of advanced titanosilicate selective oxidation catalysts - a review, *Catal. Rev. – Sci. Eng.*, 2018, **60**, 71–131.
35 W. Fan, B. Fan, X. Shen, J. Li, P. Wu, Y. Kubota and T. Tatsumi, Effect of ammonium salts on the synthesis and catlytic properties of TS-1, *Microporous Mesoporous Mater.*, 2009, **122**, 301–308.
36 A. Thangaraj and S. Sivasanker, An Improved Method for TS-1 Synthesis: ^{29}Si NMR Studies, *J. Chem. Soc., Chem. Commun.*, 1992, **20**, 123–124.
37 D. Lin, Q. Zhang, Z. Qin, Q. Li, X. Feng, Z. Song, Z. Cai, Y. Liu, X. Chen, D. Chen, S. Mintova and C. Yang, Reversing Titanium Oligomer Formation towards High-Efficiency and Green Synthesis of Titanium Containing Molecular Sieves, *Angew. Chem., Int. Ed.*, 2021, **60**, 3443–3448.
38 J. Xing, D. Yuan, H. Liu, Y. Tong, Y. Xu and Z. Liu, Synthesis of TS-1 zeolites from a polymer containing titanium and silicon, *J. Mater. Chem. A*, 2021, **9**, 6205–6213.
39 M. Tamura, W. Chaikittisilp, T. Yokoi and T. Okubo, Incorporation process of Ti species into the framework of MFI type zeolite, *Microporous Mesoporous Mater.*, 2008, **112**, 202–210.
40 Q. Guo, Z. Feng, G. Li, F. Fan and C. Li, Finding the "Missing Components" during the Synthesis of TS-1 Zeolite by UV Resonance Raman Spectroscopy, *J. Phys. Chem. C*, 2013, **117**, 2844–2848.
41 Z. Shan, Z. Lu, L. Wang, C. Zhou, L. Ren, L. Zhang, X. Meng, S. Ma and F.-S. Xiao, Stable Bulky Particles Formed by TS-1 zeolite Nanocrystals in the presence of H_2O_2, *ChemCatChem*, 2010, **2**, 407–412.
42 T. Ge, Z. Hua, J. Lv, J. Zhou, H. Guo, J. Zhou and J. Shi, Hydrophilicity/hydrophobicity modulated synthesis of nanocrystalline and hierarchically structured TS-1 zeolites, *CrystEngComm*, 2017, **19**, 1370–1376.
43 W. Fan, R. G. Duan, T. Yokoi, P. Wu, Y. Kubota and T. Tatsumi, Synthesis, crystallization mechanism and catalytic properties of Ti-rich TS-1 free of extraframework Ti species, *J. Am. Chem. Soc.*, 2008, **130**, 10150–10164.
44 M. G. Clerici, G. Bellussi and U. Romano, Synthesis of Propylene Oxide from Propylene and Hydrogen Peroxide Catalyzed by Titanium Silicalite, *J. Catal.*, 1991, **129**, 159–167.
45 M. Signorile, V. Crocellà, A. Damin, B. Rossi, C. Lamberti, F. Bonino and S. Bordiga, Effect of Ti Speciation on Catalytic Peroformance of TS-1 in the Hydrogen Peroxide to Propylene Oxide Reaction, *J. Phys. Chem. C*, 2018, **122**, 9021–9034.
46 M. Zhang, S. Ren, Q. Guo and B. Shen, Synthesis of hierarchically porous zeolite TS-1 with small crystal size and its performance of 1-hexene epoxidation reaction, *Microporous Mesoporous Mater.*, 2021, **326**, 111395.
47 M. Liu, J. Li, X. Chen, J. Song, W. Wei, Y. Wen and X. Wang, Preparation of anatase-free hierarchical titanosilicalite-1 in favor of allyc chloride epoxidation, *Microporous Mesoporous Mater.*, 2021, **326**, 111388.
48 Y. Jiao, A. L. Adedigba, Q. He, P. Miedziak, G. Brett, N. F. Dummer, M. Perdjon, J. Liu and G. J. Hutchings, Inner-connection and open pore hierarchical TS-1 with controlled framework titanium for catalytic cyclohexene epoxidation, *Catal. Sci. Technol.*, 2018, **8**, 2211–2217.
49 Y. Zuo, M. Liu, T. Zhang, L. Hong, X. Guo, C. Song, Y. Chen, P. Zhu, C. Jaye and D. Fischer, Role of pentahedrally coordinated titanium in titanium silicalite-1 in propene epoxidation, *RSC Adv.*, 2015, **5**, 17897–17904.
50 W. Song, G. Xiong, H. Long, F. Jin, L. Liu and X. Wang, Effect of treatment with different bases on the catalytic properties of TS-1/SiO_2 extrudates in propylene epoxidation, *Microporous Mesoporous Mater.*, 2015, **212**, 48–55.

51 A. Esposito, M. Taramasso and C. Neri, *US Pat*, 4396783, 1983.
52 Y. Liu, C. Zhao, B. Sun, H. Zhu and W. Xu, Preparation and modification of Au/TS-1 catalyst in the direct epoxidation of propylene with H_2 and O_2, *Appl. Catal., A*, 2021, **624**, 118329.
53 X. Nie, X. Ji, Y. Chen, X. Guo and C. Song, Mechanistic investigation of propylene epoxidation with H_2O_2 over TS-1: Active site formation, intermediate identification, and oxigen transfer pathway, *Mol. Catal.*, 2017, **441**, 150–167.
54 D. H. Wells, A. M. Joshi, W. N. Delgass and K. T. Thomson, A quantum chemical study of comparison of various propylene epoxidation mechanism using H_2O_2 and TS-1 catalyst, *J. Phys. Chem. B*, 2006, **110**, 14627–14639.
55 J. Limtrakul, C. Inntam and T. N. Truong, Density funcitonal theory study of the ethylene epoxidation over Ti-substituted silicalite (TS-1), *J. Mol. Catal.*, 2004, **207**, 139–148.
56 Z. Wu, B. Wang, J. Shi, P. Rui, X. Xie, W. Liao and X. Shu, The silanization process or the hydrothermal synthesis of hierarchical titanium silicalite-1, *Microporous Mesoporous Mater.*, 2021, **327**, 111407.
57 H. Liu, Y. Wang, T. Ye, F. Wang, S. Ran, H. Xie, J. Liu, Y. Li, B. Li, Y. Liu, Y. Chai and L. Wang, Fully utilizing seeds solution for solvent-free synthesized nanosized TS-1 zeolites with efficient epoxidation of cholopropene, *J. Solid State Chem.*, 2022, **307**, 122844.
58 L. Zhang, X. Zhu, X. Wang and C. Shi, The synthesis of pure and uniform nanosized TS-1 crystals with a high titanium content and a high space-time yield, *Inorg. Chem. Front.*, 2021, **8**, 5260–5269.
59 Y. Liu, F. Wang, X. Zhang, Q. Zhang, Y. Zhai, G. Lv, M. Li and M. Li, One-step synthesis of anatase-free hollow titanium silicalite-1 by the solid-phase conversion method, *Microporous Mesoporous Mater.*, 2022, **331**, 111676.
60 M. Li, Y. Zhai, X. Zhang, F. Wang, G. Lv, A. Rosine, M. Li, Q. Zhang and Y. Liu, $(NH_4)_2SO_4$-assisted synthesis of thin-walled Ti-rich hollow titanium silicalite-1 zeolite for 1-hexene epoxidation, *Microporous Mesoporous Mater.*, 2022, **331**, 111655.
61 J. Su, G. Xiong, J. Zhou, W. Liu, D. Zhou, G. Wang, X. Wang and H. Guo, Amorphous Ti species in titanium silicalite-1: Structural features, chemical properties, and inactivation with sulfosalt, *J. Catal.*, 2012, **288**, 1–7.
62 R. Millini, E. Previde Massara, G. Perego and G. Bellussi, Framework Composition of Titanium Silicalite-1, *J. Catal.*, 1992, **137**, 497–503.
63 A. Tuel and Y. Ben Taârit, Influence of the nature of silicon and titanium alkoxides on the incorporation of titanium in TS-1, *Appl. Catal., A*, 1994, **110**, 137–151.
64 G. J. Hutchings, D. F. Lee and A. R. Minihan, Epoxidation of allyl alcohol to glycidol using titanium silicalite TS-1: effect of the method of preparation, *Catal. Lett.*, 1995, **33**, 369–385.
65 J. Blanchard, S. Barboux-Doeuff, J. Maquet and C. Sanchez, Investigation on hydrolysis-condensation reactions of titanium(IV) butoxide, *New J. Chem.*, 1995, **19**, 929–941.
66 J. Muhlebach, K. Muller and G. Schwarzenbach, The Peroxo Complexes of Titanium, *Inorg. Chem.*, 1970, **9**, 2381–2390.
67 R. G. Brereton, *Applied Chemometrics for Scientists*, Wiley, 2007.
68 G. Ricchiardi, A. Damin, S. Bordiga, C. Lamberti, G. Spanò, F. Rivetti and A. Zecchina, Vibrational Structure of Titanium Silicate Catalyst. A Spectroscopic and Theoretical Study, *J. Am. Chem. Soc.*, 2001, **123**, 11409–11419.
69 A. Damin, S. Bordiga, A. Zecchina and C. Lamberti, Reactivity of Ti(IV) sites in Ti-zeolites: An embedded cluster approach, *J. Chem. Phys.*, 2002, **117**, 226–237.
70 F. Bonino, A. Damin, G. Ricchiardi, M. Ricci, G. Spanò, R. D'Aloisio, A. Zecchina, C. Lamberti, C. Prestipino and S. Bordiga, Ti-Peroxo Species in the TS-1/H_2O_2/H_2O System, *J. Phys. Chem. B*, 2004, **108**, 3573–3583.
71 M. Signorile, A. Damin, F. Bonino, V. Crocellà, G. Ricchiardi, C. Lamberti and S. Bordiga, Computational Assessment of Relative Sites Stabilities and Site Specific Adsorptive Properties of Titanium Silicalite-1, *J. Phys. Chem. C*, 2018, **122**, 1612–1621.
72 Modde 13 Software; Umeå, Sweden, 2020, Available Online: **https://www.sartorius.com/en/products/process-analytical-technology/data-analytics-software/doe-software/modde?gclid=CjwKCAjwiuuRBhBvEiwAFXKaNM5XdB5p1oonkutonEjqk72uuSniQRNaZNqpIKZe3pQs0t2VRutWkRoCNvYQAvD_BwE** (accessed on 23 March 2022).
73 The R Project for Statistical Computing, **https://www.r-project.org/**, (accessed 23 February 2022).
74 Å. Rinnan, Pre-processing in vibrational spectroscopy - when, why and how, *Anal. Methods*, 2014, **6**, 7124–7129.
75 R. Ravishankar, C. Kirschhock, B. J. Schoeman, P. Vanoppen, P. J. Grobet, S. Storck, W. F. Maier, J. A. Martens, F. C. De Schryver and P. A. Jacobs, Physicochemical Characterization of Silicalite-1 Nanophase Material, *J. Phys. Chem. B*, 1998, **102**, 2633–2639.
76 M. Signorile, L. Braglia, V. Crocellà, P. Torelli, E. Groppo, G. Ricchiardi, S. Bordiga and F. Bonino, Titanium Defective Sites in TS-1: Structural Insights by Combining Spectroscopy and Simulation, *Angew. Chem., Int. Ed.*, 2020, **59**, 18145–18150.
77 F. G. Dwyer and E. E. Jenkins, *US Pat*, 3941872, 1976.
78 A. Corma, State of the art and future challenges of zeolite as catalysts, *J. Catal.*, 2003, **216**, 298–312.
79 S. Gontier and A. Tuel, Synthesis of titanium silicalite-1 using amorphous SiO_2 as silicon source, *Zeolites*, 1996, **16**, 184–195.

Microporous and Mesoporous Materials 366 (2024) 112924

Contents lists available at ScienceDirect

Microporous and Mesoporous Materials

journal homepage: www.elsevier.com/locate/micromeso

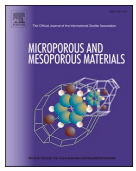

Insight on MWW siliceous zeolites: From 2D precursors toward 3D structure

Francesca Rosso [a], Alessia Airi [a,1], Matteo Signorile [a], Eddy Dib [b,**], Silvia Bordiga [a], Valentina Crocellà [a], Svetlana Mintova [b], Francesca Bonino [a,*]

[a] Department of Chemistry, NIS and INSTM Reference Centre, Università di Torino, Via G. Quarello 15, 10135 and Via P. Giuria 7, 10125, Torino, Italy
[b] Normandie Univ, ENSICAEN, UNICAEN, CNRS, Laboratorie Catalyse et Spectrochimie, 14000, Caen, France

ARTICLE INFO

Keywords:
ITQ-1
MWW
Siliceous zeolite
Spectroscopic characterization
Structure directing agent

ABSTRACT

ITQ-1 layered zeolites, with MWW framework, were prepared using different synthesis and calcination procedures and fully characterized by means of X-ray diffraction, scanning electron microscopy, N_2 sorption and vibrational and nuclear magnetic resonance spectroscopies. Exploring different compositions of the precursor gel, the role of the Organic Structure Directing Agent (OSDA) was definitely disclosed. We proved that the concentration of OSDA in the synthesis gel affects the short-range crystalline order of zeolite crystals. In particular, diluted precursor gels led to the formation of low-density materials in the form of hollow spheres, with partially disordered layers, thinner crystals and high defectivity. In general, all ITQ-1 samples had the same crystalline structure but different morphology, either rose-like or hollow spheres. Moreover, the calcination procedure had an impact on the structural defects of the ITQ-1 zeolite: the higher the removal rate of the OSDA, the higher the defectivity degree of the zeolite.

1. Introduction

In the group of nanostructured materials, layered zeolites offer the possibility to combine the high reactivity and thermal stability of zeolites catalysts with the versatility of layered solids [1–3]. Among the known layered zeolites, those with FER [4], MWW [5] and MFI [6,7] framework types are notable. The MCM-22 [8–10] (aluminosilicate with MWW [5] topology) is used for the industrial production of ethylbenzene [1,11,12]. The MWW framework features two independent pore systems. The first is composed by 10 Member-Ring (MR) sinusoidal channels (ø ≈ 5.2 Å), running intralayer, whereas the second is composed of internal super-cages with a dimension of 7.1 Å × 18.2 Å, connected to each other by the 10 MR apertures. The MWW zeolites are distinguished by different connection modes between the layers and the connections vary depending on the synthesis procedure. MCM-22(P), the parent of the MCM-22 material [10], is composed of MWW single layers, stacked by the means of hydrogen bonds and dispersion forces [13] with the Organic Structure Directing Agent (OSDA) i.e. hexamethyleneimine (HMI) [8,9]. Upon calcination, the layers condense to form the MCM-22 zeolite [8,14]. If the hydrogen bonds system of MCM-22(P) is swollen, the material can be pillared to form a hierarchical analogue named MCM-36 [15]. Alternatively, the swollen precursor can be delaminated, to form a material with separated single layers named ITQ-2 [16]. By varying the composition of the synthesis gel is it also possible to synthesize a precursor where the single layers are already condensed before the calcination (MCM-49) [17] or scattered from MCM-22(P) (MCM-56) [18–20]. An interesting interpretation of the condensation phenomenon yielding MCM-22 or MCM-56 from MCM-22 (P) predicts that this is governed by the balance between dispersions forces and hydrogen bonds between layers and OSDA molecules [13].

When layered precursors are involved, the 10 MR channels are formed during the hydrothermal crystallization of the zeolite in the presence of the OSDA and the interlayer super-cages are formed throughout the calcination procedure, i.e. during the removal of the OSDA.

For the siliceous analogue, i.e. ITQ-1, the transition between all possible structures is still blurred. This zeolite is promising in catalysis, both as support for active phases nanoparticles or for the insertion of heteroatoms in the framework [21–24]. In this context, a comprehensive study of ITQ-1 combining both structural and morphological aspects is necessary to understand the effects of the synthesis parameters. The synthesis of ITQ-1 is reported to occur with the N,N,

* Corresponding author.
** Corresponding author.
E-mail addresses: eddy.dib@ensicaen.fr (E. Dib), francesca.bonino@unito.it (F. Bonino).
[1] Present address: Istituto Nazionale di Ricerca Metrologica (INRiM), Strada delle Cacce 91, Torino, 10135, Italy.

https://doi.org/10.1016/j.micromeso.2023.112924
Received 22 October 2023; Received in revised form 15 November 2023; Accepted 29 November 2023
Available online 3 December 2023

Table 1
ITQ-1 samples synthesized from different precursor gels, exploiting different calcination procedures.

Sample	Gel molar composition	Calcination procedure
rose-ITQ-1-HS	1 SiO_2 : 0.2 TMAdaOH : 0.3 HMI : 0.07 K_2O : 0.07 CO_3^{2-} : 30 H_2O	none
rose-ITQ-1-calcA	1 SiO_2 : 0.2 TMAdaOH : 0.3 HMI : 0.07 K_2O : 0.07 CO_3^{2-} : 30 H_2O	A
rose-ITQ-1-calcB	1 SiO_2 : 0.2 TMAdaOH : 0.3 HMI : 0.07 K_2O : 0.07 CO_3^{2-} : 30 H_2O	B
sf-ITQ-1-HS	1 SiO_2 : 0.25 TMAdaOH : 0.31 HMI : 44 H_2O	none
sf-ITQ-1-calcA	1 SiO_2 : 0.25 TMAdaOH : 0.31 HMI : 44 H_2O	A
sf-ITQ-1-calcB	1 SiO_2 : 0.25 TMAdaOH : 0.31 HMI : 44 H_2O	B

N-trimethyl-adamantil-ammonium hydroxide (TMAdaOH) as OSDA, but the concurrent use of HMI is necessary for a reproducible procedure [22,25].

In this work, two different compositions of the precursor synthesis gel were chosen as starting point. They differ in water (H_2O) content, ratio between the OSDAs, OH and Si and the presence of alkali cations. Particular attention was paid to the as-synthesized ITQ-1 material to understand the role of OSDAs either during the hydrothermal synthesis or during the calcination. In particular, the role of OSDAs during the synthesis and calcination procedures was disclosed using a combination of spectroscopic, thermogravimetric and elemental analyses on both the organic and inorganic fractions of the materials. The differences in the morphological and structural properties of the ITQ-1 samples were carefully determined by means of diffraction methods, electron microscopy and spectroscopic techniques and the origin of the differences was found to be the amount and location of OSDAs and H_2O molecules in the as-synthesized material.

2. Experimental

2.1. Materials

For the ITQ-1 samples synthesis, Aerosil® 200 (from Evonik Industries), TMAdaOH (25 wt% in water, from TCI), HMI (99 % from Sigma Aldrich), potassium carbonate (K_2CO_3, anhydrous, ACS reagent, from Sigma Aldrich) and Milli-Q water (18.2 MΩ cm) were used. All the reagents were used as received without further purification.

2.2. Synthesis of the ITQ-1 samples

Two sets of ITQ-1 samples using different gels were hydrothermally synthesized. The molar composition of the first gel was 1 SiO_2 : 0.2 TMAdaOH : 0.3 HMI : 0.07 K_2O : 0.07 CO_3^{2-} : 30 H_2O [22]. In a typical procedure, 8.45 g of TMAdaOH solution, 1.49 g of HMI and 0.4837 g of K_2CO_3 were added to 20.68 g of Milli-Q water in this order. The solution was stirred at room temperature for 30 min to allow complete dissolution of K_2CO_3 and then 3.004 g of Aerosil® 200 were gradually added under vigorous stirring, until a homogeneous gel was obtained. The molar composition of the second gel was 1 SiO_2 : 0.25 TMAdaOH : 0.31 HMI : 44 H_2O [25]. In a typical procedure, 7.29 g of TMAdaOH solution and 1.06 g of HMI were added to 21.89 g of Milli-Q water. Thus, 2.0728 g of SiO_2 were gradually added to the above solution under vigorous stirring, until a homogeneous gel was obtained.

Each gel (approximately 30 ml each) was transferred into a 45 ml Telfon lined stainless steel digestor and heated at 150 °C for 5 days under tumbling conditions, at 60 rpm. After the hydrothermal crystallization, the samples were recovered by filtration, washed with deionized water until a pH < 8 was reached and dried at room temperature. Two as-synthesized samples obtained from gels with different molar compositions are called rose-ITQ-1-HS and sf-ITQ-1-HS respectively. A portion of each as-synthesized sample was calcined in a tubular oven with two different procedures: *procedure A* consists in the heating of the sample with a rate of 1 °C/min till 550 °C under flow of dry air, followed by 7 h heating under the same flow; *procedure B* consists in heating the sample with a ramp of 1 °C/min till 580 °C, under a flow of N_2, followed by 3 h heating under a flow of O_2. The temperatures (580 or 550 °C) and the length (7 or 3 h) of the isotherms, coupled with each atmosphere were chosen to obtain samples with more divergent properties, based on preliminary results (not shown for the sake of brevity). Thus, the calcined zeolite samples are called rose-ITQ-1-calcA, rose-ITQ-1-calcB, sf-ITQ-1-calcA and sf-ITQ-1-calcB. The synthesis conditions and the sample names are summarized in Table 1.

2.3. Characterization of ITQ-1 samples

X-Rays Diffraction (XRD) patterns were collected on the as-synthesized and calcined samples with a Cu K_α radiation, on a PANanalytical X'Pert diffractometer (Bragg-Brentano geometry), equipped with a X'celerator strip detector, in the range $5° \leq 2\theta \leq 50°$, with a step of 0.02° and 50 s/° of integration. Cu K_β was suppressed with a Ni filter.

Scanning Electron Microscopy (SEM) images of the as-synthesized and calcined samples were obtained using a Mira\\Tescan microscope. The images were collected on the metal sputtered samples (70:30 Pt:Pd film of thickness of 2 nm). The distribution of zeolite particles with different thicknesses (particles dimension along the *c* axis) was measured based on at least 175 particles per samples.

N_2 physisorption isotherms of the calcined samples were recorded on a Micromeritics 3Flex instrument at −196 °C. Prior to the measurement, the powders were outgassed overnight at 120 °C and at least 7 h at 400 °C. The Specific Surface Areas (SSAs) were determined with both the Brunauer-Emmett-Teller (BET) and Langmuir models. The models were applied in pressure ranges suitable for obtaining a monolayer capacity included in the selected p/p^0 (for the BET) or p (for the Langmuir) linearization range [26]. The cumulative pore volume and the pore size distribution were obtained by applying the Non-Local Density Functional Theory (NL-DFT); the pores were modelled as slit pores, using the "N_2@ 77-Carbon, original DFT" available in the Microactive software [27]. The model was applied in the whole range of p/p^0 with a regularization of 10^{-3}.

The infrared (IR) spectra of the calcined samples were recorded both in transmission and in Attenuated Total Reflectance (ATR) mode. The transmission IR spectra were collected with a Bruker Vertex 70 spectrophotometer, equipped with a Mercury Cadmium Telluride (MCT) cryo-detector on a self-supporting pellet of the pure sample, placed inside a quartz cell with KBr windows. The pellet was mechanically protected by a gold envelope and treated prior to the acquisition to remove the physisorbed molecules and possible organic pollutants. The treatment provides a 5 °C/min ramp to 500 °C followed by 30 min in isothermal conditions at 500 °C while outgassing. Then, 100 mbar of pure O_2 were dosed in the cell while at 500 °C and left in contact with the sample for 30 min to oxidize organic residues. The sample was then outgassed at 500 °C until the final pressure was $<10^{-3}$ mbar. The spectrum was acquired under vacuum at *ca.* 40 °C (the temperature reached by the sample under the IR beam), by accumulating 32 scans (64 for the background) at 2 cm^{-1} of resolution. The spectra intensity was internally normalized to the overtones bands of bulk vibration modes (bands peaked at 1990, 1877 and 1665 cm^{-1}). The ATR-IR spectra were collected on the powdered sample without pre-treatment

accumulating 64 scans (128 for the background) at 2 cm^{-1} of resolution on a Bruker Vertex 70 spectrophotometer equipped with a Deuterated TriGlycine Sulfate (DTGS) detector and an ATR Platinum accessory, equipped with a single reflection diamond internal reflection element. The spectra were internally normalized in intensity using the symmetric Si–O–Si stretching band, centered at 800 cm^{-1}.

The Raman spectra of the calcined samples were measured in air without pre-treatment using the 244 nm excitation line (Coherent MotoFred 300C, frequency doubled Ar^{+} laser) on a Renishaw inVia Raman microscope spectrometer, equipped with 3600 line/mm grating and UV-enhanced Charge-Coupled Device (CCD) detector. The laser was focused on the sample through a 15x objective.

One Pulse (OP) ^{29}Si and Cross Polarization (CP) $^{29}Si\{^{1}H\}$ Magic-Angle Spinning (MAS) Nuclear Magnetic Resonance (NMR) spectra were acquired at 79.4 MHz on a Bruker Avance III-HD 400 (9.4 T), using 4.0-mm outer diameter probe. For OP, a radiofrequency of 30 kHz and a recycle delay of 15 s was used. A recycle delay of 5 s and a contact time of 5 ms were used for ^{29}Si CP-MAS experiments. For ^{29}Si OP- and CP-MAS experiments 4096 and 2048 transients were acquired respectively. The ^{29}Si OP-MAS spectra of the calcined rose-ITQ-1-calcA and rose-ITQ-1-calcB and of the as-synthesized rose-ITQ-1-HS samples were deconvoluted with Lorentzian peaks, using the program Fityk. For the calcined samples, the deconvoluted peaks were added at chemical shift values that were kept coherent with theoretical chemical shifts computed with the following equation (eq. (1)) [28].

$$\delta_{iso} = 11.531\langle r_{SiO}\rangle + 27.280\sigma(r_{SiO}) + 83.7430\cos(\langle\theta_{SiOSi}\rangle) + 0.20246\sigma(\theta_{SiOSi}) - 59.999 \quad (1)$$

Where δ_{iso} is the chemical shift (ppm), $\langle r_{SiO}\rangle$ is the average Si–O distance, $\sigma(r_{SiO})$ is its standard deviation, $\langle\theta_{SiOSi}\rangle$ is the average Si–O–Si angle and $\sigma(\theta_{SiOSi})$ is its standard deviation. The Si–O–Si angles and the Si–O distances were obtained from the cif file for the MWW framework, downloaded from the Database of Zeolite Structures present on the website of the International Zeolite Association (IZA) [29], without further refinement.

^{13}C OP-MAS-NMR spectra of the as-synthesized rose-ITQ-1-HS and sf-ITQ-1-HS samples were acquired at 100.6 MHz on a Bruker Avance III-HD 400 (9.4 T), using 4.0-mm outer diameter probe. Radiofrequency pulses of 38.5 kHz and a recycle delay of 2 s were used. For each spectrum, 6000 transients were acquired.

The elemental analysis of the as-synthesized samples was performed using a Thermo Nicolet FlashEA 1112 Series CHNS analyzer; the measurement was repeated three times for each as-synthesized sample and the results were averaged.

The Thermogravimetric (TG) analyses of the as-synthesized samples were performed with a SDT Q600 analyzer by TA instrument, placing approximately 6 mg of sample inside the alumina pan. Each as-synthesized sample was analyzed with the following two procedures. *Procedure A:* heating ramp of 1 °C/min to 550 °C under dry air flow, followed by heating for 3 h under the same flow. *Procedure B:* heating ramp of 1 °C/min to 580 °C under N_2 flow, followed by a 3 h heating under dry air flow. The flow was set to 100 ml/min and the isotherm of *procedure A* was limited to 3 h because the plateau was already achieved.

The calcination procedure of the samples was followed by transmission IR; a self-supporting pellet of pure as-synthesized samples, mechanically protected by a gold envelope was used. The pellet was placed inside the heating element of an AABSPEC CXX cell, equipped with two thermocouples to control the temperature of the sample and to work under gas flow. Each as-synthesized sample was measured with the following experimental procedures. *Procedure A*: 30 min under flow at 30 °C for the sake of equilibration, heating ramp of 1 °C/min to 550 °C under a flow of 20 vol% O_2 in Ar, followed by 3 h heating under the same flow. *Procedure B*: 30 min under flow at 30 °C for the sake of equilibration, heating ramp of 1 °C/min to 550 °C under a flow of pure Ar, followed by 3 h heating under a flow of 20 vol% O_2 in Ar. Ar was used as inert gas instead of N_2 for the mass analysis. The spectra of the pelletized sample during the heating were collected each 4 min accumulating 32 scans, with a resolution of 4 cm^{-1}, on a Thermo Scientific Nicolet iS50 FTIR spectrometer, equipped with an MCT detector. The gas phase downstream to the cell was analyzed by mass spectrometry (Quadrupole Pfeiffer Omnistar GSD 301).

3. Results and discussion

3.1. Characterization of crystalline structure and morphology of ITQ-1 samples

Fig. 1 shows the XRD patterns of the as-synthesized rose-ITQ-1-HS and sf-ITQ-1-HS samples (a) and of the calcined rose-ITQ-1-calcA, rose-ITQ-1-calcB (b), sf-ITQ-1-calcA and sf-ITQ-1-calcB (c) samples in the 5°–50° 2θ range. The XRD patterns of the samples reveal the MWW topology, and the positions and bandwidth of the reflections are consistent with what reported in the literature [22,25,30]. A pronounced difference between the as-synthesized and the corresponding calcined patterns can be noted. It testifies a significant structural change that induces variation of specific reflections. The Bragg peaks with Miller indexes *hk*0 (e.g. 100, 200, 220 and 310, corresponding to directions parallel to the *ab* plane) do not move upon calcination, while those with Miller indexes *hkl* with $l \neq 0$ (e.g. 002, 101 and 102, directions that have a component perpendicular to the *ab* plane) shift to high 2θ angles [9,30] (Fig. S1). This indicates that the as-synthesized rose-ITQ-1-HS and sf-ITQ-1-HS samples are formed of separated single layers, as MCM-22(P), that condense upon calcination, causing the contraction of the unit cell along the *c* direction, as already reported [22,25,30].

Both the as-synthesized and calcined samples display sharp and broad reflections. The sharp ones have Miller indexes *hk*0, suggesting a pronounced preferential growth of the crystal parallel to the *ab* plane. Moreover, among the broad peaks (having Miller indexes *hkl* with $l \neq 0$), those in the XRD patters of samples sf-ITQ-1-HS, -calcA and -calcB are even broader and less resolved than their analogue in samples rose-ITQ-1-HS, -calcA and -calcB. This indicates that the broadening occurs along the *c* direction. It could be a lower degree of order or a lower crystal dimension along the *c* axis in sample sf-ITQ-1 compared to sample rose-ITQ-1.

To clarify this point, SEM images were recorded at different magnifications (Fig. 2 and Figs. S2–S7). No relevant difference in morphology is observed comparing each as-synthesized sample (rose-ITQ-1-HS and sf-ITQ-1-HS) with the corresponding calcined ones, so the calcination procedure does not seem to affect the morphology. Modifications in the aggregation way are instead observed by comparing samples obtained with different molar composition of the synthesis gel (namely rose-ITQ-1-HS, -calcA or -calcB on one hand and sf-ITQ-1-HS, -calcA or -calcB on the other). The low magnification images of the rose-ITQ-1 show rose-like small agglomerates of uniform size and shape (Fig. 2a,e,i), while sf-ITQ-1 samples form hollow macro-sized sphere aggregates (Fig. 2c,g,k). The properties of the hollow spheres (sf-ITQ-1) were investigated: the average particle diameter (Table 2) and the corresponding size distribution (Fig. S9) were measured. The size distribution is very similar among the as-synthesized and the calcined samples and it is not affected by the calcination procedure. The

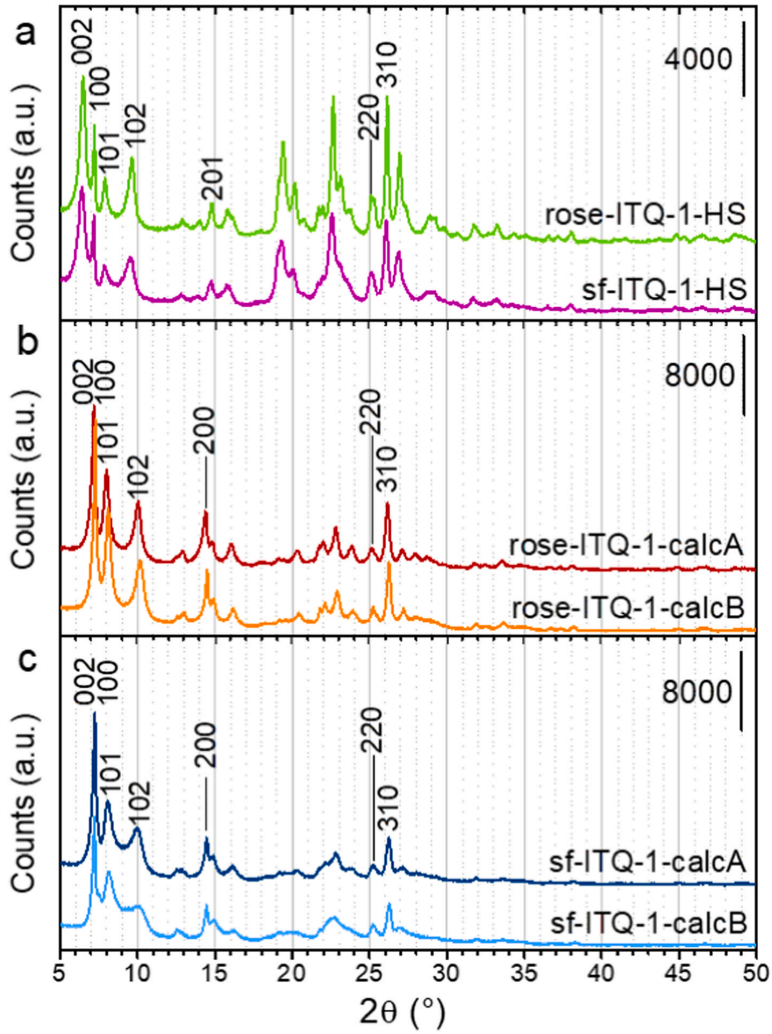

Fig. 1. XRD patterns of the as-synthesized rose-ITQ-1-HS and sf-ITQ-1-HS samples (a), calcined rose-ITQ-1-calcA and rose-ITQ-1-calcB (b), and calcined sf-ITQ-1-calcA and sf-ITQ-1calcB (c) samples.

aggregation in zeolites with MWW framework was already reported in the literature, but it was obtained by employing a carbon black [31] or BP 2000 [32] as hard templates or di-quaternary ammonium surfactants [33] as soft templates in the case of MCM-22. In our study, it is possible that higher TMAdaOH/SiO_2 and HMI/SiO_2 ratios in the precursor synthesis gel used for preparation of sample sf-ITQ-1-HS give rise to the formation of aggregated hollow macro-sized spheres. In contrast, rose-like small aggregates are obtained at lower TMAdaOH/SiO_2 and HMI/SiO_2 ratios. Further studies are needed to clarify the effect of OSDAs on the macro-sphere formation.

Regardless of how they are assembled, the primary particles of ITQ-1 are nanosheets of nearly hexagonal morphology, as shown in Fig. 2b,d,f, h,j,l. The average nanosheet thickness (Table 2) and the corresponding thickness size distribution (Table S1 and Fig. S8) were measured. The sf-ITQ-1-HS, -calcA and -calcB samples have slightly thinner particles than the rose-ITQ-1-HS, -calcA and -calcB. The thickness size distribution plots are quite superimposed, but the maximum of each distribution is clearly distinguishable and different for each sample. The variation of the nanosheet thickness can be related to the differences in peaks broadening observed in the XRD patterns, by applying the following assumptions: (1) the size of the crystallite domain could be compared to the size of the hexagonal nanosheets visible in the SEM images and (2) the broadening of the XRD peaks is the manifestation of the average crystallite dimension, mediated on the bulk of the material (represented by the slight shift of the thickness size distribution). Accordingly, the sf-ITQ-1-HS, -calcA and -calcB samples, that display a greater peak broadening along *c* axis, are composed of thinner particles compared to rose-ITQ-1-HS, -calcA or -calcB. Furthermore, the lower particle thickness causes a lower coherence in diffraction along *c* axis. If the layers stack in an uneven way during the hydrothermal treatment, the crystal growth would probably be more frequently interrupted and the crystals would be thinner. We observe that the layer stack in the rose-ITQ-1 sample occurs in a more aligned way, resulting in crystals growth along the *c* axis (sharper Bragg reflections), while, in the sf-ITQ-1 samples, a slight mismatch between the layers hinders the growth along *c* axis and thinner nanosheets are formed. The thickness size distribution

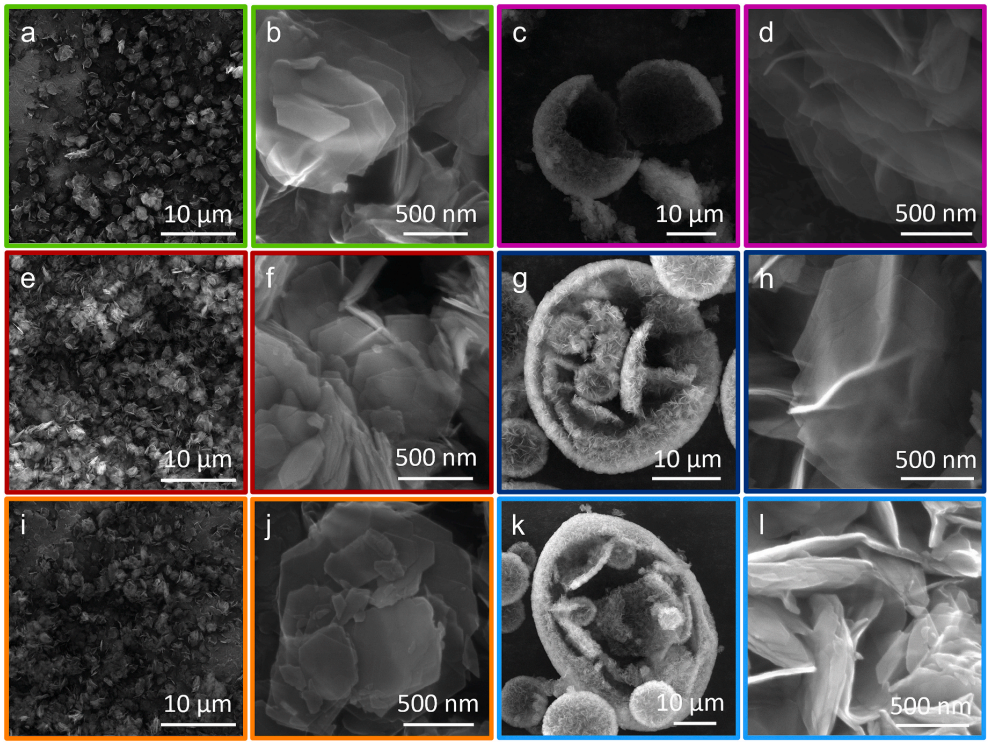

Fig. 2. SEM images at different magnifications of samples rose-ITQ-1-HS (a, b - green), sf-ITQ-1-HS (c, d - purple), rose-ITQ-1-calcA (e, f - red), sf-ITQ-1-calcA (g, h - blue), rose-ITQ-1-calcB (i, j - orange) and sf-ITQ-1-calcB (k, l – light blue). For each sample, the image on the left is at high magnification and the image on the right is at low magnification.

Table 2
Average nanosheets thickness (particle dimension along the *c* axis) of all the samples and sphere diameters of sf-ITQ-1 samples.

Sample	Particle thickness (nm)	Spheres diameter (µm)
rose-ITQ-1-HS	21 ± 1	–
rose-ITQ-1-calcA	23 ± 1	–
rose-ITQ-1-calcB	18 ± 1	–
sf-ITQ-1-HS	14 ± 2	14 ± 1
sf-ITQ-1-calcA	14 ± 1	13 ± 1
sf-ITQ-1-calcB	13 ± 1	11 ± 1

is also moderately affected by the calcination procedure, since the rose-ITQ-1-calcA and sf-ITQ-1-calcA samples are slightly thicker than their analogues rose-ITQ-1-calcB and sf-ITQ-1-calcB, respectively.

The textural properties of all the calcined samples were studied by N_2 physisorption at −196 °C. The N_2 physisorption isotherms plotted in linear (a) and logarithmic (b) scale are reported in Fig. 3. All isotherms are of type I, typical of microporous materials, with a H3 hysteresis loop at high relative pressure values (arising from the filling of interparticle voids between plate-like particles) [26]. The SSAs obtained with the BET and Langmuir models and the micropore volume (Table 3, S2, S3 and Figs. S10–S12) are coherent with the zeolitic framework type [5]. The samples calcined with *procedure B* exhibit a significantly lower micropore volume and SSAs values than those calcined with *procedure A* (Fig. 3c), probably due to a partial occlusion of the pores during the heating ramp under inert flow. This is particularly evident for sf-ITQ-1-calcB. Moreover, sf-ITQ-1 samples show an additional family of voids in the micropore range (10–20 Å), not related with the crystalline framework structure. This could be ascribed to random voids located in the interlayer space as a consequence of the mismatch in the layers stacking.

3.2. Spectroscopic characterization of ITQ-1 samples

The differences between the ITQ-1 samples at an atomic scale were revealed by an IR spectroscopic study. The low frequency region of ATR-IR and Raman spectra of the ITQ-1 samples are depicted in Fig. 4a and b. The vibrations are collective bending modes of groups of atoms that have specific positions. Information about the structural order can be obtained from the broadening of the bands [19,34,35]. In the ATR-IR spectra of zeolites with MWW topology, bands assigned to the stretching of double-6-ring (D6R) [36–38] units are present. They are centered at 611 and 562 cm^{-1} in the ATR-IR spectra of all the samples, but appear broader and less intense in the sf-ITQ-1 than in rose-ITQ-1 samples, probably due to their higher defectivity. This is in line with what observed by XRD. The low frequency region of the Raman spectra (Fig. 4b) provides similar information. Bands assigned to collective vibrations of rings composed of different number of tetrahedra are present [39,40]. In our spectra, a group of bands at 522, 483 and 345 cm^{-1} could be assigned to the bending vibrations of 4-, 5- and 6-member ring groups in the MWW framework, respectively [39]. The above mentioned bands have a lower intensity for sf-ITQ-1-calcA and sf-ITQ-1-calcB samples compared to rose-ITQ-1-calcA and rose-ITQ-1-calcB. This further confirms the higher defectivity of sf-ITQ-1 samples.

In the higher frequency region of the ATR-IR spectra (Fig. 4a), a broad band at 960 cm^{-1} covering almost the whole transparency window between the asymmetric (1300-900 cm^{-1}) and symmetric (850-750 cm^{-1}) Si–O–Si stretching bands is observed [35]. The band at 960

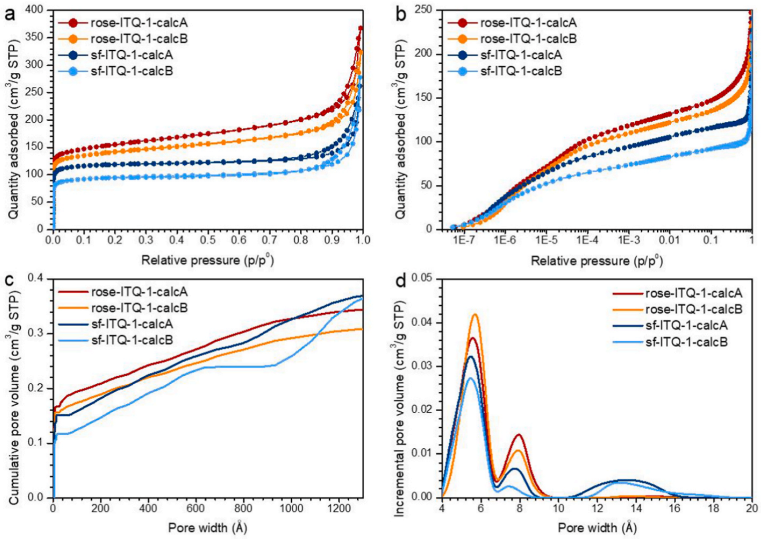

Fig. 3. Volumetric N_2 adsorption/desorption isotherms at - 196 °C in the whole relative pressure range, plotted in linear (a) and semi-logarithmic scale (b). Cumulative pore volume plot in the 0–1300 Å pore size range (c) and pore size distributions in the micropore size range (<20 Å, points connected by a B-spline function) (d), computed by NL-DFT method applied to the N_2 adsorption isotherms in the whole relative pressure range.

Table 3
SSAs calculated with the BET and Langmuir models and micropore (V_{micro}) and interparticle voids (V_{ipv}) volumes computed using the NL-DFT method.

Sample	BET SSA[a] (m^2/g)	Langmuir SSA[b] (m^2/g)	V_{micro}[c] (cm^3/g STP)	V_{ipv}[d] (cm^3/g STP)
rose-ITQ-1-calcA	586 ± 1	676 ± 5	0.17	0.03
rose-ITQ-1-calcB	538 ± 1	616 ± 4	0.16	0.03
sf-ITQ-1-calcA	465 ± 2	525 ± 1	0.15	0.03
sf-ITQ-1-calcB	368 ± 1	417 ± 2	0.12	0.03

[a] Calculated in the 0.008–0.08 p/p^0range.
[b] Calculated in the 15–200 mbar pressure range.
[c] Calculated from the cumulative pore volume plot for pores size <20 Å
[d] Calculated from the cumulative pore volume plot by difference of the total pore volume by V_{micro}.

cm^{-1} was already observed in siliceous zeolites such as silicalite-1 and it is associated to a localized stretching mode of the O_3Si–OH group [35]. The presence of silanols groups in a siliceous material constitutes an irregularity in the periodic crystalline structure and hence silanols are considered as "point defects" in the zeolite framework. When silanols are located at the crystal surface, they are generally described as isolated, while when they are associated to the vacancy of a Si atom they are described as silanol nests. Unfortunately, the localized stretching mode of the O_3Si–OH group does not allow discriminating the amount or kind of hydroxyl groups. For this reason, the O–H stretching region (3800-3000 cm^{-1}) of the IR spectra recorded in transmission mode is presented in Fig. S13. Here, the higher frequency component (3745 cm^{-1}) is associated to external isolated silanols, while the presence of chains of hydrogen bonded (H-bonded) silanols is testified by a couple of signals due to the terminal OH group and to the OH involved in the H-bond chain. The vibration of the terminal OH group is centered at 3740 cm^{-1} in rose-ITQ-1 and at 3730 cm^{-1} in sf-ITQ-1 samples and the vibration of the H-bonded OH is present in the region 3650-3500 cm^{-1} as a broad shoulder. These hydroxyls are probably located in the interparticle space between adjacent nanosheets. The frequency of the band associated to the chain-terminal and H-bonded OH depends on the length of the chain: the longer the chain, the stronger the interaction and the lower the frequency of the signal observed [41–44]. At even lower frequency, a broad band assigned to silanol nests is present. This band has a different intensity in the four samples, corresponding to a distinct amount of "point defects" in the materials, with the following order: rose-ITQ-1-calcB < rose-ITQ-1-calcA < sf-ITQ-1-calcB < sf-ITQ-1-calcA. The higher defectivity of sf-ITQ-1 samples is coherent with their lower long-range crystalline order and lower particle thickness. Additionally, a difference in the number of defective sites depending on the calcination procedure is clearly observed. The rose-ITQ-1-calcB and sf-ITQ-1-calcB samples, calcined with *procedure B,* are slightly less defective than their analogues rose-ITQ-1-calcA and sf-ITQ-1-calcA, calcined with *procedure A*.

The effect of chemical composition of the synthesis gel and the calcination procedure on the long-range crystalline order and defectivity of the samples will be explained in the following section.

Fig. 4c shows the ^{29}Si MAS-NMR spectra recorded with OP experiments of all the calcined and as-synthesized ITQ-1 samples. The as-synthesized samples show well resolved signals, independently of the composition of the synthesis gel (rose-ITQ-1-HS or sf-ITQ-1-HS). After the calcination, the resolution is preserved for the rose-ITQ-1-calcA and rose-ITQ-1-calcB samples while it is lost for the sf-ITQ-1-calcA and sf-ITQ-1-calcB samples. This is due to a higher local disorder (wider angular distribution) or to a higher amount of structural defects, which is in accordance with the higher silanols concentration (see transmission

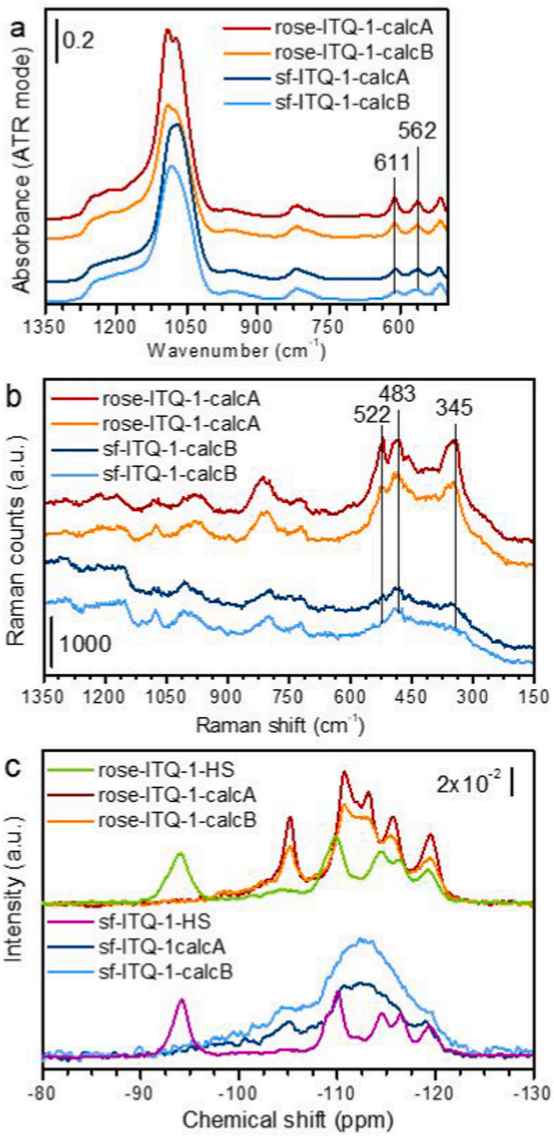

Fig. 4. ATR-IR spectra in the 1350-500 cm^{-1} range (a) and Raman spectra in the 1350-150 cm^{-1} range (b) of the calcined rose-ITQ-1-calcA, rose-ITQ-1-calcB, sf-ITQ-1-calcA, sf-ITQ-1-calcB samples, and ^{29}Si-OP-NMR spectra of the as-synthesized rose-ITQ-1-HS and sf-ITQ-1-HS and calcined rose-ITQ-1-calcA, rose-ITQ-1-calcB, sf-ITQ-1-calcA and sf-ITQ-1-calcB samples (c).

IR spectra in Fig. S13). Indeed, the ^{29}Si isotropic chemical shift observed in purely siliceous zeolites is linked to several structural parameters, among which $\langle\theta_{SiOSi}\rangle$ at each crystallographic site is the most relevant. In principle, each crystallographic site would produce a distinct signal in the ^{29}Si OP-MAS-NMR spectrum, at a distinct chemical shift value depending on $\langle\theta_{SiOSi}\rangle$. If the $\langle\theta_{SiOSi}\rangle$ distribution for a given site (namely its angular distribution) is wide, the corresponding NMR signal will broaden. Hence, the signal broadening increases together with the local disorder of the structure. Therefore, a reduced signal resolution as observed in sf-ITQ-1-calcA and sf-ITQ-1-calcB samples is an indication of the degree of local disorder.

A peculiarity is found in the spectra of the as-synthesized rose-ITQ-1-HS and sf-ITQ-1-HS samples. They show an intense signal at −94 ppm, that may correspond to a Q^3 site (tetrahedral Si site connected to three Si atoms and an atom different from Si) or to a Q^2 site (tetrahedral Si site connected to two Si atoms and two atoms different from Si). The intensity of this signal is an indication of the high amount of silanols in the as-synthesized materials and of their distinguished angular configuration. The peak at −94 ppm is relatively sharp, compared to the Q^3 site signals in the ^{29}Si CP-MAS-NMR spectra of calcined samples, obtained with a {^{1}H–^{29}Si} cross polarization (Fig. S15). This suggests that the signal at −94 ppm could be ascribed to a specific crystallographic position and that it could not be representative of a statistical distribution of silanol defective sites (as the Q^3 signals of calcined samples are). Such a big change in the ^{29}Si OP-MAS-NMR spectra before and after calcination suggests an important structural change, that occurs jointly with the layer condensation. The ^{29}Si OP-MAS-NMR spectral components of the calcined rose-ITQ-1-calcA and rose-ITQ-1-calcB samples were deconvoluted keeping the number of peaks coherent with the number of crystallographic sites of the MWW framework (eight crystallographic sites, named as reported in the Database of Zeolites Structure in the IZA website) [5]. The number of peaks used to deconvolute the spectrum of rose-ITQ-1-HS was considered the same as in the calcined samples, assuming that no modification of the hexagonal symmetry system occurs upon calcination, save the contraction of the *c* cell parameter [14,45]. This is a rough approximation, since the Si–OH groups at the surface of the single layers in rose-ITQ-1-HS, that may contribute to the signal at −94 ppm, are in principle 4 over 72 Si atoms in a unit cell (≈5 %). The relative integrated intensity of the signal at −94 ppm is too high to be exclusively due to 4 Si–OH per unit cell (vide infra), note that the structure refinement of the as-synthesized form of a zeolite with MWW framework has never been published [30]. The calculation of the initial peak positions is performed using equation (1) and the details are reported in Tables S4–S9. Fig. S15 shows the deconvoluted spectra. The relative integrated area of the spectral components of the calcined samples is consistent with the multiplicity of the crystallographic sites in the unit cell: three and five peaks show an integrated relative area coherent with a multiplicity of four and twelve respectively (Tables S7–S9). The deconvolution of the spectrum of the as-synthesized rose-ITQ-1-HS sample assuming two peaks at −94 and −93 ppm was performed. The two components are likely to be Q^3 sites [14] and hence an exceptionally high amount of Si–OH groups is present in the as-synthesized material (≈22 %), already reported in the literature [45,46]. Despite the high amount of silanol groups, rose-ITQ-1-HS sample is crystalline, thanks to the presence of the coordinated OSDAs molecules. As previously reported, the Si–OH groups present in the as-synthesized material should condense upon calcination, by H_2O removal, generating the 3D zeolite [14,30,46]. The amount of Si–OH groups in the purely siliceous as-synthesized zeolite ITQ-1 is too high to be ascribed to a simple condensation of perfectly formed separated layers (as what occurs e.g. in the borosilicate analogue) [14] and for this reason a more complex phase transition must occur.

3.3. Role of OSDA in ITQ-1 synthesis

The ITQ-1 samples synthesized here show different properties: the macroscopical aggregation and the primary particle thickness (related to a long-range crystalline order, as highlighted by XRD and SEM microscopy) and the amount of defective sites and the difference in angular distribution at the crystallographic sites (related to a short-range crystalline order, as depicted by spectroscopic methods). These features seem to be affected by both the composition of the synthesis gel and by the calcination procedure. The effect of the synthesis gel composition was examined by studying the organic fraction in the as-synthesized material and the presence of alkali cations in the framework. The effect of the calcination procedure resulting in the OSDA removal was

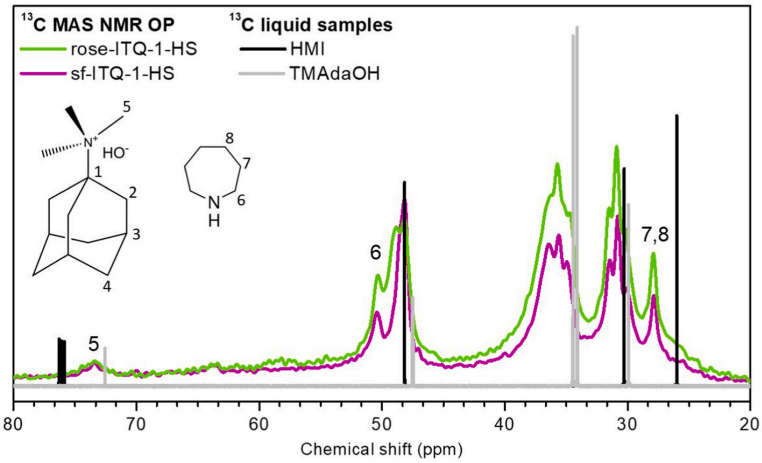

Fig. 5. ^{13}C OP-NMR spectra of as-synthesized rose-ITQ-1-HS and sf-ITQ-1-HS samples, compared with the liquid phase spectra of the pure OSDAs (HMI and TMAdaOH).

Table 4
C/N ratio, OSDAs per unit cell and OSDAs ratio for the rose-ITQ-1 and sf-ITQ-1 synthesis gels and for the as-synthesized samples determined by elemental analysis CHNS. 72 Si atoms are used to calculate the $TMAda^+$, HMI and H_2O molar ratio per unit cell in the synthesis gel composition.

	Synthesis gel		As-synthesized samples	
	rose-ITQ-1-HS	sf-ITQ-1-HS	rose-ITQ-1-HS	sf-ITQ-1-HS
C/N	8.80	9.13	9.91	9.92
$TMAda^+$/HMI	0.67	0.81	1.27	1.27
$TMAda^+$/unit cell	14.4	18.00	3.95	3.60
HMI/unit cell	21.6	22.32	3.11	2.83
$TMAda^+/H_2O$ ($*10^{-3}$)	6.67	5.68	–	–
HMI/H_2O ($*10^{-3}$)	10.00	7.05	–	–
H_2O/SiO_2	30	44	–	–
Si/K	7.14	∞	1326	∞

examined by TG analysis and variable temperature IR experiments.

The ^{13}C OP-MAS-NMR spectra of the as-synthesized rose-ITQ-1-HS and sf-ITQ-1-HS samples are depicted in Fig. 5, compared with the liquid phase spectra of the two OSDA used (HMI and TMAdaOH). The signals in the ^{13}C OP-MAS-NMR spectra are affected by the type and amount of the organic molecules, by their location and by the possible interactions between them. The spectra contain similar signals, thus the different cavities in the two samples host the same organic molecule. If the same molecule would be placed in pores of different shape, its signals would be split or broadened. In MCM-22, HMI is reported to locate in both cavities and $TMAda^+$ is reported to be located only inside the supercages [25,45,46]. The main difference between the spectrum of rose-ITQ-1-HS and sf-ITQ-1-HS is the relative intensity of the signals. The absolute intensity is proportional to the absolute amount of organics in the zeolite, while the relative intensity is associated to the relative concentration of the two OSDAs. A complete assignment of the spectra is ventured due to the overlapping of chemical shifts [46,47]. The different absolute intensity suggests, however, that the amount of organic molecules is not the same in both samples. For this reason, CHNS elemental analysis was performed, and the results are summarized in Tables 4 and S10. The $TMAda^+$/HMI molar ratio is the same in both samples (Table 4), but the total amount of organics is higher in the rose-ITQ-1-HS than in the sf-ITQ-1-HS. Less OSDA molecules are incorporated in sample sf-ITQ-1-HS during the hydrothermal crystallization. The reduced incorporation could be ascribed to the stronger gel dilution (lower HMI/H_2O and $TMAda^+/H_2O$ ratios in Table 4). This may be the reason behind different stackings of the layers and the lower order along the *c* axis as shown by the sf-ITQ-1-HS, -calcA and -calcB samples. This is even more evident when the amount of $TMAda^+$ per unit cell is considered. Since $TMAda^+$ is the only OSDA placed in the internal supercages, it is the main directing agent responsible for the stacking. Considering that its theoretical amount should be 4 cations/unit cell [45], this number is perfectly respected in sample rose-ITQ-1-HS, while it is not the case for sf-ITQ-1-HS sample. A shortage of $TMAda^+$ cations will induce a more frequent layer mismatch, that generates more Si–OH defective groups at the junctions. The HMI/unit cell (in principle 3), as well, is in slight excess in the rose-ITQ-1-HS sample. The lower amount of HMI in the sf-ITQ-1-HS sample makes impossible to supply for the lack of $TMAda^+$ and probably induces the formation of additional Si–OH groups, justifying the higher amount of silanol nests visible in the transmission IR spectra of sf-ITQ-1-calcA and sf-ITQ-1-calcB samples. Despite the lack of OSDA molecules, sample sf-ITQ-1-HS crystallized in the excess of H_2O molecules, that acts as space filler.

Furthermore, the higher OH/Si ratio in sf-ITQ-1 in respect to that one of rose-ITQ-1 may influence the surface charge of the layers. This could obstacle the correct stacking and consequently the $TMAda^+$ incorporation.

The lower defectivity exhibited for rose-ITQ-1-calcA and -calcB samples compared to samples sf-ITQ-1-calcA and -calcB could also be influenced by the presence of K^+ cations, coming from the K_2CO_3 used for the preparation of the precursor gels, sometimes acting as inorganic SDA. However, no K^+ was detected by chemical analysis, since it is not retained in the structure and its residual amount in the structure is negligible (Tables 4 and S11).

The transmission IR spectra (Fig. S13) showed that the defectivity of the calcined samples was also slightly affected by the calcination procedure, the gel composition being equal, as highlighted by the behavior of band assigned to Si–OH nests in the different samples. The calcination procedure was further followed by TG and variable temperature transmission IR spectroscopy, adopting the same calcination procedures (*procedure A* and *procedure B*). The TG curves (Fig. 6) show weight losses tentatively explained by using the DTG curves and the IR experiments. The species expected to degrade/leave the sample during the calcination are the HMI, the $TMAda^+$ and the H_2O produced upon condensation of the Si–OH groups. The OSDAs degradation occurs in the same way, when the same calcination procedure was used, regardless of the

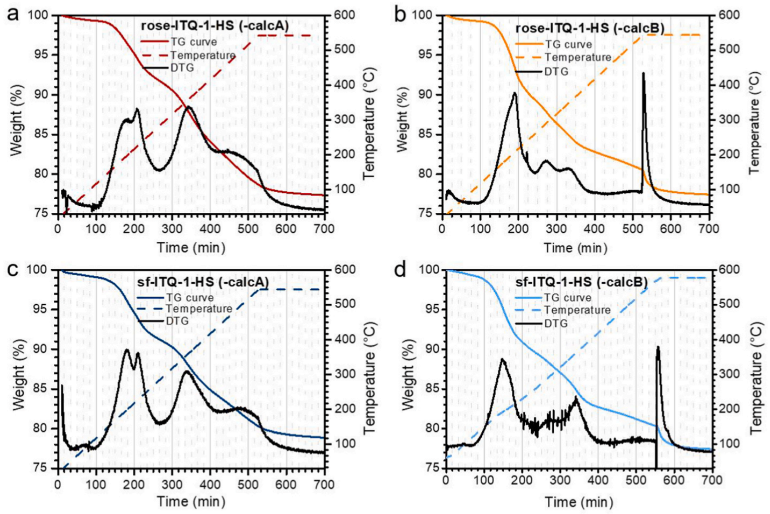

Fig. 6. TG analyses of rose-ITQ-1-HS sample calcined with *procedure A* (a), rose-ITQ-1-HS sample calcined with *procedure B* (b), sf-ITQ-1-HS sample calcined with *procedure A* (c) and sf-ITQ-1-HS sample calcined with *procedure B* (d). *Procedure A*: 1 °C/min up to 550 °C under dry air, followed by 3 h in isothermal conditions under the same flux. *Procedure B*: 1 °C/min up to 580 °C under N_2 flux, followed by 3 h in isothermal conditions under dry air.

synthesis gel composition (rose-ITQ-1-HS or sf-ITQ-1-HS). The DTG curves of the samples calcined with *procedure A* (Fig. 6a,c) present four peaks, suggesting that the degradation of the organic molecules proceed by several steps. The DTG curves of those calcined with *procedure B* (Fig. 6b,d) show instead three broad signals and one very sharp peak, which is due to the sudden oxidation of any organic residuals occurring by switching from N_2 to air flow. A moderately sharp peak is visible at around 200 °C in the DTG of all the samples, and it is probably due to the H_2O loss. The results are consistent with the previous reports on phase transition between separated single layers and calcined zeolite phases [14]. The combination of the elemental CHNS analysis data with the TG analysis allows also justifying the exceptionally high amount of Si–OH groups visible in the ^{29}Si OP-MAS-NMR spectra of the as-synthesized samples (Fig. 4c). The amount of H_2O produced upon calcination, determined by difference between the quantification with TG and with CHNS analysis, was coherent with the equivalent number of H_2O molecules generated during the condensation of the amount of Si–OH groups before the calcination as determined by the ^{29}Si OP-NMR spectra shown in Fig. 4c. This means that, even if a simple condensation of the layers is unlikely to occur as explained earlier by the deconvolution of the ^{29}Si NMR spectra, we saw that an exceptionally high amount of Si–OH groups in the as-synthesized material (≈22 %) undergoes

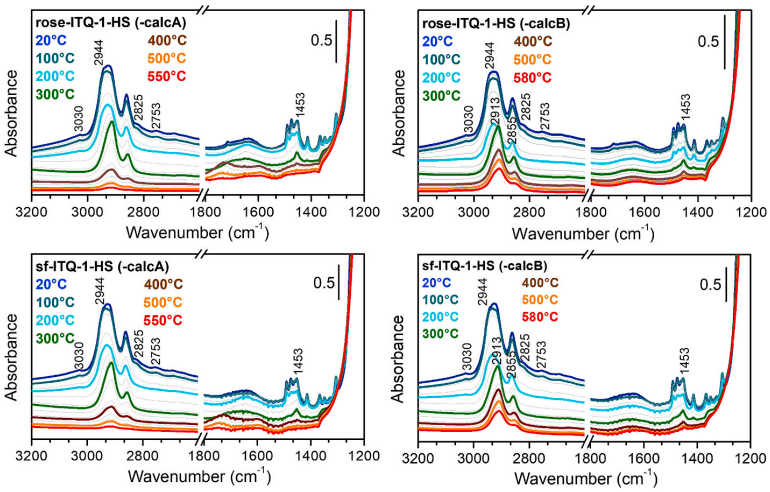

Fig. 7. Transmission IR spectra of rose-ITQ-1-HS sample calcined with *procedure A* (a), rose-ITQ-1-HS sample calcined with *procedure B* (b), sf-ITQ-1-HS sample calcined with *procedure A* (c) and sf-ITQ-1-HS sample calcined with *procedure B* (d). The grey spectra shown are recorded every 20 min. The colored spectra correspond to the temperatures: 20 °C blue, 100 °C dark cyan, 200 °C light cyan, 300 °C green, 400 °C brown, 500 °C orange and 550 °C (a and c panels) or 580 °C (c and d panels) red. *Procedure A*: 1 °C/min up to 550 °C under 20 vol% O_2 in Ar, followed by 3 h in isothermal conditions under the same flux. *Procedure B*: 1 °C/min up to 580 °C under pure Ar flux, followed by 3 h in isothermal conditions under 20 vol% O_2 in Ar.

condensation during the phase transition between the 2D precursor to the 3D calcined zeolite. Details about the determination of the H_2O molecules loss are reported in section 2.3.1 of the ESI.

The identification of several degradation steps of the OSDA molecules were further explored by simulating the calcination procedure and recording the IR spectra during the heating ramps and at 550 °C and 580 °C. Fig. 7 shows the spectra recorded during the heating ramp of the two as-synthesized samples (rose-ITQ-1-HS and sf-ITQ-1-HS), calcined with the two procedures (-calcA or -calcB), reported in the 3200-1200 cm^{-1} spectral range. The full spectra are presented in Fig. S17. The signals of the OSDA molecules are localized in the 3050-2800 cm^{-1} and 1550-1250 cm^{-1} regions. The 3050-2800 cm^{-1} region hosts the C–H stretching mode bands, while the C–H bending and deformation mode bands fall in the 1500-1250 cm^{-1} region. The degradation pathway of the OSDA molecules revealed by diminishing of the IR bands intensity upon the temperature increase. As observed in the TG plots (Fig. 6), the degradation path is only affected by the calcination procedure (*A* or *B*) and not by the synthesis gel composition (the bands decrease in the same way and at the same temperature in panels a–c and b-d, corresponding to the *procedures A* and *B*, respectively). Below 300 °C, the degradation occurs similarly by heating in an oxidant or inert atmosphere. Upon increasing the temperature from 30 °C to 300 °C (see blue, dark cyan, light cyan and green spectra in Fig. 7), the thermal degradation of trimethylamine (TMA) is observed (signals at 3050, 2825 and 2753 cm^{-1}). The TMA is a fragment of the $TMAda^+$ OSDA. The fragmentation of $TMAda^+$ to give TMA and adamantane group (Ada) can occur during the calcination or already during the hydrothermal treatment. The vibrational bands present in the spectra recorded at 30 °C, before starting the calcination (blue spectra in Fig. 7), suggest that the two scenarios are both possible. The bands at 2825 and 2753 cm^{-1} are assigned to the symmetric stretching of CH_3 groups ($\nu_{sym}(CH_3)$) of TMA, meaning that the TMA is already present before the calcination and hence it is partially formed during the hydrothermal treatment. The band at 3030 cm^{-1} is associated to the asymmetric stretching of CH_3 groups ($\nu_{asym}(CH_3)$) in trimethylammonium cations, testifying that $TMAda^+$ is still present in the as-synthesized sample. At 300 °C, the degradation of TMA is completed (note the disappearance of the signals at 3030, 2825, 2753 cm^{-1} in the green spectra). Around 200 °C, the degradation of HMI starts (light cyan spectra) and at 400 °C it is almost finished (brown spectra), as shown by the complete disappearance of the signals at 1453 and 2944 cm^{-1} assigned to a deformation of the CH_2 groups next to the N in HMI ($\delta(CH_2)$) and to the asymmetric stretching of CH_2 ($\nu_{asym}(CH_2)$) and of the signals between 1570 and 1300 cm^{-1} (deformations of the CH_2 group in aliphatic chains). Above 300 °C the degradation pathway deviates depending on the procedure (*A* or *B*). Here the oxidation or the thermal degradation of the Ada fraction of $TMAda^+$ starts. The Ada removal can be followed observing the CH stretching region of the spectra, where signals at 2913 and 2855 cm^{-1} are preserved, and the CH_2 deformation range (band at 1455 cm^{-1}) that is barely visible after the complete elimination of the TMA and of the HMI. When an oxidant atmosphere is used (*procedure A*, shown in Fig. 7a and c) the bands assigned to the Ada group almost completely disappear at the end of the heating ramp (red spectrum). In contrast, in the presence of an inert atmosphere, a significant quantity of Ada is preserved till the end of the heating ramp, at a higher temperature that its sublimation point (109–112 °C), as shown by the presence of both stretching and bending modes of Ada in the red spectra (Fig. 7b,d). In this case Ada is probably trapped into the internal super-cages of the framework, due to its large size (6.8 x 7.6 × 7.4 Å) [48], bigger than the 10 MR apertures. It is, however, immediately burned when O_2 was sent in the flow, (see the lower plots of Figs. S16b and d). This is confirmed by the mass spectrometry analyses of the gas phase downstream to the IR spectrophotometer (Fig. S17). The IR experiments allow disclosing the reason of the slight lower amount of silanol nests in rose-ITQ-1-calcB and sf-ITQ-1-calcB samples compared to rose-ITQ-1-calcA and sf-ITQ-1-calcA materials, respectively. When the *procedure B* is used, a fraction of the OSDAs (the Ada group) is preserved at high temperature, and it is immediately burned by sending O_2 in the flow. The presence of the OSDA at high temperature probably helps healing the defects, determining the lower amount of silanols nests in rose-ITQ-1-calcB and sf-ITQ-1-calcB.

4. Conclusions

In this work, four siliceous zeolitic samples with MWW framework were prepared using different compositions of the precursor synthesis gel and calcination procedures. The XRD and SEM results revealed that the samples differ in particle thickness and crystalline order along the *c* axis. The two properties are related, since when the MWW single layers are stacked in a partially disordered way, the growth along the *c* axis is hindered, because of the more frequent interruption of the crystalline order. The different degree of short crystalline ordering is also observed by IR, Raman and ^{29}Si NMR spectroscopies. The combination of TGA, elemental analysis (CHNS) and ^{13}C NMR spectroscopy allow understanding that the amount of OSDA incorporated in the crystalline sample is higher when the synthesis gel is more concentrated (higher OSDA/H_2O molar ratio), and that this condition is necessary for obtaining the ITQ-1 material with perfectly stacked layers. In particular, the $TMAda^+$, located in the internal super-cages, is responsible for the correct stacking of the layers, while the HMI, located in the sinusoidal channels, is responsible for the formation of individual layers during the hydrothermal treatment [8,22,25]. In the sf-ITQ-1 sample, both the OSDA are in stoichiometric defect, but this is counterbalanced by an excess of H_2O that is acting as space filler. The lack of OSDAs also resulted in the formation of high amount of silanol sites present in the sf-ITQ-1 samples. The zeolites with low order along the *c* axis are more defective, and the defects are probably located at the points where the mismatch between the layers occurs. The defectivity was also proved to be slightly affected by the calcination procedure: indeed, by calcining the sample under inert atmosphere, a fraction of the OSDA was preserved inside the framework even at high temperature and suddenly burned by contact with pure O_2. A slightly lower defectivity of the samples calcined by heating under inert atmosphere was observed instead. Finally, these samples were shown to spontaneously aggregate into hollow macro-spheres and that the way of aggregation is probably regulated by the gel dilution and by the ratio between the two used OSDAs. This property must surely be further investigated due to the boost that macro-voids can give to diffusivity properties.

CRediT authorship contribution statement

Francesca Rosso: Writing – original draft, Visualization, Validation, Methodology, Investigation, Formal analysis, Conceptualization. **Alessia Airi:** Writing – review & editing, Supervision, Investigation, Conceptualization. **Matteo Signorile:** Writing – review & editing, Supervision, Conceptualization. **Eddy Dib:** Writing – review & editing, Validation, Supervision, Methodology, Investigation, Formal analysis, Conceptualization. **Silvia Bordiga:** Writing – review & editing, Resources, Funding acquisition, Conceptualization. **Valentina Crocellà:** Writing – review & editing, Supervision, Conceptualization. **Svetlana Mintova:** Writing – review & editing, Supervision, Conceptualization. **Francesca Bonino:** Writing – review & editing, Supervision, Resources, Project administration, Funding acquisition, Conceptualization.

Declaration of competing interest

The authors declare that they have no known competing financial interests or personal relationships that could have appeared to influence the work reported in this paper.

Data availability

Data will be made available on request.

Acknowledgements

ED and SM acknowledge the support of the Centre for Zeolites and Nanoporous Materials, Label of Excellence, Normandy Region (CLEAR). FR, AA, MS, SB, VC and FB acknowledge support from the Project CH4.0 under the MUR program "Dipartimenti di Eccellenza 2023-2027" (CUP: D13C22003520001).

Appendix A. Supplementary data

Supplementary data to this article can be found online at https://doi.org/10.1016/j.micromeso.2023.112924.

References

[1] W.J. Roth, P. Nachtigall, R.E. Morris, J. Čejka, Chem. Rev. 114 (2014) 4807–4837.
[2] J. Přech, P. Pizarro, D.P. Serrano, J. Cejka, Chem. Soc. Rev. 47 (2018) 8263–8306.
[3] U. Díaz, A. Corma, Dalton Trans. 43 (2014) 10292–10316.
[4] C. Baerlocher, L.B. McCusker, Database of Zeolite Structures, 1978.
[5] C. Baerlocher, L.B. McCusker, Database of Zeolite Structures, 1997.
[6] C. Baerlocher, L. McCusker, Database of Zeolite Structures, 1978.
[7] M. Choi, K. Na, J. Kim, Y. Sakamoto, O. Terasaki, R. Ryoo, Nature 461 (2009) 246–249.
[8] A. Corma, C. Corell, J. Pérez-Pariente, Zeolites 15 (1995) 2–8.
[9] M.E. Leonowicz, J.A. Lawton, S.L. Lawton, M.K. Rubin, 1979, Science 264 (1994) 1910–1913.
[10] M.K. Rubin, P. Chu, Composition of synthetic porous crystalline material, its synthesis and use, Science 325 (4) (1990) 954.
[11] S.I. Zones, Microporous Mesoporous Mater. 144 (2011) 1–8.
[12] T.F. Degnan, C.M. Smith, C.R. Venkat, Appl. Catal. Gen. (2001) 283–284.
[13] M. Položij, H.V. Thang, M. Rubeš, P. Eliášová, J. Čejka, P. Nachtigall, Dalton Trans. 43 (2014) 10443–10450.
[14] R. Millini, G. Perego, W.O. Parker, G. Bellussi, L. Carluccio, Microporous Mater. 4 (1995) 221–230.
[15] H.K. Beyer, H.G. Karge, I. Kiricsi, J.B. Nagy, W.J. Roth, C.T. Kresge, J.C. Vartuli, M. E. Leonowicz', A.S. Fung, S.B. Mccullen, Stud. Surf. Sci. Catal. (1995) 301–308.
[16] A. Corma, V. Fornés, J.M. Guil, S. Pergher, T.L.M. Maesen, J.G. Buglass, Microporous Mesoporous Mater. 38 (2000) 301–309.
[17] S.L. Lawton, A.S. Fung, G.J. Kennedy, L.B. Alemany, C.D. Chang, G.H. Hatzikos, D. N. Lissy, M.K. Rubin, H.K.C. Timken, S. Steuernagel, D.E. Woessner, J. Phys. Chem. 100 (1996) 3788–3798.
[18] A.S. Fung, S.L. Lawton, J. Roth, Wieslaw, Synthetic layered MCM-56, its synthesis and use, US 5,362,697 (1994).
[19] B. Gil, W.J. Roth, W. Makowski, B. Marszalek, D. Majda, Z. Olejniczak, P. Michorczyk, Catal. Today 243 (2015) 39–45.
[20] G.G. Juttu, R.F. Lobo, Microporous Mesoporous Mater. 40 (2000) 9–23.
[21] P. Wu, T. Tatsumi, T. Komatsu, T. Yashimay, J. Catal. 202 (2001) 245–255.
[22] H. Xu, Y. Guan, X. Lu, J. Yin, X. Li, D. Zhou, P. Wu, ACS Catal. 10 (2020) 4813–4819.
[23] T. Wan, F. Jin, X. Cheng, J. Gong, C. Wang, G. Wu, A. Liu, Appl. Catal. Gen. 637 (2022) 118542–118554.
[24] P.M. Piccione, C. Laberty, S. Yang, M.A. Camblor, A. Navrotsky, M.E. Davis, J. Phys. Chem. B 104 (2000) 10001–10011.
[25] M.A. Camblor, A. Corma, M.J. Díaz-Cabañas, C. Baerlocher, J. Phys. Chem. B 102 (1998) 44–51.
[26] M. Thommes, K. Kaneko, A.V. Neimark, J.P. Olivier, F. Rodriguez-Reinoso, J. Rouquerol, K.S.W. Sing, Pure Appl. Chem. 87 (2015) 1051–1069.
[27] Micromeritics Instrument Corporation, 2012.
[28] D.M. Dawson, R.F. Moran, S.E. Ashbrook, J. Phys. Chem. C 121 (2017) 15198–15210.
[29] C. Baerlocher, L.B. McCurker, Database of Zeolite Structures, 2016.
[30] M. Fabbiani, A. Morsli, G. Confalonieri, T. Cacciaguerra, F. Fajula, J. Haines, A. Bengueddach, R. Arletti, F. Di Renzo, Microporous Mesoporous Mater. 332 (2022) 111678–111685.
[31] N. Chu, J. Wang, Y. Zhang, J. Yang, J. Lu, D. Yin, Chem. Mater. 22 (2010) 2757–2763.
[32] A. Schwanke, J. Villarroel-Rocha, K. Sapag, U. Díaz, A. Corma, S. Pergher, ACS Omega 3 (2018) 6217–6223.
[33] S. Cao, Y. Shang, Y. Liu, J. Wang, Y. Sun, Y. Gong, G. Mo, Z. Li, P. Liu, Microporous Mesoporous Mater. 315 (2021) 110910–110921.
[34] M. Król, W. Mozgawa, W. Jastrzbski, K. Barczyk, Microporous Mesoporous Mater. 156 (2012) 181–188.
[35] D. Scarano, A. Zecchina, S. Bordiga, F. Geobaldo, G. Spoto, G. Petrini, G. Leofanti, M. Padovan, G. Tozzola, J. Chem. Soc., Faraday Trans. 89 (1993) 4123–4130.
[36] K. Ogorzały, B. Gil, M. Mazur, W. Makowski, W.J. Roth, Microporous Mesoporous Mater. 324 (2021) 111300–111307.
[37] B. Gil, W. Makowski, B. Marszalek, W.J. Roth, M. Kubu, J. Čejka, Z. Olejniczak, J. Chem. Soc. Dalton Trans. 43 (2014) 10501–10511.
[38] W. Mozgawa, W. Jastrzębski, M. Handke, J. Mol. Struct. (2005) 663–670.
[39] Y. Yu, G. Xiong, C. Li, F.-S. Xiao, Microporous Mesoporous Mater. 46 (2001) 23–34.
[40] F. Fengtao, F. Zhaochi, L. Can, Chem. Soc. Rev. 39 (2010) 4794–4801.
[41] M. Signorile, V. Crocellà, A. Damin, B. Rossi, C. Lamberti, F. Bonino, S. Bordiga, J. Phys. Chem. C 122 (2018) 9021–9034.
[42] S. Bordiga, I. Roggero, P. Ugliengo, A. Zecchina, V. Bolis, G. Artioli, R. Buzzoni, G. Marra, F. Rivetti, G. Spano, C. Lamberti, J. Chem. Soc. Dalton Trans. (2000) 3921–3929.
[43] S. Bordiga, P. Ugliengo, A. Damin, C. Lamberti, G. Spoto, A. Zecchina, G. Spanò, R. Buzzoni, L. Dalloro, F. Rivetti, Top. Catal. 15 (2001) 43–52.
[44] F. Pascale, P. Ugliengo, B. Civalleri, R. Orlando, P. D'Arco, R. Dovesi, J. Chem. Phys. 117 (2002) 5337–5346.
[45] S.L. Njo, H. Van Konigsveld, B. Van De Graaf, C. Barelocher, L.B. Mccusker, in: M. M.J. Treacy, B.K. Marcus, M.E. Bisher, J.B. Higgins (Eds.), 12th International Zeolite Conference, 1999, pp. 2519–2524.
[46] P. Lu, L. Gómez-Hortigüela, M.A. Camblor, Chem. Eur J. 25 (2019) 1561–1572.
[47] S. Sabnis, V.A. Tanna, J. Gulbinski, J. Zhu, S.S. Nonnenmann, G. Sheng, Z. Lai, H. H. Winter, W. Fan, Microporous Mesoporous Mater. 315 (2021) 110883–110890.
[48] F. Jiménez-Cruz, J.L. García-Gutiérrez, Arab. J. Chem. 13 (2020) 8592–8599.

Spectroscopic Characterization of Ti Sites in MWW Zeolite in Presence of Hydrogen Peroxide

Francesca Rosso,[1] Alessia Airi,[1] Matteo Signorile,[1] Silvia Bordiga,[1] Valentina Crocellà,[1] Francesca Bonino[1]*

[1] Department of Chemistry, NIS and INSTM Reference Centre, Università di Torino, Via G. Quarello 15, 10135 and Via P. Giuria 7, 10125, Torino, Italy.

Abstract

Ti-MWW zeolite is a promising catalyst for partial oxidation reactions. In the present work, a Ti-MWW sample with high TiO_2 loading was synthesized. It was revealed that the Ti insertion in the purely siliceous MWW framework mainly occurs during the post treatment washing with HNO_3, when the double structure directing agent synthetic method is used. By exploiting carbon monoxide, acetonitrile, pyridine and ammonia as probe molecules in infrared spectroscopy and diffuse reflectance ultraviolet spectroscopy, the acidic behavior of the Ti sites and the interaction of the Ti sites with hydrogen peroxide (H_2O_2) were revealed. The Ti Lewis acid sites showed stronger acidity than the one observed in Titanium Silicalite-1 (TS-1), with MFI framework. This is coherent with previously reported results, suggesting that a significative fraction of the Ti sites in Ti-MWW are $TiOH(SiO)_3$ instead of $Ti(OSi)_4$. The Ti-peroxo and -hydroperoxo complexes formed upon H_2O_2 were shown to be more labile than in TS-1 and they were shown to be completely reversible upon calcination.

Introduction

Titanium (Ti) doped zeolites are used as shape selective catalysts for partial oxidation reactions (e.g. epoxidations[1–6] or hydroxylations[7–10]), using hydrogen peroxide (H_2O_2) as oxidizing agent.[1,11] A small percentage (2-3%) of silicon (Si) atoms are isomorphously substituted by Ti in the zeolite structure, in absence of other heteroatoms. The isomorphous substitution of Ti provides uncoordinated sites that adsorb H_2O_2 and form Ti-hydroperoxo (Ti-OOH) or -peroxo (Ti-OO) complexes.[12] The transfer of an active oxygen (O) to the organic substrate, with production of a water (H_2O) molecule, ends the catalytic cycle.

The most renowned Ti-zeolite is the Titanium Silicalite-1 (TS-1)[13] with a MFI framework, discovered in 1983 and still the best known and most studied system. From the TS-1 discovery many efforts were made to enhance the performances of Ti-zeolites in the same target reaction. These include refining the properties of the catalyst [14–27]or acting on the reaction conditions.[7,28–30] Among the former, modifications of the synthetic

procedures to improve the amount and speciation of Ti,[11,31–38] diffusion boosting with additional porosity levels[15–19] and changes of the crystalline zeolitic framework [14,20–22,27,39] are the most important. In this work, the attention was focused on Ti-zeolites with MWW framework (Ti-MWW) which have recently been showing very promising catalytic outcomes, tested in many partial oxidation reactions.[5,6,27,40] MWW is a layered framework type[41,42] and hosts two independent pore systems. 10 Member-Ring (MR) sinusoidal channels (diameter of 5.2 Å) run intralayer and a system of internal super-cages with dimension of 7.1 Å x 18.2 Å is located in the interlayer space, connected to the outside via 10 MR apertures. The super-cages are cut at the crystal external surface and form hemi-cages, that catalytically behave as 12 MR channels (7.1 Å diameter). The 12 MR hemi-cages impose the same shape selectivity of a 12 MR channel without the need of diffusing reagents and products in real channels and hence hindering the deactivation by coke formation.[41,43–45] Ti-MWW was first synthesized in 2001, in co-presence of boron (B) and Ti.[44] Subsequently, a deboronation procedure and a direct synthesis of Ti-MWW in absence of B were developed,[27,46] to obtain materials without additional catalytic sites, except for Ti. The Ti insertion in the MWW framework is reported to occur in the vacant sites formed during the deboronation by acid washing of the Ti-B-MWW[46] and an acid treatment is also necessary after the direct synthesis of Ti-MWW, to remove the extra-framework anatase. [27] Here, a deep study of the effect of the acid treatment on the directly synthesized Ti-MWW is reported and the role of the acid treatment in the formation of Ti active sites is unveiled.

The increasing attention for this catalytic system imposes to reach a clear understanding of the Ti-MWW active sites, as has already been done for a long time with the well-known TS-1 case. Indeed, during the years an in-depth knowledge of the active sites and species in TS-1 has been achieved. For TS-1, the Ti insertion can occur in substitutional “perfect” tetrahedral sites, in octahedral coordination as bulk anatase or in the so-called “amorphous” Ti species (i.e. intermediate conditions between the previously described, e.g. hexa-coordinated, in a distorted octahedral geometry, maybe in the presence of alkali metal cations) depending on the synthetic procedure and Ti loading.[4,34,35,47] The Ti sites in TS-1 showed preferential location in specific crystallographic sites, and both the speciation and location were extensively studied by spectroscopy,[34,47–53] diffraction[54–56] and computational methods.[47,50,53,57–59] The knowledge gained by studying TS-1 is very useful for understanding which active site must be pushed in synthetic studies and to design catalysts with different levels of porosity.[31] However, when the crystalline framework is modified, the Ti microenvironment and, consequently, the behavior of the Ti-OOH (hydroperoxo) and Ti-OO (peroxo) active species can be different, as in the case of Ti-MWW. The vibrational fingerprint that testifies the presence of “perfect” Ti sites $Ti(OSi)_4$ in Ti-zeolites (the band at 960 cm^{-1} in the TS-1 vibrational spectrum), [53] in Ti-MWW is composed of two bands peaked at 960 and 930 cm^{-1}.[27,44] This suggests the presence of different Ti microenvironments and computational studies[27,60] confirm this hypothesis. The computational studies revealed the co-presence of $Ti(OSi)_4$ and $TiOH(OSi)_3$ species in comparable abundance in Ti-MWW and that $TiOH(OSi)_3$ locates selectively at the T1 crystallographic site. A commonly accepted view regarding the comparison among the catalytic

activity of the different Ti sites is not achieved yet,[1,61–64] but some studies[63–65] report that $TiOH(OSi)_3$ are more active than $Ti(OSi)_4$ sites in epoxidation reactions. The reason of the possible higher activity of $TiOH(SiO)_3$ sites was ascribed to their stronger Lewis acidity compared to the one of $Ti(OSi)_4$ sites, but the experimental work published in this field [65] does not directly compare the two zeolitic frameworks for providing a complete description of the different activity of the sites generated in the two different frameworks. On the other side, the in-depth spectroscopical analysis of the Ti sites and of the formation of the Ti-OOH and Ti-OO complexes upon interaction with H_2O_2 is lacking. In this work, we present a combined synthetic and spectroscopical study of the acidic properties of the Ti-MWW catalyst and of its interaction with H_2O_2. The effect of the post-treatment washing with nitric acid (HNO_3) on the process of Ti insertion in the MWW framework was studied by comparing a washed and not washed Ti-MWW samples. A combination of vibrational (infrared, IR) and electronic (ultraviolet-visible, UV-Vis) spectroscopies, in presence of probe molecules, when necessary, was adopted to shed light on the reason of the catalytic behavior of Ti-MWW and to provide a direct means of comparison with TS-1.

Experimental Section

Chemicals

Aerosil ® 200 (from Evonik Industries) and tetrabutylorthotitanate (TBOT, reagent grade 97% from Sigma Aldrich), were used as Si and Ti source. N,N,N-trimethyl-adamantil-ammonium hydroxide (TMAdaOH, 25 wt% in water, from TCI), hexamethylenimine (HMI, 99% from Sigma Aldrich) were used as Organic Structure Directing Agent (OSDA); potassium carbonate (K_2CO_3, anhydrous, ACS reagent, from Sigma Aldrich) was used as additive for the synthesis; Milli-Q water (18.2 MΩ cm) was used as solvent and nitric acid (HNO_3, 65% for analysis-ISO, from Carlo Erba Reagents) was used for the washings of Ti-MWW samples. Hydrogen peroxide (H_2O_2) aqueous solution (≥ 30 %, for trace analysis, from Sigma Aldrich) was used as oxidizing agent.

Synthesis of the Ti-MWW sample

The preparation of the Ti-MWW sample was reproduced from Xu et al.[27] In a typical synthesis, 8.45 g of TMAdaOH solution, 1.49 g of HMI and 0.2416 g of K_2CO_3 were added to 20.68 g of Milli-Q water in this order. After the complete dissolution of K_2CO_3, 0.34 g of TBOT were added dropwise under vigorous stirring. The solution was stirred at room temperature for 30 min to allow complete hydrolysis of the Ti precursor and then 3.004 g of Aerosil® 200 were gradually added and the gel was stirred until it was fully homogeneous. The final composition of the synthesis gel was: 1 SiO_2 : 0.02 TiO_2 : 0.2 TMAdaOH : 0.3 HMI : 0.035 K_2O : 30 H_2O. The gel (approximately 30 ml) was then transferred to a 45 ml Teflon lined stainless steel digestor and it was crystallized by autogenous pressure at 150 °C, in tumbling conditions at 60 rpm. The gel was filtered, washed with abundant water and dried at 65 °C overnight (to obtain Ti-MWW-as, “as” meaning “as-synthesized”). A

portion of Ti-MWW-as was washed with a 2 M HNO_3 solution for 20 h at 100 °C, under reflux conditions, using a solid to liquid ratio of 1 g : 50 ml, to obtain Ti-MWW-HNO_3-as. Ti-MWW-as and Ti-MWW-HNO_3-as were calcined at 550 °C under air flux, using a heating ramp of 1 °C/min followed by 7 h of isotherm, to obtain Ti-MWW-calc and Ti-MWW-HNO_3-calc.

The reference ITQ-1 material was synthesized as described elsewhere,[66] using the following composition of the synthesis gel: 1 SiO_2 : 0.25 TMAdaOH : 0.31 HMI : 44 H_2O and calcined at 550 °C under air flux, using a heating ramp of 1 °C/min followed by 7 h of isotherm. ITQ-1-as and ITQ-1-calc are the references before and after the calcination, respectively.

Characterization techniques

Powder X-Rays Diffraction (PXRD) patterns were obtained using Cu K_α radiation, on a PANanalytical X'Pert diffractometer (Bragg-Brentano geometry), equipped with a X'celerator strip detector, in the range $5° \leq 2\theta \leq 45°$, with a step of 0.02° and 50 s/° of integration. Cu K_β was suppressed with a Ni filter.

N_2 physisorption isotherms were recorded on a Micromeritics 3Flex instrument at -196 °C. The powders were treated before the measurement, by outgassing overnight at 120 °C and then 7 h at 400 °C. The Specific Surface Areas (SSAs) were determined by the Brunauer-Emmett-Teller (BET) and Langmuir models, applied in pressure ranges suitable for obtaining a monolayer capacity included in the selected p/p^0 (for the BET) or p (for the Langmuir) linearization range.[67] The cumulative pore volume and the pore size distribution were obtained by applying the Non-Local Density Functional Theory (NL-DFT); the pores were modelled as slit pores, using the "N_2@ 77-Carbon, original DFT" available in the Microactive software.[68] The model was applied in the whole range of p/p^0 with a regularization of 10^{-2}.

The TiO_2 wt% was determined by an Energy Dispersive X-Rays (EDX) spectroscopy detector (Oxford – Detector, equipped with an AZTEC software) coupled with a Field Emission (FE) Scanning Electron Microscope (SEM) Tescan S9000G. Elemental maps were also acquired.

Diffuse Reflectance (DR) Ultraviolet-visible (UV-Vis) spectra were collected on a Varian Cary5000 spectrophotometer, using Spectralon® as 100% Reflectance reference. The samples were measured both as such and after a pretreatment for removing water and possible organic pollutants on Ti coordination (the procedure is referred as "activation" in the following). ≈ 50 mg of sample were inserted in a quartz tube suitable for high temperature in vacuo treatments and the same portion of sample was analyzed by UV-Vis and by Attenuated Total Reflectance (ATR) Infrared (IR) (described later) spectroscopies. The procedure involves outgassing the sample at room temperature (RT) until reaching the residual pressure of $< 10^{-3}$ mbar; then the samples were heated up to 500 °C with a 5 °C/min ramp. After 30 min of outgassing at 500 °C, 100 mbar of pure O_2 were dosed on the sample and left in contact for at least 30 min. O_2 was finally outgassed

and the temperature was kept at 500 °C till a residual pressure < $5x10^{-4}$ mbar (≈ 1 h). After cooling to RT, the quartz tube was transferred in a N_2 glove-box for filling the sample holder for UV-Vis spectroscopy under controlled atmosphere.

The Attenuated Total Reflectance (ATR)-IR spectra were collected on a Bruker Alpha II spectrophotometer located directly inside the N_2 glove-box on the same fraction of sample activated for the UV-Vis measurements. The spectrophotometer is equipped with a Deuterated TriGlycine Sulfate (DTGS) detector and an ATR Platinum accessory (internal reflection element made of diamond). 64 scans were mediated (128 for the background) and a resolution of 2 cm^{-1} was used.

The transmission IR spectra were collected with a Bruker Vertex 70 spectrophotometer, equipped with a Mercury Cadmium Telluride (MCT) cryo-detector on a self-supporting pellet of the pure sample, placed inside a home-made quartz cell with KBr windows, designed for thermal outgassing prior to the measurement. The pellet was mechanically protected by a gold envelope and activated as previously described. The spectra were acquired under vacuum accumulating 32 scans (64 for the background) at 2 cm^{-1} of resolution.

The acidic properties of Ti-MWW-HNO_3-calc and the reference ITQ-1-calc were studied by dosing gaseous basic probe molecules on the sample under acquisition, by connecting the home-made cell (equipped with KBr or CaF_2 windows depending on the probe) to a vacuum glass-line. The spectral changes were detected during the adsorption/desorption of carbon monoxide (CO), [69,70] deuterated acetonitrile (CD_3CN),[71] pyridine (Py)[71] and ammonia (NH_3)[48]. The specific experimental settings for each molecule are reported elsewhere.[48,69–71]

The interaction of H_2O_2 with the Ti sites in Ti-MWW-HNO_3-calc was studied in situ by UV-Vis and IR spectroscopies. The powder was put in contact with H_2O_2 aqueous solution, rapidly dried (≈ 20 min in air at RT) and milled to obtain an pale orangepowder. The orange powder was left aging consecutively for 24 and 96 h and then was again put in contact with H_2O_2. After further 24 h aging the powder was regenerated by calcination in a tubular oven, with a heating ramp of 1 °C/min, at 550 °C for 4 h, under dry air flow. UV-Vis spectra were recorded after each step. Parallely, the degradation of the complexes for short-elapse times (2, 3 and 4 h) was followed and finally the effect of contact with H_2O was observed.

The interaction with H_2O_2 was studied by IR spectroscopy in transmission mode (same parameters and equipment described before) by wetting a pellet with a drop of H_2O_2, drying it rapidly in air at RT (till the residues of solution were not visible on the surface by naked eye) and then placing it in a IR cell with KBr windows. The pellet was quickly outgassed, to remove the air and the excess of water. Then, 60 mbar of pure propylene were dosed on the sample to observe the formation of propylene oxide. The spectra of propylene and propylene oxide dosed on the sample without H_2O_2, were recorded as reference.

Results and Discussion

Crystalline structure and defects analysis

The PXRD patterns of the as-synthesized ITQ-1-as, Ti-MWW-as and Ti-MWW-HNO_3-as and calcined ITQ-1-calc, Ti-MWW-calc and Ti-MWW-HNO_3-calc samples are shown in Figure 1. The position and bandwidth of the reflections is coherent with what reported in literature[27,41,66,72] and the presence of different zeolitic phases or of bulk anatase (in Ti containing samples) in detectable amounts is excluded. The calcined samples show shifted (among others, 002, 101 and 102) and fixed (e.g. the 100) reflections, compared with the as-synthesized samples. The shifted reflections have a component along the *c* direction and their shift is due to the contraction of the *c* axis of the unit cell that occurs upon calcination.[27,41,66,72] As observed before, [73] the partial elimination of the OSDA during the acid treatment gives rise to the hybrid pattern of Ti-MWW-HNO_3-as. The slight peak broadening, observed upon the acid treatment suggests a possible etching of the crystals or the reduction of the crystallite size. The SSA and micropore volume of Ti-MWW-calc are lower compared to ITQ-1-calc and Ti-MWW-HNO_3-calc (Table 1), as also visible at a first glance from the comparison of the N_2 isotherms (Figure S1, S2), suggesting a possible partial occlusion of the Ti-MWW-calc microchannels.

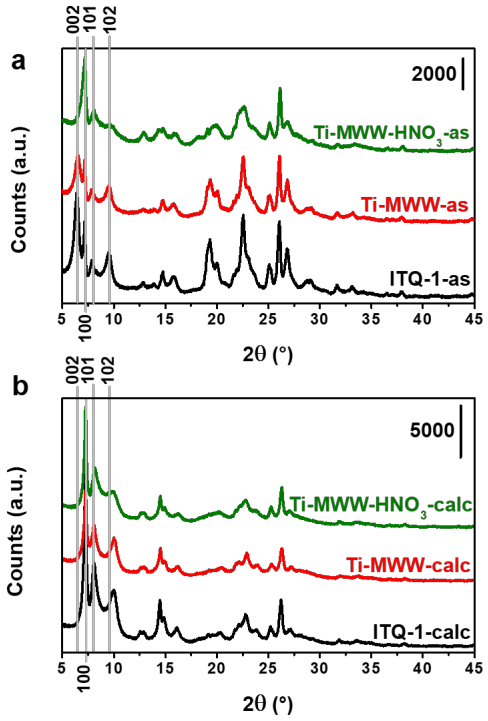

Figure 1. PXRD patterns in the 5° to 45° 2Θ range. (a) As-synthesized samples: ITQ-1-as (black), Ti-MWW-as (red) and Ti-MWW-HNO_3-as (olive). (b) Calcined samples: ITQ-1-calc (black), Ti-MWW-calc (red) and Ti-MWW-

HNO_3-calc (olive). The vertical light gray lines refer to the position of the 002, 100, 101 and 102 reflections of samples ITQ-1-as and Ti-MWW-as both in *a* and *b* directions. The diffractograms are vertically shifted for sake of clarity.

Table 1. SSAs calculated with the BET and Langmuir models and micropore (V_{micro}) volume computed using the NL-DFT method.

Sample	BET SSA[1] (m^2/g)	Langmuir SSA[2] (m^2/g)	V_{micro}[3] (cm^3/g STP)
ITQ-1-calc	465 ± 2	525 ± 1	0.15
Ti-MWW-calc	350 ± 2	384 ± 1	0.10
Ti-MWW-HNO_3-calc	498 ± 1	581 ± 2	0.15

[1] Calculated in the 0.008 – 0.08 p/p^0 range.
[2] Calculated in the 15 – 200 mbar pressure range.
[3] Calculated from the cumulative pore volume plot for pores size < 20 Å.

The effect of the HNO_3 washing on the calcination is also visible in the hydroxyls stretching (ν(OH)) range of silanols (Si-OH) and/or titanols (Ti-OH) (see IR spectra of Figure 2 between 3800-3000 cm^{-1}). [69,74–77] The sharp absorption at 3747 cm^{-1} is due to external isolated -OH groups. At lower wavenumber, the absorption of -OH groups is affected by a progressively more complex net of H-bonds. Among others, the Si-OH chain terminal at 3733 cm^{-1} and the Si-OH nests, generated by one or more Si missing atoms (broad absorption around 3500 cm^{-1}) are evident. It is worth noting that, in Ti-MWW-calc, isolated Si(Ti)-OHs are the only species absorbing in this region, due to defect healing phenomenon occurring upon direct calcination. A new band at 3688 cm^{-1} appears in Ti-MWW-HNO_3-calc spectrum. This signal was rarely observed before in a study regarding the Ti-MCM-41,[78] and was tentatively assigned to Ti-OH groups. We will see below that the assignment of this component is a difficult task, due to the small difference between the ν(OH) stretching frequency of Si-OH and Ti-OH species. Moreover, Ti-MWW-HNO_3-calc exhibits a comparable amount of defective species (silanol nest) to the reference ITQ-1-calc sample.

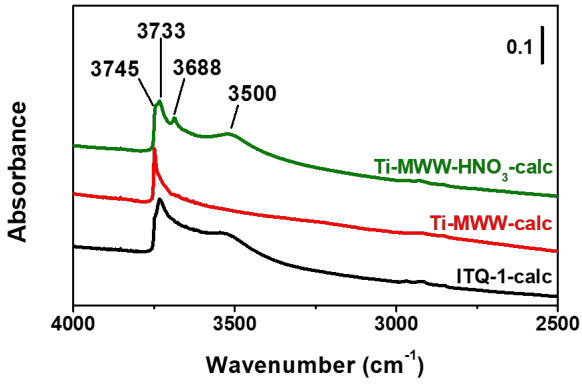

Figure 2. Transmission IR spectra of ITQ-1-calc (black), Ti-MWW-calc (red) and Ti-MWW-HNO_3-calc (olive) in the 4000-1250 cm^{-1} spectral range. The spectra are recorded after activation, internally normalized at the Si-O-Si stretching overtone absorptions, and vertically shifted for the sake of comparison.

Ti active site characterization

The limited amount of metal that can be inserted in Ti-zeolites is one of the main issues in the preparation and use of these catalysts. The Ti content (Table 2) and the maps of the distribution of the elements were acquired by EDX-SEM (Figures S3-S4) to verify the uniformity of the incorporation in our samples. The maps show no differences in the distribution of the elements between the acid washed and the directly calcined sample, whereas the total TiO_2 content of Ti-MWW-HNO_3-calc (2.91 wt%) is significantly higher than the one of Ti-MWW-calc (1.75 wt%). The limit value for the TiO_2 loading in TS-1 is 2.76 wt% of TiO_2 and it was experimentally obtained at industrial scale.[4,79,80] At laboratory scale, it was rarely replicated without the compromise of co-presence of extra-framework species.[31,81–86] The obtained TiO_2 loading for Ti-MWW-HNO_3-calc is an intriguing result, because it opens up the possibility of even higher loadings, considering that the higher limit for the MWW framework was not determined yet.

The directly calcined sample, without acid treatment, exhibits a definitely lower amount of inserted Ti compared to Ti-MWW-HNO_3-calc (Table 2). Based on the combination of the experimental results, an explanation of the phenomenon can be traced by the following. A loss of Ti species occurs during the hydrothermal crystallization: the Ti/Si molar ratio diminishes from 0.02 (nominal, used in the synthesis gel) to 0.0134 in Ti-MWW-calc, probably due to the incomplete hydrolysis of the Ti source in the crystallization conditions.[31] Subsequently, the acid treatment determines a steep increase of the Ti content. The Ti enrichment could be due to a loss of silicate species or to the solubilization-recrystallization of Ti-rich aggregates possibly present in the sample. The second hypothesis could be more probable because, even if Ti-rich aggregates were not detected by EDX-SEM (Figure S1-S2), (i) the loss of silicate species is highly unfavored in acidic conditions and (ii) the yield of Ti-MWW-HNO_3-calc is 93.7% compared to reagents. Such a high yield is not consistent with a presumed silicates loss. Hence, we do believe that Ti-rich aggregates formed in the hydrothermally synthesized sample, may be dissolved during the HNO_3 washing providing available Ti species. The nature of such aggregates is unknown, but they could be related to the presence of potassium, detected in the elemental maps of Ti-MWW-calc (Figure S3) but not in Ti-MWW-HNO_3-calc (Figure S4).

Table 2. Quantification of the total Ti content by SEM-EDX.

Sample	Ti/Si*	TiO_2 (wt%)*	σ**
Ti-MWW-calc	0.0134	1.75	0.17
Ti-MWW-HNO_3-calc	0.0226	2.91	0.52

* Average on 4 points.

** Standard deviation referred to the TiO_2 wt%.

The spectroscopic characterization of the Ti sites in the two samples corroborates the hypothesis regarding the Ti insertion in Ti-MWW-HNO_3-calc. In the UV-Vis spectra (Figure 3a and Figure S5), the Ligand to Metal Charge Transfer (LMCT) electronic transition involving Ti is present. The band edge and maximum (visually the minimum when spectra are plotted in reflectance (%) scale) are sensitive to the environment around Ti atoms in the sample. For comparison, it must be considered that in fully dehydrated TS-1 samples, maxima at 210 nm and 310 nm testify the presence of "perfect" tetrahedral Ti sites and octahedrally coordinated Ti (anatase) respectively (Figure S6a).[4,47] The presence of additional maxima between 210 and 310 nm is due to Ti species in intermediate conditions (e.g. isolated octahedral or distorted Ti species penta- or hexa-coordinated, see Figure S6a).[4,34,35,47] In Ti-MWW the situation is analogue. Ti-MWW-HNO_3-calc shows a single band at 205 nm, doubtless assigned to framework tetrahedral Ti species.[17,27,44] Ti-MWW-calc spectrum does not present any clear maximum around 210 nm, while a broad absorption at 235 nm with a shoulder at 280 nm is visible. This band can originate from intermediate Ti species in the framework and its wavelength is compatible with the LMCT in $TiOH(OSi)_3$ species.[64] The same signal is also slightly visible as shoulder in Ti-MWW-HNO_3-calc spectrum. However, it does not directly suggest that Ti-MWW-calc contains more $TiOH(OSi)_3$ species than in Ti-MWW-HNO_3-calc, considering that, a computational study revealed that, as an example, the $Ti(OSi)_4$ and $TiOH(OSi)_3$ species cannot be distinguished based on their UV-Vis spectrum.[47]

The framework vibration region of the ATR-IR spectra is shown in Figure 3b. Here, in the transparency window (990-850 cm^{-1}), between the asymmetric (ν_{asym}(SiOSi)=1100 cm^{-1}) and symmetric (ν_{sym}(SiOSi)=800 cm^{-1}) stretching bands, the ν_{asym}(SiOSi) vibrational mode, perturbed by the presence of Ti in the framework, is expected (see Figure S6b).[53] Ti-MWW-calc does not show bands in this region. Contrary, Ti-MWW-HNO_3-calc spectrum reveals two bands at 965 and 930 cm^{-1} related to the presence of Ti atoms in slightly different environments. [27,44] The first one is analogous, although slightly shifted to the band at 960 cm^{-1} present in dehydrated TS-1 and other Ti-zeolites (e.g. Ti-beta, Ti-CHA),[20,36,39,51,87] and it testifies the presence of Ti atoms in tetrahedral coordination. The component at 930 cm^{-1} is typical of Ti-MWW catalysts[27,44] and of some amorphous mesoporous silicates, as Ti-MCM-41, depending on the synthetic procedure.[22,78] It was assigned to grafted Ti species ($(TiOH(OSi)_3$ or $Ti(OH)_2(SiO)_3$) in Ti-MCM-41[78] and to defective $TiOH(OSi)_3$ at the T1 crystallographic site in Ti-MWW.[27,44] Hence, a fraction of Ti atoms, in Ti-MWW-HNO_3-calc is tetra-coordinated, probably in a distorted tetrahedral coordination, due to the presence of the hydroxyl ligand.

The spectroscopic characterization suggests that the HNO_3 treatment is almost the only responsible for the Ti insertion in the zeolite framework. This could indicate that the Ti insertion occur when the zeolitic framework is already formed. Looking at the literature data, a reduced amount of interacting Si-OH groups was observed in TS-1 compared to S-1, suggesting a possible healing effect of Ti sites on Si-OH nests.[88] In Ti-MWW-HNO_3-calc this effect is not observed compared with ITQ-1-calc, but this could be due to an effect of

the HNO_3 washing on the Si-OH population of Ti-MWW-HNO_3-calc. Support to the possibility of Ti insertion in defective position in Ti-MWW-HNO_3-calc arises from the preferential location of $TiOH(OSi)_3$ reported to occur at the T1 crystallographic site,[27] coupled with the fact that the T1 is surely a Si-OH species during the acid treatment.[42] Further studied are needed to clarify this point.

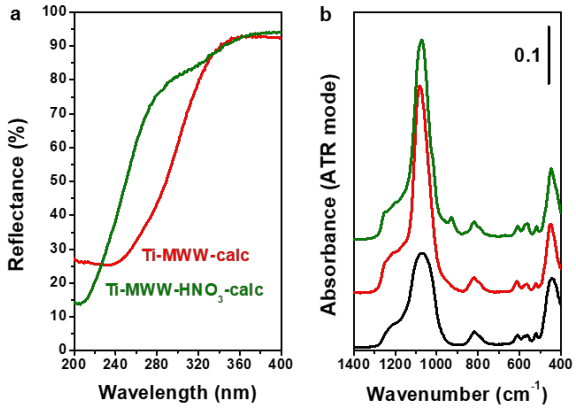

Figure 3. (a) UV-Vis spectra of activated samples: Ti-MWW-HNO_3-calc (olive) and Ti-MWW-calc (red). (b) Vertically shifted ATR-IR spectra of activated samples; from top to bottom: Ti-MWW-HNO_3-calc (olive), Ti-MWW-calc (red) and ITQ-1-calc (black).

Study of acid sites and hydroxyls group using probe molecules

The possible acidic sites present in Ti-zeolites generally are (i) the Ti(IV) sites in tetrahedral coordination, acting as Lewis centers and (ii) the hydroxyl groups (Si-OH and Ti-OH), acting as weak Brønsted sites. IR spectroscopy in presence of basic probe molecules is a powerful technique to evaluate the strength and location of these sites, whose study is of fundamental importance for their possible effects on the catalytic activity involving by-products formation.[4,89] In this work, probe molecules with different protonic affinity, namely CO (Figures S4-S5), CD_3CN (Figure 4), Py (Figure 5) and NH_3 (Figure S7) were employed to study the Ti(IV) Lewis sites of Ti-MWW-HNO_3-calc compared to those of the Ti-free reference ITQ-1-calc and their Si(Ti)-OH population. For the sake of brevity, the detailed description of the spectral properties connected to the adsorption of each probe molecule on the sample surface is reported in the ESI file, while the useful information is reported here. In all the figures, the effect of the maximum coverage is reported in bold (olive and black for Ti-MWW-HNO_3-calc and ITQ-1-calc respectively), while the spectra collected after the progressive outgassing are reported in grey.

Unfortunately, CO (Figure S7-S8) is a poorly informative probe, since its low proton affinity does not allow its interaction with the Ti(IV) Lewis sites when it is in tetrahedral coordination, and the very similar stretching frequency of Si-OH and Ti-OH prevent the discrimination between probe molecules interacting with Ti-OH respect to Si-OH groups.[4] For this reason, no significant differences are present between the spectra recorded during the experiment of CO adsorbed on Ti-MWW-HNO_3-calc and on ITQ-1-calc (Figures S7-S8).

In contrast, CD_3CN (Figure 4) is a stronger base than CO, allowing the detection of Ti(IV) in tetrahedral coordination in Ti-MWW-HNO_3-calc (Figure 4a, c). Upon CD_3CN dosage, the Si(Ti)-OH---$NCCD_3$ complex forms, determining the consumption of the bands above 3600 cm^{-1} (Figure 4a), associated to external, internal and terminal hydroxyls groups, and the parallel formation of a broad band, in the OH stretching region, with apparent maximum at around 3400 cm^{-1} (Figure 4a).[71,90] The corresponding spectra of CD_3CN adsorbed on the reference ITQ-1-calc sample exhibit the same behavior in the high frequency region (Figure 4d).

In the CN stretching spectral range (Figure 4b), the bands of physisorbed, H-bonded and interacting with Ti(IV) CD_3CN are present at 2264, 2274 and 2307 cm^{-1} respectively. The interaction of hydroxyls groups and Ti(IV) sites is reversible at RT, except for the band at 3688 cm^{-1}. However, it is not possible to determine if this band could be ascribed to strong (or medium strength) Brønsted acid sites, since the presence of the band assigned to CN stretching of CD_3CN coordinated on Brønsted acid sites at 2284 cm^{-1} [90] is not evident. It is worth noting that the spectrum of the reference ITQ-1-calc reports only the components at 2264 and 2274 cm^{-1} generated by weakly physisorbed and interacting with OH groups CD_3CN respectively (Figure 4e).

The band at 2307 cm^{-1}, observed in the CN stretching (ν(CN)) region of Ti-MWW-HNO_3-calc, is assigned to CD_3CN in interaction with Ti(IV) Lewis acid sites in tetrahedral coordination. The same band was observed in TS-1 at 2303 cm^{-1}.[71] The shift to higher frequencies (+43 cm^{-1} compared to the ν(CN) frequency of weakly physisorbed CD_3CN) testifies the stronger acid character of the Ti(IV) Lewis acid site in Ti-MWW-HNO_3-calc compared to the same site in TS-1 (shift of +37 cm^{-1}).[71,88] In comparison, the formation of Al(III)---$NCCD_3$ adducts in ZSM-5 gives rise to a higher upward shift (+50 cm^{-1}), as expected for a strong Lewis site.[71] It implies that the Ti(IV) sites in Ti-MWW have a medium acid strength. The stronger acidity of Ti(IV) in Ti-MWW is coherent with the presence of $TiOH(SiO)_3$ species, indicated as more acidic than the fully coordinated tetrahedral sites.[64,65] Moreover, this peculiarity helps explaining the interesting catalytic activity in epoxidation reactions already reported for Ti-containing MWW zeolites.[27,44] Figures 4c and 4f show the spectra of Ti-MWW-HNO_3-calc and ITQ-1-calc in the framework vibrations region upon CD_3CN dosing and outgassing. In Ti-MWW-HNO_3-calc, the band at 930 cm^{-1} present on activated sample and typical of Ti-MWW materials upward shifts to 944 cm^{-1}, as similarly occurred to the 960 cm^{-1} band in a similar experiment performed on TS-1 (shift of +10 cm^{-1}).[71] The shift observed for the 944 cm^{-1} band is totally reversible, indeed, after CD_3CN outgassing, it comes back to its original position. In contrast, upon CD_3CN dosage, the band at 965 cm^{-1}, related to the presence of Ti atoms in tetrahedral coordination, increases in intensity and broadens without shifting.

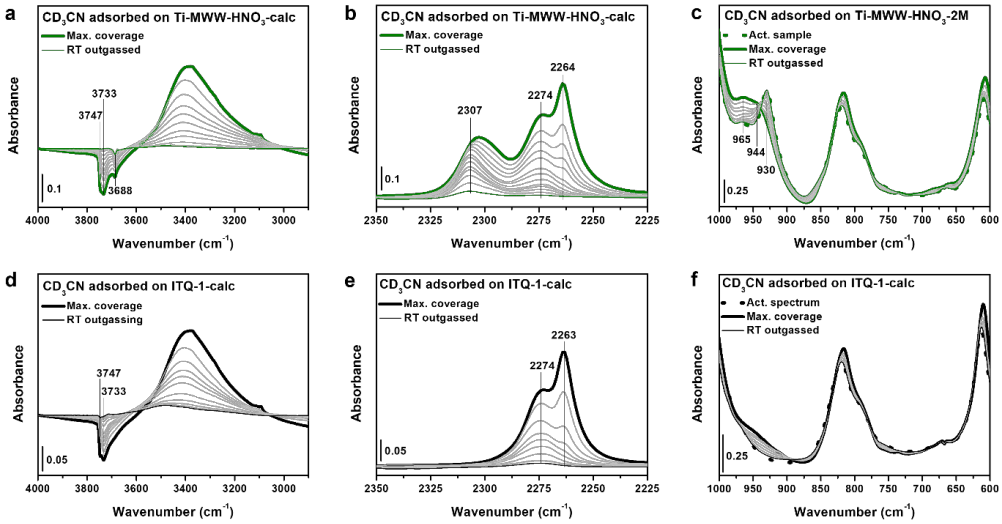

Figure 4. Background subtracted IR spectra of (a, b) Ti-MWW-HNO_3-calc and (d, e) ITQ-1-calc after contact with CD_3CN at RT, in the (a, d) 4000-2900 cm^{-1} and (b, e) 2350-2225 cm^{-1} spectral regions. The spectrum of the sample after outgassing at 500 °C was used as background. IR spectra of (c) Ti-MWW-HNO_3-calc and (f) ITQ-1-calc after contact with CD_3CN in the framework vibration region (1000-600 cm^{-1}).

Figure S9 shows the background subtracted IR spectra of adsorbed Py on Ti-MWW-HNO_3-calc (a, b) and ITQ-1-calc (c, d) in the hydroxyl and ring deformation spectral regions (4000-2600 and 1650-1350 cm^{-1} respectively). The assignment of the signals related to Py adsorbed on Ti-MWW-HNO_3-calc are summarized in Table S1. Concerning Ti-MWW-HNO_3-calc, the OH groups are partially perturbed by the interaction with Py (Figure S9a). This molecule, despite its wider kinetic diameter (0.57 nm) is still able to enter in the micropores of zeolites with MWW framework, but it cannot interact with a fraction of the hydroxyl groups present in defective sites (nests) (Figure S10). It also interacts with the family of Si(Ti)-OH absorbing at 3688 cm^{-1}, suggesting that they are not located inside the fraction of the smallest nests. The adsorption of Py on the ITQ-1-calc sample (Figure S9c) shows an analogous behavior in the OH stretching spectral range.

The last probe used in this work is the NH_3 (Figure S11), the stronger base usually employed for IR studies. This choice was done to explore the possible presence of medium strength Bronsted acid sites. Actually, the bands at 1477 and 1483 cm^{-1}, in Ti-MWW-HNO_3-calc and ITQ-1-calc respectively, can be detected after NH_3 adsorption and can be tentatively assigned to NH_4^+ bending modes (usually found in the 1500-1350 cm^{-1} range).[91–93] The signal is present independently of the Ti presence in the framework and, contrarily to the usual signal of protonated NH_4^+ generated by strong Brønsted acidic sites, it completely disappears upon outgassing at RT. The same spectral behavior was already reported for zeolites free from heteroatoms.[51,78]

Study of the interaction with H_2O_2

Figure 5 shows the effect of the interaction with H_2O_2 on the optical properties of Ti-MWW-HNO_3-calc. The olive curve in both panels is the spectrum of Ti-MWW-HNO_3-calc in air, without any activation. For this reason, a fraction of H_2O molecules is still present in the sample, causing the broadening of the LMCT electronic transition involving Ti observed comparing the UV-Vis spectrum in air with the activated one (Figure S5b). The spectrum in air of Ti-MWW-HNO_3-calc exhibits a minimum at 225 nm, compared to the corresponding minimum in the spectrum of TS-1 recorded in air, at 220 nm.[12] The higher shift could be due to an increased distortion of the tetrahedral geometry when H_2O molecules expand the coordination sphere of the Ti sites.[94,95] This is coherent with the presence of $TiOH(SiO)_3$ sites, whose geometry is less constrained than $Ti(OSi)_4$ one.

Upon interaction with H_2O_2, a pale orange wet powder is obtained (orange full curves in Figure 6). The baseline in the visible and NIR regions of the spectrum decreased in reflectance due to the presence of liquid H_2O in the interparticle voids, that strongly modifies the scattering profile of the powder. The excess of H_2O can be seen from the intensity of the signals at 1900 and 1400 nm in the NIR region, assigned to combination and overtone modes of H_2O.[12] Drying the powder for 24 h at RT, a significant decrease of the adsorbed H_2O is visible. Simultaneously, the scattering baseline converged to that of the naturally hydrated powder (comparison of ocher/yellow spectra with olive one), except for the inevitable slight difference due to powder positioning in the sample holder. A longer drying (96 h) does not lead to further modification in the NIR region. In the orange spectrum, as observed in TS-1,[12] the LMCT band involving Ti shows a broadening due to the water excess and a shoulder around 385 nm, assigned to the LMCT of a "side-on" peroxo ligand to the Ti center (Ti-OO), which confers to the material the typical yellow color.[12] Upon dehydration, the stable complex, Ti-OOH forms.[12] The degradation of the Ti-OOH/Ti-OO complexes occurs during the sample dehydration. Indeed, 24 h of drying give rise to an increase of the reflectance at 385 nm from 17% (orange spectrum) to 62% (yellow spectrum); an elapsed drying of 96 h (ocher spectrum) causes a further increase to 73%. Considering what reported[12] for an analogous experiment performed on TS-1, the degradation of the Ti-OOH/Ti-OO complex seems to occur faster in Ti-MWW than in TS-1, and consequently the complexes appear to be more labile at RT and ambient pressure in Ti-MWW respect to what happens in TS-1. The Ti atoms in $TiOH(OSi)_3$ species are less constrained and less bound to the framework respect to fully coordinated $Ti(OSi)_4$ species and consequently the formed complexes are less stable in time. The same powder, wet with H_2O_2 and then dried for 96 h, was put again in contact with H_2O_2 to verify the cyclability of the Ti-OOH/Ti-OO complexes (dashed spectra in Figure 6b). The process turned out to be fully reversible. The dashed orange and dashed yellow curves show that the Ti-OOH/Ti-OO complexes are formed again (at a similar level of hydration) and that their degradation occurs again in 24 h.

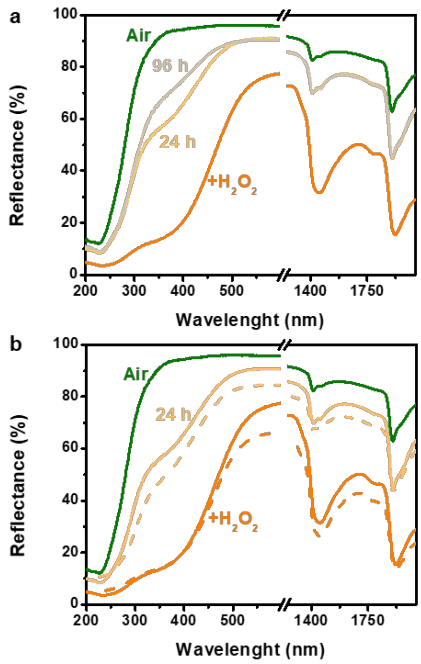

Figure 5. UV-Vis-NIR spectra in DR mode, recorded in different conditions. (a) First contact of Ti-MWW-HNO_3-calc with H_2O_2 (+H_2O_2, full orange), dried for 24 (full yellow) and 96 (full ocher) h, respect to the reference Ti-MWW-HNO_3-calc as-such in air (full olive). (b) The same as in panel a, compared to the second contact with H_2O_2 (dashed orange) and subsequent drying for 24 h (dashed yellow).

Figure S12 shows the effect of rehydration after H_2O_2 contact and consecutive drying for 4 h (a) or 96 h (b). Water affects the equilibrium $Ti-OOH+nH_2O \rightleftarrows [Ti-OO]^- + H_3O^+(H_2O)_{n-1}$. In TS-1 the partial regeneration of the Ti-OO species occurs upon rehydration,[12] without further contact with H_2O_2. The regeneration of Ti-OO species is also observed in Ti-MWW-HNO_3-calc upon contact with H_2O after 4 h of drying (Figure S12a), as highlighted by the decrease of reflectance at 385 nm. In contrast, the sample dried for 96 h does not exhibit the same behavior (Figure S12b). Visually, upon rehydration of 4 h dried sample, the pale orange powder comes back to bright orange, while it does not occur on the 96 h dried Ti-MWW-HNO_3-calc. Probably, at prolonged drying times, the residual amount of Ti-OOH species is too low to regenerate the Ti-OO complex.

Finally, the sample contacted twice with H_2O_2 was regenerated by calcination and the Ti content and speciation were determined by EDX analysis and UV-Vis (Figure S12c) and ATR-IR spectroscopies (Figure S12d). The quantification of the TiO_2 loading (2.35 wt% of TiO_2, σ=0.37) indicates that a slight leaching of Ti species occurred compared to the starting Ti-MWW-HNO_3-calc sample (2.91 wt% of TiO_2, σ=0.52). The formation of a shoulder at high wavelength in the UV-Vis spectra (dashed light green curve in Figure S12c) and the decrease of the band at 930 cm^{-1} ascribed to in framework Ti in the ATR-IR spectra (light green

spectrum in Figure S12d) suggest that a fraction of Ti has come out of the framework, but that most of the Ti atoms are still located in framework positions.

The H_2O_2 interaction with Ti-MWW-HNO_3-calc was further studied by *in situ* IR spectroscopy (Figure 6a). The use of IR spectroscopy is complicated by the impossibility of dosing H_2O_2 in vapor phase on the pelletized sample, but it has the advantage of observing *in situ* the formation of the reaction products. The experiment was conducted on a pellet soaked with an aqueous H_2O_2 solution (30 wt%). The H_2O_2 and H_2O excesses were rapidly outgassed and, when the H_2O bending mode at 1630 cm^{-1} disappeared, 40 mbar of gaseous propylene were dosed on the sample. For comparison, spectra recoded during H_2O outgassing on pure Ti-MWW-HNO_3-calc are reported in Figure S13. The difficulty of this experimental procedure lies in the need to remove the larger fraction of molecularly adsorbed H_2O, to avoid overlapping of the intense H_2O signals with the bands related to propylene and propylene oxide (Figure 6b), and, at the same time without leading to the degradation of the Ti-OOH/Ti-OO complexes, labile in vacuum conditions.[96]

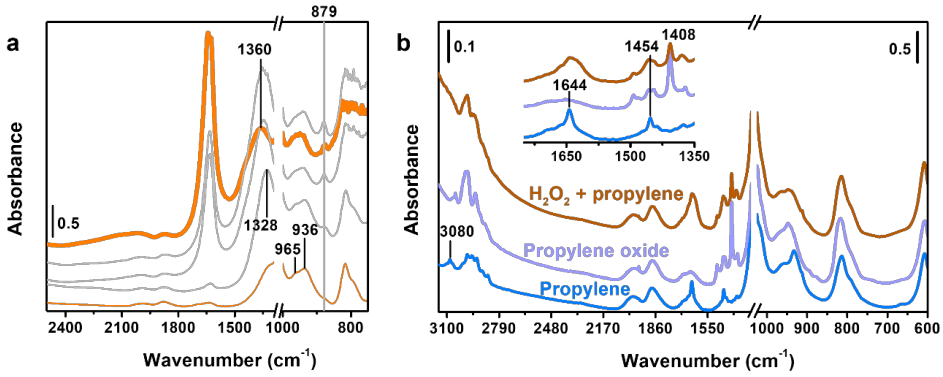

Figure 6. IR spectra in the 2500-600 cm^{-1} spectral range of (a) Ti-MWW-HNO_3-calc recorded after soaking the pellet with a H_2O_2/H_2O 30 wt% solution (bold orange), during the outgassing of the H_2O_2/H_2O excess (top to bottom, grey to orange curves). The spectra are vertically shifted for the sake of clarity. (b) IR spectrum recorded after 5 min from the dosing of 40 mbar of propylene on the H_2O_2 soaked/outgassed sample (dark orange) and on the RT outgassed sample (blue) and after dosing propylene oxide on the RT outgassed sample (light purple); the spectra are vertically shifted for the sake of clarity.

The presence of liquid H_2O_2 on the pellet is visible from the bending vibration of the -OH group of H_2O_2 that shifts from 1360 to 1328 cm^{-1} and degrease in intensity upon removing the excess of H_2O_2 and H_2O.[96] The stretching mode of O-O group in H_2O_2 is present at 879 cm^{-1}, overlapped to the O-O stretching of Ti-OO and Ti-OOH complexes (Figure 6a).[96] When propylene was dosed, the formation of propylene oxide was almost immediate (Figure 6b). The orange curve shows the signals due to propylene oxide (among the others, the signal at 1408 cm^{-1}, assigned to CH_3 deformation is representative), after 5 minutes from the dose. The conversion is testified by the absence in the orange spectrum of the signal at 3080 cm^{-1}, assigned to the C-H ν_{asym} of CH_2 in vinyl groups, [97] present in propylene, and by the shift of the sharp, medium strength band

assigned to the CH_3 deformation from 1454 cm^{-1} in propylene,[97] to 1408 cm^{-1} in propylene oxide.[98] On the other hand, the fate of the signal at 1644 cm^{-1}, assigned to the C=C stretching vibration of the vinyl group,[97] is difficult to foresee, due to the overlap with the broad signal assigned to the bending mode of H_2O (byproduct of the reaction) and the out-of-scale Si-O-Si stretching vibration that at 1300 cm^{-1} completely covers the breathing mode of the epoxide ring (in the 1290-1235 cm^{-1} range).[97,98]

Conclusions

In this work, the synthesis of Ti-MWW was reproduced from the literature and unexpectedly high Ti loadings, were reached (2.91 wt% of TiO_2), almost entirely in tetrahedral coordination. On the synthetic side, the effect of the HNO_3 post-treatment washing was investigated. The oxidant properties of HNO_3 helped in the OSDA removal, starting its elimination already during the acid treatment. Moreover, the acidic conditions cause the removal of any K residuals from the framework. This is extremely important, since the presence of alkaline metals is detrimental to the Ti insertion in the tetrahedral positions of the framework. By analysing the ATR-IR and the UV spectra of the washed (Ti-MWW-HNO_3-calc) and not washed (Ti-MWW-calc) samples, the HNO_3 treatment was demonstrated to be the only responsible for the Ti insertion in the framework.

On the spectroscopic side, the use of IR spectroscopy and targeted probe molecules allows determining that the Lewis acid sites embodied by the uncoordinated Ti tetrahedral sites are stronger than the corresponding ones in TS-1. This is due to the massive presence of acidic $TiOH(SiO)_3$ sites in the Ti-MWW.

The interaction of the Ti sites of Ti-MWW with H_2O_2 was studied by IR and UV-Vis spectroscopy. The Ti-OO and Ti-OOH complexes appears to be more labile than in TS-1, as their degradation at RT and under ambient pressure seems faster than in TS-1. This study proved that after two cycles of contacts with H_2O_2 and consequent drying, the Ti-MWW-HNO_3-calc sample was regenerated by simple calcination. The regeneration step was accompanied by only a slight leaching of tetrahedral Ti species. However, the regeneration and stability of the Ti species in reaction conditions, such as in methanol/H_2O_2 solution (often used in reactions instead of H_2O medium) deserve to be explored further.[99,100] Despite the differences in the stability of the complexes and the differences in the Ti sites acidity, the Ti-MWW-HNO_3-calc sample is demonstrated to be active in the epoxidation of propylene, as the TS-1 catalyst is.

Acknowledgments

The authors acknowledge support from the Project CH4.0 under the MUR program "Dipartimenti di Eccellenza 2023-2027" (CUP: D13C22003520001).

References

(1) Smeets, V.; Gaigneaux, E. M.; Debecker, D. P. Titanosilicate Epoxidation Catalysts: A Review of Challenges and Opportunities. *Chem. Cat. Chem.* **2022**, *14* (1). https://doi.org/10.1002/cctc.202101132.

(2) Nie, X.; Ji, X.; Chen, Y.; Guo, X.; Song, C. Mechanistic Investigation of Propylene Epoxidation with H_2O_2 over TS-1: Active Site Formation, Intermediate Identification, and Oxygen Transfer Pathway. *Mol. Catal.* **2017**, *441*, 150–167. https://doi.org/10.1016/j.mcat.2017.08.011.

(3) Clerici, M. G.; Ingallina, P. Epoxidation of Lower Olefins with Hydrogen Peroxide and Titanium Silicalite. *J. Catal.* **1993**, *140*, 71–83.

(4) Signorile, M.; Crocellà, V.; Damin, A.; Rossi, B.; Lamberti, C.; Bonino, F.; Bordiga, S. Effect of Ti Speciation on Catalytic Performance of TS-1 in the Hydrogen Peroxide to Propylene Oxide Reaction. *J. Phys. Chem. C* **2018**, *122* (16), 9021–9034. https://doi.org/10.1021/acs.jpcc.8b01401.

(5) Yin, J.; Xu, H.; Wang, B.; Tian, W.; Yin, J.; Jiang, J.; Wu, P. Highly Selective 1-Pentene Epoxidation over Ti-MWW with Modified Microenvironment of Ti Active Sites. *Catal. Sci. Technol.* **2020**, *10* (17), 6050–6064. https://doi.org/10.1039/d0cy00478b.

(6) Shima, H.; Tatsumi, T.; Kondo, J. N. Direct FT-IR Observation of Oxidation of 1-Hexene and Cyclohexene with H_2O_2 over TS-1. *Microporous Mesoporous Mater.* **2010**, *135* (1–3), 13–20. https://doi.org/10.1016/j.micromeso.2010.06.005.

(7) Wróblewska, A. Water as the Solvent for the Process of Phenol Hydroxylation over the Ti-MWW Catalyst. *React. Kinet. Mech. Catal.* **2013**, *108* (2), 491–505. https://doi.org/10.1007/s11144-012-0517-2.

(8) Klaewkla, R.; Kulprathipanja, S.; Rangsunvigit, P.; Rirksomboon, T.; Nemeth, L. Phenol Hydroxylation Using Ti- and Sn-Containing Silicalites. *Chem. Comm.* **2003**, *3* (13), 1500–1501. https://doi.org/10.1039/b303455k.

(9) Esposito, A.; Taramasso, M.; Neri, C. Hydroxylating Aromatic Hydrocarbons. US Patent 4396783, 1983.

(10) Liu, H.; Lu, G.; Guo, Y.; Guo, Y. Synthesis of TS-1 Using Amorphous SiO_2 and Its Catalytic Properties for Hydroxylation of Phenol in Fixed-Bed Reactor. *Appl. Catal. A Gen.* **2005**, *293* (1–2), 153–161. https://doi.org/10.1016/j.apcata.2005.07.021.

(11) Bellussi, G.; Millini, R. Background and Recent Advances in Ti-Containing Zeolite Materials. **2017**, 1–52. https://doi.org/10.1007/430_2017_15.

(12) Bonino, F.; Damin, A.; Ricchiardi, G.; Ricci, M.; Spanò, G.; D'Aloisio, R.; Zecchina, A.; Lamberti, C.; Prestipino, C.; Bordiga, S. Ti-Peroxo Species in the TS-1/H_2O_2/H_2O System. *J. Phys. Chem. B* **2004**, *108* (11), 3573–3583. https://doi.org/10.1021/jp036166e.

(13) Taramasso, M.; Perego, G.; Notari, B. Preparation of Porous Crystalline Synthetic Material Comprised of Silicon and Titanium Oxides. 1983. https://patents.google.com/patent/US4410501A/en.

(14) Pena, M. L.; Dellarocca, V.; Rey, F.; Corma, A.; Coluccia, S.; Marchese, L. Elucidating the Local Environment of Ti(IV) Active Sites in Ti-MCM-48: A Comparison between Silylated and Calcined Catalysts. *Microporous Mesoporous Mater.* **2001**, *44*, 345–356.

(15) Bai, R.; Song, Y.; Bai, R.; Yu, J. Creation of Hierarchical Titanosilicate TS-1 Zeolites. *Adv. Mater. Interfaces,* **2021**, *8*, 2001095.

(16) Wu, Z.; Wang, B.; Shi, J.; Rui, P.; Xie, X.; Liao, W.; Shu, X. The Silanization Process for the Hydrothermal Synthesis of Hierarchical Titanium Silicalite-1. *Microporous Mesoporous Mater.* **2021**, *327*, 111407. https://doi.org/10.1016/j.micromeso.2021.111407.

(17) Zhang, J.; Jin, S.; Deng, D.; Liu, W.; Tao, G.; Luo, Q.; Sun, H.; Yang, W. Insight into the Formation of Framework Titanium Species during Acid Treatment of MWW-Type Titanosilicate and the Effect of Framework Titanium State on Olefin Epoxidation. *Microporous Mesoporous Mater.* **2021**, *314*. https://doi.org/10.1016/j.micromeso.2020.110862.

(18) Smeets, V.; Gaigneaux, E. M.; Debecker, D. P. Hierarchical Micro-/Macroporous TS-1 Zeolite Epoxidation Catalyst Prepared by Steam Assisted Crystallization. *Microporous Mesoporous Mater.* **2020**, *293*, 109801. https://doi.org/10.1016/j.micromeso.2019.109801.

(19) Kong, Z.; Yue, B.; Deng, W.; Zhu, K.; Yan, M.; Peng, Y.; He, H. Direct Synthesis of Hierarchically Porous TS-1 through a Solvent-Evaporation Route and Its Application as an Oxidation Catalyst. *Appl. Organomet. Chem.* **2014**, *28* (4), 239–243. https://doi.org/10.1002/aoc.3115.

(20) Blasco, T.; Camblor, M. A.; Corma, A.; Esteve, P.; Guil, J. M.; Martínez, A.; Perdigón-Melón, J. A.; Valencia, S. Direct Synthesis and Characterization of Hydrophobic Aluminum-Free Ti-Beta Zeolite. *J. Phys. Chem. B* **1998**, *102*, 75–88.

(21) Wilkenhöner, U.; Gammon, D. W.; Steen, E. Van. Intrinsic Activity of Titanium Sites in TS-1 and Al-Free Ti-Beta. *Stud. Surf. Sci. Catal.* **2002**, *142 A*, 619–626. https://doi.org/10.1016/s0167-2991(02)80081-7.

(22) Blasco, T.; Corma, A.; Navarro, T.; Pariente, J. P. Synthesis, Characterization, and Catalytic Activity of Ti-MCM-41 Structures. *J. Catal.* **1995**, *156*, 65–74.

(23) Corma, A.; Kan, Q.; Rey, F. Synthesis of Si and Ti Si-MCM-48 Mesoporous Materials with Controlled Pore Sizes in the Absence of Polar Organic Additives and Alkali Metal Ions. *Chem. Comm.* **1998**, 579–580.

(24) Damin, A.; Bordiga, S.; Zecchina, A.; Doll, K.; Lamberti, C. Ti-Chabazite as a Model System of Ti(IV) in Ti-Zeolites: A Periodic Approach. *J. Chem. Phys.* **2003**, *118* (22), 10183–10194. https://doi.org/10.1063/1.1571516.

(25) Díaz-Cabañas, M. J.; Villaescusa, L. A.; Camblor, M. A. Synthesis and Catalytic Activity of Ti-ITQ-7: A New Oxidation Catalyst with a Three-Dimensional System of Large Pore Channels. *Chem. Comm.* **2000**, 9, 761–762. https://doi.org/10.1039/b000539h.

(26) Wu, P.; Tatsumi, T. Preparation of B-Free Ti-MWW through Reversible Structural Conversion. *Chem. Comm.* **2002**, *2* (10), 1026–1027. https://doi.org/10.1039/b201170k.

(27) Xu, H.; Guan, Y.; Lu, X.; Yin, J.; Li, X.; Zhou, D.; Wu, P. Relation of Selective Oxidation Catalytic Performance to Microenvironment of Ti^{IV} Active Site Based on Isotopic Labeling. *ACS Catal.* **2020**, *10* (8), 4813–4819. https://doi.org/10.1021/acscatal.0c00439.

(28) Waal, J. C. Van Der; Bekkum, H. Van. Zeolite Titanium Beta: A Versatile Epoxidation Catalyst. Solvent Effects. *J. Mol. Catal. A Chem.* **1997**, *124*, 137–146.

(29) Hulea, V.; Dumitriu, E.; Patcas, F.; Ropot, R.; Graf®n, P.; Moreau, P. Cyclopentene Oxidation with H_2O_2 over Ti-Containing Zeolites. *Appl. Catal. A Gen.* **1998**, *170*, 169–175.

(30) Kwon, O.; Ayla, E. Z.; Potts, D. S.; Flaherty, D. W. Effects of Solvent-Pore Interaction on Rates and Barriers for Vapor Phase Alkene Epoxidation with Gaseous H_2O_2 in Ti-BEA Catalysts. *ACS Catal.* **2023**, *13* (9), 6430–6444. https://doi.org/10.1021/acscatal.3c00730.

(31) Rosso, F.; Rizzetto, A.; Airi, A.; Khoma, K.; Signorile, M.; Crocellà, V.; Bordiga, S.; Galliano, S.; Barolo, C.; Alladio, E.; Bonino, F. Rationalization of TS-1 Synthesis through the Design of Experiments. *Inorg. Chem. Front.* **2022**, *9* (14). https://doi.org/10.1039/d2qi00643j.

(32) Ahn, W. S.; Lee, D. H.; Kim, T. J.; Kim, J. H.; Seo, G.; Ryoo, R. Post-Synthetic Preparations of Titanium-Containing Mesopore Molecular Sieves. *Appl. Catal. A Gen.* **1999**, *181*, 39–49.

(33) Zhang, S.; Jin, S.; Tao, G.; Wang, Z.; Liu, W.; Chen, Y.; Luo, J.; Zhang, B.; Sun, H.; Wang, Y.; Yang, W. The Evolution of Titanium Species in Boron-Containing Ti-MWW Zeolite during Post-Treatment Revealed by UV Resonance Raman Spectroscopy. *Microporous Mesoporous Mater.* **2017**, *253*, 183–190. https://doi.org/10.1016/j.micromeso.2017.07.006.

(34) Su, J.; Xiong, G.; Zhou, J.; Liu, W.; Zhou, D.; Wang, G.; Wang, X.; Guo, H. Amorphous Ti Species in Titanium Silicalite-1: Structural Features, Chemical Properties, and Inactivation with Sulfosalt. *J. Catal.* **2012**, *288*, 1–7. https://doi.org/10.1016/j.jcat.2011.12.006.

(35) Zuo, Y.; Liu, M.; Zhang, T.; Hong, L.; Guo, X.; Song, C.; Chen, Y.; Zhu, P.; Jaye, C.; Fischer, D. Role of Pentahedrally Coordinated Titanium in Titanium Silicalite-1 in Propene Epoxidation. *RSC Adv* **2015**, *5* (23), 17897–17904. https://doi.org/10.1039/c5ra00194c.

(36) Liu, Y.; Wang, F.; Zhang, X.; Zhang, Q.; Zhai, Y.; Lv, G.; Li, M.; Li, M. One-Step Synthesis of Anatase-Free Hollow Titanium Silicalite-1 by the Solid-Phase Conversion Method. *Microporous Mesoporous Mater.* **2022**, *331*, 111676. https://doi.org/10.1016/j.micromeso.2021.111676.

(37) Li, M.; Zhai, Y.; Zhang, X.; Wang, F.; Lv, G.; Rosine, A.; Li, M.; Zhang, Q.; Liu, Y. (NH4)2SO4-Assisted Synthesis of Thin-Walled Ti-Rich Hollow Titanium Silicalite-1 Zeolite for 1-Hexene Epoxidation. *Microporous Mesoporous Mater.* **2022**, *331*, 111655. https://doi.org/10.1016/j.micromeso.2021.111655.

(38) Lucas, A. De; Rodríguez, L.; Sánchez, P. Optimization of the Molar Composition of the Gel in the Synthesis of Titanium Silicalite TS-2. *Chem. Eng. Res. Des.* **2000**, *78* (1), 136–144. https://doi.org/10.1205/026387600526979.

(39) Eilertsen, E. A.; Bordiga, S.; Lamberti, C.; Damin, A.; Bonino, F.; Arstad, B.; Svelle, S.; Olsbye, U.; Lillerud, K. P. Synthesis of Titanium Chabazite: A New Shape Selective Oxidation Catalyst with Small Pore Openings and Application in the Production of Methyl Formate from Methanol. *Chem. Cat. Chem.* **2011**, *3* (12), 1869–1871. https://doi.org/10.1002/cctc.201100281.

(40) Pitinova-Stekrova, M.; Eliášová, P.; Weissenberger, T.; Shamzhy, M.; Musilová, Z.; Čejka, J. Highly Selective Synthesis of Campholenic Aldehyde over Ti-MWW Catalysts by α-Pinene Oxide Isomerization. *Catal Sci Technol* **2018**, *8* (18), 4690–4701. https://doi.org/10.1039/c8cy01231h.

(41) Leonowicz, M. E.; Lawton, J. A.; Lawton, S. L.; Rubin, M. K. MCM-22: A Molecular Sieve with Two Independent Multidimensional Channel Systems. *Science (1979)* **1994**, *264* (5167), 1910–1913. https://doi.org/10.1126/science.264.5167.1910.

(42) Millini, R.; Perego, G.; Parker, W. O.; Bellussi, G.; Carluccio, L. Layered Structure of ERB-1 Microporous Borosilicate Precursor and Its Intercalation Properties towards Polar Molecules. *Microporous Mater.* **1995**, *4* (2–3), 221–230. https://doi.org/10.1016/0927-6513(95)00013-Y.

(43) Ostroumova, V. A.; Maksimov, A. L. MWW-Type Zeolites: MCM-22, MCM-36, MCM-49, and MCM-56 (A Review). *Petrol. Chem.* **2019**, *59* (8), 788–801. https://doi.org/10.1134/S0965544119080140.

(44) Wu, P.; Tatsumi, T.; Komatsu, T.; Yashima, T. A Novel Titanosilicate with MWW Structure. I. Hydrothermal Synthesis, Elimination of Extraframework Titanium, and Characterizations. *J. Phys. Chem. B* **2001**, *105* (15), 2897–2905. https://doi.org/10.1021/jp002816s.

(45) Položij, M.; Thang, H. V.; Rubeš, M.; Eliášová, P.; Čejka, J.; Nachtigall, P. Theoretical Investigation of Layered Zeolites with MWW Topology: MCM-22P vs. MCM-56. *Dalton Trans.* **2014**, *43* (27), 10443–10450. https://doi.org/10.1039/c4dt00414k.

(46) Tang, Z.; Yu, Y.; Liu, W.; Chen, Z.; Wang, R.; Liu, H.; Wu, H.; Liu, Y.; He, M. Deboronation-Assisted Construction of Defective $Ti(OSi)_3OH$ Species in MWW-Type Titanosilicate and Their Enhanced Catalytic Performance. *Catal. Sci. Technol.* **2020**, *10* (9), 2905–2915. https://doi.org/10.1039/d0cy00126k.

(47) Signorile, M.; Braglia, L.; Crocellà, V.; Torelli, P.; Groppo, E.; Ricchiardi, G.; Bordiga, S.; Bonino, F. Titanium Defective Sites in TS-1: Structural Insights by Combining Spectroscopy and Simulation. *Angew. Chem. Int. Ed.* **2020**, *59* (41), 18145–18150. https://doi.org/10.1002/anie.202005841.

(48) Bordiga, S.; Damin, A.; Bonino, F.; Ricchiardi, G.; Zecchina, A.; Tagliapietra, R.; Lamberti, C. Resonance Raman Effects in TS-1: The Structure of Ti(IV) Species and Reactivity towards H_2O, NH_3 and H_2O_2: An in Situ Study. *Phys. Chem. Chem. Phys.* **2003**, *5* (20), 4390–4393. https://doi.org/10.1039/b306041c.

(49) Bolis, V.; Bordiga, S.; Lamberti, C.; Zecchina, A.; Carati, A.; Rivetti, F.; Spanò, G.; Petrini, G. A Calorimetric, IR, XANES and EXAFS Study of the Adsorption of NH_3 on Ti-Silicalite as a Function of the Sample Pre-Treatment. *Microporous Mesoporous Mater.* **1999**, *30* (1), 67–76. https://doi.org/10.1016/S1387-1811(99)00016-5.

(50) Dong, J.; Zhu, H.; Xiang, Y.; Wang, Y.; An, P.; Gong, Y.; Liang, Y.; Qiu, L.; Zheng, A.; Peng, X.; Lin, M.; Xu, G.; Guo, Z.; Chen, D. Toward a Unified Identification of Ti Location in the MFI Framework of High-Ti-Loaded TS-1: Combined EXAFS, XANES, and DFT Study. *J. Phys. Chem. C* **2016**, *120* (36), 20114–20124. https://doi.org/10.1021/acs.jpcc.6b05087.

(51) Astorino, E.; Peri, J. B.; Willey, R. J.; Busca, G. Spectroscopic Characterization of Silicalite-1 and Titanium Silicalite-1. *J. Catal.* **1995**, *157*, 482–500.

(52) Gallo, E.; Bonino, F.; Swarbrick, J. C.; Petrenko, T.; Piovano, A.; Bordiga, S.; Gianolio, D.; Groppo, E.; Neese, F.; Lamberti, C.; Glatzel, P. Preference towards Five-Coordination in Ti Silicalite-1 upon Molecular Adsorption. *Chem. Phys. Chem.* **2013**, *14* (1), 79–83. https://doi.org/10.1002/cphc.201200893.

(53) Ricchiardi, G.; Damin, A.; Bordiga, S.; Lamberti, C.; Spanò, G.; Rivetti, F.; Zecchina, A. Vibrational Structure of Titanium Silicate Catalysts. A Spectroscopic and Theoretical Study. *J. Am. Chem. Soc.* **2001**, *123* (46), 11409–11419. https://doi.org/10.1021/ja010607v.

(54) Lamberti, C.; Bordiga, S.; Zecchina, A.; Carati, A.; Fitch, A. N.; Artioli, G.; Petrini, G.; Salvalaggio, M.; Marra, G. L. Structural Characterization of Ti-Silicalite-1: A Synchrotron Radiation X-Ray Powder Diffraction Study. *J. Catal.* **1999**, *183* (2), 222–231. https://doi.org/10.1006/jcat.1999.2403.

(55) Henry, P. F.; Weller, M. T.; Wilson, C. C. Structural Investigation of TS-1: Determination of the True Nonrandom Titanium Framework Substitution and Silicon Vacancy Distribution from Powder Neutron Diffraction Studies Using Isotopes. *J. Phys. Chem. B* **2001**, *105* (31), 7452–7458. https://doi.org/10.1021/jp0107715.

(56) Hijar, C. A.; Jacubinas, R. M.; Eckert, J.; Henson, N. J.; Hay, P. J.; Ott, K. C. The Siting of Ti in TS-1 Is Non-Random. Powder Neutron Diffraction Studies and Theoretical Calculations of TS-1 and FeS-1. *J. Phys. Chem. B* **2000**, *104* (51), 12157–12164. https://doi.org/10.1021/jp002167k.

(57) Signorile, M.; Damin, A.; Bonino, F.; Crocellà, V.; Ricchiardi, G.; Lamberti, C.; Bordiga, S. Computational Assessment of Relative Sites Stabilities and Site-Specific Adsorptive Properties of Titanium Silicalite-1. *J. Phys. Chem. C* **2018**, *122* (3), 1612–1621. https://doi.org/10.1021/acs.jpcc.7b10104.

(58) Gale, J. D. A Periodic Density Functional Study of the Location of Titanium within TS-1. *Solid State Sci.* **2006**, *8* (3-4 SPEC. ISS.), 234–240. https://doi.org/10.1016/j.solidstatesciences.2006.02.011.

(59) Njo, S. L.; Koningsveld, H. Van; Graaf, B. Van De. A Combination of the Monte Carlo Method and Molecular Mechanics Calculations: A Novel Way to Study the Ti(IV) Distribution in Titanium Silicalite-1. *J. Phys. Chem. B* **1997**, *101* (48), 10065–10068. https://doi.org/10.1021/jp971451h.

(60) Zhou, D.; Zhang, H.; Zhang, J.; Sun, X.; Li, H.; He, N.; Zhang, W. Density Functional Theory Investigations into the Structure and Spectroscopic Properties of the Ti^{4+} Species in Ti-MWW Zeolite. *Microporous Mesoporous Mater.* **2014**, *195*, 216–226. https://doi.org/10.1016/j.micromeso.2014.04.037.

(61) Přech, J. Catalytic Performance of Advanced Titanosilicate Selective Oxidation Catalysts – a Review. *Catal. Rev. Sci. Eng.* **2018**, *60* (1), 71–131. https://doi.org/10.1080/01614940.2017.1389111.

(62) Tatsumi, T.; Nakamura, M.; Negishi, S.; o. Tominaga, H. Shape-Selective Oxidation of Alkanes with H2O2 Catalysed by Titanosilicate. *J. Chem. Soc. Chem. Commun.* **1990**, *202* (6), 476–477. https://doi.org/10.1039/C39900000476.

(63) Wells, D. H.; Delgass, W. N.; Thomson, K. T. Evidence of Defect-Promoted Reactivity for Epoxidation of Propylene in Titanosilicate (TS-1) Catalysts: A DFT Study. *J. Am. Chem. Soc.* **2004**, *126* (9), 2956–2962. https://doi.org/10.1021/ja037741v.

(64) Wu, L.; Tang, Z.; Yu, Y.; Yao, X.; Liu, W.; Li, L.; Yan, B.; Liu, Y.; He, M. Facile Synthesis of a High-Performance Titanosilicate Catalyst with Controllable Defective $Ti(OSi)_3OH$ Sites. *Chem. Comm.* **2018**, *54* (49), 6384–6387. https://doi.org/10.1039/c8cc02794c.

(65) Yu, Y.; Tang, Z.; Wang, J.; Wang, R.; Chen, Z.; Liu, H.; Shen, K.; Huang, X.; Liu, Y.; He, M. Insights into the Efficiency of Hydrogen Peroxide Utilization over Titanosilicate/H_2O_2 Systems. *J. Catal.* **2020**, *381*, 96–107. https://doi.org/10.1016/j.jcat.2019.09.045.

(66) Camblor, M. A.; Corma, A.; Díaz-Cabañas, M. J.; Baerlocher, C. Synthesis and Structural Characterization of MWW Type Zeolite ITQ-1, the Pure Silica Analog of MCM-22 and SSZ-25. *J. Phys. Chem. B* **1998**, *102* (1), 44–51. https://doi.org/10.1021/jp972319k.

(67) Thommes, M.; Kaneko, K.; Neimark, A. V; Olivier, J. P.; Rodriguez-Reinoso, F.; Rouquerol, J.; Sing, K. S. W. Physisorption of Gases, with Special Reference to the Evaluation of Surface Area and Pore Size Distribution (IUPAC Technical Report). *Pure Appl. Chem.* **2015**, *87* (9–10), 1051–1069. https://doi.org/10.1515/pac-2014-1117.

(68) Corporation, M. I. Microactive. 2012.

(69) Bordiga, S.; Roggero, I.; Ugliengo, P.; Zecchina, A.; Bolis, V.; Artioli, G.; Buzzoni, R.; Marra, G.; Rivetti, F.; Spano, G.; Lamberti, C. Characterisation of Defective Silicalites. *J. Chem. Soc., Dalton Trans.* **2000**, 21, 3921–3929. https://doi.org/10.1039/b004794p.

(70) Zecchina, A.; Bordiga, S.; Spoto, G.; Marchese, L.; Petrini, G.; Leofanti, G.; Padovan, M. Silicalite Characterization. 1. Structure, Adsorptive Capacity, and IR Spectroscopy of the Framework and Hydroxyl Modes. *J. Phys. Chem.* **1992**, *96* (12), 4985–4990. https://doi.org/10.1021/j100191a047.

(71) Bonino, F.; Damin, A.; Bordiga, S.; Lamberti, C.; Zecchina, A. Interaction of CD_3CN and Pyridine with the Ti(IV) Centers of TS-1 Catalysts: A Spectroscopic and Computational Study. *Langmuir* **2003**, *19* (6), 2155–2161. https://doi.org/10.1021/la0262194.

(72) Tempelman, C. H. L.; Portilla, M. T.; Martínez-Armero, M. E.; Mezari, B.; Caluwé, N. G. R. De; Martínez, C.; Hensen, E. J. M. One-Pot Synthesis of Nano-Crystalline MCM-22. *Microporous Mesoporous Mater.* **2016**, *220*, 28–38. https://doi.org/10.1016/j.micromeso.2015.08.018.

(73) Fabbiani, M.; Morsli, A.; Confalonieri, G.; Cacciaguerra, T.; Fajula, F.; Haines, J.; Bengueddach, A.; Arletti, R.; Renzo, F. Di. On the Chemical Condensation of the Layers of Zeolite Precursor MCM-22(P). *Microporous Mesoporous Mater.* **2022**, *332*, 111678–111685. https://doi.org/10.1016/j.micromeso.2021.111678.

(74) Bordiga, S.; Ugliengo, P.; Damin, A.; Lamberti, C.; Spoto, G.; Zecchina, A.; Spanò, G.; Buzzoni, R.; Dalloro, L.; Rivetti, F. Hydroxyls Nests in Defective Silicalites and Strained Structures Derived upon Dehydroxylation: Vibrational Properties and Theoretical Modelling. *Top. Catal.* **2001**, *15* (1), 43–52. https://doi.org/10.1023/A:1009019829376.

(75) Pascale, F.; Ugliengo, P.; Civalleri, B.; Orlando, R.; D'Arco, P.; Dovesi, R. Hydrogarnet Defect in Chabazite and Sodalite Zeolites: A Periodic Hartree-Fock and B3-LYP Study. *J. Chem. Phys.* **2002**, *117* (11), 5337–5346. https://doi.org/10.1063/1.1499477.

(76) Medeiros-Costa, I. C.; Dib, E.; Nesterenko, N.; Dath, J. P.; Gilson, J. P.; Mintova, S. Silanol Defect Engineering and Healing in Zeolites: Opportunities to Fine-Tune Their Properties and Performances. *Chem Soc Rev* **2021**, *50* (19), 11156–11179. https://doi.org/10.1039/d1cs00395j.

(77) Dubray, F.; Dib, E.; Medeiros-Costa, I.; Aquino, C.; Minoux, D.; van Daele, S.; Nesterenko, N.; Gilson, J. P.; Mintova, S. The Challenge of Silanol Species Characterization in Zeolites. *Inorg. Chem. Front.* **2022**, *9* (6), 1125–1133. https://doi.org/10.1039/d1qi01483h.

(78) Gianotti, E.; Dellarocca, V.; Marchese, L.; Martra, G.; Coluccia, S.; Maschmeyer, T. NH3 Adsorption on MCM-41 and Ti-Grafted MCM-41. FTIR, DR UV-Vis-NIR and Photoluminescence Studies. *Phys. Chem. Chem. Phys.* **2002**, *4* (24), 6109–6115. https://doi.org/10.1039/b207231a.

(79) Bellussi, G.; Carati, A.; Clerici, M. G.; Maddinelli, G.; Millini, R. Reactions of Titanium Silicalite with Protic Molecules and Hydrogen Peroxide. *J. Catal.* **1992**, *133* (1), 220–230. https://doi.org/10.1016/0021-9517(92)90199-R.

(80) Millini, R.; Massara, E. P.; Perego, G.; Bellussi, G. Framework Composition of Titanium Silicalite-1. *J. Catal.* **1992**, *137* (2), 497–503. https://doi.org/10.1016/0021-9517(92)90176-I.

(81) Lin, D.; Zhang, Q.; Qin, Z.; Li, Q.; Feng, X.; Song, Z.; Cai, Z.; Liu, Y.; Chen, X.; Chen, D.; Mintova, S.; Yang, C. Reversing Titanium Oligomer Formation towards High-Efficiency and Green Synthesis of Titanium-Containing Molecular Sieves. *Angew. Chem. Int. Ed.* **2021**, *60* (7), 3443–3448. https://doi.org/10.1002/anie.202011821.

(82) Thangaraj, A.; Eapen, M. J.; Sivasanker, S.; Ratnasamy, P. Studies on the Synthesis of Titanium Silicalite, TS-1. *Zeolites* **1992**, *12*, 943–950.

(83) Xing, J.; Yuan, D.; Liu, H.; Tong, Y.; Xu, Y.; Liu, Z. Synthesis of TS-1 Zeolites from a Polymer Containing Titanium and Silicon. *J. Mater. Chem. A Mater.* **2021**, *9* (10), 6205–6213. https://doi.org/10.1039/d0ta11876a.

(84) Tamura, M.; Chaikittisilp, W.; Yokoi, T.; Okubo, T. Incorporation Process of Ti Species into the Framework of MFI Type Zeolite. *Microporous Mesoporous Mater.* **2008**, *112* (1–3), 202–210. https://doi.org/10.1016/j.micromeso.2007.09.044.

(85) Guo, Q.; Feng, Z.; Li, G.; Fan, F.; Li, C. Finding the "Missing Components" during the Synthesis of TS-1 Zeolite by UV Resonance Raman Spectroscopy. *J. Phys. Chem. C* **2013**, *117* (6), 2844–2848. https://doi.org/10.1021/jp310900a.

(86) Shan, Z.; Lu, Z.; Wang, L.; Zhou, C.; Ren, L.; Zhang, L.; Meng, X.; Ma, S.; Xiao, F.-S. Stable Bulky Particles Formed by TS-1 Zeolite Nanocrystals in the Presence of H_2O_2. *Chem. Cat. Chem.* **2010**, *2*, 407–412.

(87) Bordiga, S.; Lamberti, C.; Bonino, F.; Travert, A.; Thibault-Starzyk, F. Probing Zeolites by Vibrational Spectroscopies. *Chem. Soc. Rev.* **2015**, *44* (20), 7262–7341. https://doi.org/10.1039/c5cs00396b.

(88) Armaroli, T.; Milella, F.; Notari, B.; Willey, R. J.; Busca, G. A Spectroscopic Study of Amorphous and Crystalline Ti-Containing Silicas and Their Surface Acidity. *Top. Catal.* **2001**, *15* (1), 63.

(89) Wu, L.; Zhao, S.; Lin, L.; Fang, X.; Liu, Y.; He, M. In-Depth Understanding of Acid Catalysis of Solvolysis of Propene Oxide over Titanosilicates and Titanosilicate/H_2O_2 Systems. *J. Catal.* **2016**, *337*, 248–259. https://doi.org/10.1016/j.jcat.2016.01.028.

(90) Pelmenschikov, A. G.; Santen, R. A. Van; Jánchen, J.; Meijer, E. CD_3CN as a Probe of Lewis and Bronsted Acidity of Zeolites. *J. Phys. Chem.* **1993**, *97*, 11071–11074.

(91) Zecchina, A.; Marchese, L.; Bordiga, S.; Pazè, C.; Gianotti, E. Vibrational Spectroscopy of NH^{4+} Ions in Zeolitic Materials: An IR Study. *J. Phys. Chem. B* **1997**, *101*, 10128–10135.

(92) Giordanino, F.; Borfecchia, E.; Lomachenko, K. A.; Lazzarini, A.; Agostini, G.; Gallo, E.; Soldatov, A. V; Beato, P.; Bordiga, S.; Lamberti, C. Interaction of NH_3 with Cu-SSZ-13 Catalyst: A Complementary FTIR, XANES, and XES Study. *J. Phys. Chem. Lett.* **2014**, *5* (9), 1552–1559. https://doi.org/10.1021/jz500241m.

(93) Datka, J.; Góra-Marek, K. IR Studies of the Formation of Ammonia Dimers in Zeolites TON. *Catal. Today* **2006**, *114* (2–3), 205–210. https://doi.org/10.1016/j.cattod.2006.01.009.

(94) Signorile, M.; Damin, A.; Bonino, F.; Crocellà, V.; Lamberti, C.; Bordiga, S. The Role of Dispersive Forces Determining the Energetics of Adsorption in Ti Zeolites. *J. Comput. Chem.* **2016**, *37*, 2659–2666. https://doi.org/10.1002/jcc.24509.

(95) Bordiga, S.; Damin, A.; Bonino, F.; Zecchina, A.; Spanò, G.; Rivetti, F.; Bolis, V.; Prestipino, C.; Lamberti, C. Effect of Interaction with H_2O and NH_3 on the Vibrational, Electronic, and Energetic Peculiarities of Ti(IV) Centers TS-1 Catalysts: A Spectroscopic and Computational Study. *J. Phys. Chem. B* **2002**, *106* (38), 9892–9905. https://doi.org/10.1021/jp026106t.

(96) Tozzola, G.; Mantegazza, M. A.; Ranghino, G.; Petrini, G.; Bordiga, S.; Ricchiardi, G.; Lamberti, C.; Zulian, R.; Zecchina, A. On the Structure of the Active Site of Ti-Silicalite in Reactions with Hydrogen Peroxide: A Vibrational and Computational Study. *J. Catal.* **1998**, *179* (1), 64–71. https://doi.org/10.1006/jcat.1998.2205.

(97) Colthup, N. B.; Daly, L. H.; Wiberley, S. E. Ethers, Alcohols and Phenols. In *Introduction to Infrared and Raman Spectroscopy*; Elsevier, 1990; pp 327–337. https://doi.org/10.1016/b978-0-08-091740-5.50013-2.

(98) Hudson, R. L.; Loeffler, M. J.; Yocum, K. M. Laboratory Investigations into the Spectra and Origin of Propylene Oxide: A Chiral Interstellar Molecule. *Astrophys. J.* **2017**, *835* (2), 225.

https://doi.org/10.3847/1538-4357/835/2/225.

(99) Goebbel, H.-G.; Bassler, P.; Teles, J. H.; Rudolf, P.; Mueller, U.; Forlin, A.; Schulz, M.; Weidenbach, M. Process for Epoxidizing Propene. US Patent 7786317 B2, 2010.

(100) Haas, T.; Brasse, C.; Woll, W.; Hofen, W.; Jaeger, B.; Stochniol, G.; Ullrich, N. Process for the Epoxidation of Propene. US Patent 6878836 B2 2005.

Appendix C

Appendix C contains the paper published during the PhD, not related to the topic of the project.

Journal of CO2 Utilization 55 (2022) 101815

Contents lists available at ScienceDirect

Journal of CO2 Utilization

journal homepage: www.elsevier.com/locate/jcou

Efficient and reversible CO_2 capture in bio-based ionic liquids solutions

Giulio Latini [a,b,e], Matteo Signorile [b], Francesca Rosso [b], Andrea Fin [c], Marta d'Amora [e], Silvia Giordani [d,e], Fabrizio Pirri [a,e], Valentina Crocellà [b,*], Silvia Bordiga [b], Sergio Bocchini [e,*]

[a] Department of Applied Science and Technology, Politecnico di Torino, Corso Duca degli Abruzzi 24, 10129, Turin, Italy
[b] Department of Chemistry, NIS and INSTM Centers, Università di Torino, via G. Quarello 15 and via P. Giuria 7, 10125, Turin, Italy
[c] Department of Drug Science and Technology, Università di Torino, via P. Giuria 9, 10125, Turin, Italy
[d] School of Chemical Sciences, Dublin City University (DCU), Glasnevin, D09 C7F8, Dublin, Ireland
[e] Center for Sustainable Future Technologies, Istituto Italiano di Tecnologia, via Livorno 60, 10144, Torino, Italy

ARTICLE INFO

Keywords:
CO_2 capture
Ionic liquids
Amino-acids
In-situ ATR-IR spectroscopy
In vivo toxicity assessment

ABSTRACT

Choline/amino acid-based ionic liquids were synthetized *via* ionic metathesis and their CO_2 absorption performances evaluated by employing different experimental approaches. In order to overcome any viscosity-related problem, dimethyl sulfoxide (DMSO) was employed as solvent. IL-DMSO solutions with different IL concentrations were evaluated as absorbents for CO_2, also investigating their good cyclability as desirable for real industrial CO_2 capture technologies. ^{1}H-NMR and *in-situ* ATR-IR experiments were the toolbox to study the CO_2 chemical fixation mechanism under different experimental conditions, proving the formation of distinct chemical species (carbamic acid and/or ammonium carbamate). In general, these ILs demonstrated molar uptakes higher than classical 0.5 mol CO_2/mol IL and the capacity to release CO_2 in extremely mild conditions. The possible biological adverse effects were also analyzed, for the first time, in zebrafish (*Danio rerio*) during the development, by assessing for different toxicological endpoints, proving the non-toxicity and high biocompatibility of these bio-inspired ILs.

1. Introduction

The atmospheric concentration of carbon dioxide (CO_2) has increased due to the anthropogenic contribution overstepped 400 ppm in 2015 [1,2]. Fossil fuel combustion for energy production, transportation and industrial processes establishes the main contribution to human emission. Purification of post-combustion gases, storage and conversion/utilization of CO_2 represent a straightforward measure to reduce anthropogenic emissions.

Different CO_2 separation techniques are available based on different physico-chemical phenomena: absorption or adsorption, either physical or chemical, membrane or cryogenic-based separation. Besides the working principle, energy consumption, toxicity and operating cost must be taken into account for the technologic implementation [3]. Amine scrubbing process is the most notable and widespread technology: the first process was patented in 1930 [4]. Alkylamine aqueous solutions chemically fix the CO_2 molecule, as shown in Scheme 1. Primary and secondary amines produce ammonium-carbamate species, whereas ammonium-carbonate species are formed from tertiary amine and water (see Scheme 1) [5–7]. After the capture, the amine solution is regenerated at 100−120 °C *via* water evaporation and the released CO_2 is compressed to 100−150 bar for sequestration and transportation [8].

The CO_2 release from amine aqueous solutions requires solvent evaporation/condensation, an intensive energy demanding process. Moreover, amine scrubbing has several drawbacks related to the toxicity and the corrosiveness of the sorbent phase. Solving these issues would positively affect both the environmental and the economic impact of the CO_2 capture procedure. Indeed, a lower energy consumption reduces the operational costs and carbon footprint of the entire process, as well as non-corrosive, non-toxic materials are more suitable from the environmental and plant safety point of view.

Ionic liquids (ILs), usually defined as salts with melting temperature lower than 100 °C [9,10], are emerging as promising candidates for CO_2 capture and conversion [11–14]. ILs can solve some critical issues of amine-based aqueous systems, as they feature negligible vapor pressure, non-corrosiveness and high thermal stability [15–19]. Beyond physical

* Corresponding authors at: Center for Sustainable Future Technologies, Istituto Italiano di Tecnologia, via Livorno 60, 10144, Torino, Italy and Department of Chemistry, NIS and INSTM Centers, Università di Torino, via G. Quarello 15 and via P. Giuria 7, 10125, Turin, Italy.
E-mail addresses: valentina.crocella@unito.it (V. Crocellà), sergio.bocchini@iit.it (S. Bocchini).

https://doi.org/10.1016/j.jcou.2021.101815
Received 14 July 2021; Received in revised form 24 October 2021; Accepted 18 November 2021
Available online 29 November 2021

$$2\,R_1R_2NH + CO_2 \;\leftrightarrows\; R_1R_2NH^+ + R_1R_2NCOO^-$$

$$R_1R_2R_3N + CO_2 + H_2O \;\leftrightarrows\; R_1R_2R_3NH^+ + HOCOO^-$$

Scheme 1. Chemical reaction of CO_2 with: (a) a primary/secondary amine; or (b) a tertiary amine in the presence of water.

absorption (which becomes relevant at high pressure), the ILs affinity towards CO_2 can be increased by chemically functionalizing the anion and/or the cation, *i.e.* by introducing an amine group or other basic moieties [20]. Amine-based and amino-tethered ILs capture CO_2 more efficiently through the formation of carbamate species, with a ILs:CO_2 2:1 stoichiometry [20,21], thus also activating the molecule and opening the path for further reactivity [22,23]. Nonetheless, despite the epithet of "green solvent" [24], ILs commonly tested for CO_2 capture are based on imidazolium and pyridinium cations and fluorinated anions, that hamper their biodegradability and biocompatibility [25,26]. In a green perspective, the choice of non-toxic and biocompatible cations/anions represents a key step to develop a sustainable CO_2 capture process based on ILs. In this scenario, the combination of choline (Cho), a non-toxic, essential nutrient cation, and amino acids (AAs, proteins building block, in the anionic form) could drive to the synthesis of an environmental-friendly class of ILs. In particular, AAs are very convenient anions for a CO_2 capture application, owing to the coexistence of an amine moiety (*i.e.* a specific interaction site for CO_2) and of a carboxylic anion (that enhances the affinity with the sorptive) [27–29], as practically demonstrated by some literature works. Zou et al. tested the capture performance of a choline prolinate - polyethylene glycol 200 ([Cho][Pro]-PEG200) system at a pressure of 1.1 bar, yielding to a 0.6 CO_2-IL molar ratio [30]. Lu and co-workers studied aqueous solution of choline glycinate, alaninate and prolinate up to 15 bar of CO_2, obtaining CO_2-IL molar ratios up to 2 and conversion of the carbamate to carbonate, due to the presence of water as solvent and the high pressure involved [31]. More recently, our group revealed closely equimolar CO_2 absorption capacity by some AAs -based ILs (synthetized using Choline as cation and glycine or proline as anions) in dimethyl sulfoxide (DMSO) solution, also investigating the role of the IL concentration on the capture performances [32]. Furthermore, materials based on Cho and AAs (in principle achievable from renewable feedstock) [33,34] have demonstrated good biocompatibility and biodegradability [35–38].

Despite the interesting physico-chemical [39–41] and toxicological [35–38] properties, the employment of these ILs have not spread yet. A first limitation to their employment is the use of choline hydroxide in the usual synthetic procedure. This precursor in expensive, dangerous (it is a corrosive strong base) and difficult to handle. The titration synthesis of neutral AAs by choline hydroxide provides high yields (>90 %) at long reaction times [35–38], involving the aforementioned chemical threats. These factors limit the scalability of this synthetic strategy. In a recent study, we overcome this issue by applying a synthetic approach based on ionic metathesis, suitable for producing higher amounts of choline-based AAILs with a safer procedure [32,42]. The only drawback is the lower purity of the final product due to the presence of halide salts as impurities (< 5 wt% of KCl). However, regarding the application of these ILs in CO_2 capture, this contamination does not seem to affect their performances [32]. Another general drawback of ILs is their high viscosity, which, unfortunately, further increases upon CO_2 interaction [43]. An excessive viscosity prevents gas diffusion into the liquid, negatively affecting the overall capture performances. As a solution, the dilution with proper solvents decreases the viscosity and, at the same time, can also improve the overall absorption capacity thanks to possible solvent-IL synergy and enhanced transport properties [13,14].

In the present work, six different choline-based AAILs, [Cho][AA] ILs, were synthetized *via* ionic metathesis and their CO_2 absorption capacity evaluated by a multi-technique approach in order to evaluate if the presence of different functional groups in the AA anion affects the CO_2 capture performance. To overcome any viscosity-related issue, dimethyl sulfoxide (DMSO) was selected as solvent, thanks to its high boiling point (189 °C) and its polar and aprotic character. IL-DMSO solutions with different IL concentrations were evaluated as absorbents for CO_2 (also investigating their cyclability). The effective CO_2 chemical fixation was proved by ^{1}H-NMR and *in-situ* ATR-IR experiments. Furthermore, potential *in vivo* developmental toxicity induced by one of the synthesized ILs has been evaluated on zebrafish (*Dario rerio*), as emerging vertebrate *in vivo* models for nanotoxicity screening, to stress the biocompatibility of this new class of ILs [44–47]. Here, the effects of this ionic liquid were analysed for different toxicological endpoints, including cardiac toxicity, behavioral and possible growth perturbations in zebrafish embryos/larvae. Notably, [Cho][AA] ILs were found to be non-toxic and IL solutions in DMSO demonstrated a molar uptake >0.5 mol CO_2/mol IL and the capacity to release CO_2 in mild condition, *i.e.* avoiding the solvent evaporation.

2. Experimental

2.1. Materials and syntheses

The ILs were prepared by ionic metathesis and purified as previously reported and described in detail in the Supporting Information (Section S1 and Scheme S1) [32,42]. The employed amino acids are glycine, alanine, serine, proline, phenylalanine and sarcosine and the corresponding choline [Cho][AA] ILs are choline glycinate ([Cho][Gly]), choline alaninate ([Cho][Ala]), choline serinate ([Cho][Ser]), choline prolinate ([Cho][Pro]), choline phenylalaninate ([Cho][Phe]) and choline sarcosinate ([Cho][Sar]) respectively, whose structures are shown in Scheme 2.

The syntheses were confirmed by means of ATR-IR (Fig. S1 and Table S1) and ^{1}H-NMR (Figs. 3, S2 and Table S2) spectroscopies. The residual KCl content (usually lower than 3 wt%) was evaluated by TG analysis (Fig. S3 and Table S3). AA salts were also prepared as reference materials, as described in Section S1 of Supporting Information. When needed, [Cho][AA] ILs were dissolved in DMSO (supplied by Merck, purity ≥ 99 %) with different concentration. Solutions were prepared as follows: the IL was weighted in a glass vial, and then the DMSO was added, by adjusting its quantity in order to obtain the desired concentration. About 5 g of solution were produced for each concentration. Viscosities and gravimetric densities of AAILs and their DMSO solutions were assessed and listed in Table S4.

3. Instrumental methods

3.1. CO_2 absorption

The absorption properties of the DMSO-IL systems were evaluated by means of two different experimental setups. A gravimetric approach was employed to measure the CO_2 capacity, whereas multiple absorption/desorption cycles were studied in a custom-made batch reactor with an IR CO_2 sensor to obtain information about the regenerability of the systems.

3.1.1. Gravimetric measurements

The CO_2 absorption was quantified using a gravimetric method. Different IL dilution in DMSO were tested: 50, 33, 20 and 12.5 wt%. Approximately 3 mL of solution were poured in a batch reactor (~4.5 mL), purged for 10 min with N_2 (30 mL/min) and weighted. Then, CO_2 (30 mL/min) was bubbled until no mass increase was observed. The captured CO_2 was calculated by mass difference before and after CO_2 contact, considering the reactor headspace contribution. Two quantities were calculated: CO_2 loading, defined as percentage of captured CO_2 over the total mass of DMSO-IL solution, and the molar efficiency, defined as the molar ratio between captured CO_2 and the amount of IL. The solvent evaporation was previously evaluated on pure DMSO and

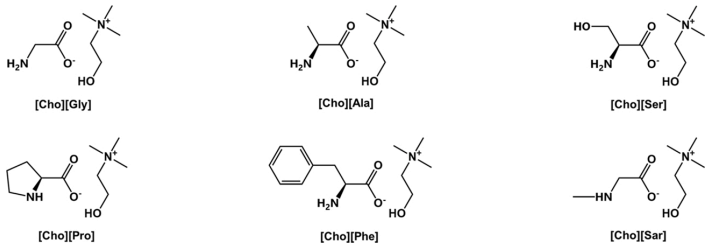

Scheme 2. Molecular structures of the synthetized [Cho][AA] ILs and their labels.

estimated to be lower than the balance sensitivity. The error was estimated by propagation starting from instrument sensitivity.

The adsorption capacity of pure ionic liquids has not been evaluated due to their high viscosity, which further increases when they react with CO_2 (until gel and foam formation), hampering the CO_2 diffusion into the bulk liquid phase. The first preliminary tests pointed out a negligible increase in weight also due to the loss of IL stripped by the gas flow.

3.1.2. Adsorption/desorption cycles

Multiple absorption and desorption cycles were carried out in a custom-made reactor provided by HEL Group (schematic is reported in Fig. S4). In a typical experiment, ~5 mL of DMSO-IL solution were used, according to the following steps: (i) purging with a N_2 flow (100 mL/min) for 10 min; (ii) absorption with a synthetic flue gas (20 %v CO_2 in N_2 [48] – 100 mL/min) until saturation (inlet and outlet gas stream had the same composition); (iii) desorption in N_2 flow (100 mL/min) increasing the temperature to 80 °C at 10 °C/min (this temperature was kept until all the CO_2 is released, *i.e.* when the CO_2 is no more detected in the outlet gas stream); (iv) cooling in N_2 flow (100 mL/min). Absorption/desorption cycles lasted similarly, approximately ~90 min. The steps from (ii) to (iv) were repeated 10 times.

3.1.3. NMR

^{1}H-NMR and ^{1}H-COSY analyses were performed to confirm the molecular structure of the [Cho][AA] ILs in 12.5 wt% solutions with DMSO-d_6. After that, [Cho][AA] ILs solutions were also investigated upon exposure to a pure CO_2 atmosphere (1 h until saturation) directly inside the NMR tube. Measurements were carried out on a JEOL 600 MHz.

3.1.4. IR spectroscopy

Attenuated total reflection infrared spectroscopy (ATR-IR) was employed to characterize pure ILs and to evaluate the interaction between CO_2 and DMSO-IL solutions. Measurements were carried out on a Bruker Invenio R Fourier transform spectrophotometer equipped with a mercury-cadmium-telluride (MCT) cryogenic detector. The spectra were acquired by accumulating the 32 scans (64 for the background spectrum) in 4000 – 600 cm^{-1} range with a resolution of 2 cm^{-1}.

An *in situ* IR experiment was specifically designed to mimic real operating condition: a synthetic flue gas mixture was employed (20 %v CO_2 in N_2) was adopted, whereas pure N_2 was chosen as inert gas. The interaction between the synthetic flue gas and DMSO-IL solutions was studied by using an Axiom-Hellma TNL 130H multiple reflections ATR cell designed for liquids analysis. The cell is equipped with an AMTIR-1 refractive element and the thermal control was ensured by a recirculating thermostatic bath. The gas composition and flow rates were controlled by means of a modified version of the setup described in ref. [32] (scheme reported in Fig. S5). In a typical experiment, 3 mL of 12.5 wt% IL-DMSO solution were injected in the cell and undergone to (i) purging, (ii) primary CO_2 absorption, (iii) thermal desorption, (iv) cooling and (v) secondary CO_2 absorption. In detail, the solution was: (i) purged with N_2 (100 mL/min) for 10 min to desorb water and other volatile impurities; the temperature was initially set to 25 °C; (ii) exposed to the synthetic flue gas (50 mL/min) at 25 °C; (iii) purged with N_2 (50 mL/min) while increasing the temperature to 80 °C with a 1 °C/min rate; (iv) cooled down to 25 °C under N_2 flow (20 mL/min); and (v) re-exposed to the synthetic flue gas (50 mL/min) for a second absorption step. Spectra were acquired continuously across each step.

3.2. In vivo toxicity assessment

3.2.1. Zebrafish maintenance

Adult zebrafish were maintained as previously reported [49]. Briefly, zebrafish were kept at 14h:10 h light-dark cycle and a temperature of 28 °C and were fed three times a day.

3.2.2. Developmental toxicity evaluation of ILs

Embryos at 4 h post-fertilization (hpf) were selected and placed in 24 well-culture plates in the medium [50]. Embryos were incubated at 26 ± 1 °C with four concentrations of [Cho][Ser] aqueous IL test solutions (10, 50, 100, and 200 ppm), and medium as a negative control. Survival and hatching rates were measured daily, while the frequency of movements and the heartbeat rate were calculated in zebrafish larvae at 72 hpf. All the analyses were performed by using a stereomicroscope equipped with a CCD camera. All the experiments were done in triplicates. All animal experiments were performed in full compliance with the revised directive 2010/63/EU.

3.2.3. Statistical analysis

All data were presented as mean ± S.D. Differences among the treatments were analysed by one-way analysis of variance (ANOVA) in combination with Holm-Sidak post hoc. A difference between the treated and the control group was considered to be statistically significant at $p<0.01$.

4. Results and discussion

4.1. CO_2 absorption capacity

The CO_2 absorption capacity of all [Cho][AA] ILs was assessed in DMSO solution at different concentration, by means of a gravimetric setup (described in detail in the experimental section). Tests were performed by bubbling pure CO_2 (1 atm) directly inside the solutions until saturation. The results (reported in Fig. 1 and in detail in Table S5) were similar for all the amino acids tested as IL anions, however all the [Cho][AA]-DMSO solutions exhibited absorption performances significantly higher compared to literature data of pure DMSO (which report values of about 0.5 wt% at 1 atm) [51]. It is worth noting that by decreasing the IL concentration in DMSO, the solution absorption capacity decreases, whereas the molar efficiency increases. This behavior is in line with previous results reported for [Cho][Gly]-DMSO and [Cho][Pro]-DMSO solutions [32]. Indeed, the higher distance of the ionic couples in less concentrated solutions affects the absorption mechanism, favoring the formation of carbamic acid and, at the same time, hindering the proton transfer involved in the ammonium-carbamate generation.

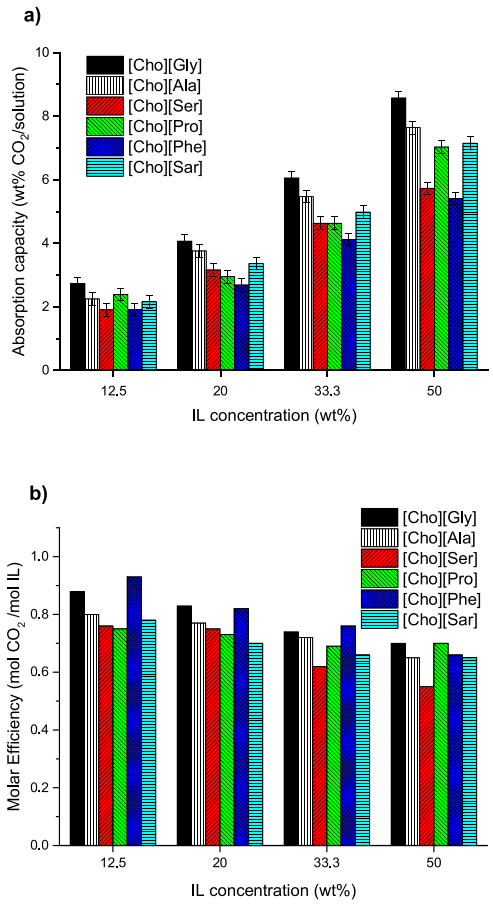

Fig. 1. CO_2 absorption data of [Cho][AA] ILs at different dilutions in DMSO. Panel (a): CO_2 uptake. Panel (b): molar efficiencies.

In general, the various ILs exhibit not so different molar efficiencies (Fig. 1, part b), whereas [Cho][Gly] and [Cho][Phe] possess the highest and the lowest absorption capacities at any concentration, respectively (Fig. 1, part a). Similarly to what previously observed for [Cho][Gly] [32], a solid precipitate forms in [Cho][Ala] solutions during the CO_2 capture process, already in the early stages of the experiment. The precipitate revealed to be solid alanine as testified by the ATR-IR spectra collected on the solid formed during the CO_2 absorption and not reported for the sake of brevity. Being irreversibly degraded during the first absorption cycle, [Gly] and [Ala] containing ILs were not tested in the following cyclic measurements.

Table 1 reports the absorption capacities obtained in the present work (at 50 wt% of IL in DMSO), compared with results obtained with other ILs. Both traditional and [Cho][AA] ILs are reported for completeness. It is worth noting that the significant difference between [bmim][BF_4] (AC = 0.26 and ME = 0.0133) and all the other IL-solvent systems is due to the simple physisorption process occurring in the presence of [bmim][BF_4], compared to the chemisorption of functionalized ILs. Among the functionalized ILs, the absorption capacity (AC) spreads approximately from 4 to 15 wt%, while the molar efficiency (ME) from ~ 0.2 to 0.9 mol/mol. Even though the set of ILs recently studied by Xiong et al. shows notably high absorption capacities, our samples have significantly higher MEs and, at the same time, the great

Table 1
CO_2 absorption capacity (AC, g(CO_2)/g(IL) wt% and g(CO_2)/g(solution) wt% in brackets), and molar efficiency (ME, mol(CO_2)/mol(IL)) for different ILs. Presence of solvent, concentration (wt%), temperature (°C) and pressure (bar) employed are reported in brackets, in the first column. Within each block, ILs are reported in order of increasing ME.

IL	AC	ME	Reference
[bmim][BF_4][a] (none, 100, 40, 1)	0.26 (0.26)	0.0133	[52]
[DBUH][1,2,3-triaz][a] (none, 100, 40, 1)	2.8 (2.8)	0.14	
[DBNH][1,2,3-triaz][a] (none, 100, 40, 1)	3.4 (3.4)	0.15	[53]
[DBUH][1,2,4-triaz][a] (none, 100, 40, 1)	5.0 (5.0)	0.25	
[DBNH][1,2,4-triaz][a] (none, 100, 40, 1)	6.2 (6.2)	0.27	
[E_1Py][SCN][a] (none, 100, 30, 15)	4.3 (4.3)	0.19	
[E_1Py][N(CN)$_2$][a] (none, 100, 30, 15)	8.3 (8.3)	0.38	[54]
[E_1Py][C(CN)$_3$][a] (none, 100, 30, 15)	9.2 (9.2)	0.48	
[$BuNH_2PrIM$][BF_4][b] (none, 100, 25, 1)	7.4 (7.4)	0.5	[20]
[bmin][Pro][a] (none, 100, 25, 2)	5.6 (5.6)	0.32	
[bmin][Gly][a] (none, 100, 25, 2)	7.9 (7.9)	0.38	[27]
[bmin][Ala][a] (none, 100, 25, 2)	7.6 (7.6)	0.39	
[bmin][Arg][a] (none, 100, 25, 2)	8.8 (8.8)	0.62	
[DBNH][Im][a] (none, 100, 40, 1)	14.9 (14.9)	0.65	
[DBNH][Py][a] (none, 100, 40, 1)	14.9 (14.9)	0.65	[55]
[DBUH][Im][a] (none, 100, 40, 1)	13.6 (13.6)	0.68	
[DBUH][Py][a] (none, 100, 40, 1)	13.4 (13.4)	0.67	
[Bmmorp][OAc][a] (H_2O, 40, 25, 18.8)	7.9 (19.6)	0.65	[29]
[Cho][Lys][b] (H_2O, 50, 22, 1)	19.4 (38.8)	2.2	[56]
[Cho][Pro][b] (PEG200, 50, 35, 1)	6 (12)	0.61	[30]
[Cho][Gly][b] (DMSO, 50, 25, 1)	8.6 (17.2)	0.78	
[Cho][Ala][b] (DMSO, 50, 25, 1)	7.6 (15.3)	0.79	
[Cho][Ser][b] (DMSO, 50, 25, 1)	5.7 (11.5)	0.61	This work
[Cho][Pro][b] (DMSO, 50, 25, 1)	7.0 (14.1)	0.84	
[Cho][Phe][b] (DMSO, 50, 25, 1)	5.4 (10.8)	0.70	
[Cho][Sar][b] (DMSO, 50, 25, 1)	7.2 (14.3)	0.71	

[a] Apparatus: CO_2 atmosphere on the absorbent.
[b] Apparatus: CO_2 stream.

advantage of good biocompatibility.

The 12.5 wt% concentration, exhibiting a slightly higher molar efficiency in previous gravimetric analyses (Fig. 1), was selected to test the cyclability of all [Cho][AA] ILs aiming to assess the feasibility of cyclic absorption/desorption in a demonstrator unit, simulating the experimental conditions of an industrial CO_2 capture technology. In this experimental setup, the adsorption capacity reflects the absorption and desorption rates of the IL solutions, rather than the real thermodynamic equilibrium, as in the gravimetric measurements. As reported in Fig. 2 (left axis), all [Cho][AA] ILs (and especially [Cho][Phe] and [Cho][Sar]) possess the highest CO_2 absorption capacity during the first cycle, then

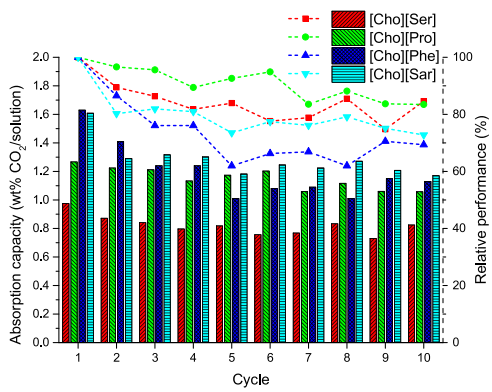

Fig. 2. Cyclic CO_2 absorption measurements over 10 absorption/desorption cycles. Left axis refers to the bars graphs reporting the CO_2 absorption capacity in wt% (w(CO_2)/w(solution)). Right axis refers to the relative performance (%) as the ratio between the absorbed CO_2 in the ith cycle and the absorbed CO_2 in the first cycle.

the CO_2 loading gradually decreases along the other absorption/desorption cycles. The CO_2 uptakes are definitely lower if compared to the results obtained for the same IL concentration in the gravimetric measurements of Fig. 1a, due to the lower partial pressure of CO_2 employed in the cyclic experiments. The data of CO_2 uptake highlight that [Cho][Phe] and [Cho][Sar] ILs are the most performing at this concentration and that their absorption capacities suddenly decrease, being soon comparable to the values computed for the [Cho][Pro] solution. In contrast, [Cho][Ser] solution exhibits the lowest values of CO_2 loading. Considering instead the relative performance data of Fig. 2 (right axis) we observe that: (i) the [Cho][Phe] solution, with the highest absorption capacity, possesses the lowest stability along cycles, with an average relative performance of around 65 %; (ii) [Cho][Ser] and [Cho][Sar] solutions have a medium stability, exhibiting relative performances of 75 % during the last three absorption/desorption cycles; (iii) the [Cho][Pro] solution shows the highest relative performance during the last cycles (around 85 %), despite its lower CO_2 uptake, being in some way the best compromise between the capacity to capture CO_2 and the stability along the absorption cycles.

It is worth highlighting that the IL containing the phenyl moiety exhibits the best absorption performances during the first cycle, but its absorption capacity decreases more during the cycles. In contrast, the IL containing a heterocyclic moiety with a secondary amine ([Cho][Pro]) possesses a lower absorption capacity, but it clearly maintains its capture performance during the cyclic experiments. Instead, the presence of a secondary amine inserted in a linear aliphatic chain does not seem affecting the capture performance and stability of [Cho][Sar].

In general, we can conclude that a direct comparison of the cyclic experiments with the gravimetric results is not straightforward, being the CO_2 absorption/desorption equilibria affected by different parameters, among which the IL concentration, the viscosity changes, the surface tension and the CO_2 diffusivity in the solution [57].

4.2. Assessment of the absorption mechanism

The CO_2 absorption process into a bulk [Cho][AA] IL is associated with a real chemical reactivity occurring between the CO_2 molecule and the amine group of the amino acid anion. Therefore, beside the evaluation of the absorption capacities of the DMSO-IL systems, we also investigated their interaction mechanism with CO_2 at a molecular level by means of ^{1}H-NMR and *in situ* ATR-IR spectroscopies.

4.3. NMR spectroscopy

In ^{1}H-NMR spectra collected upon interaction of the ILs/DMSO-d_6 solutions with CO_2 (in similar conditions to those adopted in the gravimetric absorption measurements, *i.e.* employing a pure CO_2 stream), the formation of carbamate/carbamic acid species was depicted by a remarkable de-shielding of the signals of the α and β protons to the AA amine moiety, as reported for [Cho][Sar] IL and [Cho][Ser] IL in Fig. 3. These ILs feature a primary and a secondary amine moiety respectively, and are representative for all the other [Cho][AA] ILs. When the [Cho][Ser] solution (12.5 wt%) interacts with pure CO_2, the α proton undergo a downshift from 2.91 ppm to 3.42 ppm, overlapping to the choline signal, while the well-defined β protons in the pending group at 3.33 and 3.27 ppm shifts to 3.56 ppm (Fig. 3a). [Cho][Sar] IL solution exhibits a similar behavior upon CO_2 absorption, both the α protons pattern and the sarcosinate N-Methyl group signal undergo a downshift from 2.77 to 3.56 ppm and from 2.22 to 2.67 ppm respectively (Fig. 3b). The choline signals were not affected by the CO_2 interaction as well as the equimolar [Cho][AA] ILs component ratio based on the signal integration for all the [Cho][AA] ILs (see Figs. 3 and S2).

After CO_2 absorption, the ^{1}H-NMR pattern suggests the neat prevalence of a unique chemical species with no traces of side products or degradation in the presence of both primary and secondary amine moieties. Considering the previous gravimetric results reporting the reaction with pure CO_2 and a ILs concentration of 12.5 wt%, these results are in perfect agreement with the molar efficiency values close to 1 obtained for [Cho][Gly] and [Cho][Phe] testifying the formation of carbamic acid. Concerning the other ILs, ([Cho][Sar], [Cho][Ala], [Cho][Pro] and [Cho][Ser]) gravimetric analyses show the concurrent formation in small concentrations of other species, such as carbamate or protonated amines. The absence of multiple signals should be substantiated: the identification and quantification by NMR spectroscopy of these species is not straightforward due to their low concentration, high viscosity of the media and potential overlap with peaks proper of the main species before and/or after the CO_2 absorption.

The protons in α to the amine in the reactive AAs are the most indicative to evaluate the presence and the formation of new speciesFor [Cho][Ser], [Cho][Pro] and [Cho][Sar] these signals end up overlapping to the choline pattern around 3.5 ppm (Figs. 3 and S2) upon CO_2 contact, thus preventing a precise signal integration. Moreover, it is reasonable to speculate a very close chemical shift for the α protons of very similar species like carbamic acid or carbamate derivative of the same AA. Finally, the high viscosity of AAILs causes the broadening of the proton signals which could hamper the identification of very diluted species.

A comprehensive list of ^{1}H-NMR peaks is reported in Table S2 pointing out a similar behavior for all the [Cho][AA] ILs.

4.4. In situ IR spectroscopy

The CO_2 capture and release were monitored by means of *in situ* ATR-IR spectroscopy, under experimental conditions close to the cyclic absorption measurements, in order to identify the chemical species generated by the CO_2 reaction with [Cho][AA] ILs. Room temperature absorption and following desorption at 80 °C were monitored by *in situ* ATR-IR experiments using 12.5 wt% IL-DMSO solutions of all the synthetized [Cho][AA] ILs. Spectra collected before and after CO_2 interaction and after CO_2 desorption at 80 °C are compared in Fig. 4. For the sake of brevity, only the results of [Cho][Ser] and [Cho][Sar]

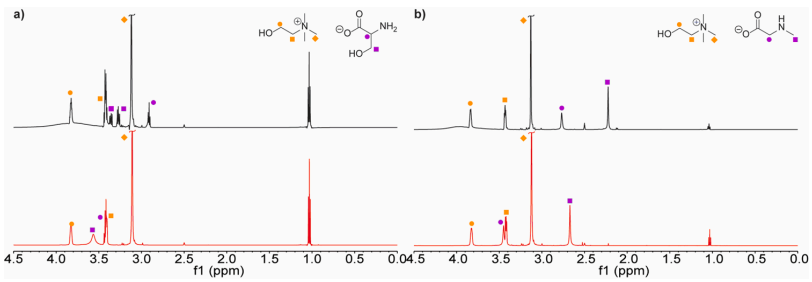

Fig. 3. ^{1}H-NMR spectra of a) [Cho][Ser] and b) [Cho][Sar] before (black) and after (red) pure CO_2 absorption at atmospheric pressure. Proton signals are labelled for choline (orange) and amino acids (purple).

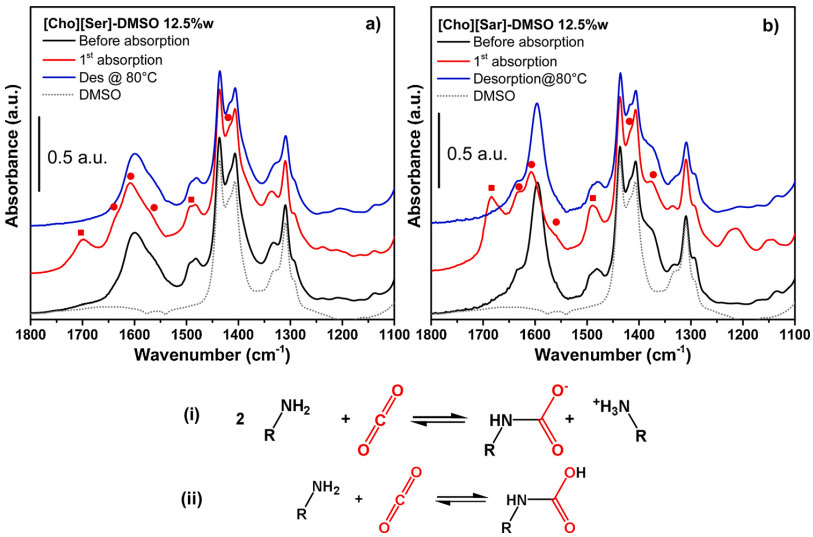

Fig. 4. Upper part: *in situ* ATR-IR spectra in the 1800-1100 cm^{-1} spectral region of (a) [Cho][Ser]-DMSO solution 12.5 wt%; and (b) [Cho][Sar]-DMSO solution 12.5 wt% before CO_2 absorption (black curves), after CO_2 absorption (red curves) and after desorption at 80 °C (blue curves). Dark red circles (●) and squares (■) highlight relevant spectral modifications related to the formation of ammonium carbamate and carbamic acid species, respectively. Lower part: chemical reactions between amines and CO_2 forming (i) ammonium carbamate and (ii) carbamic acid. The spectrum of bare DMSO is reported as reference (grey dotted curve).

(containing a primary or a secondary amine moiety in the AA, respectively) are reported in the main text. The spectra of the remaining ILs are available in Fig. S6 and the detailed summary of the spectral modification generated by the absorption of CO_2 in the different IL-DMSO solutions is reported in Table S6. All reported spectra were collected in different stages of the adsorption/desorption process (as reported in the legend of the figures) after reaching the equilibrium (*i.e.*, when spectral modifications were no more observable).

Spectra of [Cho][Ser]-DMSO 12.5 wt% solution are reported in Fig. 4a. Upon CO_2 absorption (*i.e.* passing from the black to the red curve), different spectral modifications occur. They are related to the reaction paths reported in the lower part of Fig. 4, *i.e.* to the formation of ammonium carbamate (i) and carbamic acid (ii) species, whose IR bands are labelled in Fig. 4 by circles and squares, respectively. In particular, the formation of the ammonium moiety is testified by the appearance in the red spectrum of [Cho][Ser]-DMSO of the shoulder at 1650 cm^{-1} and of the band at 1495 cm^{-1}, ascribed to the asymmetric and the symmetric bending modes of the NH_3^+ ion. A further confirmation arises from the changes in the vibrational modes of carboxylate species: a +15 cm^{-1} shift of the OCO- asymmetric stretching is indeed evident, suggesting the formation of new carboxylate species (*i.e.*, present in the carbamate moiety). The formation of carbamic acid, instead, is testified by the growth of an intense band at 1700 cm^{-1}, ascribed to the stretching mode of its carbonyl group. All the IL-DMSO solutions containing primary amines (*i.e.*, [Cho][Gly], [Cho][Ala] and [Cho][Phe]) show the same spectral behavior (see Fig. S6).

In contrast, the [Cho][Sar]-DMSO 12.5 wt% solution (see Fig. 4b) spectroscopically behaves in a slightly different way. Indeed, in the presence of [Cho][Sar], the protonation occurs on a secondary amine moiety, giving rise to NH_2^+ species when the ammonium carbamate forms. The asymmetric and symmetric NH_2^+ bending modes appear at 1630 and 1490 cm^{-1}, respectively. The formation of ammonium carbamate species is further confirmed by the evolution of the OCO- stretching vibrations: upon CO_2 interaction the asymmetric mode undergoes an upward shift from 1595 to 1610 cm^{-1} while it decreases in intensity, partly overlapping to the signal of protonated amines. The formation of carbamic acid is instead confirmed by the appearance of a peak at around 1700 cm^{-1}, ascribed to the stretching mode of the carbonyl moiety. A similar behavior is observed for [Cho][Pro] (containing an AA with a heterocyclic secondary amine) [32]. In all the [Cho][AA] solutions, the spectra obtained *in situ* after CO_2 desorption by heating at 80 °C, (see Figs. 4 and S6, blue curves) exhibit a spectral profile very similar to the pristine [Cho][AA] IL. Indeed, all the aforementioned signals disappear, testifying that, during the ATR-IR experiments carried out *in situ*, the CO_2 captured in the form of carbamic acid and ammonium carbamate species is totally released at 80 °C, without any solvent evaporation. *In situ* ATR-IR measurements proved the capacity of CO_2 to effectively react with all the considered amine moieties. In particular, two possible reactions paths were detected: the 1:2 reaction of two amine functional groups (deriving from two distinct IL molecule) with one CO_2 molecule, forming an ammonium carbamate couple (reaction path (i) in Fig. 4), and the 1:1 reaction of a single amine group with one CO_2 molecule, producing carbamic acid (reaction path (ii) in Fig. 4).

The gravimetric absorption measurements proved that the overall [Cho][AA] IL:CO_2 stoichiometry (determined by the molar efficiency) varies according to the [Cho][AA] IL concentration in the DMSO solution. Now, after the spectroscopic identification of two distinct reaction paths, we can infer the IL concentration likely determines the preferred absorption mechanism, occurring *via* the "ammonium carbamate route" in the more concentrated solutions or preferentially through "the carbamic acid route" in the less concentrated ones.

We further checked the cyclability of the absorption process on the [Cho][Ser]-DMSO 12.5 wt% solution by means of *in situ* ATR-IR spectroscopy, by performing a secondary absorption run (always at room temperature), after the primary desorption step at 80 °C. As reported in Fig. S7, spectra collected *in situ* immediately after the first and the second absorption cycle, show negligible differences. This result again highlights the excellent cyclability of these IL-DMSO solutions.

These last results seem to be in contrast with the data of the multiple absorption/desorption cycles collected using the custom-made reactor (to mimic the experimental conditions of a real CO_2 capture technology) and reported in Fig. 2. For this reason, we decided to collect ATR-IR spectra of one of the IL-DMSO solution immediately after the synthesis (fresh) and after ten CO_2 absorption/desorption cycles (used: 10 cycles) in the custom-made reactor, to explain the decrease of the absorption performances observed after several cycles employing this setup. The [Cho][Phe]-DMSO solution was selected due to its more pronounced decrease of the CO_2 absorption capacity during the cyclic tests. Spectra are reported in the Supporting Information (Section S3.3, Fig. S8). Before the ATR-IR measurements, the 10th cycle has been followed by a final desorption step at 80 °C, until CO_2 was no more detected in the

outlet gas stream. It means that, if the absorption process is totally reversible, the spectra collected on fresh sample (black curve) and on the solution after the 10th absorption/desorption cycle (red curve) should coincide. Fig. S8 reports the spectra of the [Cho][Phe]-DMSO solution at the concentration of 12.5 wt% in the 1800-1100 cm^{-1} spectral range, where the bands generated by the reaction with CO_2 are mainly located. The spectrum collected after 10 cycles (red) does not show any spectral evidence of possible degradation phenomena of the IL and exhibits only the bands generated by the chemical absorption of CO_2. The presence of the signals due to the species generated by the chemical reaction of CO_2 with the IL proves that the specific conditions used in cyclic experiment performed in the custom-made reactor do not allow a complete regeneration of the IL-DMSO solution upon several absorption/desorption cycles. Despite these results, the *in situ* ATR-IR measurements clearly highlighted the great potentiality of these bio-based ionic liquids solutions that can ideally release all the absorbed CO_2 in mild conditions.

4.5. In vivo toxicity assessment

To evaluate the developmental toxicity of the [Cho][AA] ILs on zebrafish, we treated the embryos with various concentrations (10, 50, 100, and 200 ppm) of [Cho][Ser] for 120 hpf, and we measured the different toxicological endpoints. The resulting graphs are reported in Fig. 5. In particular, the hatching and survival rates were monitored every 24 h. Following the exposure with IL from 10 ppm up to 200 ppm, the survival rates showed a profile time and concentration-dependent with no relevant decrease during the temporal window analysed (Fig. 5a). At the highest concentration investigated (200 ppm) and after 120 hpf, the value of survival was up to 95 %. In addition, the ability to successfully hatch (hatching rates) of the treated groups showed negligible reduction compared to the control group (Fig. 5b). The treated embryos hatched in the normal temporal window (between 48 and 72 hpf). In fact, at 72 hpf, 95 % of embryos treated with the highest concentration of [Cho][Ser] hatched. In accordance with the OECD guidelines [58], the profiles and trends of the hatching and survival rates of zebrafish treated with [Cho][Ser] indicated that the investigated IL did not have adverse effects on the embryogenesis of zebrafish.

To further investigate the effects of the IL on zebrafish, we measured the heartbeat rates and frequency of movements of treated larvae at 72 hpf. The heartbeat rates of larvae exposed to the [Cho][Ser] showed no significant decrease or increase compared to the control groups (Fig. 5c). Similarly, the frequency of movements of 72 hpf larvae exposed to [Cho][Ser] (Fig. 5d), presented no perturbations in comparison with the control samples. The values of heartbeat rate and frequency of movements indicated that [Cho][Ser] did not influence the cardiac and swimming activities of treated larvae, further confirming that the IL did not affect the embryogenesis.

5. Conclusions

In this work, we presented the complete advanced characterization of different amino acid-based ILs ([Cho][AA] ILs), as such or during their reaction with CO_2. The toxicity of one [Cho][AA] IL was assessed as well, to definitely prove the high bio-compatibility of these systems.

The synthetic method developed was proven to be generally suitable for different AAs, with a minimal content of residual impurity (as such KCl). The interaction between the [Cho][AA] ILs and CO_2 was first tested by means of gravimetric measurements carried out at different dilutions in DMSO. The dependence of the molar efficiency on the concentration of [Cho][AA] ILs in DMSO suggested that different interaction mechanisms could be involved, as already proposed in our previous work [32]. Except for [Cho][Gly] and [Cho][Ala] solutions,

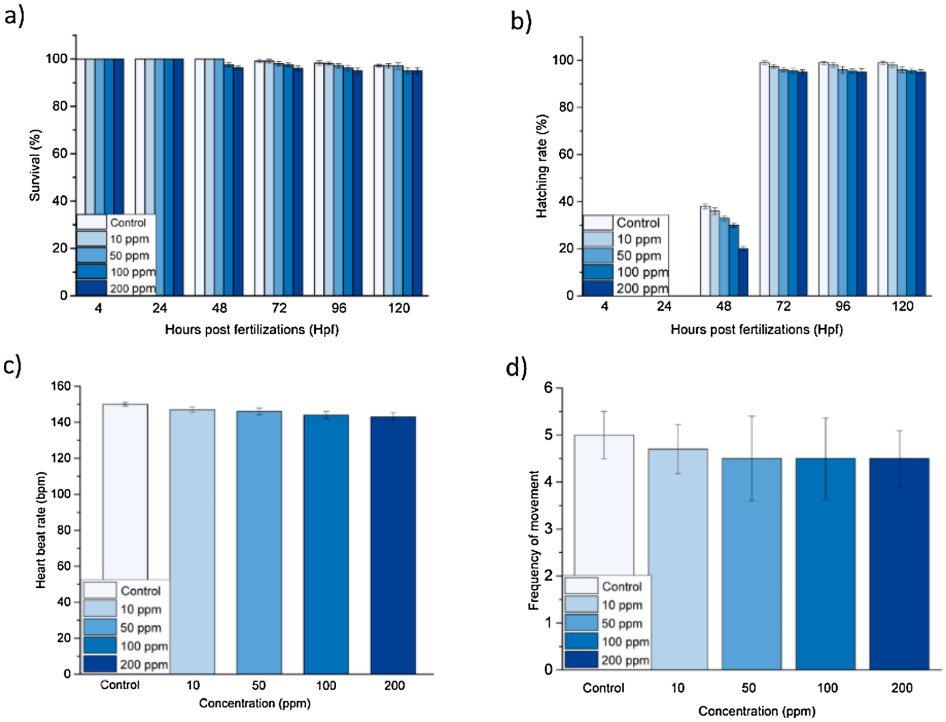

Fig. 5. (a) Survival rate (b) hatching rates, (c) heat beat rate and (d) frequency of movements of zebrafish treated with [Cho][Ser]. Data are calculated as means ± S. D., from three independent experiments, n = 80; *p ≤ 0.1 in comparison to the control.

undergoing AA precipitation upon CO_2 exposure, subsequent cyclic absorption/desorption tests with a custom-made reactor demonstrated the effectiveness of [Cho][AA] IL-DMSO systems in the liquid phase CO_2 capture process, even for several cycles, as desirable for real applications. In particular, the [Cho][Phe] solution possessed the highest CO_2 uptake during the first cycle, but its absorption capacity suddenly decreased in the following cycles. On the other hand, the [Cho][Pro] solution, containing a heterocyclic moiety with a secondary amine, exhibited the highest stability along the absorption cycles, loosing just the 15 % of its absorption performance during the first ten cycles. Further studies are needed to really understand the main reason of this peculiar behavior and to explain how the presence of different functionalities in the IL affects the final absorption performances.

The CO_2 capture and release mechanisms were studied in detail by means of ^{1}H-NMR and *in situ* ATR-IR spectroscopies under different experimental conditions. ^{1}H-NMR spectroscopy confirmed the neat prevalence of a unique species identified with carbamic acid when the sorbents are exposed to a pure CO_2 stream until saturation. ATR-IR spectroscopy, performed employing a synthetic flue gas stream (*i.e.* in the presence of diluted CO_2) proved the formation of both carbamic acid and ammonium carbamate species, justifying the CO_2: AAIL stoichiometry in the 0.5–1 range observed in the gravimetric experiments. It is evident that the CO_2 relative pressure in the gas stream and the different experimental conditions could be responsible for the preferable absorption pathway giving rise to distinct species (carbamic acid and/or ammonium carbamate). Indeed, the high CO_2 pressure employed in NMR experiments probably promotes the formation of a single product (carbamic acid).

Another important result concerns the CO_2 temperature release of the [Cho][AA] IL-DMSO solutions. Indeed, it is worth noting that, compared to the classical aqueous amine solutions (requiring temperatures higher than 100 °C to achieve a complete CO_2 release), these ILs totally desorbs CO_2 at milder conditions (the total release of CO_2 occurs at 70−80 °C, as clearly proved by *in situ* ATR-IR experiments).

Finally, the present study reported, for the first time, the *in vivo* evaluation of the toxicological profile of a [Cho][AA] IL in vertebrate systems, demonstrating the non-toxicity and high biocompatibility of [Cho][Ser] in zebrafish during the development. More in general, the results reported in this work proved how these bio-inspired ILs are very promising alternatives to the classical amine aqueous solutions, mainly thanks to their significantly low CO_2 release temperature, good regenerability and high biocompatibility.

Author statement

Giulio Latini: Conceptualization Methodology Validation Investigation, Data Curation, Writing - Original Draft, Writing - Review & Editing, Visualization. Matteo Signorile: Methodology, Writing - Original Draft, Writing - Review & Editing. Francesca Rosso: Investigation, Writing - Review & Editing. Andrea Fin: Investigation, Resources Writing Original Draft, Writing Review & Editing. Marta d'Amora: Validation, Formal analysis, Investigation, Writing Original Draft, Writing - Review & Editing. Silvia Giordani: Resources, Writing - Review & Editing. Fabrizio Pirri: Resources, Founding acquisition, Supervision. Valentina Crocellà Methodology, Investigation, Writing - Review & Editing, Supervision. Silvia Bordiga: Resources, Writing - Review & Editing, Supervision. Sergio Bocchini: Conceptualization, Methodology, Investigation, Resources, Writing Review & Editing, Supervision, Project Administration.

Declaration of Competing Interest

The authors declare that they have no known competing financial interests or personal relationships that could have appeared to influence the work reported in this paper.

Acknowledgements

We would like to acknowledge Ms. Maria Chiara Lombardi for her contribution to the gravimetric measures and NMR analysis. This project has received funding from the European Union's Horizon 2020 research and innovation program under grant agreement 768583– RECODE (Recycling carbon dioxide in the cement industry to produce added-value additives: a step towards a CO_2 circular economy) project.

Appendix A. Supplementary data

Supplementary material related to this article can be found, in the online version, at doi:https://doi.org/10.1016/j.jcou.2021.101815.

References

[1] Record annual increase of carbon dioxide observed at Mauna Loa for 2015, Science.gov Websites. https://www.noaa.gov/news/record-annual-increase-of-carbon-dioxide-observed-at-mauna-loa-for-2015. (Consulted 27 November 2021).
[2] Vincent Gray, Climate change 2007: the physical science basis summary for policymakers, Energy Environ. 18 (3–4) (2007) 433–440, https://doi.org/10.1260/095830507781076194.
[3] S. Bocchini, et al., The virtuous CO_2 circle or the three cs: Capture, cache, and convert, J. Nanomater. 2017 (2017) 1–14, https://doi.org/10.1155/2017/6594151.
[4] G. Corp, Seperating Acid Gases, US1783901, 1930.
[5] D. Barth, C. Tondre, G. Lappai, J.J. Delpuech, Kinetic study of carbon dioxide reaction with tertiary amines in aqueous solutions, J. Phys. Chem. 85 (November (24)) (1981) 3660–3667, https://doi.org/10.1021/j150624a027.
[6] P.M.M. Blauwhoff, G.F. Versteeg, W.P.M. Van Swaaij, A study on the reaction between CO_2 and alkanolamines in aqueous solutions, Chem. Eng. Sci. 39 (2) (1984) 207–225, https://doi.org/10.1016/0009-2509(84)80021-4.
[7] B. Arstad, R. Blom, O. Swang, CO_2 absorption in aqueous solutions of alkanolamines: mechanistic insight from quantum chemical calculations, J. Phys. Chem. A 111 (February (7)) (2007) 1222–1228, https://doi.org/10.1021/jp065301v.
[8] G.T. Rochelle, Amine scrubbing for CO_2 capture, Science (80-.) 325 (September (5948)) (2009) 1652–1654, https://doi.org/10.1126/science.1176731.
[9] P. Walden, Ueber die molekulargrosse und elektrische leitfahigkeiteiniger gesehmolzenen salze, Bull. Acad. Imper. Sci (St Petersburg) 8 (6) (1914) 405–422.
[10] N.V. Plechkova, K.R. Seddon, Applications of ionic liquids in the chemical industry, Chem. Soc. Rev. 37 (1) (2008) 123–150, https://doi.org/10.1039/b006677j.
[11] Z.Z. Yang, Y.N. Zhao, L.N. He, CO_2chemistry: task-specific ionic liquids for CO2 capture/activation and subsequent conversion, RSC Adv. 1 (4) (2011) 545–567, https://doi.org/10.1039/c1ra00307k.
[12] S. Sarmad, J.P. Mikkola, X. Ji, Carbon dioxide capture with ionic liquids and deep eutectic solvents: a new generation of sorbents, ChemSusChem 10 (January (2)) (2017) 324–352, https://doi.org/10.1002/cssc.201600987.
[13] S. Zeng, et al., Ionic-liquid-based CO_2 capture systems: structure, interaction and process, Chem. Rev. 117 (14) (2017) 9625–9673, https://doi.org/10.1021/acs.chemrev.7b00072.
[14] G. Cui, J. Wang, S. Zhang, Active chemisorption sites in functionalized ionic liquids for carbon capture, Chem. Soc. Rev. 45 (15) (2016) 4307–4339, https://doi.org/10.1039/c5cs00462d.
[15] J.P. Hallett, T. Welton, Room-temperature ionic liquids: solvents for synthesis and catalysis. 2, Chem. Rev. 111 (May (5)) (2011) 3508–3576, https://doi.org/10.1021/cr1003248.
[16] R.D. Rogers, K.R. Seddon, Ionic liquids – solvents of the future? Science (80-.) 302 (October (5646)) (2003) 792–793, https://doi.org/10.1126/science.1090313.
[17] H. Olivier-Bourbigou, L. Magna, D. Morvan, Ionic liquids and catalysis: recent progress from knowledge to applications, Appl. Catal. A Gen. 373 (1–2) (2010) 1–56, https://doi.org/10.1016/j.apcata.2009.10.008.
[18] C. Verma, I.B. Obot, I. Bahadur, E.S.M. Sherif, E.E. Ebenso, Choline based ionic liquids as sustainable corrosion inhibitors on mild steel surface in acidic medium: gravimetric, electrochemical, surface morphology, DFT and Monte Carlo simulation studies, Appl. Surf. Sci. 457 (2018) 134–149, https://doi.org/10.1016/j.apsusc.2018.06.035.
[19] C. Verma, E.E. Ebenso, M.A. Quraishi, Corrosion inhibitors for ferrous and non-ferrous metals and alloys in ionic sodium chloride solutions: a review, J. Mol. Liq. 248 (2017) 927–942, https://doi.org/10.1016/j.molliq.2017.10.094.
[20] E.D. Bates, R.D. Mayton, I. Ntai, J.H. Davis, CO_2 capture by a task-specific ionic liquid, J. Am. Chem. Soc. 124 (February (60) (2002) 926–927, https://doi.org/10.1021/ja017593d.
[21] P. Hu, et al., Absorption performance and mechanism of CO_2 in aqueous solutions of amine-based ionic liquids, Energy Fuels 29 (9) (2015) 6019–6024, https://doi.org/10.1021/acs.energyfuels.5b01062.
[22] Z.Z. Yang, L.N. He, S.Y. Peng, A.H. Liu, Lewis basic ionic liquids-catalyzed synthesis of 5-aryl-2-oxazolidinones from aziridines and CO_2 under solvent-free conditions, Green Chem. 12 (10) (2010) 1850–1854, https://doi.org/10.1039/c0gc00286k.

[23] Z.Z. Yang, L.N. He, C.X. Miao, S. Chanfreau, Lewis basic ionic liquids-catalyzed conversion of carbon dioxide to cyclic carbonates, Adv. Synth. Catal. 352 (August (13)) (2010) 2233–2240, https://doi.org/10.1002/adsc.201000239.
[24] M.J. Earle, K.R. Seddon, Ionic liquids. Green solvents for the future, Pure Appl. Chem. 72 (January (7)) (2000) 1391–1398, https://doi.org/10.1351/pac200072071391.
[25] K.M. Docherty, C.F. Kulpa, Toxicity and antimicrobial activity of imidazolium and pyridinium ionic liquids, Green Chem. 7 (4) (2005) 185–189, https://doi.org/10.1039/b419172b.
[26] R.J. Bernot, M.A. Brueseke, M.A. Evans-White, G.A. Lamberti, Acute and chronic toxicity of imidazolium-based ionic liquids on Daphnia magna, Environ. Toxicol. Chem. 24 (1) (2005) 87–92, https://doi.org/10.1897/03-635.1.
[27] Y.S. Sistla, A. Khanna, CO_2 absorption studies in amino acid-anion based ionic liquids, Chem. Eng. J. 273 (August) (2015) 268–276, https://doi.org/10.1016/j.cej.2014.09.043.
[28] N.M. Yunus, N.H. Halim, C.D. Wilfred, T. Murugesan, J.W. Lim, P.L. Show, Thermophysical properties and CO_2 absorption of ammonium-based protic ionic liquids containing acetate and butyrate anions, Processes 7 (November (11)) (2019) 820, https://doi.org/10.3390/pr7110820.
[29] C. Ma, S.K. Shukla, R. Samikannu, J.P. Mikkola, X. Ji, CO_2 separation by a series of aqueous morpholinium-based ionic liquids with acetate anions, ACS Sustain. Chem. Eng. 8 (January (1)) (2020) 415–426, https://doi.org/10.1021/acssuschemeng.9b05686.
[30] X. Li, et al., Absorption of CO_2 by ionic liquid/polyethylene glycol mixture and the thermodynamic parameters, Green Chem. 10 (August (8)) (2008) 879–888, https://doi.org/10.1039/b801948g.
[31] S. Yuan, Y. Chen, X. Ji, Z. Yang, X. Lu, Experimental study of CO_2 absorption in aqueous cholinium-based ionic liquids, Fluid Phase Equilib. 445 (2017) 14–24, https://doi.org/10.1016/j.fluid.2017.04.001.
[32] G. Latini, M. Signorile, V. Crocellà, S. Bocchini, C.F. Pirri, S. Bordiga, Unraveling the CO_2 reaction mechanism in bio-based amino-acid ionic liquids by operando ATR-IR spectroscopy, Catal. Today 336 (October) (2019) 148–160, https://doi.org/10.1016/j.cattod.2018.12.050.
[33] R.E. Kirk, et al., Kirk-Othmer Encyclopedia of Chemical Technology, 4th ed., John Wiley & Sons, Inc, 2000.
[34] T.M. Lammens, M.C.R. Franssen, E.L. Scott, J.P.M. Sanders, Availability of protein-derived amino acids as feedstock for the production of bio-based chemicals, Biomass Bioenergy 44 (September) (2012) 168–181, https://doi.org/10.1016/j.biombioe.2012.04.021.
[35] M. Petkovic, et al., Novel biocompatible cholinium-based ionic liquids toxicity and biodegradability, Green Chem. 12 (4) (2010) 643–664, https://doi.org/10.1039/b922247b.
[36] K.D. Weaver, H.J. Kim, J. Sun, D.R. MacFarlane, G.D. Elliott, Cyto-toxicity and biocompatibility of a family of choline phosphate ionic liquids designed for pharmaceutical applications, Green Chem. 12 (3) (2010) 507–551, https://doi.org/10.1039/b918726j.
[37] X.D. Hou, Q.P. Liu, T.J. Smith, N. Li, M.H. Zong, Evaluation of toxicity and biodegradability of cholinium amino acids ionic liquids, PLoS One 8 (3) (2013), https://doi.org/10.1371/journal.pone.0059145.
[38] W. Gouveia, et al., Toxicity of ionic liquids prepared from biomaterials, Chemosphere 104 (2014), https://doi.org/10.1016/j.chemosphere.2013.10.055.
[39] Q.P. Liu, X.D. Hou, N. Li, M.H. Zong, Ionic liquids from renewable biomaterials: synthesis, characterization and application in the pretreatment of biomass, Green Chem. 14 (January (2)) (2012) 304–307, https://doi.org/10.1039/c2gc16128a.
[40] S. De Santis, et al., Cholinium-amino acid based ionic liquids: a new method of synthesis and physico-chemical characterization, Phys. Chem. Chem. Phys. 17 (32) (2015) 20687–20698, https://doi.org/10.1039/c5cp01612f.
[41] D.J. Tao, Z. Cheng, F.F. Chen, Z.M. Li, N. Hu, X.S. Chen, Synthesis and thermophysical properties of biocompatible cholinium-based amino acid ionic liquids, J. Chem. Eng. Data 58 (6) (2013) 1542–1548, https://doi.org/10.1021/je301103d.
[42] E. Davarpanah, S. Hernández, G. Latini, C.F. Pirri, S. Bocchini, Enhanced CO_2 absorption in organic solutions of biobased ionic liquids, Adv. Sustain. Syst. 4 (December (1)) (2020) 1900067, https://doi.org/10.1002/adsu.201900067.
[43] K.E. Gutowski, E.J. Maginn, Amine-functionalized task-specific ionic liquids: a mechanistic explanation for the dramatic increase in viscosity upon complexation with CO_2 from molecular simulation, J. Am. Chem. Soc. 130 (44) (2008) 14690–14704, https://doi.org/10.1021/ja804654b.
[44] M. D'Amora, S. Giordani, The utility of zebrafish as a model for screening developmental neurotoxicity, Front. Neurosci. 12 (December) (2018), https://doi.org/10.3389/fnins.2018.00976.
[45] Y.J. Dai, et al., Zebrafish as a model system to study toxicology, Environ. Toxicol. Chem. 33 (January (1)) (2014) 11–17, https://doi.org/10.1002/etc.2406.
[46] L. Truong, S.L. Harper, R.L. Tanguay, Evaluation of embryotoxicity using the zebrafish model, in: Methods in Molecular Biology (Clifton, N.J.), vol. 691, 2011, pp. 271–279.
[47] A.J. Hill, H. Teraoka, W. Heideman, R.E. Peterson, Zebrafish as a model vertebrate for investigating chemical toxicity, Toxicol. Sci. 86 (July (1)) (2005) 6–19, https://doi.org/10.1093/toxsci/kfi110.
[48] J.G. Vitillo, Magnesium-based systems for carbon dioxide capture, storage and recycling: from leaves to synthetic nanostructured materials, RSC Adv. 5 (46) (2015) 36192–36239, https://doi.org/10.1039/c5ra02835c.
[49] M. d'Amora, A. Lamberti, M. Fontana, S. Giordani, Toxicity assessment of laser-induced graphene by zebrafish during development, J. Phys. Mater. 3 (June (3)) (2020) 034008, https://doi.org/10.1088/2515-7639/ab9522.
[50] A. Romero, A. Santos, J. Tojo, A. Rodríguez, Toxicity and biodegradability of imidazolium ionic liquids, J. Hazard. Mater. 151 (1) (2008) 268–273, https://doi.org/10.1016/j.jhazmat.2007.10.079.
[51] L. Hua, Thermodynamic model of solubility for CO_2 in dimethyl sulfoxide, Phys. Chem. Liq. 47 (June (3)) (2009) 296–301, https://doi.org/10.1080/00319100701788360.
[52] J. Jacquemin, M.F. Costa Gomes, P. Husson, V. Majer, Solubility of carbon dioxide, ethane, methane, oxygen, nitrogen, hydrogen, argon, and carbon monoxide in 1-butyl-3-methylimidazolium tetrafluoroborate between temperatures 283K and 343K and at pressures close to atmospheric, J. Chem. Thermodyn. 38 (April (4)) (2006) 490–502, https://doi.org/10.1016/j.jct.2005.07.002.
[53] X. Zhang, W. Xiong, Z. Tu, L. Peng, Y. Wu, X. Hu, Supported ionic liquid membranes with dual-site interaction mechanism for efficient separation of CO_2, ACS Sustain. Chem. Eng. 7 (June (12)) (2019) 10792–10799, https://doi.org/10.1021/acssuschemeng.9b01604.
[54] S. Hussain, et al., Investigation uncovered the impact of anions on CO_2 absorption by low viscous ether functionalized pyridinium ionic liquids, J. Mol. Liq. 336 (August) (2021) 116362, https://doi.org/10.1016/j.molliq.2021.116362.
[55] W. Xiong, M. Shi, L. Peng, X. Zhang, X. Hu, Y. Wu, Low viscosity superbase protic ionic liquids for the highly efficient simultaneous removal of H_2S and CO_2 from CH_4, Sep. Purif. Technol. 263 (May) (2021) 118417, https://doi.org/10.1016/j.seppur.2021.118417.
[56] C.F. Martins, et al., Modelling CO_2 absorption in aqueous solutions of cholinium lysinate ionic liquid, Chem. Eng. J. 421 (October) (2021) 127875, https://doi.org/10.1016/j.cej.2020.127875.
[57] F. Ortloff, M. Roschitz, M. Ahrens, F. Graf, T. Schubert, T. Kolb, Characterization of functionalized ionic liquids for a new quasi-isothermal chemical biogas upgrading process, Sep. Purif. Technol. 195 (April) (2018) 413–430, https://doi.org/10.1016/j.seppur.2017.12.014.
[58] OECD, Test No. 236: Fish Embryo Acute Toxicity (FET) Test, no. July, OECD, 2013.